Research Topics

Advances and applications of distributed optical fiber sensing (DOFS) in multi-scales geoscience problems

Edited by
Yibo Wang, Xiaowei Chen, Ge Jin, Baoshan Wang, Xiangfang Zeng,
Ge Zhan and Yang Zhao

Published in
Frontiers in Earth Science

ISSN 1664-8714
ISBN 978-2-83251-384-2
DOI 10.3389/978-2-83251-384-2

About Frontiers

Frontiers is more than just an open access publisher of scholarly articles: it is a pioneering approach to the world of academia, radically improving the way scholarly research is managed. The grand vision of Frontiers is a world where all people have an equal opportunity to seek, share and generate knowledge. Frontiers provides immediate and permanent online open access to all its publications, but this alone is not enough to realize our grand goals.

Frontiers journal series

The Frontiers journal series is a multi-tier and interdisciplinary set of open-access, online journals, promising a paradigm shift from the current review, selection and dissemination processes in academic publishing. All Frontiers journals are driven by researchers for researchers; therefore, they constitute a service to the scholarly community. At the same time, the *Frontiers journal series* operates on a revolutionary invention, the tiered publishing system, initially addressing specific communities of scholars, and gradually climbing up to broader public understanding, thus serving the interests of the lay society, too.

Dedication to quality

Each Frontiers article is a landmark of the highest quality, thanks to genuinely collaborative interactions between authors and review editors, who include some of the world's best academicians. Research must be certified by peers before entering a stream of knowledge that may eventually reach the public - and shape society; therefore, Frontiers only applies the most rigorous and unbiased reviews. Frontiers revolutionizes research publishing by freely delivering the most outstanding research, evaluated with no bias from both the academic and social point of view. By applying the most advanced information technologies, Frontiers is catapulting scholarly publishing into a new generation.

What are Frontiers Research Topics?

Frontiers Research Topics are very popular trademarks of the *Frontiers journals series*: they are collections of at least ten articles, all centered on a particular subject. With their unique mix of varied contributions from Original Research to Review Articles, Frontiers Research Topics unify the most influential researchers, the latest key findings and historical advances in a hot research area.

Find out more on how to host your own Frontiers Research Topic or contribute to one as an author by contacting the Frontiers editorial office: frontiersin.org/about/contact

Advances and applications of distributed optical fiber sensing (DOFS) in multi-scales geoscience problems

Topic editors
Yibo Wang — Institute of Geology and Geophysics, Chinese Academy of Sciences (CAS), China
Xiaowei Chen — University of Oklahoma, United States
Ge Jin — Colorado School of Mines, United States
Baoshan Wang — University of Science and Technology of China, China
Xiangfang Zeng — Innovation Academy for Precision Measurement Science and Technology, Chinese Academy of Sciences (CAS), China
Ge Zhan — TGS-NOPEC Geophysical Company (Norway), Norway
Yang Zhao — China University of Petroleum, Beijing, China

Citation
Wang, Y., Chen, X., Jin, G., Wang, B., Zeng, X., Zhan, G., Zhao, Y., eds. (2023). *Advances and applications of distributed optical fiber sensing (DOFS) in multi-scales geoscience problems*. Lausanne: Frontiers Media SA.
doi: 10.3389/978-2-83251-384-2

Author GZ was employed by the company TGS. The remaining authors declare that the research was conducted in the absence of any commercial or financial relationships that could be construed as a potential conflict of interest.

Table of contents

Frontiers in Earth Science

TYPE Editorial
PUBLISHED 06 January 2023
DOI 10.3389/feart.2022.1126105

OPEN ACCESS

EDITED AND REVIEWED BY
Derek Keir,
University of Southampton,
United Kingdom

*CORRESPONDENCE
Yibo Wang,
wangyibo@mail.iggcas.ac.cn

SPECIALTY SECTION
This article was submitted to Solid Earth Geophysics, a section of the journal Frontiers in Earth Science

RECEIVED 17 December 2022
ACCEPTED 21 December 2022
PUBLISHED 06 January 2023

CITATION
Wang Y, Zhao Y, Jin G, Chen X, Zhan G, Wang B and Zeng X (2023), Editorial: Advances and applications of distributed optical fiber sensing (DOFS) in multi-scales geoscience problems.
Front. Earth Sci. 10:1126105.
doi: 10.3389/feart.2022.1126105

Editorial: Advances and applications of distributed optical fiber sensing (DOFS) in multi-scales geoscience problems

Yibo Wang[1]*, Yang Zhao[2], Ge Jin[3], Xiaowei Chen[4], Ge Zhan[5], Baoshan Wang[6] and Xiangfang Zeng[7]

[1]Institute of Geology and Geophysics, Chinese Academy of Sciences, Beijing, China, [2]China University of Petroleum, Beijing, China, [3]Colorado School of Mines, Golden, CO, United States, [4]Texas A&M University, College Station, TX, United States, [5]TGS, Houston, TX, United States, [6]University of Science and Technology of China, Hefei, Anhui, China, [7]Innovation Academy for Precision Measurement Science and Technology, Chinese Academy of Sciences, Wuhan, China

KEYWORDS

editorial, distributed optical fiber sensing (DOFS), multi-scales, geoscience, advances and applications, distributed acoustic sensing (DAS)

Editorial on the Research Topic
Advances and applications of distributed optical fiber sensing (DOFS) in multi-scales geoscience problems

Introduction

Distributed optical fiber sensing (DOFS) has drawn a lot of attention in the geoscience community, taking advantage of easy-to-deploy, dense-spacing, and multi-physical measurements (temperature and strain), In contrast with traditional sensors, the optical fiber itself is used as both a sensing element and a means of data transfer. Sensing fibers can be easily deployed in harsh environments such as high-pressure and high-temperature downhole settings.

Previous studies have demonstrated the capability of DOFS in multi-scale geoscience tasks related to resource exploration and environmental hazard monitoring. While DOFS shows promise to enhance our capabilities of tackling geoscience problems, there are still challenges and problems associated with its development and applications. This Research Topic reviews many of the recent advances and applications of DOFS and shows how the technology can be improved. We hope this Research Topic may motivate more DOFS developments regarding solving geoscience problems.

Presented below is a short review of the accepted papers in this Research Topic:

a) Distributed acoustic sensing (DAS) demonstrates the robustness of subsurface imaging across different scales. Shao et al. utilize DAS to record traffic-generated seismic data in urban cities. The authors obtain the near-surface shear-wave velocity profile below the DAS cable through surface wave dispersion inversion using a Bayesian Markov Chain Monte Carlo method, which demonstrates the effectiveness of using DAS-recorded urban traffic noise for near-surface characterization. Song et al. investigate the performance of the three-station interferometry method for improving ambient-noise cross-correlation functions of a linear DAS array. The authors enhance the surface-wave signals while suppressing the non-casual signals retrieved from the data recorded by an urban internet cable, and provide high-resolution images of shallow structures in the built-up areas. Yang et al. present a case study of two survey lines with armored optical fiber cables in the Yigong Lake area of the Tibetan Plateau. Ambient noise interferometry and multichannel analysis of surface waves are performed to obtain the 2D shear-wave velocity profiles below the installed fibers. The results validate the robustness of temporary DAS monitoring in areas with extreme environments.

b) Machine learning proves its effectiveness for large-scale DAS data processing. Cong et al. propose an attention-guided denoising convolutional neural network (ADNet) to denoise seismic images and retrieve weak signals. The network adapts different kinds of convolution layers to enlarge the receptive field size and extract the global feature of the input signal. Meanwhile, the attention mechanism is introduced to extract the hidden noise from the complex background. Wang et al. propose a multi-scale interactive convolutional neural network (MSI-Net) to denoise DAS data. The proposed MSI-Net incorporates both coarse-scale and fine-scale features to advance inherent serial convolution to multi-scale parallel convolution. As demonstrated by field examples, the MSI-Net can effectively attenuate a variety of unique DAS background noise and also effectively recover weak signals. Dong et al. develop a novel multi-scale dense-connection denoising network (MDD-Net) to achieve high-accuracy processing of complex DAS-VSP background noise. MDD-Net utilizes a widened convolution block to capture the multi-scale features of the analyzed data. Both synthetic and field DAS-VSP records are processed to verify the effectiveness of MDD-Net, even for the weak upgoing signals. Tang et al. establish a rank reduction U-net (RRU-net), an integration of an encoding structure for down-sampling and a decoding structure for up-sampling, to reconstruct and denoise the DAS-VSP seismic data simultaneously. Zheng et al. propose a deep-learning approach for DAS signal extraction from the borehole-flow noise during hydraulic fracturing. The authors utilize a combination of Convolutional Neural Networks (CNNs) and Bidirectional Long Short-Term Memory Networks (BiLSTM) to extract the spatial and temporal features from the DAS data. The field data results prove its robustness for intelligent monitoring and real-time evaluation for hydraulic fracturing. Ye et al. develop a deep-learning method based on the YOLOv5 object-detection algorithm to estimate traffic flow and vehicle speed from the DAS signals acquired *via* a 500 m fiber segment in suburban Beijing. The authors evaluate the temporal traffic trend of the road section and explore vehicle classification *via* the fast-beamforming technique.

c) The Research Topic also includes a number of DAS case studies. Staněk et al. focus on reflected S-waves and use microseismic events as sources to image induced hydraulic fractures, which act as reflectors close to events and monitoring fiber. The proposed algorithm is capable of real-time fracture mapping and tracking fracture evolution in space and time. Nakajima et al. present a case study of a walk-away DAS-VSP survey applied to monitor geological CO2 storage at a pilot site in Japan. The authors obtained DAS data using a single-mode fiber *via* a casing installation. The authors apply conventional VSP processing workflows to the acquired DAS data and obtain promising images. Zhang et al. develop optimized algorithms for accurate tracking of the train position, speed, and number of trains traversing the position of the DAS system. The authors transform a 6-day set of continuous DAS data sensed by a 2-km cable into the time-velocity domain using beamforming and automatically extract train position and velocity from the time-beampower curves. It serves a supplementary role to conventional temporally and spatially discrete monitoring systems in railway traffic monitoring.

Author contributions

YW, XC, GJ, BW, XZ, GZ, and YZ edited the Research Topic "*Advances and Applications of Distributed Optical Fiber Sensing (DOFS) in Multi-scales Geoscience Problems*."

Acknowledgments

We thank all the authors for their valuable contributions to this Research Topic, the reviewers who shared their valuable time to improve the manuscripts and the members of the Frontiers Team and the Editor in Chief for their help at different stages of this Research Topic preparation.

Conflict of interest

Author GZ was employed by the company TGS.

The remaining authors declare that the research was conducted in the absence of any commercial or financial relationships that could be construed as a potential conflict of interest.

Publisher's note

frontiers | Frontiers in Earth Science

ORIGINAL RESEARCH
published: 19 July 2022
doi: 10.3389/feart.2022.907749

Fracture Imaging Using DAS-Recorded Microseismic Events

František Staněk, Ge Jin and James Simmons*

Department of Geophysics, Colorado School of Mines, Golden, CO, United States

Hydraulic fracturing enables hydrocarbon production from unconventional reservoirs. Mapping induced seismicity around newly created fractures is crucial for understanding the reservoir response and increasing the efficiency of operations. Distributed acoustic sensing (DAS) provides a large amount of high spatial resolution microseismic data acquired along the entire length of horizontal wells. We focus on the observed reflected S-waves and develop a new methodology using microseismic events as sources of energy to image induced fractures acting as reflectors in the media surrounding the events and monitoring fiber. The workflow consists of DAS data preprocessing, event location, wavefield separation, raytracing-based imaging, and image post-processing. The comparison of the resulting images with low-frequency DAS signals of fracture hits corroborates that the reflections are from fractures created by stimulation. The proposed algorithm can be used for real-time mapping of fractures and tracking fracture changes in space and time. Fracture imaging leads to a better understanding of the reservoir response to hydraulic fracturing stimulation.

Keywords: hydraulic fracturing, microseismic monitoring, fiber-optic sensing, DAS, microseismicity, fracture, reflected wave, imaging

Edited by:
Antonio Pio Rinaldi,
ETH Zurich, Switzerland

Reviewed by:
Patrick Paitz,
ETH Zürich, Switzerland
Verónica Rodríguez Tribaldos,
Berkeley Lab (DOE), United States

****Correspondence:***
František Staněk
FStanek@mines.edu

Specialty section:
This article was submitted to
Solid Earth Geophysics,
a section of the journal
Frontiers in Earth Science

Received: *30 March 2022*
Accepted: *10 June 2022*
Published: *19 July 2022*

Citation:
Staněk F, Jin G and Simmons J (2022)
Fracture Imaging Using DAS-Recorded Microseismic Events.
Front. Earth Sci. 10:907749.
doi: 10.3389/feart.2022.907749

1 INTRODUCTION

Microseismic monitoring of hydraulic fracturing has been employed to understand the reservoir response and increase the efficiency of subsurface operations (Grechka and Heigl, 2017). Similarly, induced seismicity monitoring has been used during waste-water injection (e.g., Zoback, 2012), mining (e.g., Mendecki et al., 2010), enhancing geothermal systems (e.g., Kwiatek et al., 2014), storing gas underground (e.g., Carannante et al., 2020), and CO_2 sequestration (e.g., Williams-Stroud et al., 2020) to mitigate seismic hazard.

A commonly provided result of hydraulic fracturing microseismic monitoring is a catalogue of detected microseismic events with their origin time, location of hypocenter, magnitude, and, if possible, a description of source mechanism. The main goals are to describe fracture geometry and orientation, and connectivity between individual fractures and to estimate the area of the rock volume having increased permeability. The interpretation is mostly done with discrete fracture network (Williams-Stroud et al., 2013), stimulated rock volume (Rahimi Zeynal et al., 2014), and geomechanical models (e.g., Staněk and Eisner, 2017). However, due to uncertainties in event locations and inverted fault planes, and a lack of understanding of what microseismicity really represents, more accurate knowledge of induced fracture systems is still in need.

Another technique to map induced fractures, instead of connecting located events, is reflection imaging, using microseismic events as sources of energy. Grechka et al. (2017), Reshetnikov et al. (2010), or Lin and Zhang (2016), observed reflected waves in data acquired by 3C geophone arrays and used them for microseismic imaging. Such imaging is not common, probably because it is difficult to see reflected waves in the microseismic data acquired by sparse and distant geophone arrays.

Recently, distributed fiber-optic sensing technology (Hartog, 2017) providing dense monitoring data has started to be employed as an alternative to the traditional seismic arrays in industry (e.g., Karrenbach et al., 2017; Byerley et al., 2018; Binder and Tura, 2020; Lellouch et al., 2020; Stork et al., 2020; Titov et al., 2021) as well as in global seismology (Zhan, 2019; Lindsey and Martin, 2021). Fiber-optic-based monitoring is a quickly developing technology that has been used for measuring vibrations, temperature, and strain for many different purposes (Baldwin, 2018). Specifically, distributed acoustic sensing (DAS) is being utilized for long-term seismic monitoring. The fiber working as a sensor can be installed along the whole length of the stimulated well (in-well monitoring) or offset wells (cross-well monitoring). The best practice seems to be cementing fiber behind casing for permanent monitoring, although it can also be installed temporarily. Such monitoring geometry allows detection of a high number of weak (i.e., low magnitude) microseismic events due to proximity to the stimulated area. DAS offers other advantages compared to borehole geophone arrays, such as broadband response (from mHz to tens of kHz), long aperture (several km long fiber), and dense spatial sampling (channel spacing can be < 1 m). The main downside of fiber-optic-based monitoring is a single-component axial strain measurement only in the direction along the fiber (Baird et al., 2019). This causes critical problems when locating and inverting the source mechanism of microseismic events detected by a single fiber. However, there are ways to overcome this issue using multi-component, so-called, helical optical fibers (Lim Chen Ning and Sava, 2018), monitoring carried out by a deviated or L-shaped array Verdon et al. (2020), or monitoring with two or more nearby fiber wells (e.g., Cole et al., 2018).

DAS provides high spatial resolution recordings, enabling detailed analyses of wavefields and development of new processing methods, leading to improved interpretations and better insight into the reservoir response. In passive seismic, we rely on induced microseismic events around the monitoring wells at a reasonable distance to detect them. Recorded waves (i.e., arrival times and amplitudes) contain information about event location relative to a monitoring array, radiation pattern due to source processes, and about the media between source and fiber. It also includes the structural features represented by reflected/refracted/diffracted waves arriving later after the direct P-wave arrival (Lellouch and Biondi, 2021). Moreover, in some DAS-based microseismic data, one may observe not only far-field but also near-field signals (Luo et al., 2021a) which can be used for more precise source description, and dispersive guided waves, providing properties of anomalous velocity layers and helping identification of events located inside or outside the reservoir layer (Luo et al., 2021b). While all the phenomena are recorded with high resolution, we can not only map fracture propagation based on microseismic events located along fractures but also image fractures making use of reflected waves.

Another type of fiber-optic-based measurement during hydraulic fracturing used to describe fractures is of low-frequency (< 1 Hz) DAS (LFDAS). LFDAS measures strain changes (i.e., works as hybrid distributed strain sensing, DSS) induced by hydraulic fractures (Jin and Roy, 2017; Richter et al., 2019; Ugueto et al., 2019; Ichikawa et al., 2020; Zhu and Jin, 2021). The detected strain signals represent fractures which were initiated at the offset treatment well and reached the monitoring fiber well, so-called fracture hits or frac-hits. Therefore, frac-hits are clear proof that the fractures have a half-length longer than the spacing between treatment and monitoring well. Besides the times when fractures hit the monitoring well, LFDAS data also show the time intervals when the fractures open (extension at the fractures and compression zone around) and when they close (extension zone around the fractures) due to the leak-off after injection.

In this study, we analyze selected examples of field DAS-recorded microseismic data acquired during multi-well hydraulic fracturing, focus on observed reflected S-waves, and propose a new method for imaging fractures in the vicinity of induced microseismic events. Imaged fractures are compared to LFDAS frac-hits to corroborate that the imaged waves are reflected from newly created hydraulic fractures.

2 DATA AND METHODOLOGY

2.1 DAS Data and Observations

We analyze data from the Chalk Bluff project in the Denver-Julesburg (DJ) Basin in Colorado, USA. **Figure 1** shows a map of the study area with the position of the pad of horizontal wells drilled in a N-S direction through the target unconventional reservoir formations Codell and Niobrara at depths of around 7,400–7,700 ft (TVD). The reservoir was hydraulically fractured in hundreds of stages along the lateral parts of all the horizontal wells. DAS microseismic and LFDAS monitoring of the studied area was carried out by two fibers permanently installed outside the casing of the red wells in **Figure 1**. The channel spacing was 1 m along the fiber, and the gauge length was set to 5 m.

We have analyzed several strong microseismic events visible in the continuous DAS data. The waveforms of most of the events are relatively simple with symmetrical moveouts of direct P- and S-waves, where S-wave signals are usually of higher amplitude than P-waves. In this study, we focus on events that have more complex wavefields, and demonstrate our methodology on three selected example events. DAS data and initial spatial locations (taken from the catalogue of events located from a surface array provided by the data owner) of the three example events are shown in **Figure 1** (yellow stars). Events A and C have both clear direct P- and S-waves (marked as P_D, S_D), event B has only an S-wave visible, probably because of the lower magnitude. All three events have reflected S-waves (marked as S_R) but event C has also clearly converted S to P-waves (marked as SP) and a very complex wavefield following the S-wave arrival. We also notice secondary, similarly looking, weaker events coming after and before the main event in the data of the events A and B, respectively (see S_{D2}, S_{R2} in **Figure 1**). These repeated events most likely occurred at the same locations as the main events but at slightly different times.

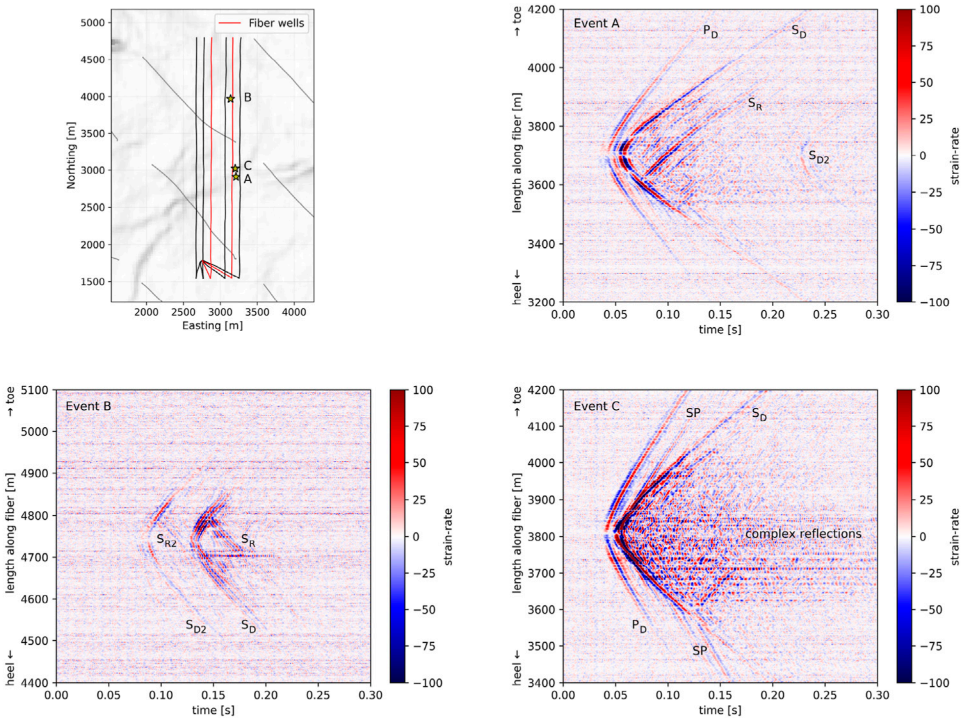

FIGURE 1 | Upper left: A map of the studied area with horizontal wells (running N-S) and their relative positions. Wells with permanently installed fiber are shown in red. The diagonal NW-SE wells shown in gray are previously drilled production wells in the Niobrara. The yellow stars represent examples of strong microseismic events (A, B, C). The seismic coherency map in the background may indicate potential faults in the Niobrara formation. Upper right and bottom: Examples of three representative microseismic events with direct P-waves (P_D), direct S-waves (S_D), converted S- to P-waves (SP), and reflected S-waves (S_R) recorded by DAS array. The events A and B are accompanied by other weaker events with very similar moveouts (S_{D2}, S_{R2}) indicating similar location but slightly different origin time. Event C shows more complicated reflections after the direct S-wave.

The observed reflected waves could represent either a fault, fracture, or velocity interface, acting as a reflector in the medium around the event location at the time when the microseismic event occurred. However, in our case, we can exclude the possibility of reflections from near-horizontal interfaces (i.e., bedding planes) based on travel time moveout. Reflection from a horizontal interface would be recorded by most of the channels along the fiber and be symmetric around the apex with a moveout similar to the direct P- and S-waves. Our observed reflected S-wave moveouts are asymmetrical and parallel to the direct S-wave moveouts. Therefore, we interpret them as reflections from approximately near-vertical faults or near-vertical fractures perpendicular to the horizontal fiber. Furthermore, the reflectors are most probably either very close to or directly intersecting the fiber, as we see that the arrivals of reflected S-waves and direct S-waves merge into the same channels where the reflectors likely intersect with the fiber well.

2.2 Fracture Imaging—Methodology

The reflected S-waves observed in the DAS data indicate the presence of reflectors in the area between the microseismic event locations and the recording fiber. From their moveouts, we may expect that the reflector orientation is near-vertical and perpendicular to the horizontal well. Our first attempt to explain the reflected S-waves was a simple traveltime modeling (Stanek and Jin, 2021). We were able to fit manually picked arrival times of P-, S-, and reflected S-waves sufficiently well with synthetic traveltimes using a homogeneous isotropic velocity model (velocity taken from an available sonic log) with a vertical reflector perpendicular to the monitoring fiber well. However, such a method is not optimal as it may require testing of many different positions, orientations, and lengths of reflector until synthetics fit the arrival times.

Here, we propose an imaging technique converting DAS microseismic data in time domain to an image with reflector position in space. The raytracing-based method is similar to that used for DAS VSP processing (Schultz, 2019). Our imaging procedure is incorporated into the seven-step workflow (see **Figure 2**):

(1) Input cut-out 0.3 s long chunk of DAS data containing a detected event (as shown in **Figure 1**) is preprocessed. We down-sample data from 10 to 1 kHz sampling rate in order to minimize data size and then apply a band-pass filter to preserve the signal of interest between 10 and 300 Hz.
(2) We manually pick (P- and) S-wave arrivals and relocate the event using a standard grid-search location algorithm, minimizing the L1-misfit. This way, we improve the origin time and initial location taken from the surface catalogue, specifically, the event location along the fiber and the

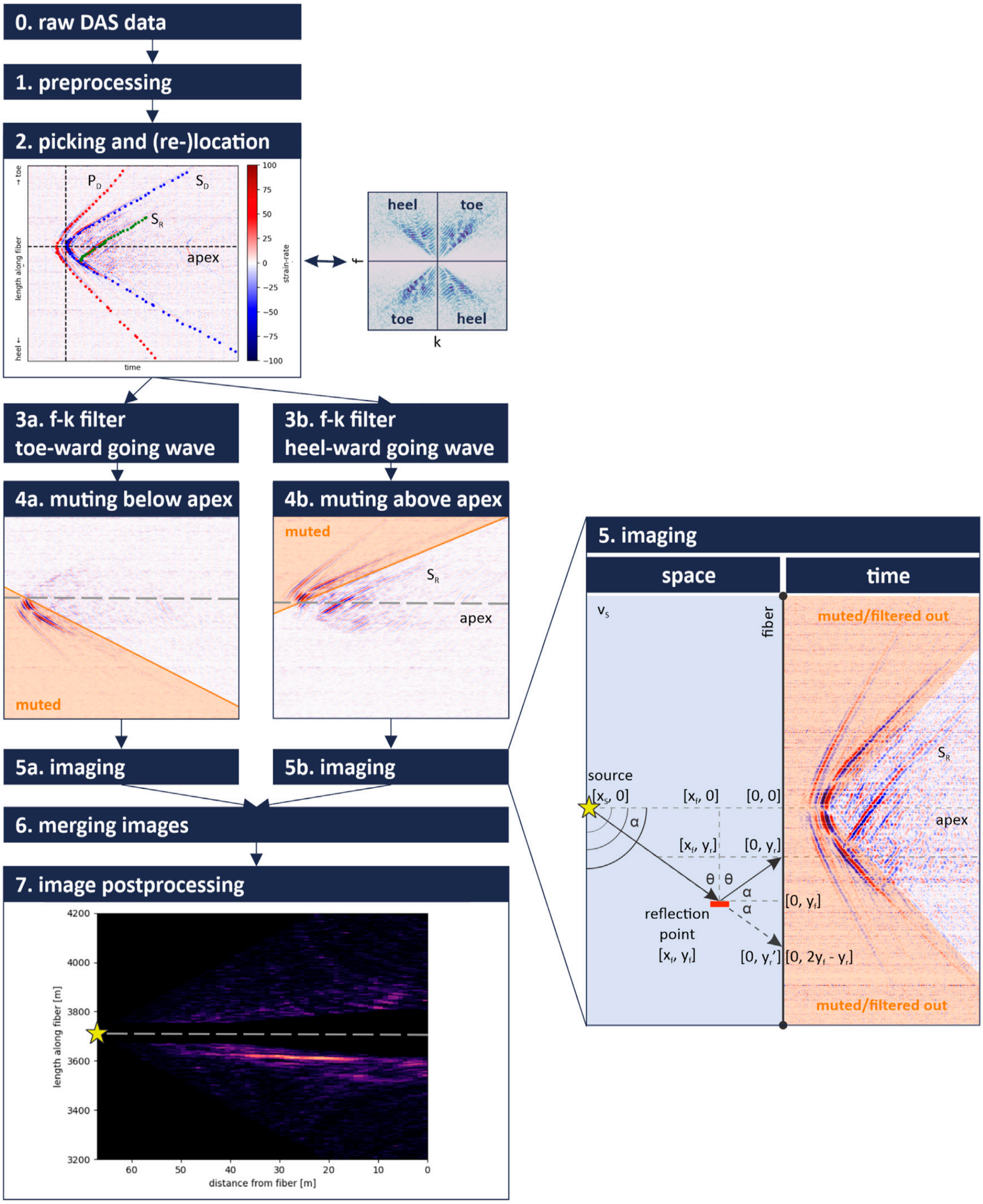

FIGURE 2 | Proposed 7-step workflow of reflector imaging using reflected S-waves recorded by DAS with an illustration of raytracing-based reflector imaging methodology.

perpendicular distance from the fiber. We cannot fully control the depth when locating events using one-well DAS data due to the single-component nature of DAS.

(3) In this step, the data are converted to the f-k domain and the workflow splits into two parallel branches. In (3a) and (3b), f-k filtering is used to separate wavefields and remove the toe-ward going and heel-ward going waves, respectively. It means that in (3a) all heel-ward going and in (3b) all toe-ward going energy (including reflected waves) is preserved and energy coming from the opposite direction (including direct P- and S-waves) is filtered out. Such splitting into two branches allows us to image reflectors on both sides of the apex.

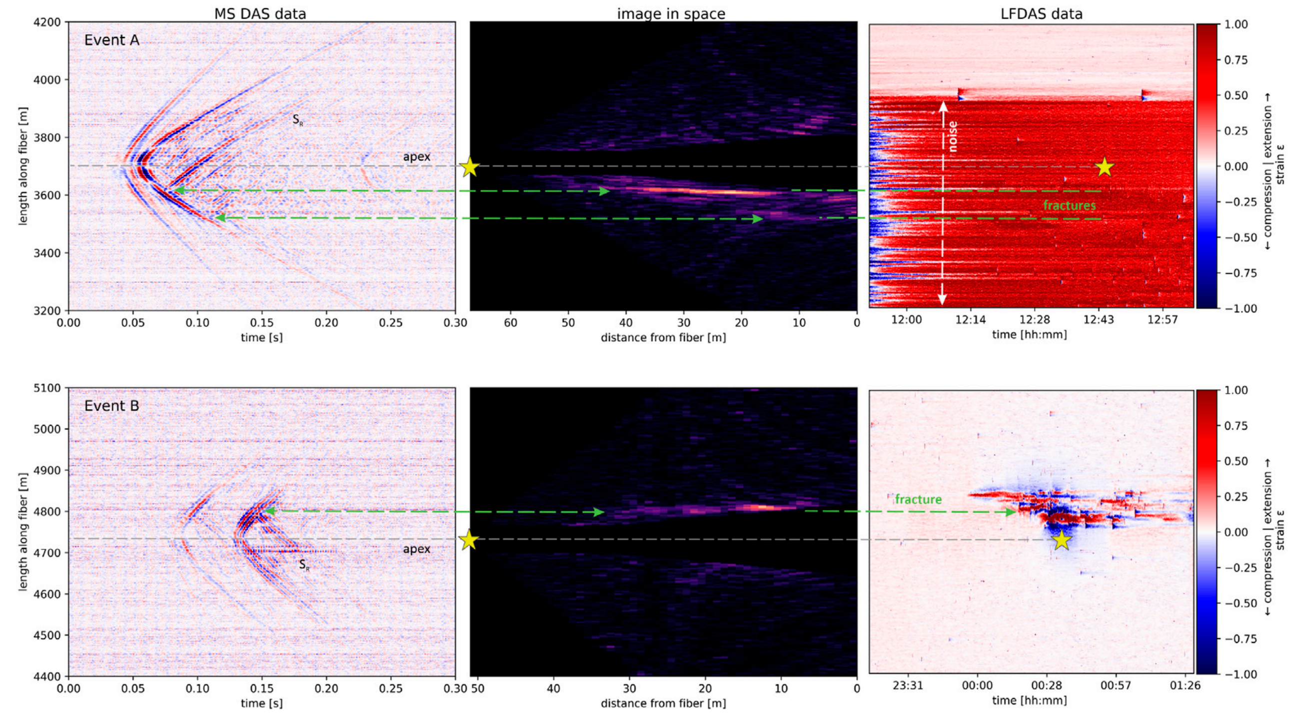

FIGURE 3 | Input DAS data, reflector images, and LFDAS data for two example events. The green dashed-line arrows highlight the positions of reflectors in the images. The yellow stars represent the location and origin time (only in the LFDAS data) of microseismic events.

(4) To get rid of the remaining part of direct arrival body waves' moveouts, we mute all the data below (4a) and above (4b) the line going through the apex with the slope equal to S-wave velocity (muted areas are highlighted by transparent orange triangles in **Figure 2**). This line needs to be slightly shifted relative to the apex to make sure that we fully mute the direct S-waves and do not deteriorate the final image. After the latter step, we should see only heel-ward going or toe-ward going reflected waves.

(5) The idea of imaging in (5a) and (5b) of the workflow is that every point between the fiber at $x = 0$ and the event location $[x_s, 0]$ acts as a potential reflection point $[x_f, y_f]$. With an assumption that the reflector is almost vertical and perpendicular to the fiber, we follow Snell's law and compute the raytracing-based travel time of the reflected S-wave tt in a homogeneous isotropic velocity model with S-wave velocity v_s:

$$tt = \frac{x_s}{v_s \cos(\alpha)}, \tag{1}$$

where $\cos(\alpha) = (x_s - x_f)/\sqrt{(x_s - x_f)^2 + y_f^2}$. The channel y_r along the fiber where the ray of reflected S-wave arrives is:

$$y_r = y_f - \frac{x_f y_f}{x_s - x_f}. \tag{2}$$

The DAS data amplitude from the channel y_r at the time tt is then assigned to the tested reflection point in space. After going through all the potential reflection points along the fiber and between the fiber and the event location (we use a regular grid with 1 m spacing), the imaging is done. The imaging result projects the signal amplitude into the imaging spatial grids without amplitude correction. The directional sensitivity of the fiber and the source radiation pattern determines the image amplitude.

The final two steps are (6) merging the two images of toe-ward going and heel-ward going reflected waves to form a complete image and (7) image post-processing. Here, we calculate signal envelopes and apply a low-pass filter to the merged image to further enhance the visibility of the reflector(s). An example of the resulting image is shown at the bottom of the workflow, where the dark color means no reflection or data coverage, and coherent near-horizontal bright spots represent positions of near-vertical reflectors approximately perpendicular to the fiber.

3 RESULTS

3.1 Imaged Reflectors

We demonstrate the processing results for two example microseismic events (Events A and B displayed in **Figure 1**) using the above-described methodology. **Figure 3** shows input DAS microseismic waveforms and the resulting images of reflectors in space in two columns on the left. Each image is a 2D plane connecting the event location and the part of the fiber from which we have DAS data.

The bright spots elongated in the direction approximately perpendicular to the fiber indicate the imaged reflectors. The length of imaged reflectors is proportional to the length of the reflected wave visible in the DAS data. The imaged reflectors usually do not intersect with the fiber (at the distance 0) because of the mute window around the direct arrivals (including a few wavelengths of high-amplitude S-wave coda). The muting must be done to avoid distortion of the final image around the apex. However, we realize that we also mute part of the reflected S-wave signal mixed with S-wave coda and thus lose information about the reflector in the vicinity of the fiber. The imaged reflectors fade out with distance from the fiber similar to the high-amplitude signal of the reflected wave in the DAS data. It does not mean that the actual reflectors cannot be longer, we image only the sections between hypocenter and fiber illuminated by the S-wave of the individual microseismic event. The signal-to-noise ratio (SNR) of reflected waves depends on event magnitude, distance of the event from the fiber (attenuation and geometrical spreading), and noise in the data.

The black color at a far distance from the fiber means no data coverage, i.e., there are no points reflecting energy back to the part of the fiber we have data from. Whereas the black spaces in a narrow zone around the apex line results from muting the direct S-wave in the input data (steps (4a) and (4b) of the workflow). All the other spaces with dark colors represent media without reflectors.

The image of Event A shows one very clear horizontal bright spot, representing a reflector within 50 m from the fiber. In the DAS data, the position of the imaged reflector along the fiber corresponds to the channel where both direct S- and reflected S-waves intersect (highlighted by green dashed-line arrow in the **Figure 3**). There is another reflector in the image which is weaker and shorter (visible within 20 m from the fiber) than the main reflector but still has coherent brightness in the approximately perpendicular direction from the fiber. The matching reflected S-wave in the DAS data is of proportionally low SNR and its amplitude quickly attenuates away from the fiber. The remaining randomly located bright spots are too small and probably result from coherent noise in the input data. Meanwhile, Event B has one approximately 30 m long reflector visible in its image.

3.2 Comparison With LFDAS and Interpretation

Up to this point, we have referred to bright spots in images as reflectors because we had no clear indication of whether they can be interpreted as newly created fractures due to hydraulic fracturing or pre-existing vertical faults in the area. To inspect whether we have imaged one or the other, we compared the images with LFDAS data. The LFDAS data are the same recorded raw DAS data as the analyzed DAS microseismic data but in a very low-frequency band (< 0.1 Hz). **Figure 3** shows DAS microseismic data in the left column, images for both microseismic events in the middle, and LFDAS data from the corresponding stage in the right column. The yellow stars placed in the LFDAS data are at the events' origin time and location along the fiber. Note that the DAS microseismic data of each event and consequently the image of reflector(s) is a snapshot of the medium around the event location at the time when event happened, whereas the LFDAS data show the evolution of measured strain during the entire stage.

The LFDAS data around the origin time and location of Event B show a very clear signal characteristic of frac-hits. The first fracture started to open (zone of compression in blue around the extensive opening zone in red) shortly before 12 a.m. Later on, other fractures hit the fiber approximately 80 m away from the first frac-hit and started to open. A few minutes later, the changes in the reservoir induced Event B, recorded by the DAS array. The comparison with LFDAS provides undeniable evidence that the observed S-wave is back-scattered from the newly created fracture to the monitoring fiber–position of the fracture in our image aligns with the position of frac-hit in the LFDAS data (see the green dashed-line arrow). The explanation of why we identified only one fracture in the image while the LFDAS shows three existing fractures at the event origin time is unclear. It is less likely to be a resolution issue as the thickness of the imaged fracture is smaller than the entire fractured zone. The first open fracture (at the top in the LFDAS) is most likely not imaged due to its narrower width or because the fracture was already closed and did not create enough seismic impedance. The third fracture (at the bottom in the LFDAS) lies in the muted zone of our image (too close to the apex of the microseismic event).

The LFDAS data for the stage of hydraulic fracturing when Event A occurred is of low quality, not allowing detection of frac-hits. The source of abnormally high low-frequency noise was an injection operation taking place in the monitoring well. This caused a large temporal change in temperature conditions in a short time before the LFDAS data were acquired. Note that the low-frequency noise does not affect the DAS microseismic data while we look at much higher frequencies where the sensitivity to temperature is negligible. As the image of Event B has been proven to be showing induced fracture(s), we may expect that the similarly looking reflectors in the image of Event A are also fractures. However, we cannot prove it by comparison with frac-hit due to the noisy LFDAS.

4 DISCUSSION

4.1 Methodology

Our methodology relies on recorded signals reflected from the fractures. We have used reflected S-waves; but analogically, reflected P-waves might be used. Visibility of reflected waves in data depends on sensitivity of the DAS monitoring system, magnitude of microseismic event, impedance contrast related to fracture geometry, width, and volume of fluids in the fracture, and relative geometry between the source, fiber, and fracture. If the fracture width is narrow and the impedance contrast in the medium is not strong enough to reflect enough energy to be detected above background noise level, we cannot see it in the image, of course. If the microseismic event is located too close to the induced fracture (relative to the distance of the event from the fiber), most of the energy is reflected to far offset channels (far from the apex line in the DAS data), and the signal of the reflected wave arrives shortly after the direct body wave and has almost the same moveout. Therefore, in our workflow, the reflected wave may be filtered out or muted together with the body wave signal, and information about fracture is lost. Remaining energy reflected from the fracture appears close to the apex where it is usually mixing with high SNR body-wave coda which we also mute. This means that fracture imaging using reflected waves is hardly possible when the event-fracture-fiber geometry does not lead to a reflected signal clearly distinguishable from the signal of direct body waves.

Our fracture imaging methodology is based on several assumptions. The raytracing is done only for reflections from vertical fractures oriented approximately perpendicular to the fiber in a homogeneous isotropic velocity model. These assumptions appear to be valid only if the fractures are near vertical. Perpendicularity of fractures to a well is expected when lateral parts of both treatment and monitoring wells are drilled in parallel and perpendicularly to the maximum horizontal stress direction in the area. In our case, the observed reflected S-waves with asymmetrical moveout parallel to the moveout of direct S-wave can be explained only with a near-vertical fracture, near-perpendicular to the fiber. The fact that microseismic events and monitor well are in the same horizontal formation allows us to assume a single velocity structure. We were able to fit both P- and S-wave moveouts with the homogeneous velocity model, i.e., without the need to use more complicated models. Similar conditions might be found in many other fields but, in general, to be able to image fractures with arbitrary orientation in a complex velocity model, we would need to use more sophisticated raytracing or advanced imaging methods such as Kirchhoff migration or reverse time migration (e.g., Li et al., 2020). However, that would require more accurate event locations and stacking of many microseismic events (sources) to get a reasonable image.

One of our first steps in the workflow is manual picking and event (re-)location as we wanted to improve the initial event locations obtained from the surface microseismic catalogue. Without the known initial location, we would still locate the event but have only very accurate information about the event position along the fiber and the relatively accurate distance from the fiber when located from one fiber only. The event location would have uncertainty of 360^o around the axis of the horizontal well because of the axial sensitivity of DAS. Therefore, we would not know the correct orientation of the imaged fractures. Note that the image is always in the plane connecting the event location and the fiber. We have not thoroughly tested the effect of uncertainty in event distance from the fiber on the imaged fracture as the uncertainty in horizontal location for our selected events is in the order of a few meters and the changes in images were negligible. Of course, P- and S-wave arrivals needed for location do not have to be picked manually if an efficient auto-picking algorithm is employed.

4.2 Application

The most obvious application of fracture imaging is the processing of continuous cross-well DAS microseismic data acquired during hydraulic fracturing to map created fractures around stimulated wells. Such detailed map can have a big impact on the precision of DFN and its reliability. With fracture imaging, we may potentially map the dynamic evolution of the fracture if several microseismic events are induced and detected during the same stage around the fracture reflecting energy. The microseismic events provide snapshots of the surrounding reservoir at their origin times. If we are able to image fractures, it means that the fracture is already open and wide enough to reflect energy emitted by nearby microseismic events. With several microseismic events following each other in time, we may see fracture growth, i.e., dynamic changes of the reflected wave visible in DAS data, and thus the lateral extent of the imaged fractures. When the fracture starts closing, seismic impedance decreases, and the fracture disappears from the image. Fracture closing was shown in LFDAS data by Jin and Roy (2017) as well as in time-lapse DAS VSP. Compared to the 4D inter-stage DAS VSP (Binder et al., 2020; Titov et al., 2021), our fracture imaging provides a better resolution due to higher frequency content (microseismic event as a source is closer to the fiber than the surface source used for VSP) and can image fractures in 3D if the event location is known.

While the fracture visibility in the images depends on impedance contrast in the medium, fracture images might be used for estimation of fracture width or volume of fluids in the fracture. However, such impedance dependency on the mentioned parameters is not known at this time. We plan to study the effect of uncertain microseismic event location on the image, perform AVO analyses on the reflector for more quantitative analyses of the imaging results, and estimate fracture properties using reflected S-wave.

Due to the above-described assumptions and limitations of the methodology, we do not claim that we are imaging all possibly existing fractures. The presented fracture imaging can be understood as a very powerful method providing important but only additional information about the whole fracture system induced by hydraulic fracturing, which may be integrated with available results of other methods mapping fractures. For example, location of microseismic events, fault planes of inverted source mechanisms (size of planes is proportional to magnitudes), or frac-hits also provide information about fracture propagation and geometry. In this study, we used LFDAS data showing frac-hits. Unfortunately, as shown in the example in **Figure 3**, LFDAS can be contaminated by noise due to temperature effects induced by injection operations in the monitor well. In such cases, fracture imaging using DAS microseismic data may provide complementary information to results from LFDAS. Furthermore, the LFDAS can detect frac-hits or strain changes only in the close vicinity of the monitoring fiber. Our fracture imaging is also able to map these frac-hits and, moreover, it has the capability to map fractures which does not intersect monitoring fiber well, as the imaging space is located between the event and the monitoring fiber. From such images, we can estimate the fracture geometry of fractures with half-length shorter than well spacing. Of course, the disadvantage is that fracture imaging is dependent on induced microseismic events, whereas LFDAS is not.

5 CONCLUSION

We have shown examples of microseismic events recorded by DAS fiber in a horizontal well during hydraulic fracturing of an unconventional reservoir. Besides direct P- and S-waves, the events have visible signals of S-waves reflected at hydraulic fractures. We developed a new processing workflow to image the fracture using the reflected waves and demonstrated the conversion of DAS-based microseismic data in time to fracture image in space. The resulting images were compared to frac-hit signals in corresponding LFDAS data, supporting that the imaged reflectors are newly created hydraulic fractures. The fracture imaging can be further developed with a potential to be used for a real-time 3-D hydraulic fracture development mapping when DAS monitoring is employed and induced microseismic events are detected in abundance.

DATA AVAILABILITY STATEMENT

The DAS microseismic data of events A and B used as examples for fracture imaging in this study are available from the corresponding author upon request.

AUTHOR CONTRIBUTIONS

FS and GJ co-developed the presented idea. FS developed the workflow, performed data processing, made all the figures, and wrote the first draft of the manuscript. GJ supervised the progress of the work and edited the manuscript. JS contributed to discussions and edited the manuscript.

FUNDING

This work was conducted with the support of the Reservoir Characterization Project (Phase XVIII.) at the Colorado School of Mines.

ACKNOWLEDGMENTS

The authors are thankful to Civitas Inc. for support, providing the data and permission to publish the results. The authors thank Alicia Downard for helping with orientation in the data and providing seismic coherence maps (used in **Figure 1**), and Xiaoyu (Rosie) Zhu for helping with the LFDAS data.

REFERENCES

Baird, A., Stork, A., Horne, S., Naldrett, G., Kendall, M., Wookey, J., et al. (2019). “Modelling of Fibre-Optic DAS Response to Microseismic Arrivals in Anisotropic Media,” in *81st EAGE Conference and Exhibition 2019* (London, UK: European Association of Geoscientists & Engineers), 1–6. doi:10.3997/2214-4609.201901244

Baldwin, C. (2018). “Fiber Optic Sensors in the Oil and Gas Industry,” in *Opto-Mechanical Fiber Optic Sensors*. Editor H. Alemohammad (Laurel, MD: Butterworth-Heinemann), 211–236. doi:10.1016/B978-0-12-803131-5.00008-8

Binder, G., Titov, A., Liu, Y., Simmons, J., Tura, A., Byerley, G., et al. (2020). Modeling the Seismic Response of Individual Hydraulic Fracturing Stages Observed in a Time-Lapse Distributed Acoustic Sensing Vertical Seismic Profiling Survey. *Geophysics* 85, T225–T235. doi:10.1190/geo2019-0819.1

Binder, G., and Tura, A. (2020). Convolutional Neural Networks for Automated Microseismic Detection in Downhole Distributed Acoustic Sensing Data and Comparison to a Surface Geophone Array. *Geophys. Prospect.* 68, 2770–2782. doi:10.1111/1365-2478.13027

Byerley, G., Monk, D., Aaron, P., and Yates, M. (2018). Time-lapse Seismic Monitoring of Individual Hydraulic Frac Stages Using a Downhole DAS Array. *Lead. Edge* 37, 802–810. doi:10.1190/tle37110802.1

Carannante, S., D’Alema, E., Augliera, P., and Franceschina, G. (2020). Improvement of Microseismic Monitoring at the Gas Storage Concession “Minerbio Stoccaggio” (Bologna, Northern Italy). *J. Seismol.* 24, 967–977. doi:10.1007/s10950-019-09879-2

Cole, S., Karrenbach, M., Kahn, D., Rich, J., Silver, K., and Langton, D. (2018). “Source Parameter Estimation from DAS Microseismic Data,” in *SEG Technical Program Expanded Abstracts 2018* (Anaheim, California: Society of Exploration Geophysicists), 4928–4932. doi:10.1190/segam2018-2995716.1

Grechka, V., and Heigl, W. M. (2017). *Microseismic Monitoring*. Tulsa, OK: Society of Exploration Geophysicists. doi:10.1190/1.9781560803485

Grechka, V., Li, Z., Howell, B., Garcia, H., and Wooltorton, T. (2017). High-resolution Microseismic Imaging. *Lead. Edge* 36, 822–828. doi:10.1190/tle36100822.1

Hartog, A. H. (2017). *An Introduction to Distributed Optical Fibre Sensors*. Boca Raton: CRC Press. doi:10.1201/9781315119014

Ichikawa, M., Uchida, S., Katou, M., Kurosawa, I., Tamura, K., Kato, A., et al. (2020). Case Study of Hydraulic Fracture Monitoring Using Multiwell Integrated Analysis Based on Low-Frequency DAS Data. *Lead. Edge* 39, 794–800. doi:10.1190/tle39110794.1

Jin, G., and Roy, B. (2017). Hydraulic-fracture Geometry Characterization Using Low-Frequency DAS Signal. *Lead. Edge*, 36. 975–980. doi:10.1190/tle36120975.1

Karrenbach, M., Ridge, A., Cole, S., Boone, K., Rich, J., Silver, K., et al. (2017). “DAS Microseismic Monitoring and Integration with Strain Measurements in Hydraulic Fracture Profiling,” in *Unconventional Resources Technology Conference* (Austin, Texas: Society of Exploration Geophysicists, American Association of Petroleum Geologists, Society of Petroleum Engineers), 241316–261330. doi:10.15530/urtec-2017-2670716

Kwiatek, G., Bulut, F., Bohnhoff, M., and Dresen, G. (2014). High-resolution Analysis of Seismicity Induced at Berlín Geothermal Field, El Salvador. *Geothermics* 52, 98–111. doi:10.1016/j.geothermics.2013.09.008

Lellouch, A., and Biondi, B. L. (2021). Seismic Applications of Downhole DAS. *Sensors* 21, 2897. doi:10.3390/s21092897

Lellouch, A., Lindsey, N. J., Ellsworth, W. L., and Biondi, B. L. (2020). Comparison between Distributed Acoustic Sensing and Geophones: Downhole Microseismic Monitoring of the FORGE Geothermal Experiment. *Seismol. Res. Lett.* 91, 3256–3268. doi:10.1785/0220200149

Li, L., Tan, J., Schwarz, B., Staněk, F., Poiata, N., Shi, P., et al. (2020). Recent Advances and Challenges of Waveform-Based Seismic Location Methods at Multiple Scales. *Rev. Geophys.* 58, e2019RG000667. doi:10.1029/2019RG000667

Lim Chen Ning, I., and Sava, P. (2018). High-resolution Multi-component Distributed Acoustic Sensing. *Geophys. Prospect.* 66, 1111–1122. doi:10.1111/1365-2478.12634

Lin, Y., and Zhang, H. (2016). Imaging Hydraulic Fractures by Microseismic Migration for Downhole Monitoring System. *Phys. Earth Planet. Interiors* 261, 88–97. doi:10.1016/j.pepi.2016.06.010

Lindsey, N. J., and Martin, E. R. (2021). Fiber-Optic Seismology. *Annu. Rev. Earth Planet. Sci.* 49, 309–336. doi:10.1146/annurev-earth-072420-065213

Luo, B., Jin, G., and Stanek, F. (2021a). Near-field Strain in Distributed Acoustic Sensing-Based Microseismic Observation. *Geophysics* 86, P49–P60. doi:10.1190/geo2021-0031.1

Luo, B., Lellouch, A., Jin, G., Biondi, B., and Simmons, J. (2021b). Seismic Inversion of Shale Reservoir Properties Using Microseismic-Induced Guided Waves

Recorded by Distributed Acoustic Sensing. *Geophysics* 86, R383–R397. doi:10.1190/geo2020-0607.1

Mendecki, A. J., Lynch, R. A., and Malovichko, D. A. (2010). “Routine Microseismic Monitoring in Mines,” in Australian Earthquake Engineering Society 2010 Conference, Perth, Western Australia. Available at: https://aees.org.au/wp-content/uploads/2013/11/56-RichardLynch.pdf.

Rahimi Zeynal, A., Snelling, P., Neuhaus, C. W., and Mueller, M. (2014). *Correlation of Stimulated Rock Volume from Microseismic Pointsets to Production Data - A Horn River Case Study*. SPE Western North American and Rocky Mountain Joint Meeting, Denver, Colorado. doi:10.2118/169541-MS

Reshetnikov, A., Kummerow, J., Buske, S., and Shapiro, S. A. (2010). “Microseismic Imaging from a Single Geophone: KTB,” in *SEG Technical Program Expanded Abstracts 2010* (Denver, CO: Society of Exploration Geophysicist SEG Technical Program Expanded Abstracts). doi:10.1190/1.3513252

Richter, P., Parker, T., Woerpel, C., Wu, Y., Rufino, R., and Farhadiroushan, M. (2019). Hydraulic Fracture Monitoring and Optimization in Unconventional Completions Using a High-Resolution Engineered Fibre-Optic Distributed Acoustic Sensor. *First Break* 37, 63–68. doi:10.3997/1365-2397.n0021

Schultz, W. (2019). *Time-lapse Multicomponent Geophone and DAS VSP Processing and Analysis*. Golden, CO: Master’s thesis, Colorado School of Mines, dept. of Geophysics.

Staněk, F., and Eisner, L. (2017). Seismicity Induced by Hydraulic Fracturing in Shales: A Bedding Plane Slip Model. *J. Geophys. Res. Solid Earth* 122, 7912–7926. doi:10.1002/2017JB014213

Stanek, F., and Jin, G. (2021). “Reservoir Characterization Using DAS Microseismic Events,” in *First International Meeting for Applied Geoscience & Energy Expanded Abstracts* (Denver, CO: Society of Exploration Geophysicists SEG Technical Program Expanded Abstracts). doi:10.1190/segam2021-3583216.1

Stork, A. L., Baird, A. F., Horne, S. A., Naldrett, G., Lapins, S., Kendall, J.-M., et al. (2020). Application of Machine Learning to Microseismic Event Detection in Distributed Acoustic Sensing Data. *Geophysics* 85, KS149–KS160. doi:10.1190/geo2019-0774.1

Titov, A., Binder, G., Liu, Y., Jin, G., Simmons, J., Tura, A., et al. (2021). Modeling and Interpretation of Scattered Waves in Interstage Distributed Acoustic Sensing Vertical Seismic Profiling Survey. *Geophysics* 86, D93–D102. doi:10.1190/geo2020-0293.1

Ugueto, G. A., Todea, F., Daredia, T., Wojtaszek, M., Huckabee, P. T., Reynolds, A., et al. (2019). Can You Feel the Strain? DAS Strain Fronts for Fracture Geometry in the BC Montney. SPE Annual Technical Conference and Exhibition, Calgary, Alberta. Groundbirch, D021S029R005. doi:10.2118/195943-MS

Verdon, J. P., Horne, S. A., Clarke, A., Stork, A. L., Baird, A. F., and Kendall, J.-M. (2020). Microseismic Monitoring Using a Fibre-Optic Distributed Acoustic Sensor (DAS) Array. *Geophysics* 1, 1–48. doi:10.1190/geo2019-0752.1

Williams-Stroud, S., Bauer, R., Leetaru, H., Oye, V., Stanek, F., Greenberg, S., et al. (2020). Analysis of Microseismicity and Reactivated Fault Size to Assess the Potential for Felt Events by CO_2 Injection in the Illinois Basin. *Bull. Seismol. Soc. Am.* 110, 2188–2204. doi:10.1785/0120200112

Williams-Stroud, S., Ozgen, C., and Billingsley, R. L. (2013). Microseismicity-constrained Discrete Fracture Network Models for Stimulated Reservoir Simulation. *Geophysics* 78, B37–B47. doi:10.1190/geo2011-0061.1

Zhan, Z. (2019). Distributed Acoustic Sensing Turns Fiber-Optic Cables into Sensitive Seismic Antennas. *Seismol. Res. Lett.* 91, 1–15. doi:10.1785/0220190112

Zhu, X., and Jin, G. (2021). “Analysis of Cross-Well Fracture Hits in DJ Basin, Colorado Using Low-Frequency DAS Data,” in *First International Meeting for Applied Geoscience & Energy Expanded Abstracts* (Denver, CO: Society of Exploration Geophysicists). doi:10.1190/segam2021-3582658.1

Zoback, M. D. (2012). Managing the Seismic Risk Posed by Wastewater Disposal. *Earth Mag.* 57, 38

Conflict of Interest: The authors declare that the research was conducted in the absence of any commercial or financial relationships that could be construed as a potential conflict of interest.

Frontiers in Earth Science

TYPE Original Research
PUBLISHED 08 August 2022
DOI 10.3389/feart.2022.943424

OPEN ACCESS

EDITED BY
Fenglin Niu,
Rice University, United States

REVIEWED BY
Hongrui Qiu,
Massachusetts Institute of Technology,
United States
Yang Zhao,
China University of Petroleum, Beijing,
China

*CORRESPONDENCE
Yibo Wang,
wangyibo@mail.iggcas.ac.cn

SPECIALTY SECTION
This article was submitted to Solid Earth Geophysics,
a section of the journal
Frontiers in Earth Science

RECEIVED 13 May 2022
ACCEPTED 07 July 2022
PUBLISHED 08 August 2022

CITATION
Shao J, Wang Y, Zheng Y, Yao Y, Wu S, Yang Z and Xue Q (2022), Near-surface characterization using urban traffic noise recorded by fiber-optic distributed acoustic sensing.
Front. Earth Sci. 10:943424.
doi: 10.3389/feart.2022.943424

Near-surface characterization using urban traffic noise recorded by fiber-optic distributed acoustic sensing

Jie Shao[1,2], Yibo Wang[1,2]*, Yikang Zheng[1,2], Yi Yao[1,2], Shaojiang Wu[1,2], Zesheng Yang[1,2] and Qingfeng Xue[1,2]

[1]Key Laboratory of Petroleum Resource Research, Institute of Geology and Geophysics, Chinese Academy of Sciences, Beijing, China, [2]The Innovation Academy for Earth Science, Chinese Academy of Sciences, Beijing, China

The recently developed fiber-optic distributed acoustic sensing (DAS) technology has attracted widespread attention in engineering applications, oil exploration, and seismological research. Compared with the conventional geophones, DAS can acquire high-resolution data due to a dense sampling and can be deployed conveniently in the complex acquisition environment. These advantages of DAS make it promising for near-surface characterization in the urban city. In this study, a DAS line was utilized to record traffic noise seismic data in the urban city and to investigate the near-surface characterization. Seismic surface waves were reconstructed from the acquired traffic noises using seismic interferometry. Thereafter, we obtain the near-surface shear wave velocity profile below the DAS line by surface wave dispersion curve inversion using a Bayesian Markov Chain Monte Carlo method. The results demonstrate the effectiveness of DAS-based urban traffic noise in near-surface characterization.

KEYWORDS

fiber-optic distributed acoustic sensing, near-surface characterization, urban traffic noise, seismic interferometry, Surface wave

Introduction

The urban underground space is increasingly being developed and utilized with the advancement of urbanization. Various underground facilities have been built and put into use in many countries, such as subways, underground parking spaces, underground shopping malls, and so on (Bobylev and Sterling, 2016). However, there are uncertainties in the construction and operation of underground engineering due to the complexity and instability of near-surface structures. Therefore, accurate near-surface characterization is important for understanding the underground condition better and reducing the potential safety risks (Von der Tann et al., 2020).

Compared with the near-surface surveys in resource exploration, near-surface characterization in the urban city presents additional challenges, which require high spatial and temporal resolution, efficient data acquisition, low cost, and minimal

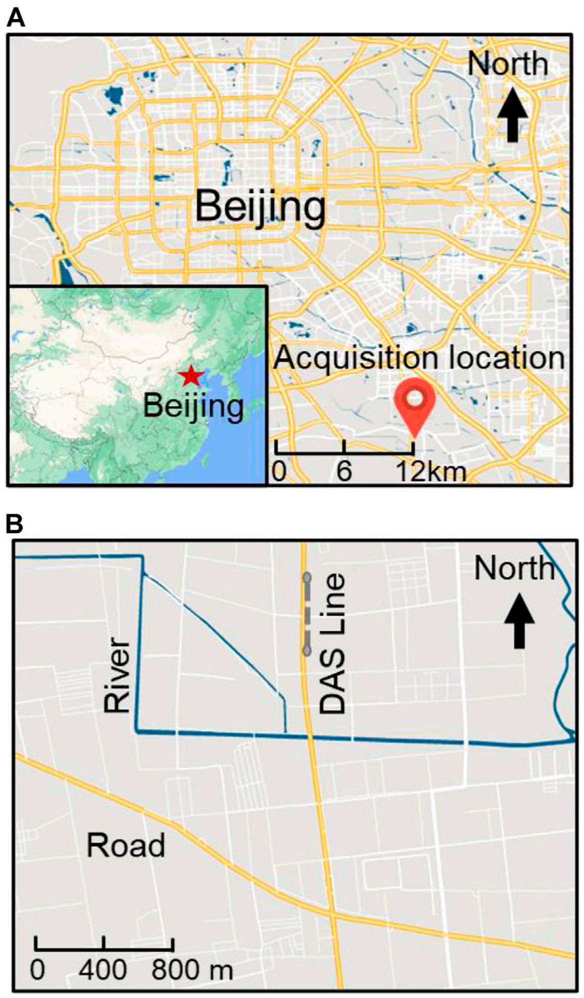

FIGURE 1
(A) Location of the data acquisition area in Beijing, China. **(B)** A zoomed-in view of the field acquisition layout. The dashed gray line indicates the DAS line along the road.

disruption to urban life. Different from the destructive active sources in the conventional near-surface surveys, the urban traffic noise provides a readily available and clean source to obtain the near-surface structure (Zhang et al., 2019; Ma and Qian, 2020). The newly developed fiber-optic distributed acoustic sensing (DAS) has emerged as a promising seismic data acquisition technology. Different from the particle displacement or velocity measurements of conventional geophones, DAS measures the strain rate or strain caused by vibrations using a fiber-optic cable (Zhan, 2020; Song et al., 2021a). Compared with the geophone, DAS can acquire high-resolution data with sampling frequencies from kHz to MHz and spatial sampling of several meters (Parker et al., 2014; Paitz et al., 2021). In addition, DAS can be deployed conveniently in the complex acquisition environment and enable long-term monitoring. The potential and advantages of DAS have been validated recently in seismic exploration (Daley et al., 2016; Lei et al., 2021; Wang et al., 2021), regional and teleseismic earthquake observations (Williams, et al., 2019; Shinohara et al., 2022), and microseismic monitoring (Walter et al., 2020). In terms of near-surface structure characterization, Fang et al. (2020) used blast signals from quarry sites to obtain the near-surface velocity changes. They picked travel times from virtual source gathers on each day and estimated the velocities by least-squares linear regression. Song et al. (2021b) analyzed the traffic noise distribution using the ambient noise from an urban city. The data were recorded by urban telecommunication fiber-optic cables. The fundamental-mode dispersion curves were extracted from the reconstructed Rayleigh surface waves in the virtual source gathers and then were inverted for the near-surface velocity structure using the ambient noise tomography with a neighborhood algorithm.

In this study, we acquired traffic noise using a DAS line deployed along a busy road in an urban city. We analyzed the recorded seismic wavefield and reconstructed seismic surface wave from 1 hour of continuous data. Then dispersion curves were extracted and inverted for the near-surface velocity below the DAS line. The inverted velocity agrees well with the prior geological knowledge. The results confirm the reliability of near-surface characterization using urban traffic noise recorded by a DAS line.

Data and preprocessing

The study site is located in an urban city (Beijing) in Northeast China, as shown in Figure 1A. The near-surface stratigraphy in this area mainly consists of horizontal layers. Data in this study were continuously acquired using a fiber-optic distributed acoustic sensing (DAS) line with a length of 402.5 m. The DAS line was installed along the road (Figure 1B) to ensure that the recorded data contained rich traffic noise. The gauge length is 5.0 m. The trace interval of acquired data is 0.5 m and the sampling frequency is 4,000 Hz.

We first analyzed the acquired urban traffic seismic noise collected by the DAS line. Figures 2A,B shows examples of 10 min recording when there are many vehicles and when no vehicles pass across the entire DAS line. As shown by the black arrows in Figure 2A, there are clear vehicle-related seismic data when vehicles pass through the DAS line. These vehicle-related seismic signals show linear events with different slopes, indicated by the green dashed lines in Figure 2A. They are excited by vehicles with different running speeds and directions. A zoomed-in view of a vehicle-related seismic event indicated by a rectangle labeled A in Figure 2A is shown in Figure 2C. The blue lines in Figure 2C indicate linear events with positive and negative slopes excited by a vehicle passing through the DAS line. The slopes of these blue

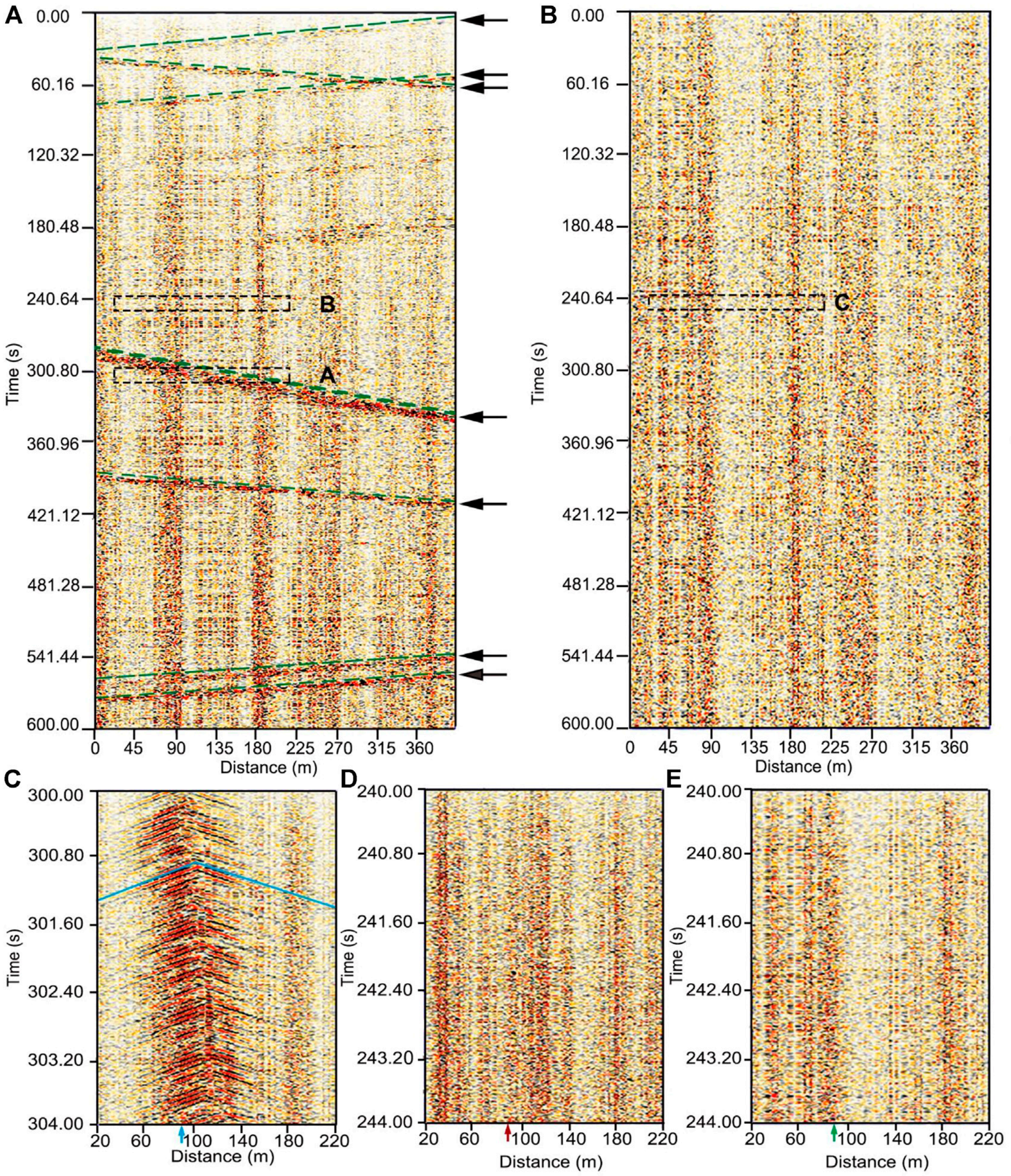

FIGURE 2
(A) Seismic data recorded by DAS line during 10 min of heavy road traffic. The black arrows indicate the vehicle-related seismic event and the green dashed lines indicate their slopes. **(B)** Seismic data recorded by DAS line during 10 min without road traffic. **(C–E)** The zoomed-in view of data indicated by the rectangles labeled A-B in **(A)** and labeled C in **(B)**. The color arrows indicate the locations of seismic waveforms and amplitude spectra in Panel 3. The blue lines in **(C)** represent the propagation velocity of wavefield excited by the vehicle.

lines represent the propagation velocity of the wavefield excited by the vehicle. Figures 2E,F shows the zoomed-in views of background noise indicated by the rectangle labeled B in Figure 2A and labeled C in Figure 2B. The two background noises are extracted from the records with and without vehicles to compare the effect of urban traffic. The waveforms and amplitude spectra of data indicated by the arrows in Figures 2C,D,E are shown in Figure 3. The vehicle-related seismic data in Figure 3A presents strong amplitude vibrations compared with the background noise in Figures 3B,C. The amplitude spectrum is distributed in a frequency range of 0–30 Hz, indicated by the blue line in Figure 3D. The red line in Figure 3D represents the amplitude spectrum of background noise extracted from a period in the vicinity of the vehicle-

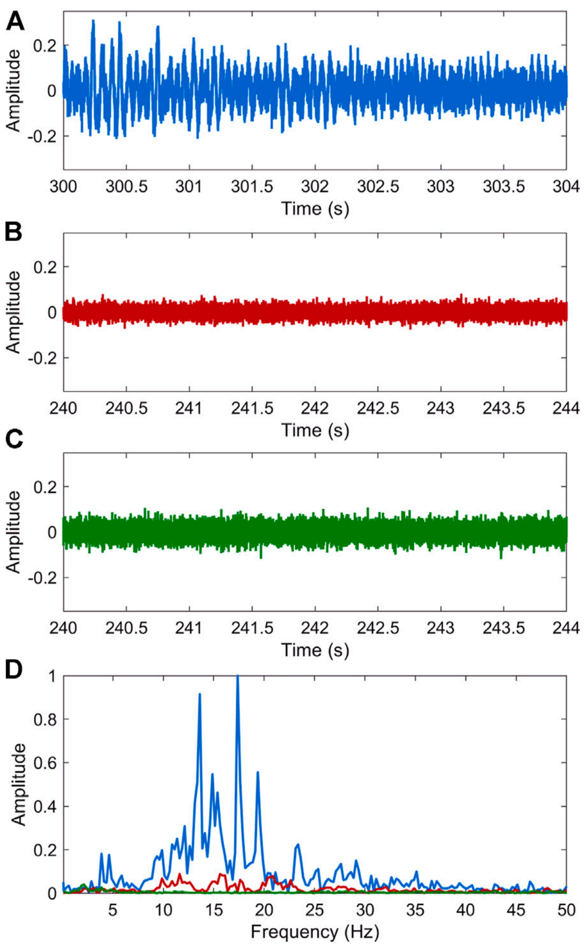

FIGURE 3
(A–C) Normalized waveforms of the traces at the locations indicated by the color arrows in Panel 2C-E. **(D)** Amplitude spectra of the traces in **(A–C)**.

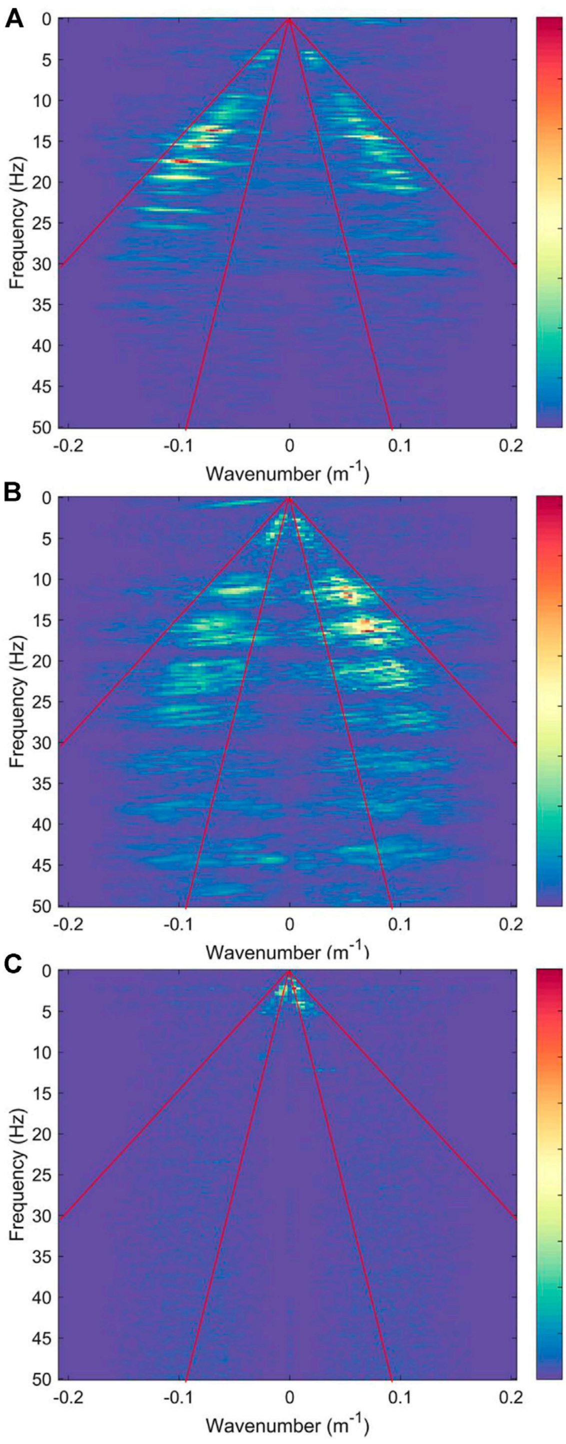

FIGURE 4
(A–C) F-K analyses of the DAS data in Panel 2C-E.

related seismic data. It shows a similar frequency band (0–30 Hz) to the vehicle-related seismic data (the blue line) but with weaker energy. In comparison, the amplitude spectrum of background noise extracted from a quiet period without vehicles has a lower frequency range of 0–10 Hz and the smallest energy. Therefore, the noise sources of urban traffic can provide a broadband frequency data than the common ambient noise. The F-K analyses of data in Figures 2C,D,E are shown in Figure 4. The energy bands in all the three F-K spectra distribute in an almost similar slope range defined by the red lines in Figure 4, indicating the similar apparent velocities of these waves.

Based on the analysis, surface waves are reconstructed by seismic interferometry using 1 h of continuous records, during which busy vehicles were moving along the road. The raw noise data are first preprocessed by a series of methods summarized in Bensen et al. (2007). They are then cut into segments with a length of 1 minute. Then, all the 1-min segments are removed mean and linear trend and are bandpass filtered to 5–25 Hz, followed by the one-bit normalization and spectral whitening Figure 5.

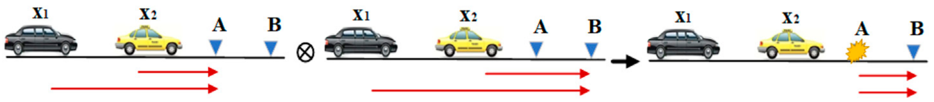

FIGURE 5
Ray diagram sketch of surface waves reconstruction by seismic interferometry.

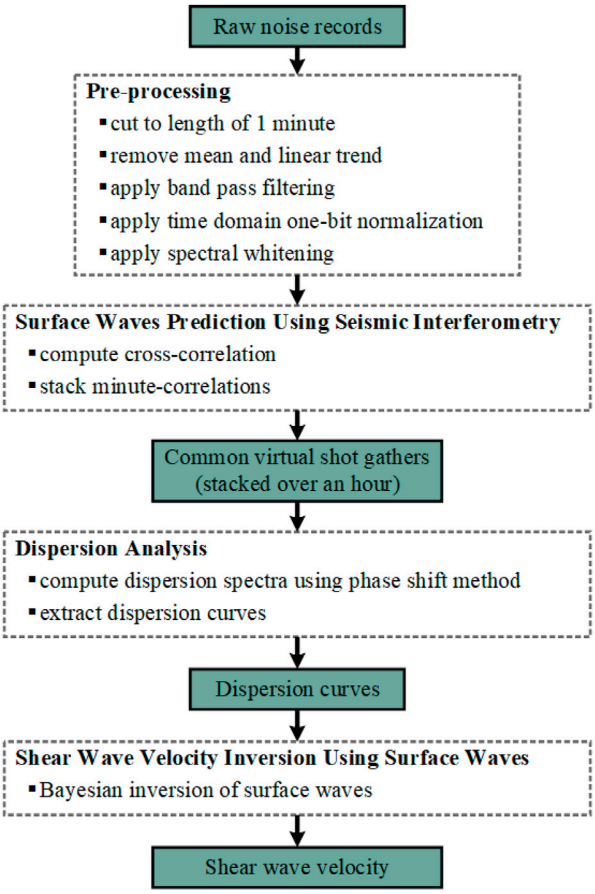

FIGURE 6
Workflow of shear wave velocity inversion using traffic noise.

Methods

Surface waves reconstruction using seismic interferometry

Seismic interferometry is used to reconstruct surface waves from continuous records, which has attracted wide attention in active and passive seismic data processing and imaging (Wang et al., 2009, 2010; Halliday et al., 2015; Shao et al., 2021; Zeng et al., 2022). Based on the reciprocity theorem of correlation type, the basic equation for seismic interferometry in the time domain is given as follows (Wapenaar, 2004):

$$G(\mathbf{B},\mathbf{A},t)+G(\mathbf{A},\mathbf{B},-t)\approx\int_{S_0}G(\mathbf{B},\mathbf{x},t)\otimes G(\mathbf{A},\mathbf{x},t)d^2\mathbf{x} \qquad (1)$$

where ⊗ represents the cross-correlation operation. The Green's functions $G(\mathbf{A},\mathbf{x},t)$ and $G(\mathbf{B},\mathbf{x},t)$ are excited by a source at $\mathbf{x}$, and received by sensors at $\mathbf{A}$ and $\mathbf{B}$, respectively. The far-field approximation is considered in Eq. 1. According to Eq. 1, traces recorded at two different locations, e.g., $G(\mathbf{A},\mathbf{x},t)$ and $G(\mathbf{B},\mathbf{x},t)$, are cross-correlated. The overlapping paths with the same ray parameters will be canceled, as shown in a ray diagram in Figure 6. Then all the cross-correlated responses over all source locations are summed to reconstruct a virtual trace received at $\mathbf{B}$ with a virtual source at $\mathbf{A}$ (Schuster, 2009; Wapenaar et al., 2010).

Shear wave velocity inversion using surface waves

After surface waves are reconstructed by seismic interferometry, dispersion analysis is implemented by the phase shift method due to its advantages in robustness and computational efficiency (Dal Moro et al., 2003). Then dispersion curves are extracted. Finally, the shear wave velocity is calculated by dispersion curves inversion using a Bayesian Markov Chain Monte Carlo (MCMC) method (Malinverno, 2002). The inversion problem is recast as a problem of statistical inference in the MCMC method. The Bayesian posterior probability density of the shear velocity model $p(m|d)$ is proportional to the product of a prior probability density $p(m)$ with a likelihood function $p(d|m)$ with:

$$p(m|d)\propto p(m)p(d|m) \qquad (2)$$

where m denotes the shear velocity model and d denotes the extracted dispersion curves characterized by surface wave phase velocities at different frequencies.

The construction of the likelihood function and the prior probability density are the main components of the Bayesian inversion. The former measures how well the forward data fits the observed data, and the latter expresses the current prior

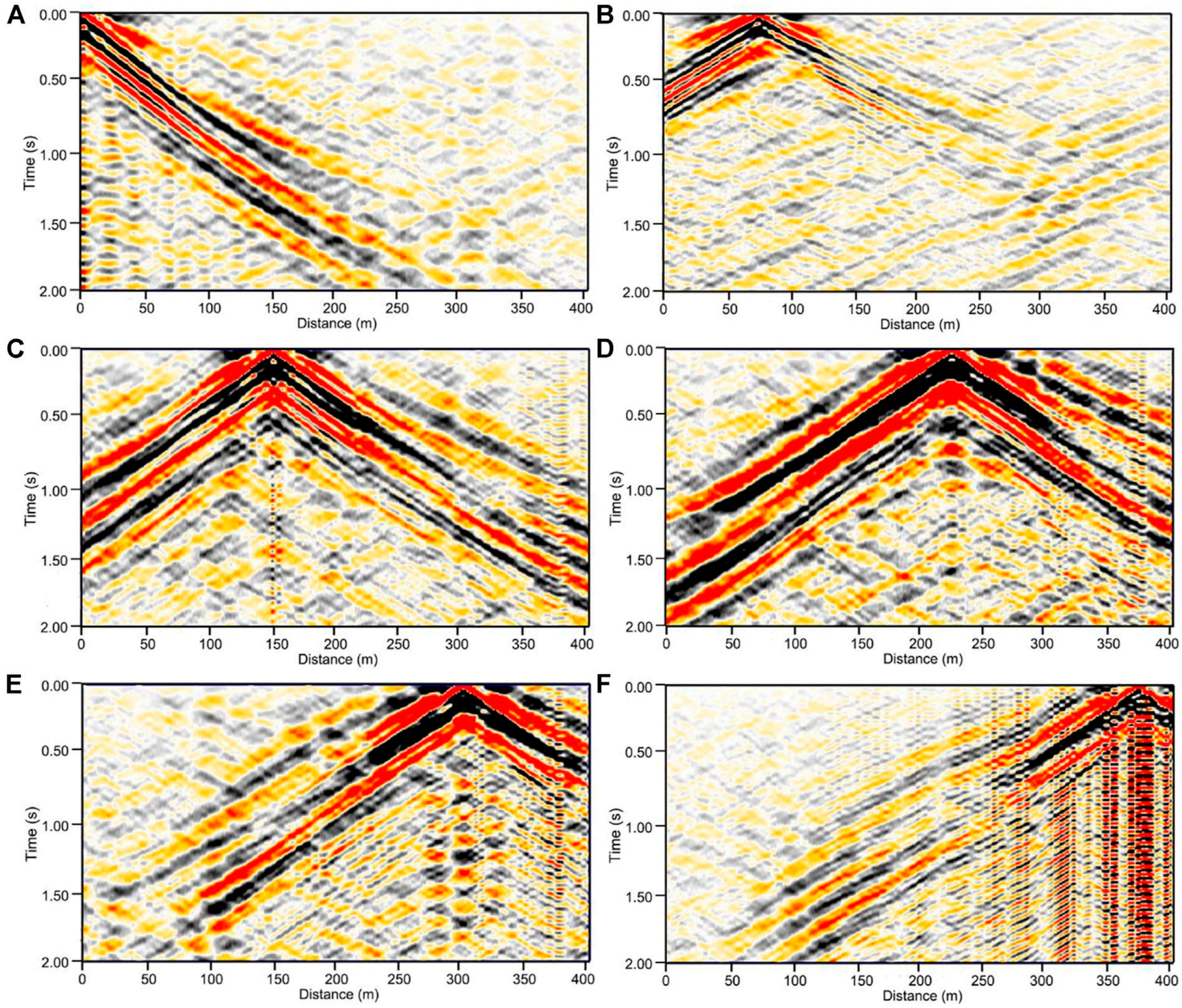

FIGURE 7
The virtual shot gather with a virtual source at **(A)** 2.5 m, **(B)** 77.5 m, **(C)** 152.5 m, **(D)** 227.5 m, **(E)** 302.5 m, and **(F)** 377.5 m.

knowledge about the model. The likelihood function $p(d|m)$ in this study is defined by the L_2 misfit between the observed and forward surface wave phase velocities, and is given as follows:

$$p(d|m) \propto \exp\left[-\left(d_{obs} - c(m)\right)^2\right] \tag{3}$$

where d_{obs} is the observed phase velocity and $c(m)$ is the forward phase velocity using the propagator-matrix method (Wathelet, 2005).

Assumed that the shear wave velocity model is uniformly distributed in a fixed range, the prior probability density is given as follows:

$$p(m) \propto \begin{cases} \prod_{i=1}^{M} \left(m_i^+ - m_i^-\right)^{-1} & m_i^+ \leq m_i \leq m_i^-, i = 1, \ldots, M \\ 0 & otherwise \end{cases} \tag{4}$$

where m_i^+ and m_i^- are the upper and lower boundary of i^{th} velocity m_i.

Finally, the posterior probability density is obtained by combining Eqs 3, 4 in Eq.2. The task of Bayesian inversion then is to evaluate the complete posterior probability density $p(m|d)$. The MCMC algorithm is used, which is an iterative method for generating samples from a probability density. The initial model is selected randomly from the prior. Then a series of models are generated in a chain according to the posterior probability density. Each model is a perturbation of the last one. The generated models are examined with an acceptance ratio which is defined as:

$$\alpha = \min\left[1, \frac{p(m')p(d|m')q(m|m')}{p(m)p(d|m)q(m'|m)}\right] \tag{5}$$

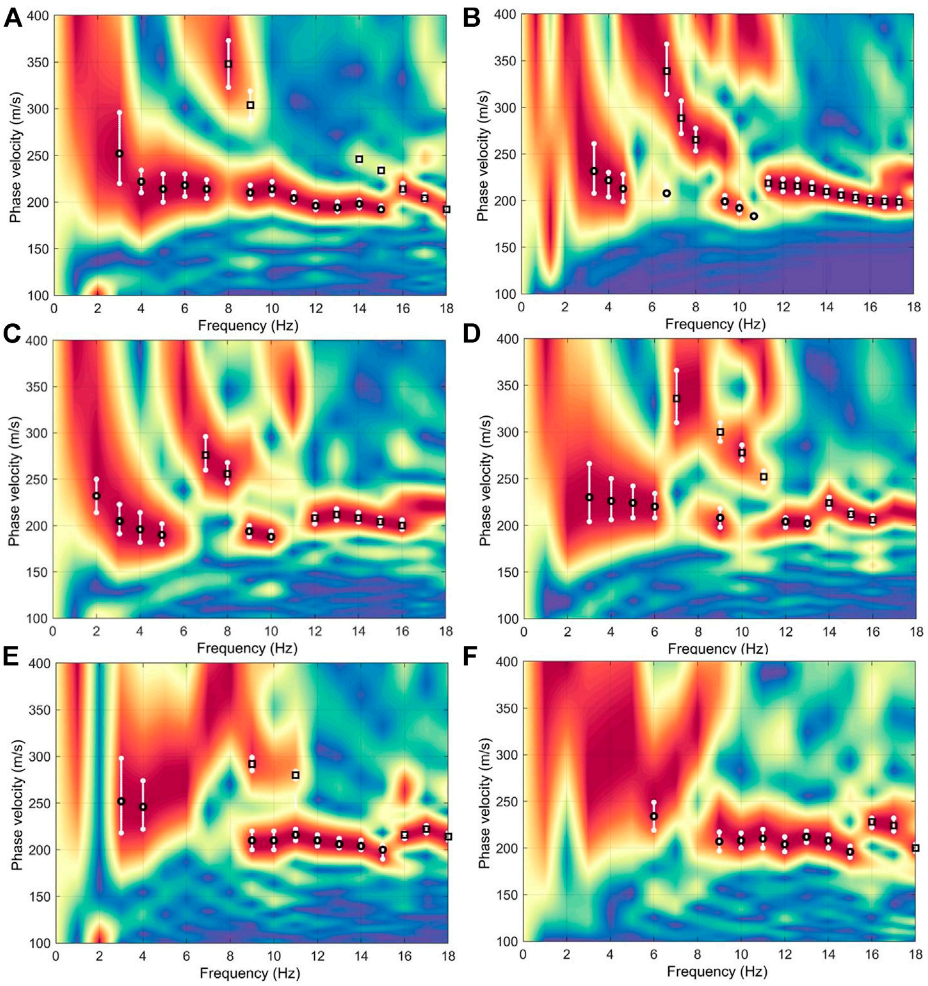

FIGURE 8
(A–F) Dispersion spectrum and the extracted dispersion curve from data in Figures 7A–F. The picked fundamental and first-order mode dispersion curves are respectively indicated by circles and rectangles.

where m' represents the generated new model from the existing model m, q represents the probability density of moving from m to m'. If the acceptance ratio α is larger than a random number $u \sim U[0,1]$, the generated new model is accepted and added to the chain. The current model is then updated. Otherwise, the generated new model is rejected and the existing model is retained as the current model.

Results

The processing workflow of shear wave velocity inversion using traffic noise is summarized in Figure 6. The reconstructed wavefields by seismic interferometry show surface waves with clear dispersive effects, as shown in the virtual shot gathers at different locations in Figure 7. Because the virtual traces at the far offset have a low signal-to-noise ratio (SNR), a window function is applied to the virtual shot gathers to extract the high SNR data at the near offset. Thereafter, dispersion spectra are calculated from the windowed data, and the multi-mode dispersion curves can be picked, as shown in Figure 8. However, the picked first-order mode dispersion curves in some virtual shot gathers are not reliable, as shown in Figures 7A,E,F. In addition, the picked surface wave dispersion curves from the virtual shot gathers at different positions show similar shapes, especially for the fundamental mode. This verifies the correct identification of multi-mode surface waves.

Different from a commonly used 2D array in the passive survey, a linear array was implemented in this study considering the limited space in the urban city. This regular 1D acquisition geometry may cause artifacts in the phase velocity maps inverted by a surface wave tomography method because of the

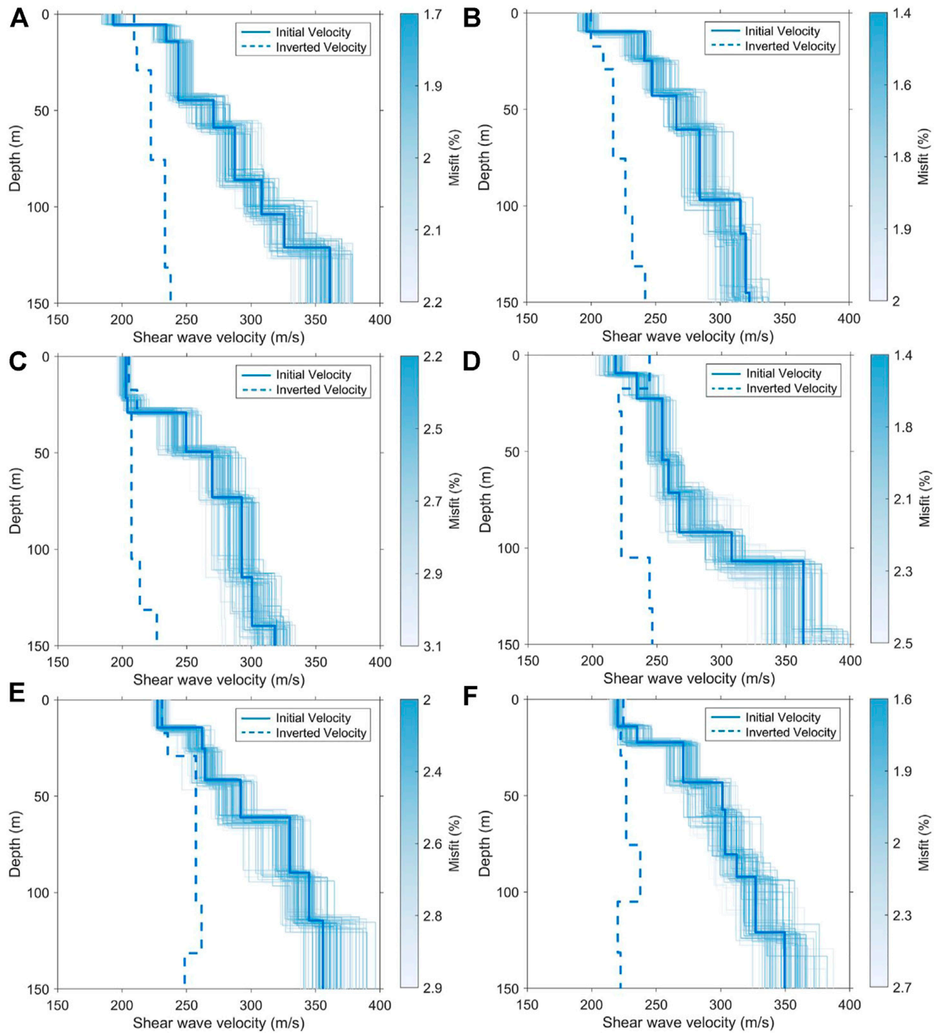

FIGURE 9
(A–F) The inverted 1D shear wave velocities using the fundamental mode dispersion curves in Figures 8A–F.

nonuniform ray coverage related to the acquisition layout (Barone et al., 2021). In addition, the subsurface structure in the study area mainly consists of horizontal layers. Therefore, we invert the 2D velocity profile using a 1D inversion scheme of multichannel analysis of surface wave (Park et al., 2007; Morton et al., 2021). This method inverts a 1D velocity from the dispersion curve picked from a virtual shot gather. Then 1D velocities inverted from all the virtual shot gathers are assembled to build a 2D velocity. We consider only the fundamental mode for the dispersion curve inversion due to the unreliability of first-order mode. Figure 9 shows the dispersion curve inversion results of the fundamental mode in Figure 8. The forward dispersion curves shown by the blue lines in Figure 10 are calculated using the best inverted velocities in Figure 9, which fits well with the picked dispersion curves (shown by the solid circles in Figure 10). The final 2D velocity profile along the DAS line is shown in Figure 11. We compared the final velocity profile with the prior geological information in the study site to validate the result. The previous study shows that the quaternary deposits in the study area include the Holocene and Pleistocene sequences (Zhao et al., 2019). Boundaries of the Holocene-Upper Pleistocene, the Upper-Middle Pleistocene, and the Middle-Lower Pleistocene are respectively located at depths of 17.35, 57.20 and 75.60 m. These stratigraphic boundaries are approximately consistent with those in the inverted velocity, as shown in the color bar in Figure 11.

Discussion

We have demonstrated the feasibility of near-surface characterization using urban traffic noise recorded by DAS.

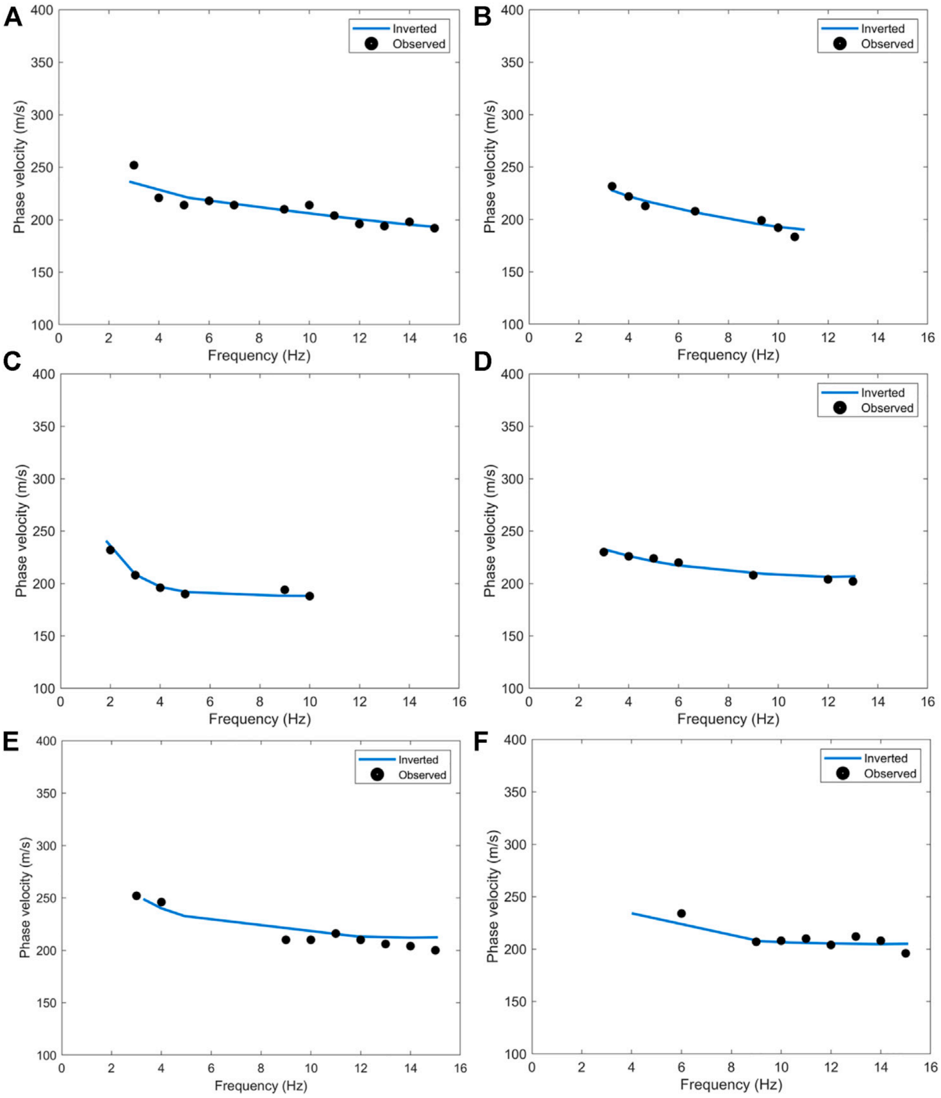

FIGURE 10
(A–F) The fit of the forward fundamental-mode dispersion curve using the inverted velocity in Figures 9A–F to the picked one in Figures 8A–F.

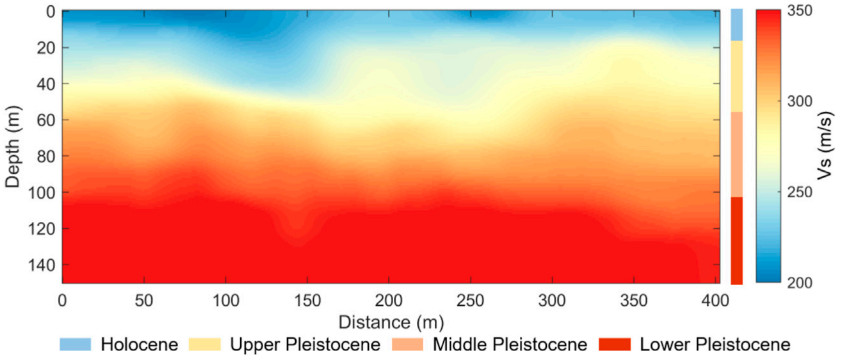

FIGURE 11
The 2D shear wave velocity profile along the DAS line. The color bar indicates the depths of key horizons according to the prior geological information in the study area.

Compared with the conventional geophones, DAS has obvious advantages in high-density sampling, which can provide a high-resolution subsurface structure. In addition, the convenient deployment of DAS makes it stand out in the near-surface characterization of urban cities and other harsh environment. However, different from the particle displacement or velocity measurement of geophones, DAS measures the strain or strain rate. This leads to the difference between the interferometric wavefield obtained from the geophone and DAS data according to the representation theorem defined by different physical quantities (velocity and strain) (Paitz, et al., 2019). Therefore, the dynamic information (waveform) of velocity and strain wavefield are obviously different. This difference should be considered for near-surface characterization using a full waveform inversion method for velocity wavefield. On the other hand, the kinematic information of the velocity and strain wavefield are similar. Therefore, the dispersion curves extracted from the two wavefields may reveal similar near-surface velocity (Martin, et al., 2015; Song, et al., 2021b). The dispersion curve inversion method for geophone data is applicable to DAS data.

Conclusion

We present the near-surface characterization in this study using traffic noise seismic data acquired by a DAS line deployed along the road in the urban city. Seismic surface waves are extracted from the traffic noise data using seismic interferometry. Compared with the common natural sources, the traffic noise source exhibits strong energy and can provide a wider frequency range. Finally, the near-surface shear wave velocity structure along the DAS line is obtained by surface wave dispersion curves inversion using a Bayesian Markov Chain Monte Carlo method. The inverted velocity agrees well with the geological structure in the study area. The results demonstrate that traffic noise can be regarded as a powerful and effective tool for high-resolution near-surface characterization in the urban city, especially when combining the DAS technique with the unused telecommunication networks in the city.

Data availability statement

The datasets presented in this article are not readily available because it is still being used for scientific research. Requests to access the datasets should be directed to the corresponding author.

Author contributions

JS and YW studied the method, processed the data and wrote the manuscript. YZ, YY, SW, ZY, and QX acquired the data underlying this study. All authors discussed the results and contributed to the final manuscript.

Funding

This study was funded by the CAS Project for Young Scientists in Basic Research (Grant No. YSBR-020) and the National Key R&D Program of China (Grant No. 2021YFA0716800).

Conflict of interest

The authors declare that the research was conducted in the absence of any commercial or financial relationships that could be construed as a potential conflict of interest.

Publisher's note

References

Barone, I., Kästle, E., Strobbia, C., and Cassiani, G. (2021). Surface wave tomography using 3D active-source seismic data. *Geophysics* 86 (1), EN13–EN26. doi:10.1190/geo2020-0068.1

Bensen, G. D., Ritzwoller, M. H., Barmin, M. P., Levshin, A. L., Lin, F., Moschetti, M. P., et al. (2007). Processing seismic ambient noise data to obtain reliable broad-band surface wave dispersion measurements. *Geophys. J. Int.* 169 (3), 1239–1260. doi:10.1111/j.1365-246x.2007.03374.x

Bobylev, N., and Sterling, R. (2016). Urban underground space: A growing imperative. *Tunn. Undergr. space Technol.* 55, 1–4. doi:10.1016/j.tust.2016.02.022

Dal Moro, G., Pipan, M., Forte, E., and Finetti, I. (2003). Determination of Rayleigh wave dispersion curves for near surface applications in unconsolidated sediments. *Seg. Tech. Program Expand. Abstr.* 22, 1247–1250. doi:10.1190/1.1817508

Daley, T. M., Miller, D. E., Dodds, K., Cook, P., and Freifeld, B. M. (2016). Field testing of modular borehole monitoring with simultaneous distributed acoustic sensing and geophone vertical seismic profiles at Citronelle, Alabama. *Geophys. Prospect.* 64 (5), 1318–1334. doi:10.1111/1365-2478.12324

Fang, G., Li, Y. E., Zhao, Y., and Martin, E. R. (2020). Urban near-surface seismic monitoring using distributed acoustic sensing. *Geophys. Res. Lett.* 47 (6), e2019GL086115. doi:10.1029/2019gl086115

Halliday, D., Bilsby, P., West, L., Kragh, E., and Quigley, J. (2015). Scattered ground-roll attenuation using model-driven interferometry. *Geophys. Prospect.* 63 (1), 116–132. doi:10.1111/1365-2478.12165

Lei, Y. H., Yin, F., Hong, H. T., Li, Y. L., and Wang, B. S. (2021). Shallow structure imaging using higher-mode Rayleigh waves based on FJ transform in DAS observation. *Chin. J. Geophys.* 64 (12), 4280–4291. doi:10.6038/cjg2021P0438

Ma, Z., and Qian, R. (2020). Overview of seismic methods for urban underground space. *Interpretation* 8 (4), SU19–SU30. doi:10.1190/int-2020-0044.1

Malinverno, A. (2002). Parsimonious Bayesian Markov chain Monte Carlo inversion in a nonlinear geophysical problem. *Geophys. J. Int.* 151 (3), 675–688. doi:10.1046/j.1365-246x.2002.01847.x

Martin, E., Ajo-Franklin, J., Lindsey, N., Daley, T., Freifeld, B., Robertson, M., et al. (2015). Applying interferometry to ambient seismic noise recorded by a trenched distributed acoustic sensing array. *SEP* 158, 247–254.

Morton, S. L., Ivanov, J., Peterie, S. L., Miller, R. D., and Livers-Douglas, A. J. (2021). Passive multichannel analysis of surface waves using 1D and 2D receiver arrays. *Geophysics* 86 (6), EN63–EN75. doi:10.1190/geo2020-0104.1

Paitz, P., Edme, P., Gräff, D., Walter, F., Doetsch, J., Chalari, A., et al. (2021). Empirical investigations of the instrument response for distributed acoustic sensing (DAS) across 17 octaves. *Bull. Seismol. Soc. Am.* 111 (1), 1–10. doi:10.1785/0120200185

Paitz, P., Sager, K., and Fichtner, A. (2019). Rotation and strain ambient noise interferometry. *Geophys. J. Int.* 216 (3), 1938–1952. doi:10.1093/gji/ggy528

Park, C. B., Miller, R. D., Xia, J., and Ivanov, J. (2007). Multichannel analysis of surface waves (MASW) - active and passive methods. *Lead. edge* 26 (1), 60–64. doi:10.1190/1.2431832

Parker, T., Shatalin, S., and Farhadiroushan, M. (2014). Distributed Acoustic Sensing - a new tool for seismic applications. *First break* 32 (2), 61–69. doi:10.3997/1365-2397.2013034

Schuster, G. T. (2009). *Seismic interferometry*. Cambridge: Cambridge University Press.

Shao, J., Wang, Y. B., and Chang, X. (2021). Radon domain interferometric interpolation of sparse seismic data. *Geophysics* 86 (5), WC89–WC104. doi:10.1190/geo2020-0878.1

Shinohara, M., Yamada, T., Akuhara, T., Mochizuki, K., and Sakai, S. I. (2022). Performance of seismic observation by distributed acoustic sensing technology using a seafloor cable off Sanriku, Japan. *Front. Mar. Sci.* 466, 844506. doi:10.3389/fmars.2022.844506

Song, Z. H., Zeng, X. F., and Thurber, C. H. (2021a). Surface-wave dispersion spectrum inversion method applied to Love and Rayleigh waves recorded by distributed acoustic sensing. *Geophysics* 86 (1), EN1–EN12. doi:10.1190/geo2019-0691.1

Song, Z. H., Zeng, X. F., Xie, J., Bao, F., and Zhang, G. B. (2021b). Sensing shallow structure and traffic noise with fiber-optic internet cables in an urban area. *Surv. Geophys.* 42, 1401–1423. doi:10.1007/s10712-021-09678-w

Von der Tann, L., Sterling, R., Zhou, Y., and Metje, N. (2020). Systems approaches to urban underground space planning and management–A review. *Undergr. Space* 5 (2), 144–166. doi:10.1016/j.undsp.2019.03.003

Walter, F., Gräff, D., Lindner, F., Paitz, P., Köpfli, M., Chmiel, M., et al. (2020). Distributed acoustic sensing of microseismic sources and wave propagation in glaciated terrain. *Nat. Commun.* 11 (1), 2436. doi:10.1038/s41467-020-15824-6

Wang, B. S., Zeng, X. F., Song, Z. H., Li, X. B., and Yang, J. (2021). Seismic observation and subsurface imaging using an urban telecommunication optic-fiber cable. *Chin. Sci. Bull.* 66, 2590–2595. doi:10.1360/tb-2020-1427

Wang, Y. B., Dong, S., and Xue, Y. W. (2009). “Surface waves suppression using interferometric prediction and curvelet domain hybrid L1/L2 norm subtraction,”the 2009 SEG Annual Meeting, Houston, Texas, October 25 2009, 3292–3296.

Wang, Y., Dong, S., and Luo, Y. (2010). Model-based interferometric interpolation method. *Geophysics* 75 (6), WB211–WB217. doi:10.1190/1.3505816

Wapenaar, K., Draganov, D., Snieder, R., Campman, X., and Verdel, A. (2010). Tutorial on seismic interferometry: Part 1—basic principles and applications. *Geophysics* 75 (5), 75A195–75A209. doi:10.1190/1.3457445

Wapenaar, K. (2004). Retrieving the elastodynamic Green’s function of an arbitrary inhomogeneous medium by cross correlation. *Phys. Rev. Lett.* 93 (25), 254301. doi:10.1103/physrevlett.93.254301

Wathelet, M. (2005).Array recordings of ambient vibrations: Surface-wave inversion. PhD Diss. Belgium: Liége University, 161.

Williams, E. F., Fernández-Ruiz, M. R., Magalhaes, R., Vanthillo, R., Zhan, Z., González-Herráez, M., et al. (2019). Distributed sensing of microseisms and teleseisms with submarine dark fibers. *Nat. Commun.* 10 (1), 5778. doi:10.1038/s41467-019-13262-7

Zeng, X., Thurber, C. H., Wang, H. F., Fratta, D., and Feigl, K. L. (2022). “High-resolution shallow structure at Brady Hot Springs using ambient noise tomography (ANT) on a trenched distributed acoustic sensing (DAS) array,” in *Distributed Acoustic Sensing in Geophysics: Methods and Applications*. Editor Y. Li (New York, NY: John Wiley & Sons), 101–110.

Zhan, Z. (2020). Distributed acoustic sensing turns fiber-optic cables into sensitive seismic antennas. *Seismol. Res. Lett.* 91 (1), 1–15. doi:10.1785/0220190112

Zhang, Y. H., Li, Y. E., Zhang, H., and Ku, T. (2019). Near-surface site investigation by seismic interferometry using urban traffic noise in Singapore. *Geophysics* 84 (2), B169–B180. doi:10.1190/geo2017-0798.1

Zhao, Y., Li, R. J., Wei, B., Wang, C. J., Sun, Y. H., and Fang, T. M. (2019). Magnetostratigraphy of borehole PGZ05 in southern daxing Uplift, Beijing Plain. *Geoscience* 33 (01), 56.

Frontiers in Earth Science

TYPE Original Research
PUBLISHED 06 September 2022
DOI 10.3389/feart.2022.952410

OPEN ACCESS

EDITED BY
Michael Zhdanov,
The University of Utah, United States

REVIEWED BY
Andrew Curtis,
University of Edinburgh,
United Kingdom
Leonardo Sigalotti,
Metropolitan Autonomous University,
Mexico

*CORRESPONDENCE
Xiangfang Zeng,
zengxf@whigg.ac.cn

SPECIALTY SECTION
This article was submitted to Solid Earth Geophysics,
a section of the journal
Frontiers in Earth Science

RECEIVED 25 May 2022
ACCEPTED 15 August 2022
PUBLISHED 06 September 2022

CITATION
Song Z, Zeng X, Chi B, Bao F and Osotuyi AG (2022), Using the three-station interferometry method to improve urban DAS ambient noise tomography.
Front. Earth Sci. 10:952410.
doi: 10.3389/feart.2022.952410

Using the three-station interferometry method to improve urban DAS ambient noise tomography

Zhenghong Song[1,2], Xiangfang Zeng[1]*, Benxin Chi[1], Feng Bao[1] and Abayomi Gaius Osotuyi[2]

[1]State Key Laboratory of Geodesy and Earth's Dynamics, Innovation Academy for Precision Measurement Science and Technology, Chinese Academy of Sciences, Wuhan, China, [2]School of Earth and Space Sciences, University of Science and Technology of China, Hefei, China

Distributed acoustic sensing (DAS) is a novel seismological observation technology based on the fiber-optic sensing method, and can transform existing urban fiber-optic cables into ultra-dense array for urban seismological researches, thus opening abundant opportunities for resolving fine details of near surface structures. While high frequency ambient noise recorded on DAS has been applied in surface wave tomography, it is often difficult to extract a clear dispersion curve for the data recorded by urban internet cable because of the effect of precursor signals on noise correlation functions due to uneven distribution of noise sources, and weak coupling between the cable and the solid earth. In this study, we investigate the performance of the three-station interferometry method for improving the noise cross-correlation functions of the linear array. We applied this method to a DAS dataset acquired in an urban area, suppressed the precursor signal, improved the measurement of the dispersion curve, and constructed a 2D S-wave profile that reveals the hidden fault beneath the city. We also observed that the convergence of noise cross-correlation functions with weak coupling was significantly accelerated using this method. We employed this method to improve the signal quality of surface waves at far offset for the long segment, thus obtaining a more accurate dispersion curve. In conclusion, the three-station interferometry is an effective method to enhance the surface wave signal and suppress the precursor signal retrieved from the data recorded by urban internet cable, which could help in providing high resolution images of shallow structures in built-up areas.

KEYWORDS

distributed acoustic sensing, urban fiber-optic cable, ambient noise tomography, noise cross-correlation function, three-station interferometry

Introduction

High-resolution imaging of subsurface structures plays an important role in urban construction planning (e.g., underground space utilization, (Bobylev, 2010)), and geological disaster prevention (e.g., sinkhole detection (Cueto et al., 2018) and earthquake intensity estimation (Chen et al., 2009)). The seismic method is an effective tool to achieve high-precision subsurface imaging by analyzing the seismic wave signals generated from controlled active sources or natural sources. Subsurface anomalies can be identified using active sources with high signal-to-noise ratio (SNR) ratio and desirable observation system (Zandomeneghi et al., 2013). At the same time, reliable results have also been achieved using passive source imaging from ambient noise which is due to human activity (e.g., Lin et al., 2013; Zeng et al., 2021; Mi et al., 2022). Moreover, thickness and shear velocity structure in the top dozens of meters beneath permanent seismic stations have been resolved from modeling converted high frequency seismic phases from local earthquakes (Li et al., 2014; Ni et al., 2014), and their studies demonstrate a few times of ground motion amplification due to near surface low shear velocity structures. Obtaining a high-resolution subsurface structure relies on short seismic wavelength requiring denser observations, which is a huge challenge in seismic data acquisitions using traditional seismometers. Distributed acoustic sensing (DAS) is a recently developed novel seismic observation system, which measures the seismic signals by analyzing the phase shift of the backscattered pulse in the optical fiber (Zhan, 2020). It is noteworthy to mention that DAS can easily be incorporated with existing urban fiber-optic cables, thereby turning the fiber-optic networks into dense seismographic networks with meter-scale spacing (Parker et al., 2014). DAS has found broad applications and has demonstrated to be a valuable tool in seismological studies such as in signal detection (e.g., Lindsey et al., 2017; Zhu and Stensrud 2019; Wang et al., 2020) and near-surface characterization (e.g., Ajo-Franklin et al., 2019; Spica et al., 2020).

Ambient noise tomography, widely used for urban subsurface structure detection, is achieved *via* calculating the cross-correlation of continuous ambient noise records (noise cross-correlation function, NCF) and stacking them to extract surface wave signals for inversion (Bensen et al., 2007). However, the precursor signals produced by heterogeneous noise distribution in urban areas seriously affect the quality of NCF and the results of ambient noise tomography (Galetti and Curtis, 2012; Retailleau and Beroza 2021). The noise excited by vehicles traveling along the fiber-optic cable is contributive, while the noise generated by vehicles across the cable and persistent localized human activities are adverse for ambient noise tomography (Song et al., 2021). Furthermore, the urban existing fiber-optic cables are packaged with different structures and deployed in a variety of ways, so the transfer function of the coupling is influenced by many factors and needed to be further studied (e.g., Lindsey et al., 2020b). We assumed that the coupling of the fiber-optic cables lying in the same polyvinyl chloride pipe is uniform but the coupling of pipeline to soil is various and the changes in phase response are ignorable. As a result of weak coupling, the amplitude response is low, which decreases the SNR of effective noise signals, and it would require a longer time span stacking to obtain a stable NCF (Lin et al., 2021). However, long-time span stacking may not obtain the correct NCF when the traffic signal is too weak to exceed the instrument's self-noise level.

Therefore, it is necessary to enhance the surface wave and suppress the precursor signals for the NCF. Stehly et al. (2008) reconstructed the surface wave signal between two stations by calculating the cross-correlation of the coda waves of the NCF between the stations with a third station (C3). Froment et al. (2011) demonstrated that C3 can well suppress the effects caused by distributions of non-isotropic sources by analyzing 150 continuously recording stations. Curtis and Halliday (2010) proposed three-station interferometry for direct wave (TSI), which used the entire NCF rather than the coda wave of the NCF. The convolution of the entire NCFs was calculated when the third station lies between the two stations, while the cross-correlation was calculated when the third station is located outside the two stations. Zhang et al., (2020a) compared the surface wave signals extracted from C3 and TSI, and suggested there are small biases in the dispersion curve. The biases arise from the geometry of the stations, which assumes the distance difference equal to 0 (distance difference is the difference between the distance of two stations and the sum/difference of the distances from the third station to the two stations when the third station lie in/out the two stations). The influence of distance difference might be negligible for a nearly straight linear array (Lin et al., 2008). Qiu et al. (2021) successfully enhanced the surface wave signals extracted from the NCF of a linear array using the TSI method, thereby making the method potentially applicable to improve ambient noise tomography results for urban linear DAS array.

In this study, we adopted the TSI method on a real-world DAS dataset and analyzed its improvement in ambient noise tomography. First, we showed a set of NCFs retrieved from the data recorded by urban internet cable in a built-up area and estimated the noise intensity and distribution around the fiber-optic cable. Then, we introduced the TSI method and used this method to denoise the precursor signals. The surface wave signals were enhanced significantly, and clear dispersion curves can be obtained to construct the subsurface structure. Finally, we demonstrate that the TSI method can effectively improve the temporal and spatial resolution of ambient noise

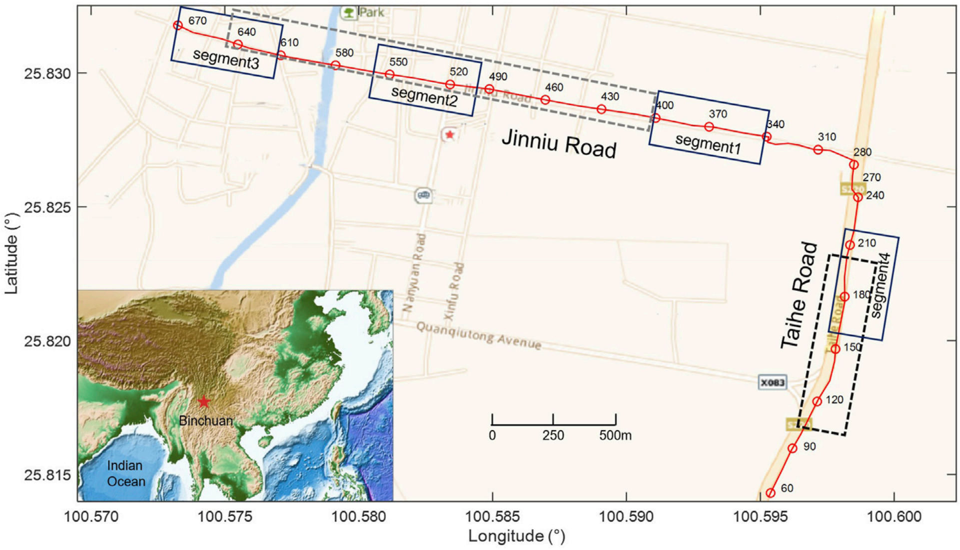

FIGURE 1
The location of the experiment. The red line is fiber-optic cable, which is distributed along two streets (Taihe Road and Jinniu Road). The numbers around the red circles are the channel indexes. The segments framed by the solid and dashed lines are used for analysis in the later section.

tomography by discussing the coupling and length of the segment.

Data and methods

The experiment was carried out in Binchuan county, Yunnan Province, southwest of China (Figure 1). A 5.2 km long internet fiber-optic cable lying in a polyvinyl chloride (PVC) pipe, which was buried at about 30 cm beneath two streets (Taihe Road and Jinniu Road, Wang et al., 2021a), was used in the experiment. The Helios Theta DAS Interrogator was connected to one end of the fiber-optic cable, with a spacing of 7.5 m (gauge length is set at 10.9 m), for 16-h continuous strain data acquisition. A previous study suggested that the noise source in the Taihe Road is distributed along the fiber-optic cable, which benefits for imaging, and the 2D S wave velocity profile has been constructed to reveal the low velocity zone along the road (Song et al., 2021). However, it is difficult to obtain clear dispersion curves along the Jinniu Road for ambient noise tomography, and we suspect this is due to the heterogeneous distribution of noise.

For instance, we choose three segments along the Jinniu Road for our analysis (segment 1, CH340-400, segment 2, CH500-560, and segment 3, CH610-670, in Figure 1). The first channel of each segment was used as the virtual source, and the other channels were virtual receivers to calculate the NCF. Song et al. (2021) suggested that the frequency range of ambient noise is 1–30 Hz and a stable NCF can be obtained with 4-h ambient noise data during the daytime. Therefore, for every channel, we resampled a 4-h continuous dataset from 500 to 100 Hz to reduce computing time and bandpass filtered it into 1–30 Hz. The dataset was cut into 30 s time windows, and normalized in time and frequency domains. Then, we calculated the cross-correlation function for each window of the virtual source and virtual receiver. The final NCF was obtained by stacking all the cross-correlation functions. The combination of the NCFs of all the virtual receivers and the virtual source is a common virtual-shot gather. Figures 2A–C are the common virtual-shot gathers of the previous three segments. For segment 1, the surface wave appears in the negative lag of the NCFs, indicating that the noise mainly comes from the direction of Taihe Road. However, the precursor seismic phases appear before the direct surface wave for segments 2 and 3 (Figure 2), and it is produced by complex traffic activities. We stacked the positive and negative lags to reduce the effects of the asymmetric noise source distribution and employed the multi-channel analysis of the surface wave method (MASW, Park et al., 1999) to extract the corresponding dispersion curve (Figures 2D–F). A low frequency (1–5 Hz) dispersion curve was achieved for segment 1, but it is difficult to obtain a continuous dispersion curve for segments 2 and 3.

To analyze the generation of the precursor signals, we estimated the noise intensity distribution around the fiber-optic cables by the back projection method (e.g., Li et al., 2020; Rabade et al., 2022). To estimate the noise intensity, we establish a 600 by 600 m^2 area where we set up the location

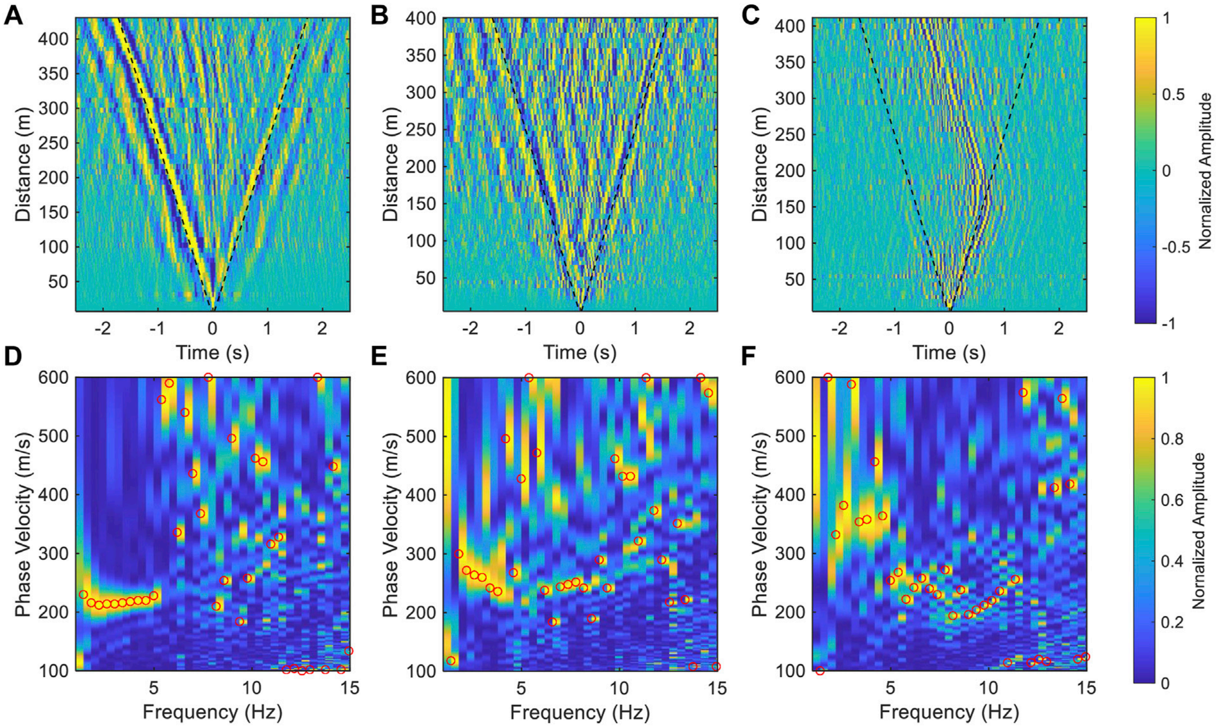

FIGURE 2
The example of common virtual-shot gathers and the dispersion spectra. **(A–C)** are the NCF waveform for segments 1, 2, and 3 in Figure 1, respectively. The black dashed lines in **(A–C)** represent a velocity of 250 m/s. **(D–F)** are the dispersion spectra of the three segments, respectively. The red circles indicate the maximum energy at each frequency.

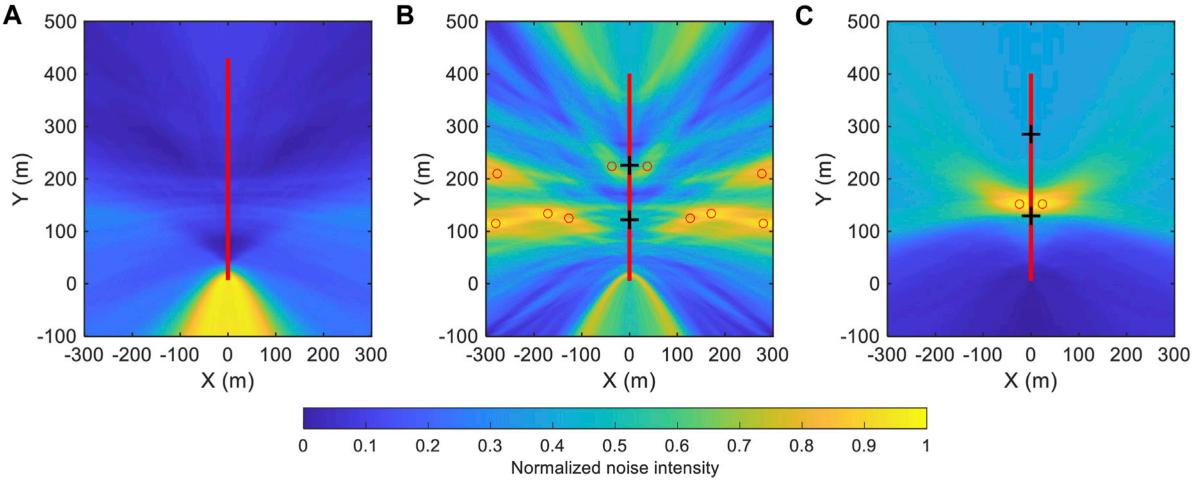

FIGURE 3
The ambient noise intensity around the fiber-optic cable. **(A–C)** are the noise intensity of segment 1, 2, and 3, respectively in Figure 1. The red lines indicate the fiber-optic cable. The black crosses in **(B,C)** are the road intersections, while the red circles are the local maxima of noise intensity.

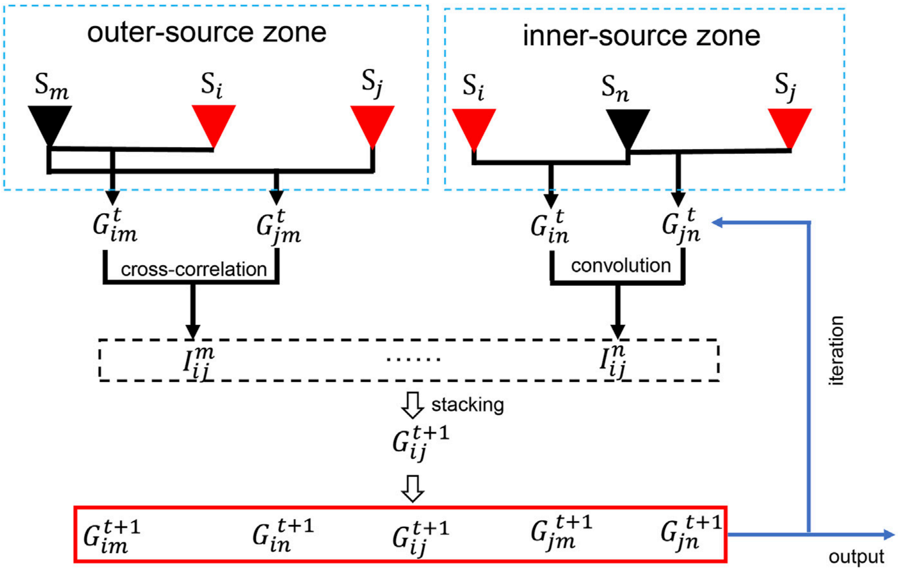

FIGURE 4
Sketch of the TSI method. The red triangles (S_i and S_j) indicate the channel pair whose NCF is to be enhanced, and the black triangles are the third channel.

of the virtual source as the origin and the direction of the cable as the y-axis. For any particular location within this area, the difference between the distance from such location to the virtual source and the virtual receiver was calculated. The difference in arrival time was obtained according to the velocity of the surface wave (about 250 m/s, Figure 2). We used a 0.2 s time window centered around the time shift in the NCF (time shift equals the value of arrival time difference), and subsequently calculated the root mean square of the waveform within the time window. The noise intensity of this particular location was obtained by the summation of all the root mean squares of the common virtual-shot gather. The ambient noise intensity distribution was derived by calculating all the locations in this area, and the results are shown in Figure 3. As mentioned earlier, the noises of segment 1 are concentrated in the direction of Taihe road. The noise intensity on the left and right sides of the fiber-optic cables cannot be distinguished because of the linear array. The noise around segment 2 comes from different directions controlled by multiple location noise sources, especially, near the two crossings (Figure 3). In contrast, the noise of segment 3 is dominated by the persistent localized noise source in the array.

To suppress the precursor seismic phases and enhance the surface waves, the TSI method was employed in this study. Figure 4 is a simplified schematic showing the processing flow as follows: First, for the two channels (S_i and S_j) whose NCF is to be enhanced, a third channel (S_k) was selected to calculate the NCFs with these two channels, respectively. Then, we stacked the positive and negative lags and computed the convolution of the two NCFs to obtain the interferometry waveform if S_k lies between S_i and S_j (inner-source zone), otherwise, we computed the cross-correlation (outer-source zone) (Eq. 1). The denoised NCF of the two stations (S_i and S_j) is obtained by looping all third channels and stacking the interferometry waveforms (Eq. 2). We arrived at the enhanced NCF between all stations by changing the channels of S_i and S_j, and by this, an iteration is completed. The same cycle is repeated until a stable result is achieved. It is worth noting that there is a pi/4 phase shift between the calculated NCF and true NCF when the source and receiver are linearly distributed (Halliday and Curtis, 2008; Lin et al., 2008; Qiu et al., 2021). The MASW method, however, measures the phase difference of the multi-channel surface wave signals to determine the phase velocity dispersion curve, so the effect of the pi/4 phase difference could be eliminated.

$$I_{ij}^{k,t}(\omega) = \begin{cases} \overline{G_{ik}^t(\omega)} \cdot G_{jk}^t(\omega), & k < i \\ G_{ik}^t(\omega) \cdot G_{jk}^t(\omega), & i < k < j \\ G_{ik}^t(\omega) \cdot \overline{G_{jk}^t(\omega)}, & j < k \end{cases} \tag{1}$$

where the $G_{ik}^t(\omega)$ and $G_{jk}^t(\omega)$ are the frequency domain NCF at *tth* iteration between S_i and S_k and S_j and S_k, respectively. $\overline{G_{ik}^t(\omega)}$ and $\overline{G_{jk}^t(\omega)}$ represent the conjugate of $G_{ik}^t(\omega)$ and $G_{jk}^t(\omega)$, respectively. t=0 represents the raw NCFs, while t=1 is the NCFs *via* one TSI. $I_{ij}^{k,t}(\omega)$ is the interferometry waveform with *tth* iteration.

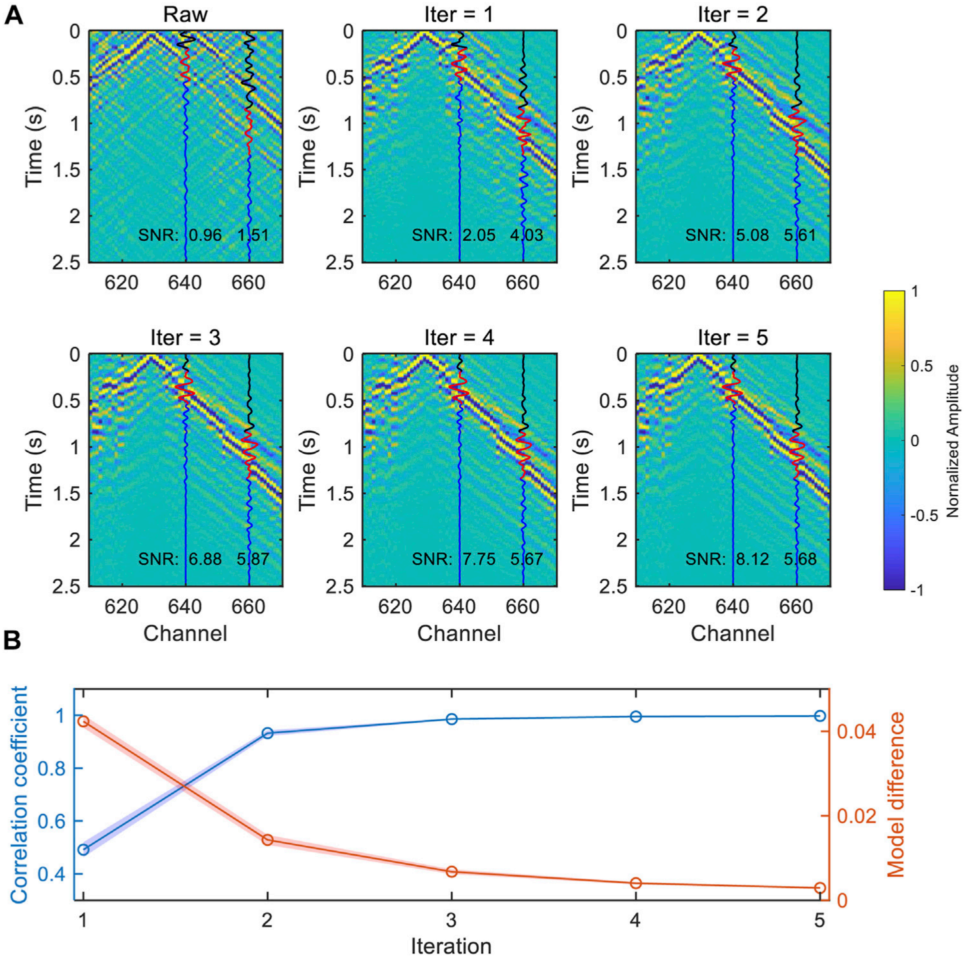

FIGURE 5
(A) The variation of the waveform of segment 3 with the iteration using the TSI method. The virtual source is located at CH630. The blue lines are the waveforms of CH640 and CH660, the black and red lines represent noise and signal windows, respectively. **(B)** The variation of model correlation coefficient and model difference with iteration. The blue and red shading represent 95% confidence intervals for the correlation coefficient and model difference, respectively.

$$G_{ij}^{t+1}(\omega) = \sum_{k=1}^{N} I_{ij}^{k,t}(\omega) \quad (2)$$

where the G_{ij}^{t+1} is the frequency domain NCF between S_i and S_j after the TSI. N represents the number of channels.

Results

Figure 5A shows the variation of the iterated waveforms of a common virtual-shot gather, when the virtual source is located at CH630. The raw NCF waveforms were tapered within a range of 100–800 m/s to decrease the unwanted body waves or noise signals. The signals at far offset were enhanced significantly and the surface waves dominated in the NCFs after 2 iterations. The improvement becomes little after several iterations and the signals converge to a stable result. The SNR, which is defined as the ratio of the maximum amplitude of the signal windows and the root mean square of the noise windows, increases up to 6 as the iteration increases (Figure 5A). The L1-norm of the difference in the model update is as low as 0.3% while the average of the correlation coefficient before and after model update of all virtual-shot gathers is up to 99.7% after 5 iterations (Figure 5B). The denoised waveforms of the three segments are shown in Figure 6. For segment 1, even if it is not affected by the noise source distribution, the random noise in the NCF was suppressed significantly. The surface wave in high frequency was improved and the frequency band of the dispersion curve was also extended to provide a higher resolution of shallow structure. For the other segments, the precursor seismic phases were removed and the surface waves were enhanced. The 1–10 Hz clear Rayleigh wave phase velocity dispersion curve was extracted to construct the S-wave velocity structure.

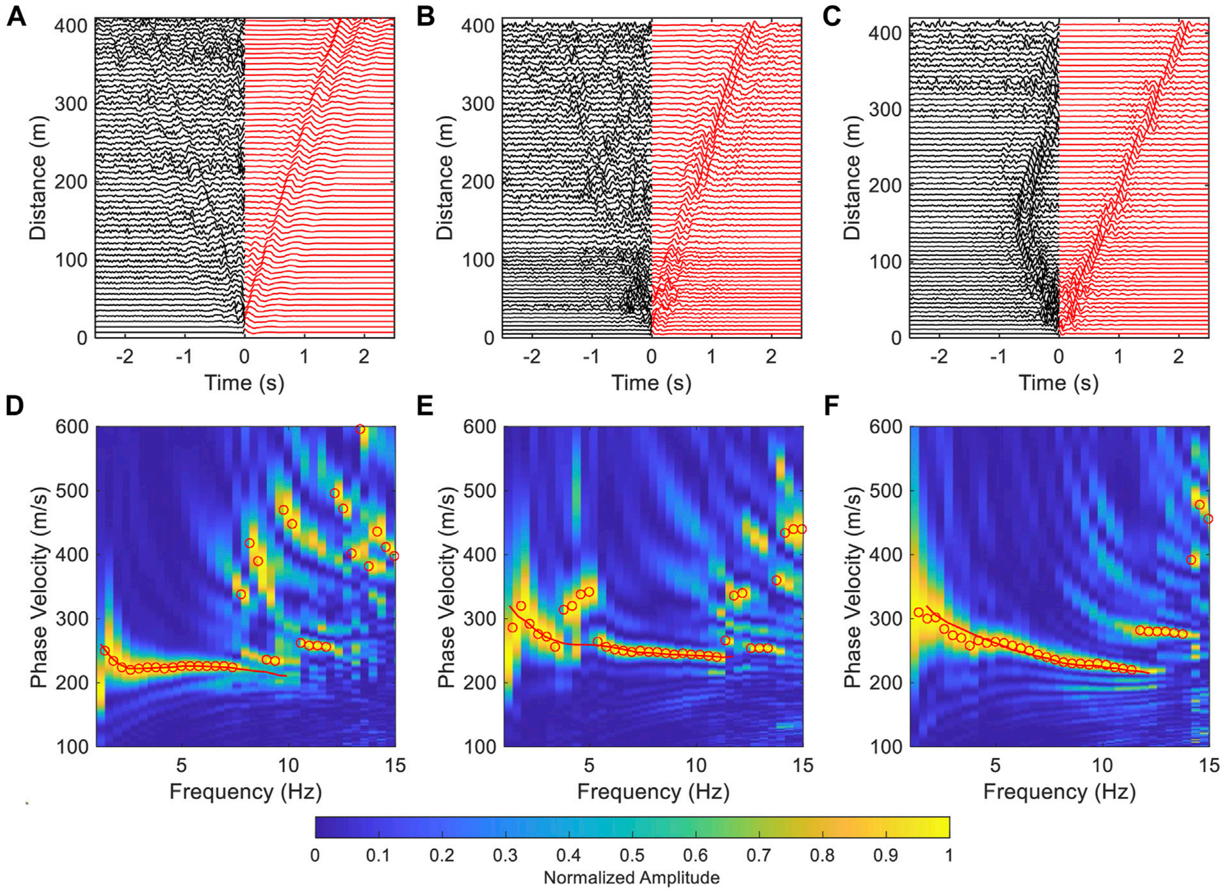

FIGURE 6
The waveform and dispersion spectra after the TSI method. **(A–C)** are the waveforms of segment 1, 2, and 3, respectively. The black lines are the symmetric to the positive lag of the raw NCFs while the red lines are the denoised NCFs. **(D–F)** are the dispersion spectra of the denoised waveforms of **(A–C)**, respectively. In **(D–F)**, the red circles represent the maximum energy at each frequency and the red lines are the picked dispersion curves.

The TSI method was utilized to enhance the surface wave along the Jinniu Road for ambient noise tomography. The array was divided into 70 segments and each segment consists of 40 channels (about 300 m) while the overlap between two consecutive segments is 35-channel long (about 262.5 m). 70 dispersion curves were extracted for 1D substructure inversion after the calculation and reconstruction of the surface wave. Typically, the maximum inversion depth is less than half of the maximum wavelength (Song et al., 2021), and in this study, the maximum wavelength is about 300 m according to the dispersion curve (Figure 6), which reveals the top 100 m subsurface structure. For the inversion, the model consists of five layers, including two 20-m layers, two 30-m layers, and a half space. Due to the lack of accurate P-wave velocity structure for this region and that the surface wave dispersion curve is not very sensitive to the P-wave velocity structure and density (Song et al., 2018), the P-wave velocity and density were determined by an empirical relationship (Brocher, 2005, Equation (3) and (4), and only the S-wave velocity was inverted.

$$V_p(km/s) = 0.9409 + 2.0947V_s - 0.8206V_s^2 + 0.2683V_s^3 - 0.0251V_s^4 \quad (3)$$

$$\rho\,(g/cm^3) = 1.74V_p^{0.25} \quad (4)$$

where the Vp and Vs are the P-wave and S-wave velocity, respectively. ρ represents the density.

The neighborhood algorithm (Sambridge 1999), a global search method was utilized for the inversion, and the forward modeling of the dispersion curve was conducted with the Computer Programs for Seismology (Herrmann 2013). The 2D profile beneath the Jinniu Road was obtained by assembling all 1D models (Figure 7A). The shallow structure (<20 m) along the Jinniu Road is homogeneous, indicating the sediment coverage is evenly distributed in the shallow layer. But,

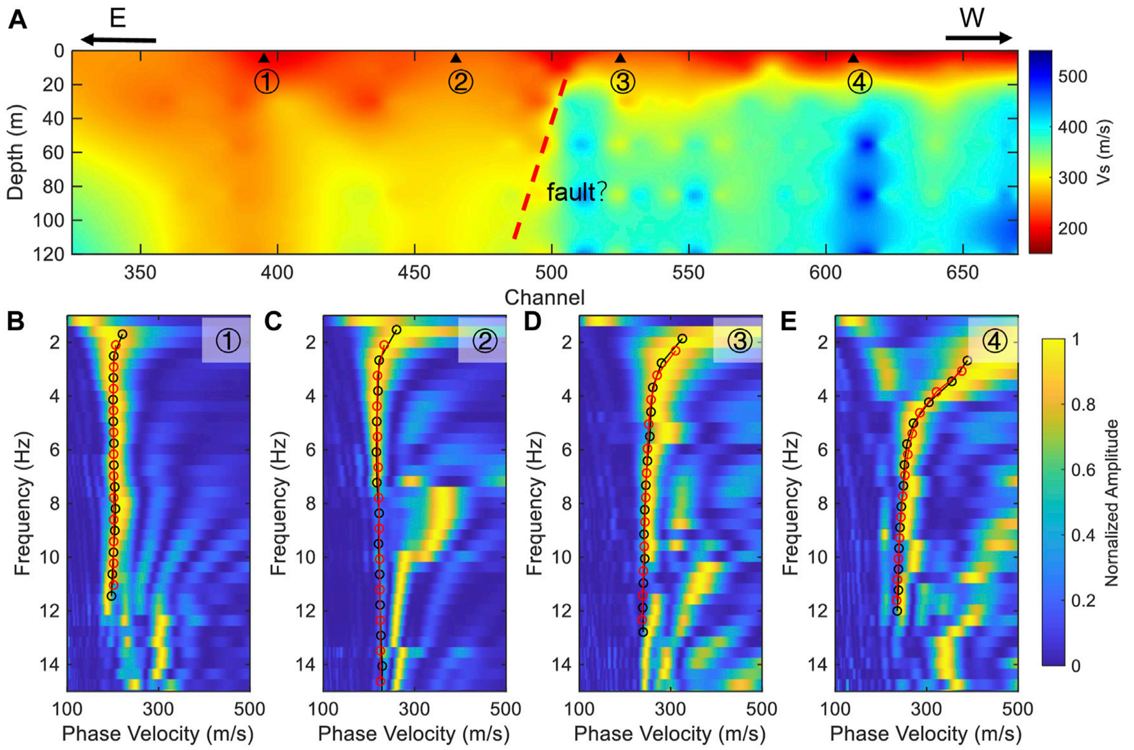

FIGURE 7
(A) The S-wave structure beneath the Jinniu Road. **(B–E)** are the dispersion curves fitting, corresponding to the positions of the four triangles in **(A)**. The black lines and red lines indicate the observed dispersion curves and the theoretical dispersion curves predicted by the inverted models, respectively.

the deep structure (>20 m) changes greatly in the lateral direction, and the velocity on the east side is lower, which is consistent with the result of Taihe Road (Song et al., 2021). The dispersion curves fitted well (Figures 7B–E) and suggested that the phase velocity at low frequency on the east side is lower than that on the west side. The north-south trending mountains on both sides of the Binchuan county cause significant velocity differences in the east-west direction. Zhang et al., 2020b suggested that there may be a hidden fault in the west of the county, which is consistent with our results. This result indicated that the combination of urban internet fiber-optic cables with DAS technology, using the TSI method for ambient noise tomography, is highly plausible for achieving ultra-high-density observations, which can be used to produce high-precision images of urban subsurface structures.

Discussion

In addition to the distribution of ambient noise, the coupling of the fiber-optic cables is also an important factor that influence ambient noise tomography in urban areas. Most of the urban fiber-optic cables are laid in the PVC pipe, and some parts are directly buried in the soil or hung in the air. It often takes stacking of data acquired over a long time span to obtain a clear surface wave signal on the NCF because of the weak coupling between the cable in the casing pipe and the solid earth (Lin et al., 2021), which decreases the temporal resolution of ambient noise tomography. Furthermore, we discussed the effect of the TSI method on the enhancement of the coherence surface wave signals in the case of weak coupling. The ambient noise in the vicinity of Taihe Road is distributed along the fiber-optic cable, and the clear surface wave signals emerged on the NCF for a 4-h data (Song et al., 2021). Assuming that the responses of all channels are the same, weak coupling reduces the SNR of the NCF for the same time span stacking. We selected a section of the fiber-optic cable (CH160-210, segment 4 in Figure 1), and used the NCF calculated with 4-h and 30-s data to simulate the results of good and weak coupling for the same time span stacking, respectively. The coherent surface wave signals cannot be seen for the weak coupling, and a continuous and accurate dispersion curve cannot be obtained (Figures 8A,D). We used the TSI method to further process the 30-s NCF result, and the surface wave signal was enhanced significantly (Figure 8C). The dispersion

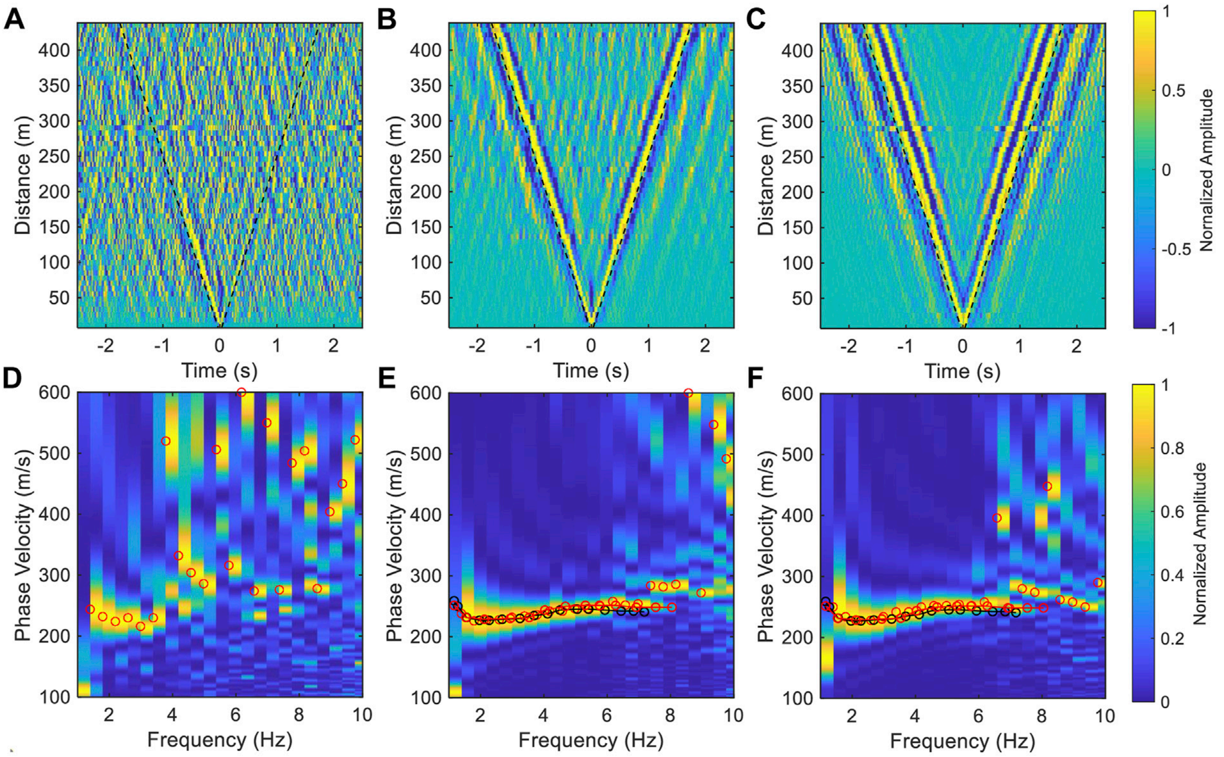

FIGURE 8
Speed-up convergence of NCF *via* the TSI. **(A,B)** are the common virtual-shot gather of segment 4 calculated with 30-s and 4-h data, respectively. **(C)** is the denoised result of **(A)**, and the negative lag of **(C)** is symmetric to its positive lag. The black dashed lines represent a velocity of 250 m/s. **(D–F)** are the dispersion spectra of **(A–C)**, respectively. The red and black lines are the picked dispersion curves of **(E,F)**, respectively.

curve of the 30-s NCF was observed to be consistent with the results obtained from the 4-h data (Figures 8E,F). This result indicated that the TSI method is suitable for an imperfectly coupled cable setup and can improve the temporal resolution of ambient noise tomography by accelerating the convergence of the NCF.

Forbriger et al. (2003) demonstrated that the resolution of the dispersion spectrum is related to the frequency and the length of the segment used for MASW (Eq. 5). That is, with a fixed length segment, the resolution of high frequency is significantly higher than that of low frequency, which has been demonstrated in the previous results (Figure 6). Therefore, increasing the length of the segment is beneficial to improving the accuracy of the dispersion curve in the low frequency range. However, due to the effect of coupling and ambient noise attenuation, the SNR at far offset is low in the real data (CH100-200, ~750 m, black dashed box in Figure 1), which limits the extraction of the dispersion curve (Figure 9). We processed this dataset with the TSI method and successfully enhanced the surface wave signal at far offset (Figure 9D). The uncertainty of the dispersion curve decreases significantly as the length of the segment increases (Figures 9E,F). Due to MASW measures the average dispersion curve of the segment, there is a tradeoff between the lateral resolution of subsurface structure and the resolution of dispersion spectrum. We can use the long segment combined with the TSI method to obtain a dispersion curve that provides a reference for the short segments. Thereby, this improves the accuracy of dispersion curve extraction without reducing the spatial resolution.

$$d = 1/fL \tag{5}$$

where d represents the relative value of resolution in the dispersion curve, which is expressed as the width of 90% maximum energy of the dispersion spectrum in this paper; f is the frequency and L is the length of the segment.

The dispersion curve extracted by the MASW method represents the average velocity beneath the investigated segment, hence, the dispersion curve cannot be obtained when there are significant variations in the subsurface structure. However, surface wave signals with high signal-to-noise ratio are useful for other seismological imaging methods such as full waveform inversion (e.g., Liu et al., 2017). The imaging result of the short segments shows that

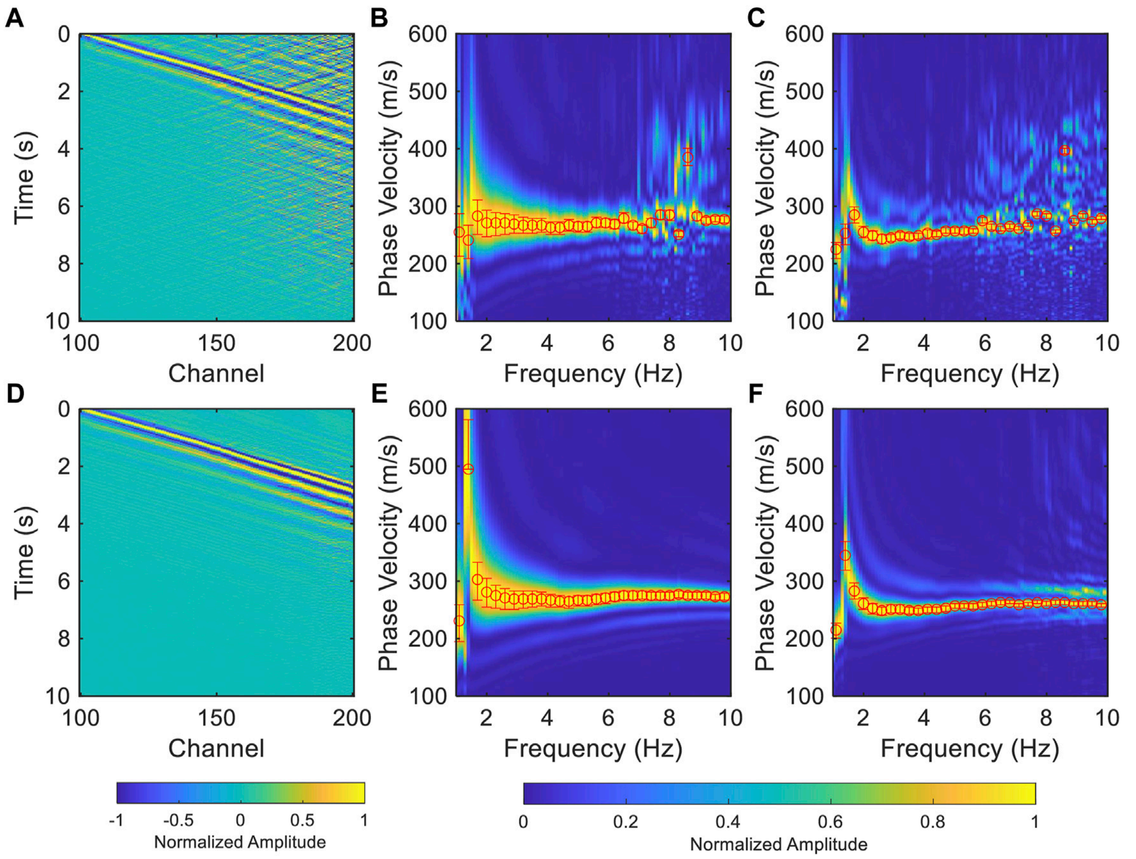

FIGURE 9
The improvement of the resolution of dispersion spectra of the long segment with the TSI method. **(A)** The NCFs of a long segment (black dashed box in Figure 1). **(B)** The dispersion spectrum is calculated using the waveforms of CH100-150, the red bars are the picked uncertainties which is defined as the zone with 90% of the maximum energy of each frequency. **(C)** is same as **(B)** but for CH100-200. **(D–F)** same as **(A–C)** but for the denoised waveforms using the TSI method.

there are obvious differences in the subsurface structure beneath the Jinniu Road (Figure 7A), at the same time, the SNR of the surface wave is also lower than that in the Taihe Road (Figure 10A). Furthermore, we selected a long segment in the Jinniu Road (CH400-650, ~1875 m, gray dashed box in Figure 1) to establish whether the TSI method is effective in the case of uneven subsurface structure. We observed a significant improvement on the raw data, revealing that the surface wave signals at the far offset are well reconstructed *via* the TSI method (Figure 10B). Because the velocity on the east side of the profile (channel index < CH500) is lower than that on the west side (channel index > CH500), we calculated the dispersion curve for the waveform of the sub-segments. Between CH400-500 (sub-segment i in Figure 10B) and CH500-600 (sub-segment ii in Figure 10B), we arrived at the respective corresponding dispersion curves shown in Figures 10C,D. The relative magnitude of the phase velocity is consistent with the previous result (Figure 7A). To verify the reliability of the results, we first separated CH400-500 and CH500-600 into different segments and thereafter utilized the TSI method to process each of the segments, individually, and extracted their dispersion curves (Figures 10E–H). The dispersion curves are very close to the previous results in Figures 10C,D, thus indicating that the TSI method is effective in resolving the uneven subsurface structure below the array.

We successfully suppressed the influence of the noise source distribution on ambient noise tomography using the TSI method. However, the characteristics of noise sources are also a common concern in seismological research (e.g., McNamara and Buland, 2004; Retailleau and Beroza, 2021; Song et al., 2021). Determining the properties and distribution of noise sources enables non-intrusive monitoring of human activities and helps to understand the signals that emerge on the NCF. In the past, researchers have analyzed traffic signals recorded by the

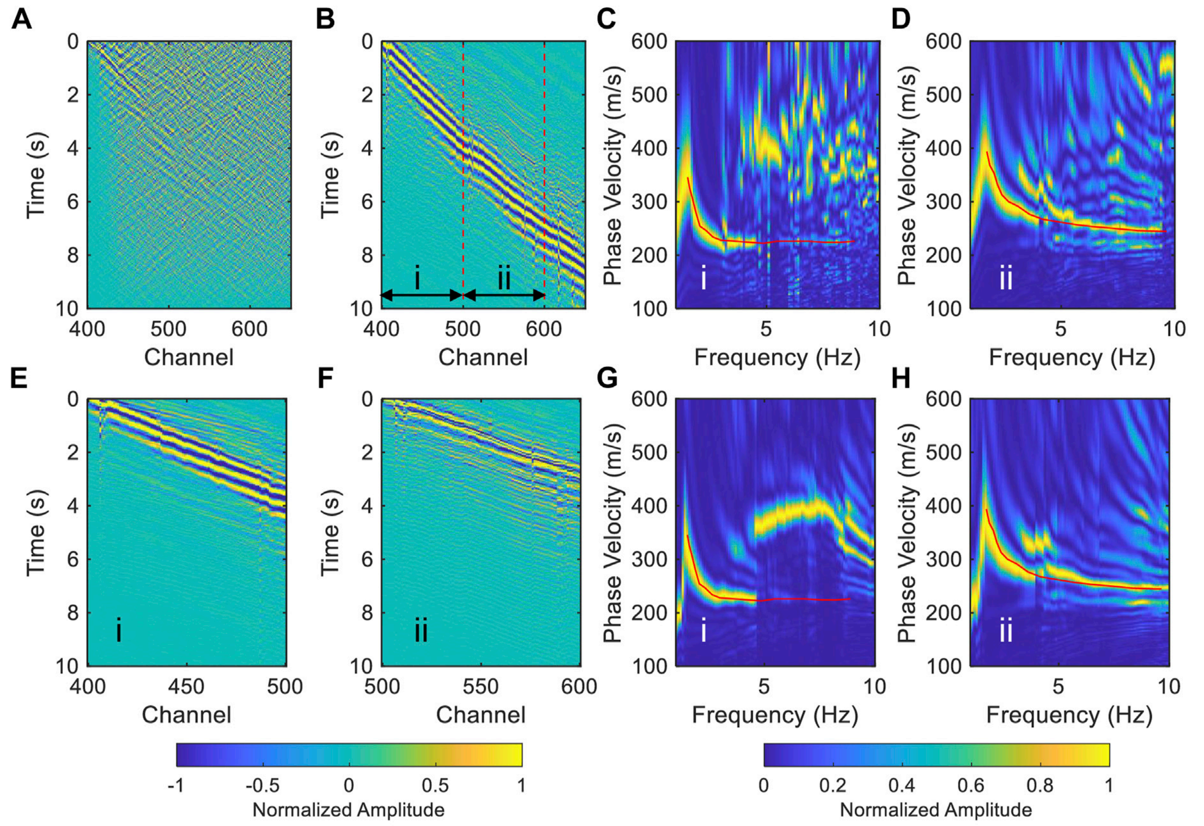

FIGURE 10
The feasibility test of the TSI method in the heterogeneous subsurface structure. **(A)** The raw common virtual-shot gather of the long segment (gray dashed box in Figure 1). **(B)** The NCFs after the TSI method. The red dashed lines divided the long segment into sub-segments i (CH400-500) and ii (CH500-600) for dispersion curve calculation. **(C,D)** are the dispersion spectra of the sub-segment (i) and (ii) cut from **(B)**. **(E,F)** are the denoised waveforms of the segments of (i) and (ii), respectively. **(G)** and **(H)** are the dispersion spectra of **(E,F)**, respectively. The red lines in **(C,G)** are the dispersion curves extracted from **(C)**, while the red lines in **(D,H)** are the dispersion curves extracted from **(D)**.

urban internet cables in application to traffic flow monitoring (e.g., Martin et al., 2018; Lindsey et al., 2020a; Wang et al., 2021b) and vehicle classification (e.g., Liu et al., 2019). High resolution subsurface structures can now better serve in the study of noise sources. Also, an inversion of the distribution of noise sources and the shallow structure can be conducted at the same time (Lehujeur et al., 2016).

Conclusion

In this study, we analyzed the ambient noise data recorded by an urban internet fiber-optic cable. The estimation of the noise intensity near the fiber-optic cable indicates significant influence from crossing traffic. Affected by the uneven noise source distribution and imperfect coupling, it is difficult to extract clear surface wave dispersion for conventional ambient noise tomography with inter-station correlation. We adopted the TSI method to this dataset and successfully suppressed the precursor seismic phases, enhanced the surface wave signals leading to better measurement of dispersion, constructed the shallow shear velocity structure, and revealed a hidden fault. Furthermore, we demonstrated that the TSI method is effective for imperfect coupling, and substantially improved the convergence of the NCF, which enhanced the temporal resolution of ambient noise tomography. For a long segment, the SNR of surface wave signals at far offset is weak due to the effect of coupling and ambient noise attenuation, which limits the accuracy of the dispersion curve extraction. The TSI method can enhance the surface wave signal at the far offset, even though there are significant differences in the subsurface structure. The TSI can improve the ambient noise tomography to construct high resolution structure, which in turn can be used for the study of noise source intensity and distribution, as well as a better understanding of the effect of the noise source distribution on the NCF. In conclusion, the TSI method is an effective method to suppress the effects of uneven noise distribution and enhance the surface wave. Using existing fiber-optic cable in combination with the TSI method for urban ambient noise tomography can produce high-resolution imaging, thus providing helpful information on subsurface structures for civil engineering construction and disaster prevention.

Data availability statement

The raw data supporting the conclusion of this article will be made available by the authors, without undue reservation.

Author contributions

ZS carried out the data processing and wrote the manuscript. XZ led the project design and supervised the data analysis. BC advised on method and commented on the manuscript. FB acquired the data. AO edited the manuscript.

Funding

National Key R&D Program of China (2021YFA0716802), National Natural Science Foundation of China (41974067).

Conflict of interest

The authors declare that the research was conducted in the absence of any commercial or financial relationships that could be construed as a potential conflict of interest.

Publisher’s note

References

Ajo-Franklin, J. B., Dou, S., Lindsey, N. J., Monga, I., Tracy, C., Robertson, M., et al. (2019). Distributed acoustic sensing using dark fiber for near-surface characterization and broadband seismic event detection. *Sci. Rep.* 9 (1), 1328. doi:10.1038/s41598-018-36675-8

Bensen, G. D., Ritzwoller, M. H., Barmin, M. P., Levshin, A. L., Lin, F., Moschetti, M. P., et al. (2007). Processing seismic ambient noise data to obtain reliable broad-band surface wave dispersion measurements. *Geophys. J. Int.* 169 (3), 1239–1260. doi:10.1111/j.1365-246x.2007.03374.x

Bobylev, N. (2010). Underground space in the Alexanderplatz area, Berlin: Research into the quantification of urban underground space use. *Tunn. Undergr. Space Technol.* 25 (5), 495–507. doi:10.1016/j.tust.2010.02.013

Brocher, T. M. (2005). Empirical relations between elastic wavespeeds and density in the Earth’s crust. *Bull. Seismol. Soc. Am.* 95 (6), 2081–2092. doi:10.1785/0120050077

Chen, Q., Liu, L., Wang, W., and Rohrbach, E. (2009). Site effects on earthquake ground motion based on microtremor measurements for metropolitan Beijing. *Sci. Bull. (Beijing).* 54 (2), 280–287. doi:10.1007/s11434-008-0422-2

Cueto, M., Olona, J., Fernández-Viejo, G., Pando, L., and López-Fernández, C. (2018). Karst-induced sinkhole detection using an integrated geophysical survey: A case study along the riyadh metro line 3 (Saudi arabia). *Near Surf. Geophys.* 16 (3), 270–281. doi:10.3997/1873-0604.2018003

Curtis, A., and Halliday, D. (2010). Source-receiver wave field interferometry. *Phys. Rev. E* 81 (4), 046601. doi:10.1103/physreve.81.046601

Froment, B., Campillo, M., and Roux, P. (2011). Reconstructing the Green’s function through iteration of correlations. *Comptes Rendus Geosci.* 343 (8-9), 623–632. doi:10.1016/j.crte.2011.03.001

Forbriger, T. (2003). Inversion of shallow-seismic wavefields: I. Wavefield transformation. *Geophysical Journal International* 153 (3), 719–734. doi:10.1046/j.1365-246X.2003.01929.x

Galetti, E., and Curtis, A. (2012). Generalised receiver functions and seismic interferometry. *Tectonophysics* 532, 1–26. doi:10.1016/j.tecto.2011.12.004

Halliday, D., and Curtis, A. (2008). Seismic interferometry, surface waves and source distribution. *Geophys. J. Int.* 175 (3), 1067–1087. doi:10.1111/j.1365-246x.2008.03918.x

Herrmann, R. B. (2013). Computer programs in seismology: An evolving tool for instruction and research. *Seismol. Res. Lett.* 84 (6), 1081–1088. doi:10.1785/0220110096

Lehujeur, M., Vergne, J., Maggi, A., and Schmittbuhl, J. (2016). Ambient noise tomography with non-uniform noise sources and low aperture networks: Case study of deep geothermal reservoirs in northern alsace, France. *Geophys. J. Int.* 208 (1), 193–210. doi:10.1093/gji/ggw373

Li, Z., Ni, S., and Somerville, P. (2014). Resolving shallow shear-wave velocity structure beneath station CBN by waveform modeling of the M w 5.8 Mineral, Virginia, earthquake sequence. *Bull. Seismol. Soc. Am.* 104 (2), 944–952. doi:10.1785/0120130190

Li, L., Tan, J., Schwarz, B., Staněk, F., Poiata, N., Shi, P., et al. (2020). Recent advances and challenges of waveform-based seismic location methods at multiple scales. *Rev. Geophys.* 58 (1), e2019RG000667. doi:10.1029/2019rg000667

Lin, F. C., Moschetti, M. P., and Ritzwoller, M. H. (2008). Surface wave tomography of the Western United States from ambient seismic noise: Rayleigh and love wave phase velocity maps. *Geophys. J. Int.* 173 (1), 281–298. doi:10.1111/j.1365-246x.2008.03720.x

Lin, F. C., Li, D., Clayton, R. W., and Hollis, D. (2013). High-resolution 3D shallow crustal structure in Long Beach, California: Application of ambient noise tomography on a dense seismic array. *Geophysics* 78 (4), Q45–Q56. doi:10.1190/geo2012-0453.1

Lin, R., Bao, F., Xie, J., Zhang, G., Song, Z., and Zeng, X. (2021). The influence of cable installment on DAS active and passive source records. *Chinese Journal of Geophysics* in press. doi:10.6038/cjg2022P0444

Lindsey, N. J., Martin, E. R., Dreger, D. S., Freifeld, B., Cole, S., James, S. R., et al. (2017). Fiber-optic network observations of earthquake wavefields. *Geophys. Res. Lett.* 44 (23), 11–792. doi:10.1002/2017gl075722

Lindsey, N. J., Yuan, S., Lellouch, A., Gualtieri, L., Lecocq, T., and Biondi, B. (2020a). City-scale dark fiber DAS measurements of infrastructure use during the COVID-19 pandemic. *Geophys. Res. Lett.* 47 (16), e2020GL089931. doi:10.1029/2020gl089931

Lindsey, N. J., Rademacher, H., and Ajo-Franklin, J. B. (2020b). On the broadband instrument response of fiber-optic DAS arrays. *J. Geophys. Res. Solid Earth* 125 (2), e2019JB018145. doi:10.1029/2019jb018145

Liu, H., Ma, J., Xu, T., Yan, W., Ma, L., and Zhang, X. (2019). Vehicle detection and classification using distributed fiber optic acoustic sensing. *IEEE Trans. Veh. Technol.* 69 (2), 1363–1374. doi:10.1109/tvt.2019.2962334

Liu, Y., Teng, J., Xu, T., Wang, Y., Liu, Q., and Badal, J. (2017). Robust time-domain full waveform inversion with normalized zero-lag cross-correlation objective function. *Geophys. J. Int.* 209 (1), 106–122. doi:10.1093/gji/ggw485

Martin, E. R., Huot, F., Ma, Y., Cieplicki, R., Cole, S., Karrenbach, M., et al. (2018). A seismic shift in scalable acquisition demands new processing: Fiber-optic seismic signal retrieval in urban areas with unsupervised learning for coherent noise removal. *IEEE Signal Processing Magazine* 35 (2), 31–40. doi:10.1109/MSP.2017.2783381

McNamara, D. E., and Buland, R. P. (2004). Ambient noise levels in the continental United States. *Bull. Seismol. Soc. Am.* 94 (4), 1517–1527. doi:10.1785/012003001

Mi, B., Xia, J., Tian, G., Shi, Z., Xing, H., Chang, X., et al. (2022). Near-surface imaging from traffic-induced surface waves with dense linear arrays: An application in the urban area of Hangzhou, China. *Geophysics* 87 (2), B145–B158. doi:10.1190/geo2021-0184.1

Ni, S., Li, Z., and Somerville, P. (2014). Estimating subsurface shear velocity with radial to vertical ratio of local P waves. *Seismol. Res. Lett.* 85 (1), 82–90. doi:10.1785/0220130128

Park, C. B., Miller, R. D., and Xia, J. (1999). Multichannel analysis of surface waves. *Geophysics* 64 (3), 800–808. doi:10.1190/1.1444590

Parker, T., Shatalin, S., and Farhadiroushan, M. (2014). Distributed Acoustic Sensing–a new tool for seismic applications. *first break* 32 (2), 34. doi:10.3997/1365-2397.2013034

Qiu, H., Niu, F., and Qin, L. (2021). Denoising surface waves extracted from ambient noise recorded by 1-D linear array using three-station interferometry of direct waves. *JGR. Solid Earth* 126 (8), e2021JB021712. doi:10.1029/2021jb021712

Rabade, S., Wu, S. M., Lin, F. C., and Chambers, D. J. (2022). Isolating and tracking noise sources across an active longwall mine using seismic interferometry. *Bull. Seismol. Soc. Am.* in press. doi:10.1785/0120220031

Retailleau, L., and Beroza, G. C. (2021). Towards structural imaging using seismic ambient field correlation artefacts. *Geophys. J. Int.* 225 (2), 1453–1465. doi:10.1093/gji/ggab038

Sambridge, M. (1999). Geophysical inversion with a neighbourhood algorithm-I. Searching a parameter space. *Geophys. J. Int.* 138 (2), 479–494. doi:10.1046/j.1365-246x.1999.00876.x

Song, Z., Zeng, X., Thurber, C. H., Wang, H. F., and Fratta, D. (2018). Imaging shallow structure with active-source surface wave signal recorded by distributed acoustic sensing arrays. *Earthq. Sci.* 31, 208–214. doi:10.29382/eqs-2018-0208-4

Song, Z., Zeng, X., Xie, J., Bao, F., and Zhang, G. (2021). Sensing shallow structure and traffic noise with fiber-optic internet cables in an urban area. *Surv. Geophys.* 42 (6), 1401–1423. doi:10.1007/s10712-021-09678-w

Spica, Z. J., Perton, M., Martin, E. R., Beroza, G. C., and Biondi, B. (2020). Urban seismic site characterization by fiber-optic seismology. *J. Geophys. Res. Solid Earth* 125 (3), e2019JB018656. doi:10.1029/2019jb018656

Stehly, L., Campillo, M., Froment, B., and Weaver, R. L. (2008). Reconstructing Green's function by correlation of the coda of the correlation (C3) of ambient seismic noise. *J. Geophys. Res.* 113 (B11), B11306. doi:10.1029/2008jb005693

Wang, B., Zeng, X., Song, Z., Li, X., and Yang, J. (2021a). Seismic observation and subsurface imaging using an urban telecommunication optic-fiber cable. *Chin. Sci. Bull.* 66, 2590–2595. doi:10.1360/tb-2020-1427

Wang, X., Williams, E. F., Karrenbach, M., Herráez, M. G., Martins, H. F., and Zhan, Z. (2020). Rose Parade seismology: Signatures of floats and bands on optical fiber. *Seismol. Res. Lett.* 91 (4), 2395–2398. doi:10.1785/0220200091

Wang, X., Zhan, Z., Williams, E. F., Herráez, M. G., Martins, H. F., and Karrenbach, M. (2021b). Ground vibrations recorded by fiber-optic cables reveal traffic response to COVID-19 lockdown measures in Pasadena, California. *Commun. Earth Environ.* 2 (1), 160–169. doi:10.1038/s43247-021-00234-3

Zhang, Y., Wang, B., Lin, G., Wang, W., Ywang, W., and Wu, Z. (2020b). Upper crustal velocity structure of Binchuan, Yunnan revealed by dense array local seismic tomography. *Chin. J. Geophys.* 63 (9), 3292–3306. doi:10.6038/cjg2020N0455

Zandomeneghi, D., Aster, R., Kyle, P., Barclay, A., Chaput, J., and Knox, H. (2013). Internal structure of Erebus volcano, Antarctica imaged by high-resolution active-source seismic tomography and coda interferometry. *J. Geophys. Res. Solid Earth* 118 (3), 1067–1078. doi:10.1002/jgrb.50073

Zeng, X., Thurber, C. H., Wang, H. F., Fratta, D., and Feigl, K. L. (2021). "High-resolution shallow structure at brady hot springs using ambient noise tomography (ANT) on a trenched distributed acoustic sensing (DAS) array," in *Distributed acoustic sensing in Geophysics: Methods and applications*, 101–110. doi:10.1002/9781119521808.ch8

Zhan, Z. (2020). Distributed acoustic sensing turns fiber-optic cables into sensitive seismic antennas. *Seismol. Res. Lett.* 91 (1), 1–15. doi:10.1785/0220190112

Zhang, S., Feng, L., and Ritzwoller, M. H. (2020a). Three-station interferometry and tomography: Coda versus direct waves. *Geophys. J. Int.* 221 (1), 521–541. doi:10.1093/gji/ggaa046

Zhu, T., and Stensrud, D. J. (2019). Characterizing thunder-induced ground motions using fiber-optic distributed acoustic sensing array. *JGR. Atmos.* 124 (23), 12810–12823. doi:10.1029/2019jd031453

frontiers | Frontiers in Earth Science

TYPE Original Research
PUBLISHED 12 September 2022
DOI 10.3389/feart.2022.990837

OPEN ACCESS

EDITED BY
Yang Zhao,
China University of Petroleum, Beijing, China

REVIEWED BY
Haoran Meng,
Southern University of Science and Technology, China
Subhayan Mukherjee,
John Deere (United States), United States

*CORRESPONDENCE
Benxin Chi,
benxin.chi@apm.ac.cn

SPECIALTY SECTION
This article was submitted to Solid Earth Geophysics,
a section of the journal
Frontiers in Earth Science

RECEIVED 10 July 2022
ACCEPTED 22 August 2022
PUBLISHED 12 September 2022

CITATION
Zhang G, Song Z, Osotuyi AG, Lin R and Chi B (2022), Railway traffic monitoring with trackside fiber-optic cable by distributed acoustic sensing Technology.
Front. Earth Sci. 10:990837.
doi: 10.3389/feart.2022.990837

Railway traffic monitoring with trackside fiber-optic cable by distributed acoustic sensing Technology

Gongbo Zhang[1,2], Zhenghong Song[1,3], Abayomi Gaius Osotuyi[3], Rongbing Lin[1,2] and Benxin Chi[1]*

[1]State Key Laboratory of Geodesy and Earth's Dynamics, Innovation Academy for Precision Measurement Science and Technology, Chinese Academy of Sciences, Wuhan, China, [2]College of Earth and Planetary Sciences, University of Chinese Academy of Sciences, Beijing, China, [3]School of Earth and Space Sciences, University of Science and Technology of China, Hefei, China

The importance of railway safety cannot be overemphasized; hence it requires reliable traffic monitoring systems. Widespread trackside telecommunication fiber-optic cables can be suitably deployed in the form of dense vibration sensors using Distributed Acoustic Sensing technology (DAS). Train-induced ground motion signals are recorded as continuous "footprints" in the DAS recordings. As the DAS system records huge datasets, it is thus imperative to develop optimized/stable algorithms which can be used for accurate tracking of train position, speed, and the number of trains traversing the position of the DAS system. In this study, we transform a 6-days continuous DAS data sensed by a 2-km cable into time-velocity domain using beamforming on phase-squeezed signals and automatically extract the position and velocity information from the time-beampower curve. The results are manually checked and the types of the trains are identified by counting the peaks of the signals. By reducing the array aperture and moving subarrays, the train speed-curve/motion track is obtained with acceptable computational performance. Therefore, the efficiency and robustness of our approach, to continuously collect data, can play a supplementary role with conventional periodic and time-discrete monitoring systems, for instance, magnetic beacons, in railway traffic monitoring. In addition, our method can also be used to automatically slice time windows containing train-induced signals for seismic interferometry.

KEYWORDS

distributed acoustic sensing, railway traffic monitoring, trackside monitoring, telecommunication fiber-optic cable, beamforming

Introduction

The growing freight volume conveyed by railway systems and the increase of high-speed trains demand more reliable train dynamics monitoring. Currently, railway traffic monitoring in use require the integration of both onboard and wayside measurement as well as data transfer in between them (Ulianov et al., 2018). Conventionally, in the aspect of large-scale railway position monitoring, onboard satellite-based positioning systems such as Global Positioning Satellite (GPS) play a fundamental role. However, when trains go through tunnels or mountains, GPS positioning could be less accurate, or even unreceivable (Sasani et al., 2015). For more stable and real-time monitoring purposes, on a small-scale aspect, magnetic beacons are deployed on railway sleepers as counters to determine if a train has passed (Bruni et al., 2007). Nonetheless, magnetic beacons may suffer from Electromagnetic Interference and lead to missed or wrong messages (Yüksel et al., 2018). Onboard speedometers or accelerometers can measure precise velocity information and need wireless transmission conditions, which could be disrupted due to wireless interference (Baldini et al., 2010).

Recently, Distributed Acoustic Sensing (DAS) technology has been extensively used in the seismological community (Dou et al., 2017; Zeng et al., 2017; Martin et al., 2018; Ajo-Franklin et al., 2019; Zhan, 2019; Lindsey et al., 2017; Spica et al., 2020). When a DAS interrogator is connected to a fiber-optic cable, laser pulses are sent. Subsequently, Rayleigh back-scattered phase shifts are measured and converted to axle strain or strain rate, thereby, the sensing cable becomes a dense array with meter-scale spatial resolutions (Parker et al., 2014). With the use of the dense array features, DAS records high-fidelity seismic wavefields and can be applied in event monitoring, such as aftershock detection (Li et al., 2021; Lv et al., 2022), icequake detection (Walter et al., 2020; Hudson et al., 2021), and urban traffic monitoring (Lindsey et al., 2020). Another advantage of DAS is in its convenient mode of deployment, whereby, widespread existing telecommunication cables can be utilized as dense array sensors, especially in highly-built cities (Lindsey et al., 2020; Song et al., 2021). It is worth noting that urban-scale DAS applications are not limited to vehicle traffic monitoring (Chambers, 2020; van den Ende et al., 2021) and interferometry studies (Dou et al., 2017; Song et al., 2021), but other moving sources like subways (Ferguson et al., 2020) and railway trains (Cedilnik et al., 2018; Wiesmeyr et al., 2020). The trackside cables connected to an interrogator can provide researchers with the opportunity to record train-induced signals, and monitor the location and speed of trains, towards enhancing the train control system.

In previous seismological studies on train-induced signals, the characteristics of the signal itself have attracted extensive attention (Fuchs and Bokelmann, 2017; Lavoué et al., 2020; Jiang et al., 2022). Another idea is to utilize train-induced signals as strong noise source in ambient noise tomography (Quiros et al., 2016; Brenguier et al., 2019; Liu et al., 2021; Sager et al., 2022). Compared to the aforementioned, railway traffic monitoring (i.e., train detection and speed estimation) using DAS could help select proper noise windows for seismic interferometry applications using noise generated from moving trains as source. Trackside DAS recordings require a lot of man-hour inspection/observation to extract the locations of moving trains; this necessitates the need to develop automatic methods for monitoring railway traffic using the high-volume original waveform data. Given that the train-induced signals are spatially continuous, and leave data “footprints” as linear features in the DAS recordings, the Kalman filter has been suggested to be an effective approach to extracting the tracks of individual trains (Wiesmeyr et al., 2020), yet the method may not achieve stable track predictions when it comes to significant speed variant cases. In addition, the method may not accurately extract/predict the locations from cross superimposed signals (Iswanto and Li, 2017), which could be the case when two trains from opposite directions move and pass each other. Train-induced signals in the “waterfall diagram” can be cut out and the signal front over time can be aligned, thereby the speed change could be extracted using spectral shifts (Cedilnik et al., 2018), yet the method requires accurate alignment of the train-induced signal fronts and the calculation of speeds are not in an automatic manner. Similar issues also apply to vehicle monitoring studies where array beamforming technique has been tested and proven to be effective in investigating traffic patterns, and dealing with heavy traffic scenarios (Chambers, 2020; Ende, 2021; van den Ende and Ampuero, 2021).

In this study, we use time-domain beamforming procedure to estimate the short-term average over long-term average traces (STA/LTA; Allen, 1978) of DAS waveform data, to extract the location and speed of individual trains, and demonstrate the effectiveness and stability of our method. In addition, our method can extract the footprint of speed variant trains by constantly moving the subarrays with acceptable real-time performance. Therefore, we first introduce the observation system and further show several typical signals induced by different kinds of trains. Thereafter, the detection and speed estimation are done by the beamforming method. In a bid to demonstrate the reliability of our method, we compare the detection results with the train schedules. Finally, we test the impacts of different signal-to-noise ratio levels and array apertures on beamforming performance, and discuss the applicability of our method.

Data

The experimental site for our study is located ~5 km north of Hangzhou Railway Station, Hangzhou, Eastern China. Towards the North, the rail tracks run directly underneath NE-SW trending Desheng expressway, while in the south lies the maintenance Depot for Electric Multiple Unit (EMU) trains (Figure 1). We connect the interrogator (HiFi-DAS provided by Puniutech) with an existing trackside telecommunication cable set at a 2-m channel spacing, and calibrate the cable into 1001 sensors. The cable is protected by polyvinyl chloride conduits underground. The data is acquired at a sampling rate of 50 Hz and the gauge length is 10 m. Strain data are continuously recorded over a period of 6 days in 2 different stages, starting

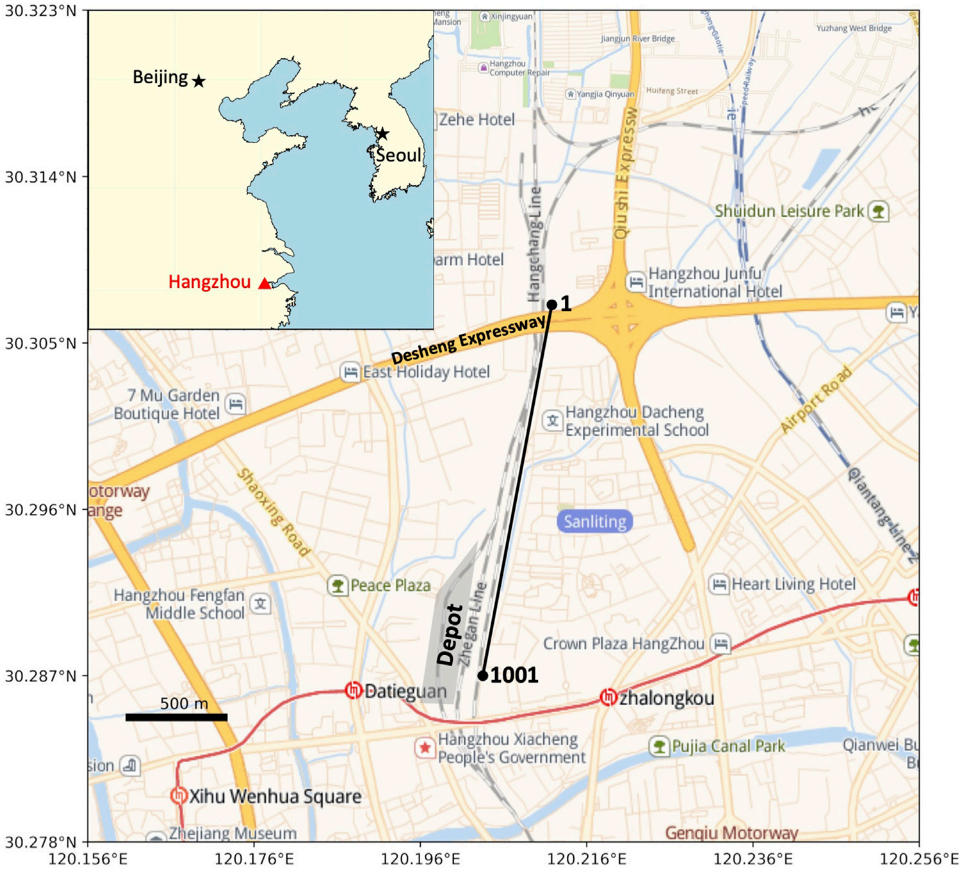

FIGURE 1
Map showing the location of the fiber-optic cable (black line) 5 km north of Hangzhou station (https://lbs.amap.com/demo/javascript-api/example/map/map-english/). Grey shade denotes the Depot. The numbers in black are the start and end channel numbers. The alternating grey and white lines are railway roads (Hanghang Line, Zhegan Line). The blue arrow indicates the direction of the train station. The yellow solid lines denote expressways, and Desheng Expressway is marked where the cable segment from channel 1 to channel 200 lies. Hangzhou (red triangle) and other major cities (black star) are also marked on the inset map.

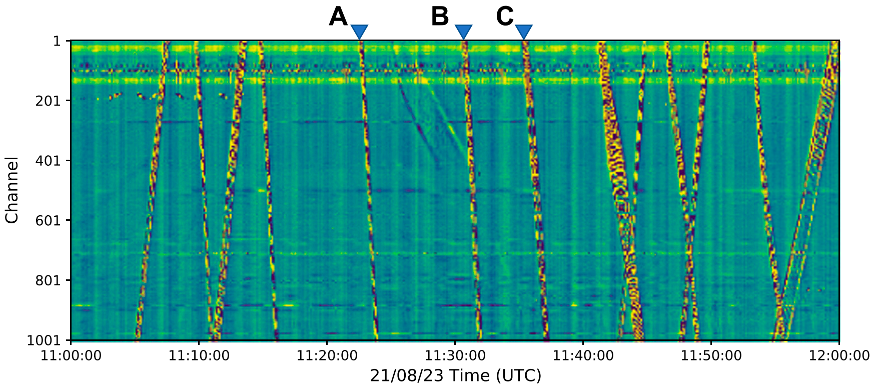

FIGURE 2
One-hour DAS data records under a heavy railway traffic scenario. The reverse blue triangles mark three typical train events shown in Figure 3 (corresponding to **(A–C)** from left to right).

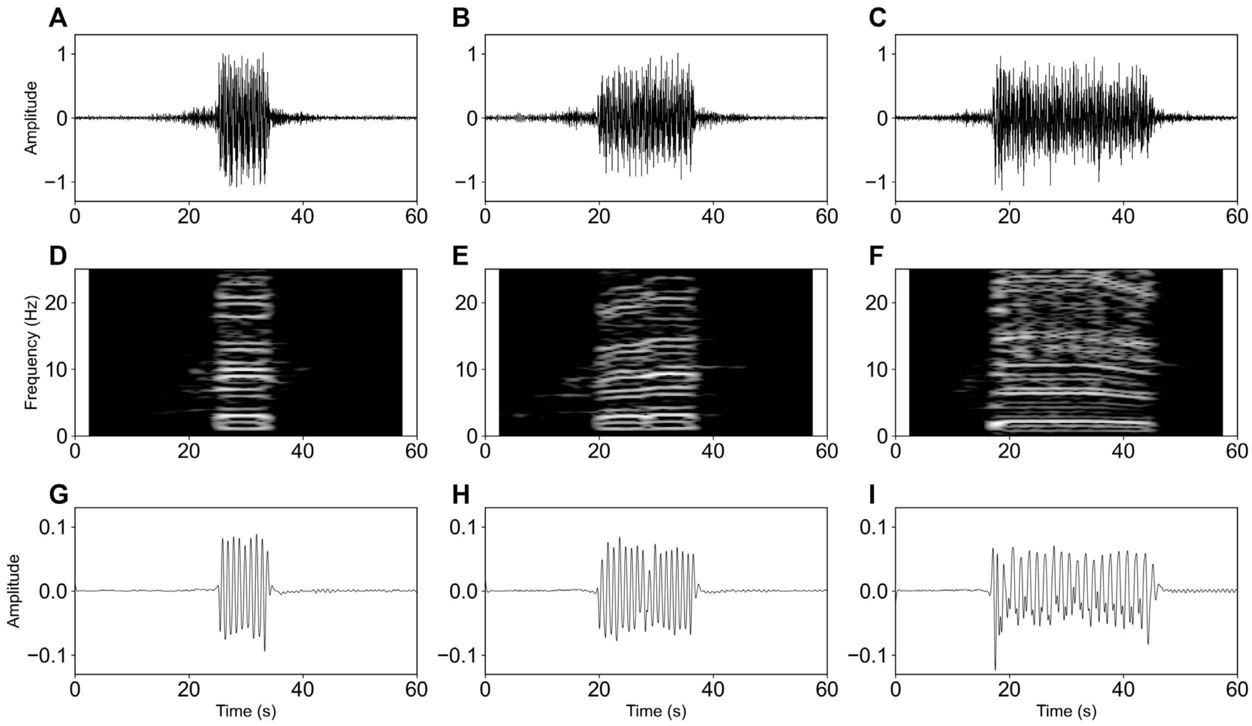

FIGURE 3
Typical train-induced signals of CH500 **(A–C)**, their spectrograms **(D–F)**, and lowpass filtered signals **(G–I)**. The blue circles denote peaks.

from 23rd to 26th in August 2021 and 2nd to 3rd in September 2021, respectively.

A 1-h DAS record for a heavy-traffic period is shown in Figure 2. We could easily identify the train-induced, quasi-static deformation signals, leaving the "footprint" of passing trains across the array. The slope of the track can be considered as the speed of individual trains, and in total, there are 13 identical slant lines which demonstrate that the trains pass our array at near constant speeds. From ~ Ch1-130, there are persistent noises that could have been generated by high-frequency vehicle traffic on Desheng expressway, yet the train-induced signals are still visible. At 11:30, there is an indication that a train moves at low-speed comes from north to south at ~5 km/h, and fades away at ~ Ch400. This is conceived to be an EMU parking event for maintenance to the Depot in the south.

Trains passing through the site include 8 or 16-wagon EMUs which is powered by each unit (~26 m in length), and the conventional or locomotive-hauled trains which typically consist of −18—21 wagons powered by the locomotive, individually. Figures 3A–C show raw waveforms recorded at Ch500 due to wagon 8, wagon 16 (from the EMU), and a conventional train, respectively. We then compute their spectrograms (Figures 3D–F) and observe that the signals cover the entire frequency band. In all the 3 cases earlier mentioned (Figure 3), no main frequency is identical and the equal-distance spectral lines observed using seismometers (in the work of Fuchs and Bokelmann, 2017) are also clear in our DAS observations. The distance in-between the spectral lines was suggested to be related to the train speed and the length of bogies (Lavoué et al., 2020). Previous studies have shown that the peaks of train-induced signals correspond to the number of bogies, usually the number of wagons plus 1 (Kowarik et al., 2020; Lavoué et al., 2020). To reduce the influence of high-frequency noise, we apply a 5 Hz lowpass filter on the three waveform signals, thereby enhancing the relatively long-period train-induced signals. After filtering, we could observe clearer periodic signals and peaks (Figures 3G–I), where the peaks correspond to the 9th (8-wangon EMU), 17th (16-wagon EMU), and 21st (20-wagon conventional train) bogies.

Materials and method

Though we could manually identify trains "footprints" from raw waveform DAS data, however, it is still a challenge to detect train-induced events and estimate their speeds automatically. In our experiment, trackside cables are

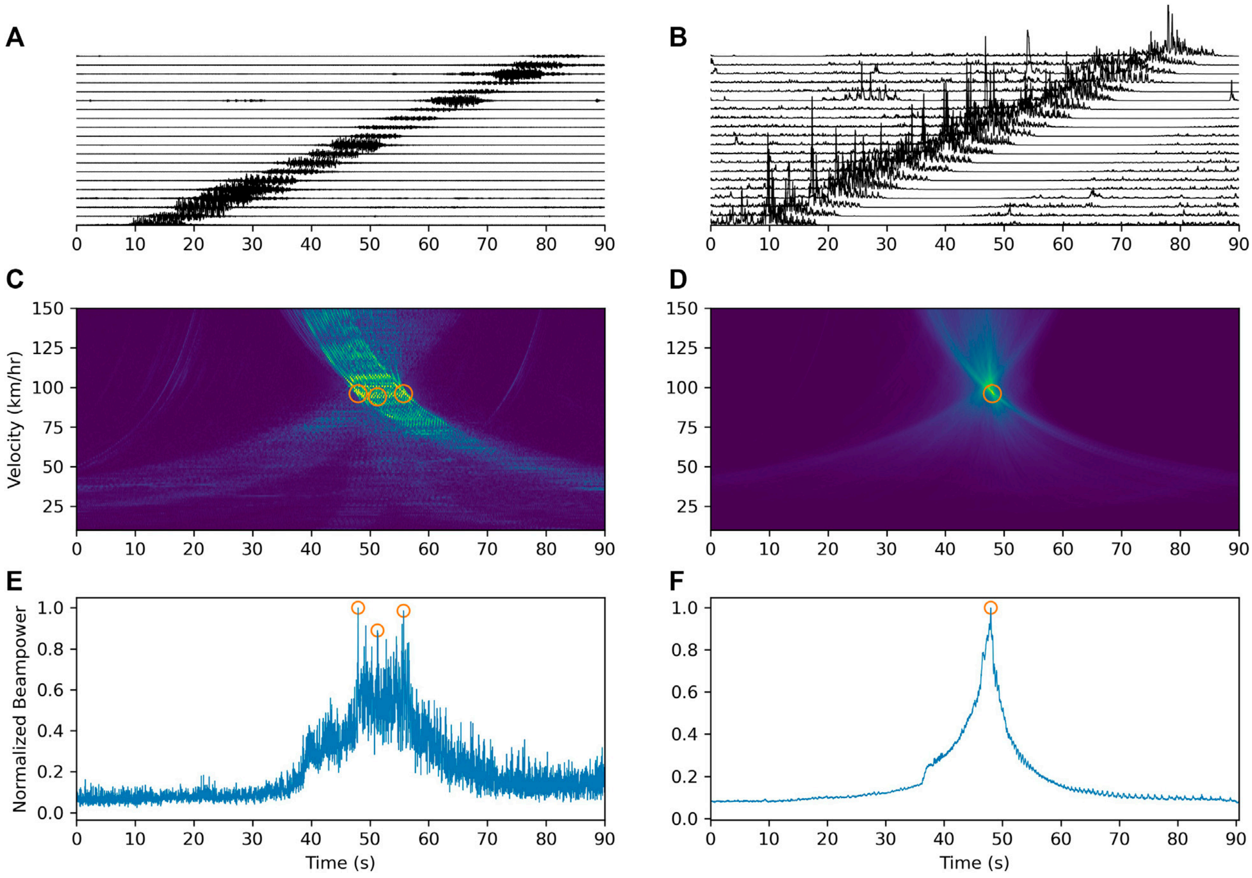

FIGURE 4
Comparison of beamforming results derived from raw signals and STA/LTA traces. **(A)** Signals extracted from the entire array every 50 channels; **(B)** STA/LTA traces of the signals shown in **(A)**; **(C)** Vespagram calculated with the whole-array raw data; **(D)** Same as **(C)** but derived from STA/LTA traces; **(E,F)** Time-beampower curves of **(C,D)**.

linearly distributed, and as an ultra-dense array, so it is suitable to use the beamforming approach to transfer the raw data to the time-velocity domain whose results are known as vespagram (eg., Rost and Thomas, 2002). The method shifts the phase of each waveform with respect to a range of velocities and then stack the time-shifted waveforms as a beam, whereby the vespagram is the result of all beams calculated all over the speed range (Meng and Ben-Zion, 2018; Nayak and Ajo-Franklin, 2021; van den Ende and Ampuero, 2021). Among the beams, the maximum value of the beampower corresponds to the apparent velocity and event detection time. The beamforming approach has been applied in the vehicle traffic monitoring fields (Chambers, 2020; van den Ende and Ampuero, 2021).

The waveforms are relatively not coherent in the DAS recordings (Figure 4A). Researchers would like to do some pre-processing on the raw data, such as median filter (Chambers, 2021; Nayak and Ajo-Franklin, 2021), or some kind of normalization and smoothing like what Chambers (2020) did by measuring the signal envelopes. Instead of that, we use STA/LTA traces to squeeze signal phases and enhance/equalize the amplitude. The time-domain beamforming technique stacks all the channel data, because the amplitude of the train-induced signals is so high that even the recordings with large noise levels still can help. We didn't find the data suffer from non-linear behaviors or spiking. Furthermore, we have tested a 7-channel time-domain median filter on our data (Nayak and Ajo-Franklin, 2021), and we didn't find differences on the results. Compared to signals generated by vehicle, train-induced signals are relatively more complex, which is mainly due to longer periods (vehicle signals with 1 period, trains at least more than 8 periods) and duration of the signal (vehicle less than 1 s, trains longer than 10 s in our study). We use the whole array data to beamform the signals generated from the EMU, having a speed ranging from 10 to 150 km/h, with speed interval of 1 km/h. Typical vespagrams generated from a set of raw and processed signals are shown in Figures 4C,D. A long duration

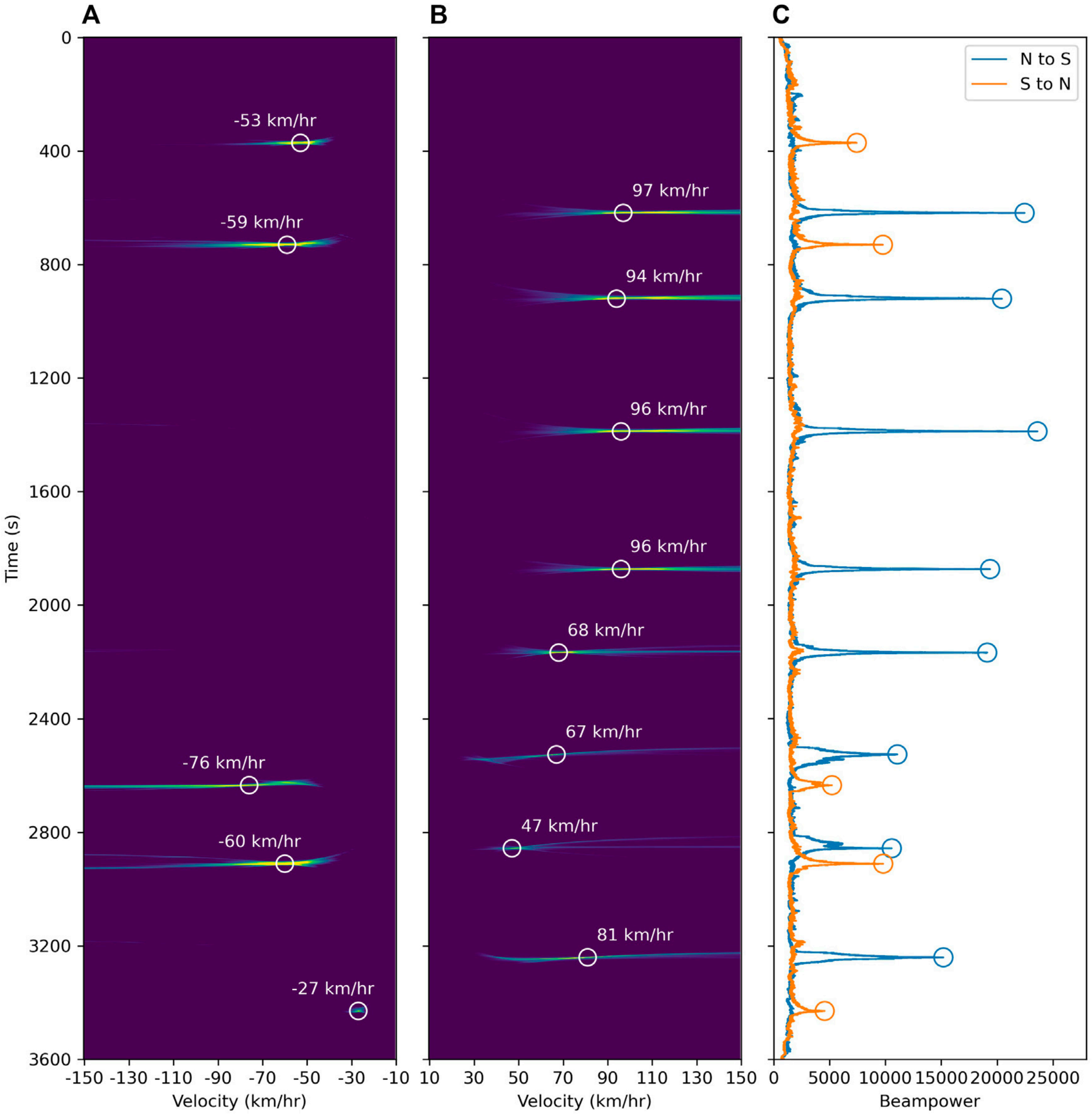

FIGURE 5
Beamforming results for a 1-h data (shown in Figure 2.). **(A,B)** Vespagrams for S-N and N-S trains and local power maximums detected from **(C)**; **(C)** Time-beampower curve derived from **(A,B)**, detected peaks denoted as circles.

of the train-induced signals could lead to low resolution on the vespagram. While after exploiting the STA/LTA algorithm on the raw data, the resolution on the vespagram is improved. To increase the sensitivity of arrivals, the STA is set as 0.1 s, while the LTA is set as 50 s, longer than the duration of the slowest train. After the processing, the signals are better enhanced and centered at arrivals, while the phases are squeezed. Next, we beamform the STA/LTA traces and the vespagram results show a better temporal resolution. The detection time is around the estimated maximum beampower at the centre of the array. We further extract the maximum value along the time axis and build the time-beampower curve (Figures 4E,F). We could observe that the curve becomes smoother and the peak becomes more prominent after the STA/LTA calculation. We select two threshold parameters namely, prominence and distance, to constrain the find-peak algorithm to estimate the maximum beampower (Virtanen et al., 2020). The prominence is used to constrain the maximum difference between the peaks and saddles, and the distance is the time difference to constrain the corresponding time of the peaks and saddles within the time distance (van den Ende and Ampuero, 2021; Virtanen

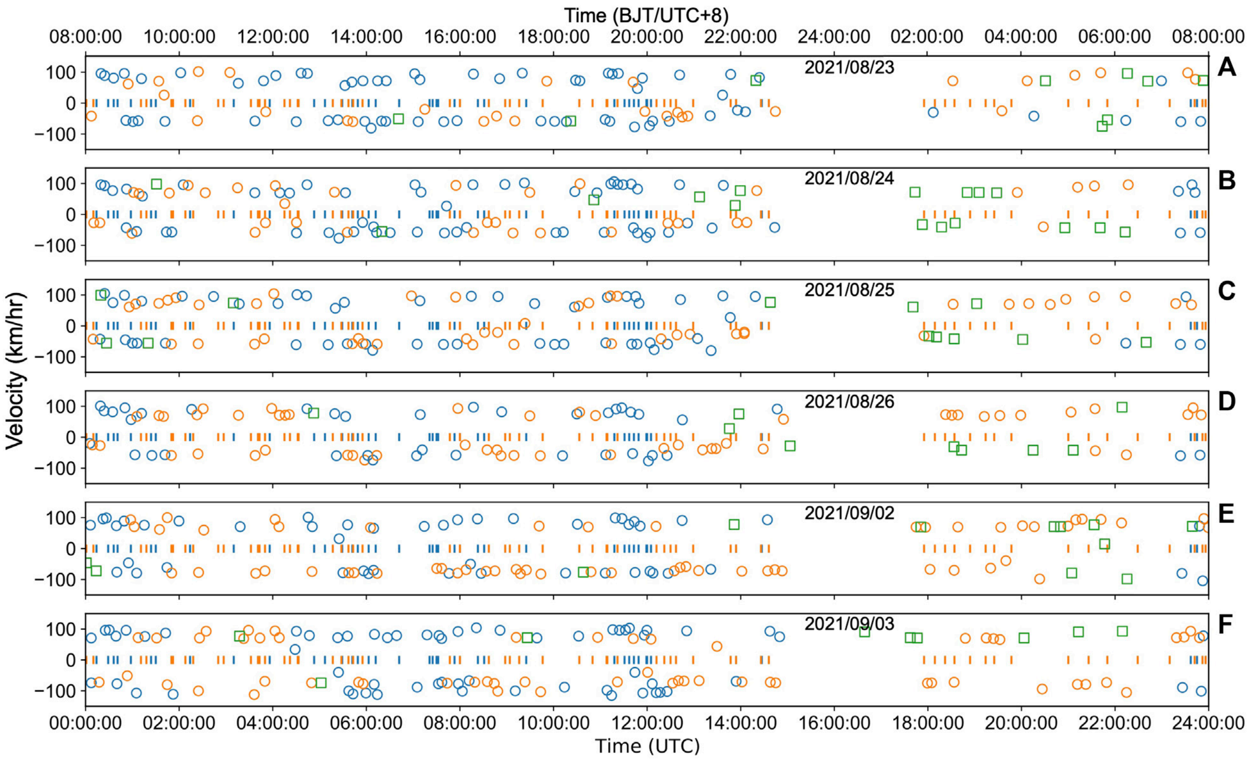

FIGURE 6
Detections, train speeds, and train types extracted from 6-days data. Negative and positive speed values correspond to N-S and S-N, respectively. Orange, blue vertical lines mark the time on the train timetable (the arrival time for N-S cases, and departure time for S-N). Orange and blue circles represent detected conventional trains and EMU trains, respectively; the hollow squares denote non-scheduled trains.

et al., 2020). When we select a small time-distance parameter, three detection results appear in the time-beampower curve of computed from the raw data (Figure 4E). Meanwhile, after calculating the STA/LTA, the signals are squeezed as sharp impulses like generated by point sources, we then obtain a more stable detection performance result from the time-beampower curve (Figure 4F).

To avoid missed detection while processing long continuous data, we choose to select a small prominence parameter (usually could be 3 times the average of the noise amplitude). Similarly, to avoid false detection, we select a time-distance parameter that is larger than the signal duration of a slow train (set as 40 s). Figure 5 shows the detection and speed estimation results of the 1-h data earlier shown in Figure 2. From the observations, the train events are localized on the vespagrams and are successfully detected from the time-beampower curve. Also, we extract the speed after obtaining the corresponding local maximum beampower. In general, the higher the speed, the higher the beampower is and the better the automatic detection process performs. For the crossing and superimposed signals, our method also retrieves reliable results which demonstrates that our method can suitably be applied to heavy railway traffic monitoring.

Result

In Figure 6, we show the data detection result over a 6-day period, where it is observed that each detection time corresponds to the time the train passes the array center at Ch500. We qualitatively verify the detection results by visually inspecting the “footprints”, and categorize the types of trains by counting the number of peaks of the lowpass filtered waveforms (typical examples are shown in Figure 3). Due to the proprietary and sensitive nature of train itinerary records, we could not determine the exact train registration number of each passing/transiting train but constrained the type of trains by observing each passing train using their scheduled departure or arrival time (https://kyfw.12306.cn/otn/queryTrainInfo/init). From these records, we observe that the activity of railway traffic is somewhat irregular throughout the 6 days. Considering that the observation site is 5 km north of the railway station, the traffic pattern may not be an exact reflection of the exact time the train departed or arrived

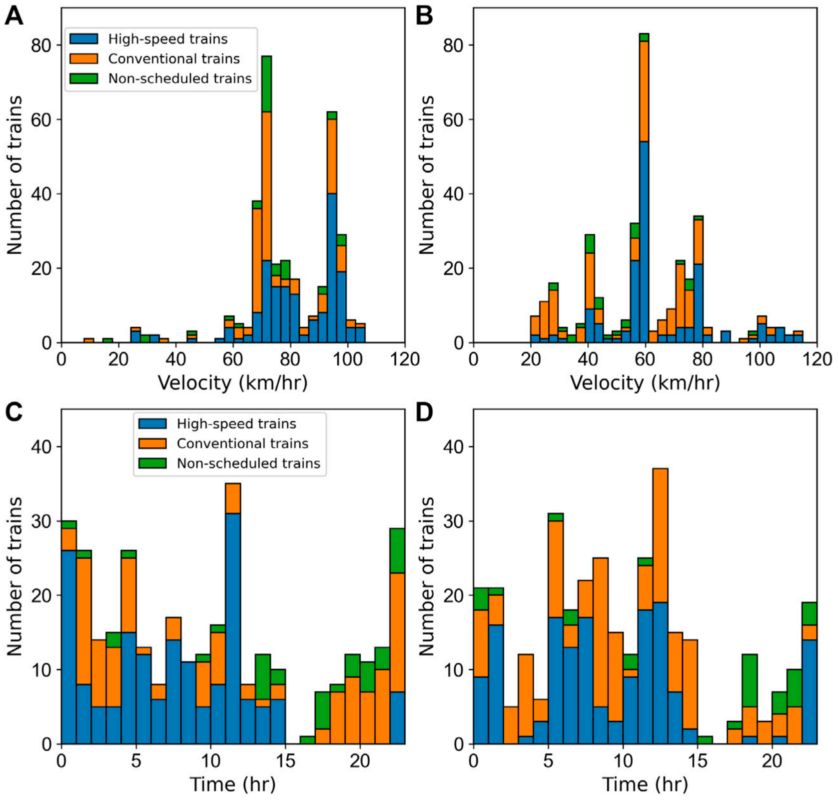

FIGURE 7
Histograms of speed distribution and hourly detections from N-S and S-N. **(A,B)** Speed distribution of all detected trains; **(C,D)** Hourly detections derived from the results shown in Figure 6.

at the station. We also find out that some detected trains do not match the schedule, which could be either temporary or emergency scheduled trains or the trains that transits through the station without stopping. These scenarios are especially observed during between 23:00 to 7:00 (UTC+8), typical of the duration when non-scheduled trains operate. More so, we observe some signals with only one period which are believed to be generated by a single locomotive.

We count the detections based on the direction, speed, and type of trains (Figures 7A,B). Generally, we observe that the average speed of the trains from the north to the south is higher than those from the south to the north. This implies that at a distance of ~5 km to the station, the deceleration time from the North to the South is shorter than the acceleration time from the South to the North. The speed is limited from block to block by the train control system (Ouyang et al., 2010; Zhang, 2008), which in practice, the train drivers adjust the speed while approaching or moving out of the train stations according to actual situations (CRC, 2004). Hence, there is no statistically significant difference in the speed of different types of trains in this case. The hourly detection histograms (Figures 7C,D) show similar railway traffic patterns on the both directions. The railway traffic becomes heavy during the morning and evening as similarly suggested in Figure 6, while turns out to be silent during the midnight.

Discussion

The cable is 2 km in length, as the cable cannot be perfectly straightened up, the real spatial distribution is theoretically shorter than the length of the cable. The estimated speed of our beamforming method is the apparent velocity along the cable, so we wish we could have the exact locations of each channel or some of them to correct this effect, however, we were not allowed to do it in the field work due to safety regulations of railways. Nevertheless, we observe that the trains pass our experimental site as constant speeds, which could be inferred from that the slope of the “footprints” is relatively constant. If the spatial distribution of the cable is complex, we could have seen twisted footprints and the beamforming results could be biased. From this point of view, we accept the shape of the cable causes

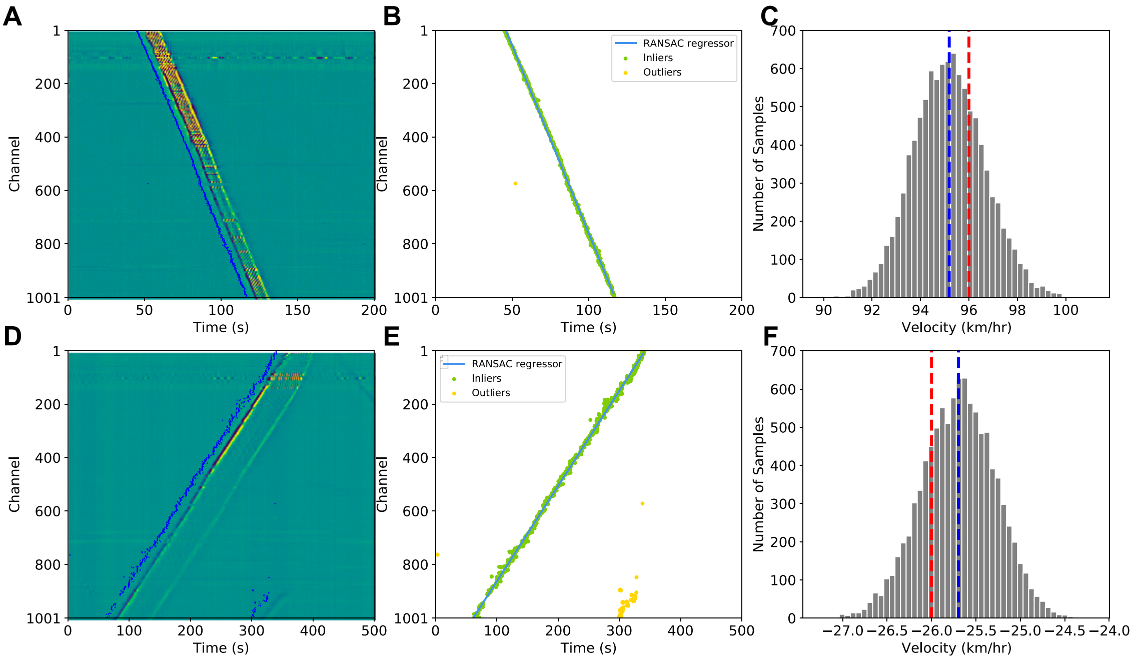

FIGURE 8
Examples of RANSAC linear regression on the relative travel times for EMU train and conventional train cases. **(A)** EMU train case and relative travel times (blue dots) picked by cross-correlation of signal envelopes; **(B)** RASAC regressor fitting the inliers, outliers excluded automatically; **(C)** Histogram of bootstrapped speeds, the red and blue dotted lines denote the beamformed speed obtained by our method and mean speed, respectively; **(D–F)** Same as **(A–C)**, but for a conventional train case.

minor effect in our study. In fact, the estimated speeds depend on the tolerance towards requirements if in real use, and we could correct the location of every channel by multiplying coefficients for the cable, thus we could exact more accurate speed of the trains passing our experimental site.

For an event generated by an individual train, an efficient way to evaluate its speed is to calculate the slope of the “footprint”, which implies, fitting linear regression on the arrival time of all the traces to verify the accuracy of the estimated speed retrieved through the beamforming method. Influenced by uneven coupling and possible orientation variations of the cable, simply utilizing STA/LTA algorithm across a dataset with equal threshold may not efficiently pick the arrival time. Considering the consistent duration of train-induced signals, we construct signal envelopes to reduce the complexity of waveforms (i.e., high-frequency noise, polarity reversals etc.), and calculate relative arrivals by conducting cross-correlation on Ch1 and the rest of the 1000 channels signal envelopes. We then apply the bootstrapping method (10,000 times) to quantify the variability of the linearly regressed velocities from the arrival times (Tichelaar and Ruff, 1989). To reduce the impact of the outliers on the regression calculation, we use the random sampling consensus algorithm (RANSAC; Fischler and Bolles, 1981; Yoo et al., 2020) to automatically exclude the outliers during each regression. Figure 8 shows the results from the linear regression of an EMU and a conventional train, respectively, as well as their bootstrapping histograms. The arrival times derived from the former have better convergence along with the signals than in the latter, thus indicating that the signals due to the EMU train are relatively more coherent. The outliers are identified and isolated by the RANSAC regressor (Figures 8B,E). The mean speed of the EMU and the conventional train are 96.18 and −25.69 km/h, respectively, whereas the standard deviations (STD) are 1.52 and 0.43 km/h, showing that the robust regression results are close to the beamforming estimations (96 and −26 km/h). Based on the STD of the speeds, the uncertainty of the EMU scenario is larger than that of the conventional train, which implies that the former has a larger speed variance. In general, the mean speeds of the two regression estimates are both within 1 km/h of the beamforming results, demonstrating that our method could achieve stable and accurate speed estimations with the DAS data.

In actual situations, the length and coupling of the cable make the recorded DAS data impacted by different level of noise (Song et al., 2021). Therefore, we test the performance of our method on two typical train-event signals (Figure 8) with different noise levels. Before the start time of the signal window (40 and 50 s shown in Figures 8A,D; as zoomed in section in Figure9A,C), we slice the noise window into equal size with the signal window, and multiply the noise with factors ranging from 0 to 30. Thereafter, we impose

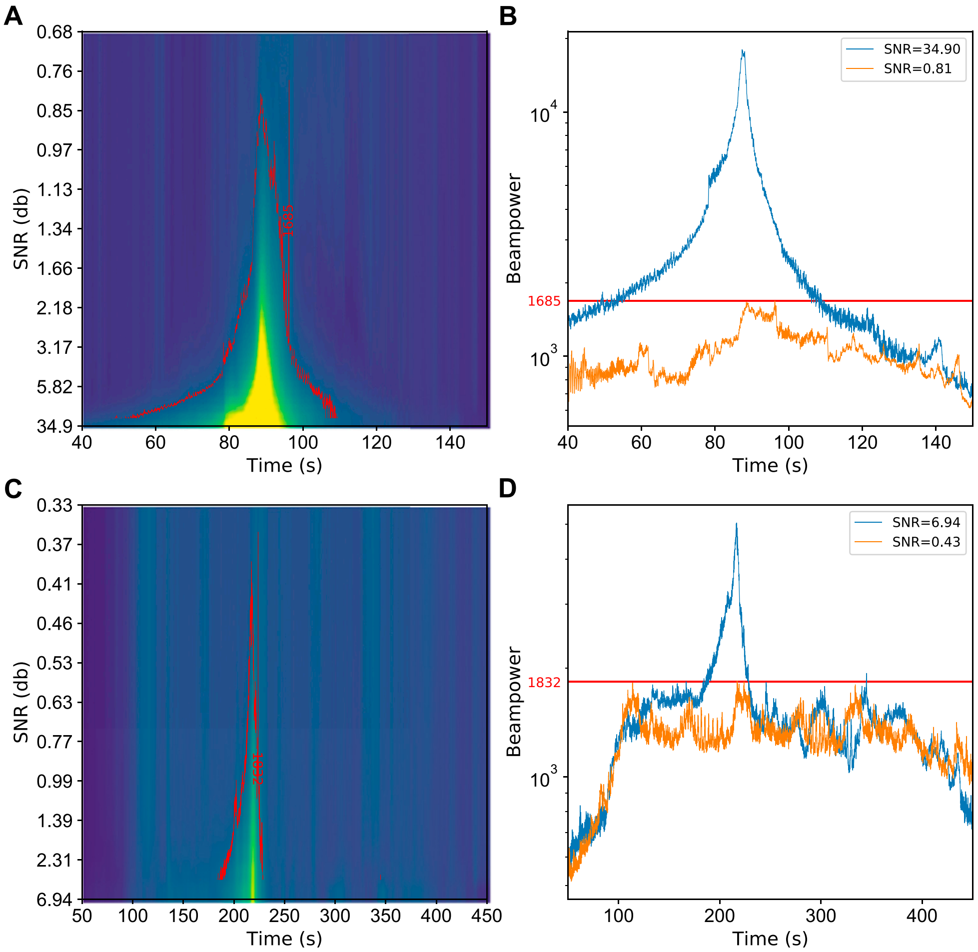

FIGURE 9
Examples of the beamforming performance influenced by different SNR levels. **(A)** Collection of time-beampower curves with different SNRs for an EMU train (sliced from the segment shown in Figure 8A), the red contour line marks the lowest beampower value leading to false detection. **(B)** Time-beampower curves under high SNR (blue line) and low SNR (red line), the latter leads to false detection. **(C)** Same as **(A)**, but sliced from the segment shown in Figure 8D; **(D)** Same as **(B)**, but extracted from **(C)**.

the noise windows on the signal windows to obtain synthetic datasets with different noise levels and define the average signal-to-noise ratio (SNR) as the array energy (sum of the squared amplitude of all samples) ratio of the signal and noise windows (Lv et al., 2022). The initial SNR of the EMU and conventional train are 34.90 and 6.94 dB, respectively. As the SNRs decrease, the beampower values also decrease, and the false detections are not triggered until the SNRs fall as low as 0.81 dB for the EMU and 0.43 dB for the conventional train, corresponding to false peaks or multiple same-level peaks in the time-beampower curve (Figures 9B,D). In addition, we note that the least SNR required by the conventional train is less than that of the EMU, which could be due to its speed distribution that is assumed to be relatively more stable (Figures 8C,F).

For trains running at constant speed, the larger the array, the higher the beampower is and the more prominent the peak stands in the time-beampower curve. To ensure the reliability of results for actual railway traffic monitoring, using a smaller aperture will better enhance real-time monitoring. Moving small-aperture subarrays contribute to effectively monitor the change in speed of trains and update the track as the trains pass. However, smaller aperture will reduce the speed resolution on the vespagram (Nayak and Ajo-Franklin, 2021; Schweitzer et al., 2012). Moreover, the amplitude and duration of train-induced signals distinctively vary according to the type and speed of trains. Meanwhile, telecommunication cables suffer from coupling issues and varying noise levels or distributions (Song et al., 2021), so it is necessary to make adjustments on array aperture in compliance with real-time requirements and speed resolution. Figure 10 shows the beamforming results of an EMU train and a conventional train (same cases as shown in Figure 9) at different array apertures for the fiber-optic cable used in our

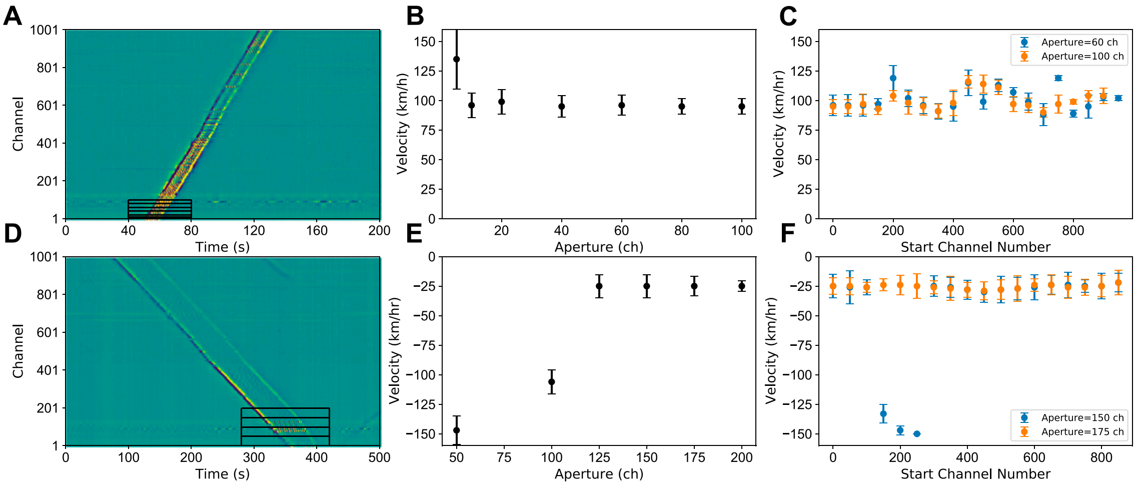

FIGURE 10
Array aperture test for an EMU train and conventional train. **(A)** EMU train case with different apertures/channels sliced as denoted by black squares; **(B)** Detection results with different apertures as shown in **(A)**; **(C)** Detection results of moving arrays with 60 and 100-channel aperture; **(D–F)** Same as **(A–C)**, but for a conventional train case.

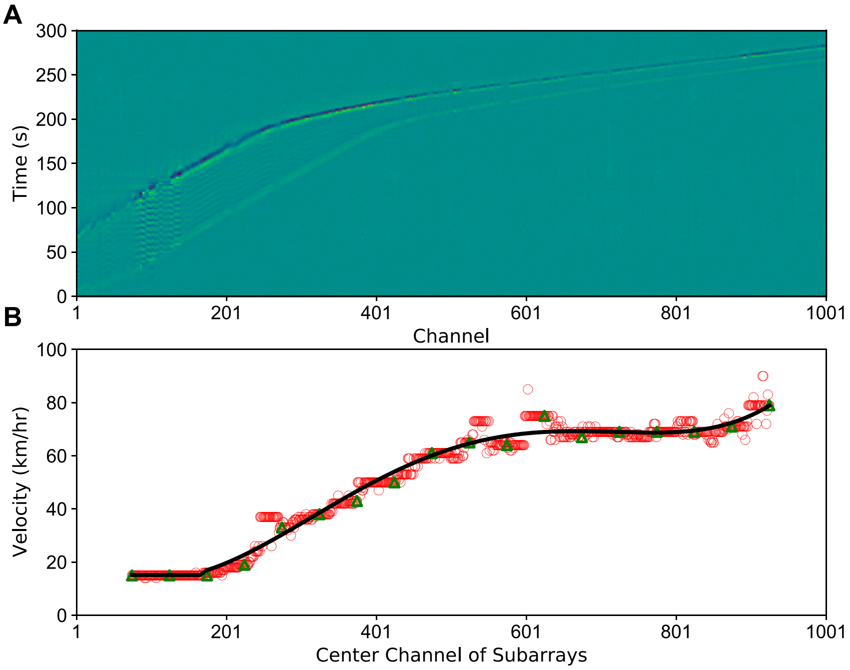

FIGURE 11
Speed and motion track estimation for a variable-speed train case. **(A)** Train-induced signals; **(B)** Detection results and speed distribution. Red circles denote the speed results estimated by moving subarrays with 149-channel overlapping, while green triangles denote the results with 100-channel overlapping. The black curve is the smoothed result of the green triangles.

experiment. We estimate the uncertainty by measuring 70% of the width of the detected peak amplitude in the time-beampower curve. With the increase of the array aperture, the results become more stable with less uncertainty (Figures 10B,E). To test the suitability of a certain aperture for the entire cable, we modify the aperture, move the array sequences every 50 channels, and beamform the data. Thus, we obtain detection results and velocity distributions as a function of array position along the cable (Figures 10C,F). For the EMU train, the speeds estimated from moving subarrays with a 60-channel aperture are sparser distribution than that of a 100-channel aperture. In the case of the conventional train, arrays with 150-channel aperture still lead to discrete speed estimations, while the 175-channel aperture produces more stable results. It is interesting to note that the edges of the train heads shown in Figure 10D are more identical than the rest wagons, which is often the case of low-speed conventional trains. We believe this is caused by the locomotive pulling the rest wagons. In practical or field situations, depending on the coupling and noise level, varying apertures can be used for different segments depending on the increase in the overlap of subarrays to obtain a denser velocity curve. Also, for seismological studies that utilize train-induced signals as noise sources, the real-time requirement is not urgent, in which case we could select a large array aperture.

Though most of the trains pass our experiment site at constant speeds, there are still individual cases where the speed changes significantly. Figure 11 shows the detection results of such a case with 150-channel moving subarrays from which the acceleration process of the train can be identified. From ~ Ch1—Ch200, the time duration of signals covers ~70 s. From–Ch200—Ch600, the duration decreases gradually to ~20 s and thereafter remain constant till the end. We obtain the speed curve/motion track by smoothening the speed values, and the change in speed shown in the curve is consistent with the observation-based analysis shown above. Both 149 and 100-channel overlapping subarrays detect results with smooth and consistent velocity curves, which show that our methods also have good applicability in detecting trains moving at varying speed. In an extreme case, a high-speed train moving at a design speed of 350 km/h would take 3.09 s to cover a 150-channel array with 2 m channel spacing. In terms of computational efficiency, a NumPy 2D array npz file with a size of 1001 × 150000 (2 km and 300 s) can be loaded on an 8 G ram M1 chip MacBook Air within 0.2 s, and computation can be completed for a 150-channel aperture subarray matrix within 0.88 s. Such computational performance implies that our method is suitable for near real-time railway traffic monitoring. In addition, the Kalman filter is another approach to smooth the train trajectories (Ferguson et al., 2020; Wiesmeyr et al., 2020), and it would be interesting to test extended and adaptive Kalman filters (Terejanu, 2008; Vullings et al., 2010) on arrival picks and the detection results beamformed by subarrays. We could delve deeper into this in the future work.

Conclusion

In this study, we conduct an investigation on railway traffic monitoring using DAS data acquired by a 2-km trackside telecommunication fiber-optic cable. We utilize the beamforming technique on STA/LTA traces to automatically detect the train induced events, to extract their speed and direction. From the results, we identify the type of trains by counting the number of peaks from the lowpass filtered signal. Using beamforming technique, we process the 6-days continuous data to quantify and characterize the results using the speed, direction, and types of trains. By reducing the aperture of the array and moving subsequent subarrays, we obtain the train speed curve/motion track. The method we propose can provide a supplementary approach and play a synergetic role with other existing railway traffic monitoring systems. Moreover, our method can be used to conduct seismic interferometry investigation along the railroad using train-induced ground motions, whereby the noise windows containing or excluding train-induced signals can be automatically determined.

Data availability statement

The raw data supporting the conclusions of this article will be made available by the authors, without undue reservation.

Author contributions

GZ, ZS, and BC contributed to conception and design of the study. RL organized the database. AO revised English manuscript. GZ wrote the first draft of the manuscript. All authors contributed to manuscript revision, read, and approved the submitted version.

Funding

National Key R&D Program of China (2021YFA0716802), Knowledge Innovation Program of Wuhan-Basic Research (S22H640301), National Natural Science Foundation of China (41974067).

Conflict of interest

The authors declare that the research was conducted in the absence of any commercial or financial relationships that could be construed as a potential conflict of interest.

Publisher's note

References

Ajo-Franklin, J. B., Dou, S., Lindsey, N. J., Monga, I., Tracy, C., Robertson, M., et al. (2019). Distributed acoustic sensing using dark fiber for near-sur- face characterization and broadband seismic event detection. *Sci. Rep.* 9, 1328. doi:10.1038/s41598-018-36675-8

Allen, R. (1978). Automatic earthquake recognition and timing from single traces. *Bull. Seismol. Soc. Am.* 68, 1521–1532. doi:10.1785/BSSA0680051521

Baldini, G., Fovino, I. N., Masera, M., Luise, M., Pellegrini, V., Bagagli, E., et al. (2010). An early warning system for detecting GSM-R wireless interference in the high-speed railway infrastructure. *Int. J. Crit. Infrastructure Prot.* 3 (3-4), 140–156. doi:10.1016/j.ijcip.2010.10.003

Brenguier, F., Boue, P., Ben-Zion, Y., Vernon, F., Johnson, C. W., Mordret, A., et al. (2019). Train traffic as a powerful noise source for monitoring active faults with seismic interferometry. *Geophys. Res. Lett.* 46 (16), 9529–9536. doi:10.1029/2019GL083438

Bruni, S., Goodall, R., Mei, T., and Tsunashima, H. (2007). Control and monitoring for railway vehicle dynamics. *Veh. Syst. Dyn.* 45 (7-8), 743–779. doi:10.1080/00423110701426690

Cedilnik, G., Hunt, R., and Lees, G. (2018). "Advances in train and rail monitoring with DAS," in 26th International Conference on Optical Fiber Sensors, Lausanne, Switzerland, September 24–28, 2018 (Optical Society of America). *Paper ThE35.* doi:10.1364/OFS.2018.ThE35

Chambers, K. (2020). Using DAS to investigate traffic patterns at brady hot springs, Nevada, USA. *Lead. Edge* 39 (11), 819–827. doi:10.1190/tle39110819.1

CRC (China Railway Corporation) (2004). *Railway Technical Management Rules (normal speed railway section)*. Beijing: China Railway Press.

Dou, S., Lindsey, N., Wagner, A. M., Daley, T. M., Freifeld, B., Robertson, M., et al. (2017). Distributed acoustic sensing for seismic monitoring of the near surface: A traffic-noise interferometry case study. *Sci. Rep.* 7 (1), 11620–11712. doi:10.1038/s41598-017-11986-4

Ferguson, R. J., McDonald, M. A. D., and Basto, D. J. (2020). Take the eh? train: Distributed acoustic sensing (DAS) of commuter trains in a Canadian city. *J. Appl. Geophy.* 183, 104201. doi:10.1016/j.jappgeo.2020.104201

Fischler, M. A., and Bolles, R. C. (1981). Random sample consensus: A paradigm for model fitting with applications to image analysis and automated cartography. *Commun. ACM* 24 (6), 381–395. doi:10.1145/358669.358692

Fuchs, F., and Bokelmann, G. (2017). Equidistant spectral lines in train vibrations. *Seismol. Res. Lett.* 89 (1), 56–66. doi:10.1785/0220170092

Hudson, T. S., Baird, A. F., Kendall, J.-M., Kufner, S.-K., Brisbourne, A. M., Smith, A. M., et al. (2021). Distributed acoustic sensing (DAS) for natural microseismicity studies: A case study from Antarctica. *JGR. Solid Earth* 126 (7), e2020JB021493. doi:10.1029/2020JB021493

Iswanto, I. A., and Li, B. (2017). Visual object tracking based on mean-shift and particle-Kalman filter. *Procedia Comput. Sci.* 116, 587–595. doi:10.1016/j.procs.2017.10.010

Jiang, Y., Ning, J., Wen, J., and Shi, Y. (2022). Doppler effect in high-speed rail seismic wavefield and its application. *Sci. China Earth Sci.* 65 (3), 414–425. doi:10.1007/s11430-021-9843-0

Kowarik, S., Hussels, M. T., Chruscicki, S., Munzenberger, S., Lammerhirt, A., Pohl, P., et al. (2020). Fiber optic train monitoring with distributed acoustic sensing: Conventional and neural network data analysis. *Sensors (Basel).* 20 (2), 450. doi:10.3390/s20020450

Lavoué, F., Coutant, O., Boué, P., Pinzon-Rincon, L., Brenguier, F., Brossier, R., et al. (2020). Understanding seismic waves generated by train traffic via modeling: Implications for seismic imaging and monitoring. *Seismol. Res. Lett.* 92 (1), 287–300. doi:10.1785/0220200133

Li, Z., Shen, Z., Yang, Y., Williams, E., Wang, X., and Zhan, Z. (2021). Rapid response to the 2019 ridgecrest earthquake with distributed acoustic sensing. *AGU Adv.* 2 (2). doi:10.1029/2021av000395

Lindsey, N. J., Martin, E. R., Dreger, D. S., Freifeld, B., Cole, S., James, S. R., et al. (2017). Fiber-optic network observations of earthquake wavefields. *Geophys. Res. Lett.* 44 (23), 11–792. doi:10.1002/2017GL075722

Lindsey, N. J., Yuan, S., Lellouch, A., Gualtieri, L., Lecocq, T., and Biondi, B. (2020). City-scale dark fiber DAS measurements of infrastructure use during the COVID-19 pandemic. *Geophys. Res. Lett.* 47 (16), e2020GL089931. doi:10.1029/2020GL089931

Liu, Y., Yue, Y., Luo, Y., and Li, Y. (2021). Effects of high-speed train traffic characteristics on seismic interferometry. *Geophys. J. Int.* 227 (1), 16–32. doi:10.1093/gji/ggab205

Lv, H., Zeng, X., Bao, F., Xie, J., Lin, R., Song, Z., et al. (2022). ADE-net: A deep neural network for DAS earthquake detection trained with a limited number of positive samples. *IEEE Trans. Geosci. Remote Sens.* 60, 1–11. doi:10.1109/tgrs.2022.3143120

Martin, E. R., Huot, F., Ma, Y., Cieplicki, R., Cole, S., Karrenbach, M., et al. (2018). A seismic shift in scalable acquisition demands new processing: Fiber-optic seismic signal retrieval in urban areas with unsupervised learning for coherent noise removal. *IEEE Signal Process. Mag.* 35 (2), 31–40. doi:10.1109/MSP.2017.2783381

Meng, H., and Ben-Zion, Y. (2018). Detection of small earthquakes with dense array data: Example from the san jacinto fault zone, southern California. *Geophys. J. Int.* 212 (1), 442–457. doi:10.1093/gji/ggx404

Nayak, A., and Ajo-Franklin, J. (2021). Distributed acoustic sensing using dark fiber for array detection of regional earthquakes. *Seismol. Res. Lett.* 92 (4), 2441–2452. doi:10.1785/0220200416

Ouyang, M., Hong, L., Yu, M.-H., and Fei, Q. (2010). STAMP-based analysis on the railway accident and accident spreading: Taking the China–Jiaoji railway accident for example. *Saf. Sci.* 48 (5), 544–555. doi:10.1016/j.ssci.2010.01.002

Parker, T., Shatalin, S., and Farhadiroushan, M. (2014). Distributed Acoustic Sensing–a new tool for seismic applications. *First Break* 32 (2). doi:10.3997/1365-2397.2013034

Quiros, D. A., Brown, L. D., and Kim, D. (2016). Seismic interferometry of railroad induced ground motions: Body and surface wave imaging. *Geophys. J. Int.* 205 (1), 301–313. doi:10.1093/gji/ggw033

Rost, S., and Thomas, C. (2002). Array seismology: Methods and applications. *Rev. Geophys.* 40 (3), 2-1–2-27227. doi:10.1029/2000rg000100

Sager, K., Tsai, V. C., Sheng, Y., Brenguier, F., Boué, P., Mordret, A., et al. (2022). Modelling P waves in seismic noise correlations: Advancing fault monitoring using train traffic sources. *Geophys. J. Int.* 228 (3), 1556–1567. doi:10.1093/gji/ggab389

Sasani, S., Asgari, J., and Amiri-Simkooei, A. R. (2015). Improving MEMS-IMU/GPS integrated systems for land vehicle navigation applications. *GPS Solut.* 20 (1), 89–100. doi:10.1007/s10291-015-0471-3

Schweitzer, J., Fyen, J., Mykkeltveit, S., Gibbons, S. J., Pirli, M., Kühn, D., et al. (2012). Chapter 9 seismic arrays, in New manual of seismological observatory practice 2 (NMSOP-2). *Dtsch. Geoforsch. GFZ*, 22–25. doi:10.2312/GFZ.NMSOP-2

Song, Z., Zeng, X., Xie, J., Bao, F., and Zhang, G. (2021). Sensing shallow structure and traffic noise with fiber-optic internet cables in an urban area. *Surv. Geophys.* 42, 1401–1423. doi:10.1007/s10712-021-09678-w

Spica, Z. J., Perton, M., Martin, E. R., Beroza, G. C., and Biondi, B. (2020). Urban seismic site characterization by fiber-optic seismology. *J. Geophys. Res. Solid Earth* 125 (3), e2019JB018656. doi:10.1029/2019JB018656

Tichelaar, B. W., and Ruff, L. J. (1989). How good are our best models? Jackknifing, bootstrapping, and earthquake depth. *Eos Trans. AGU.* 70 (20), 593–606. doi:10.1029/89EO00156

Ulianov, C., Hyde, P., and Shaltout, R. (2018). Railway applications for monitoring and tracking systems. *Sustainable Rail Transport*. Cham: Springer, 77–91. doi:10.1007/978-3-319-58643-4_6

van den Ende, M., and Ampuero, J. P. (2021). *Evaluating seismic beamforming capabilities of distributed acoustic sensing arrays*. Pacific Grove, CA: Solid earth 12 (4), 915–934. doi:10.5194/se-12-915-2021 van den Ende, M., Ferrari, A., Sladen, A., and Richard, C. (2021). "Next-generation traffic monitoring with distributed acoustic sensing arrays and optimum array processing," in 2021 55th Asilomar Conference on Signals, Systems, and Computers. doi:10.1109/IEEECONF53345.2021.9723373

Virtanen, P., Gommers, R., Oliphant, T. E., Haberland, M., Reddy, T., Cournapeau, D., et al. (2020). Author correction: SciPy 1.0: Fundamental algorithms for scientific computing in Python. *Nat. Methods* 17 (3), 352–272. doi:10.1038/s41592-020-0772-5

Walter, F., Gräff, D., Lindner, F., Paitz, P., Köpfli, M., Chmiel, M., et al. (2020). Distributed acoustic sensing of microseismic sources and wave propagation in glaciated terrain. *Nat. Commun.* 11 (1), 2436–2510. doi:10.1038/s41467-020-15824-6

Wiesmeyr, C., Litzenberger, M., Waser, M., Papp, A., Garn, H., Neunteufel, G., et al. (2020). Real-time train tracking from distributed acoustic sensing data. *Appl. Sci. (Basel).* 10 (2), 448. doi:10.3390/app10020448

Yoo, J., Mubarak, M. S., van Borselen, R., and Tsingas, C. (2020). "Line-guided first break picking via random sample consensus (RANSAC)," in *SEG technical program expanded abstracts 2020* (Society of Exploration Geophysicists), 2044–2048. doi:10.1190/segam2020-3422645.1

Yüksel, K., Kinet, D., Moeyaert, V., Kouroussis, G., and Caucheteur, C. (2018). Railway monitoring system using optical fiber grating accelerometers. *Smart Mat. Struct.* 27 (10), 105033. doi:10.1088/1361-665X/aadb62

Zeng, X., Lancelle, C., Thurber, C., Fratta, D., Wang, H., Lord, N., et al. (2017). Properties of noise cross-correlation functions obtained from a distributed acoustic sensing array at Garner Valley, California. *Bull. Seismol. Soc. Am.* 107 (2), 603–610. doi:10.1785/0120160168

Zhan, Z. (2019). Distributed acoustic sensing turns fiber-optic cables into sensitive seismic antennas. *Seismol. Res. Lett.* 91 (1), 1–15. doi:10.1785/0220190112

frontiers | Frontiers in Earth Science

TYPE Methods
PUBLISHED 30 September 2022
DOI 10.3389/feart.2022.999530

EDITED BY
Maxim Lebedev,
Curtin University, Australia

REVIEWED BY
Shuang Zheng,
Aramco Services Company,
United States
Verónica Rodríguez Tribaldos,
Berkeley Lab (DOE), United States
Salam Al-Rbeawi,
Middle East Technical University, Turkey

*CORRESPONDENCE
Yibo Wang,
wangyibo@mail.iggcas.ac.cn

SPECIALTY SECTION
This article was submitted to Solid Earth Geophysics,
a section of the journal
Frontiers in Earth Science

RECEIVED 21 July 2022
ACCEPTED 08 September 2022
PUBLISHED 30 September 2022

CITATION
Zheng Y, Wang Y, Liang X, Xue Q, Liang E, Wu S, An S, Yao Y, Liu C and Mei J (2022), A deep learning approach for signal identification in the fluid injection process during hydraulic fracturing using distributed acoustic sensing data.
Front. Earth Sci. 10:999530.
doi: 10.3389/feart.2022.999530

A deep learning approach for signal identification in the fluid injection process during hydraulic fracturing using distributed acoustic sensing data

Yikang Zheng[1,2], Yibo Wang[1,2]*, Xing Liang[3], Qingfeng Xue[1,2], Enmao Liang[4], Shaojiang Wu[1,2], Shujie An[5], Yi Yao[1,2], Chen Liu[3] and Jue Mei[3]

[1]Key Laboratory of Petroleum Resource Research, Institute of Geology and Geophysics, Chinese Academy of Sciences, Beijing, China, [2]Innovation Academy for Earth Science, Chinese Academy of Sciences, Beijing, China, [3]PetroChina Zhejiang Oilfield Company, Hangzhou, China, [4]China State Shipbuilding Corporation, Limited 715th Research Institute, Hangzhou, China, [5]Optical Science and Technology (Chengdu) Ltd, Chengdu, China

Full-cycle and real-time monitoring of the wellbore flow during hydraulic fracturing is challenging in unconventional oil and gas development. In the past few years, distributed acoustic sensing (DAS) provides opportunities to measure the acoustic energy distribution along the entire horizontal well. It is a promising tool for real-time monitoring and understanding of the fluid injection process. However, the signal identification of effective flow in the wellbore from DAS data is cumbersome and prone to error. We propose a deep learning approach to solve this problem. The neural network is a combination of Convolutional Neural Networks (CNNs) and Bidirectional Long Short-Term Memory Networks (BiLSTM) to extract the spatial and temporal features from the DAS data. The trained model is applied to the field data collected in the horizontal well. The results demonstrate its capability for intelligent monitoring and real-time evaluation for hydraulic fracturing.

KEYWORDS
distributed acoustic sensing, deep learning, signal identification, convolutional neural networks, bidirectional long short-term memory

Introduction

Hydraulic fracturing operation in horizontal wells has become the most effective stimulation technology for unconventional, low-permeability reservoirs. Real-time evaluation of the fracturing process provides important information to design the unconventional-reservoir completion and improve production (Montgomery et al., 2010). The conventional monitoring methods, such as microseismic, time-lapse seismic, and pressure monitoring, are limited to coverage and resolution. Recently, distributed acoustic sensing (DAS) is emerging as a real-time downhole sensing

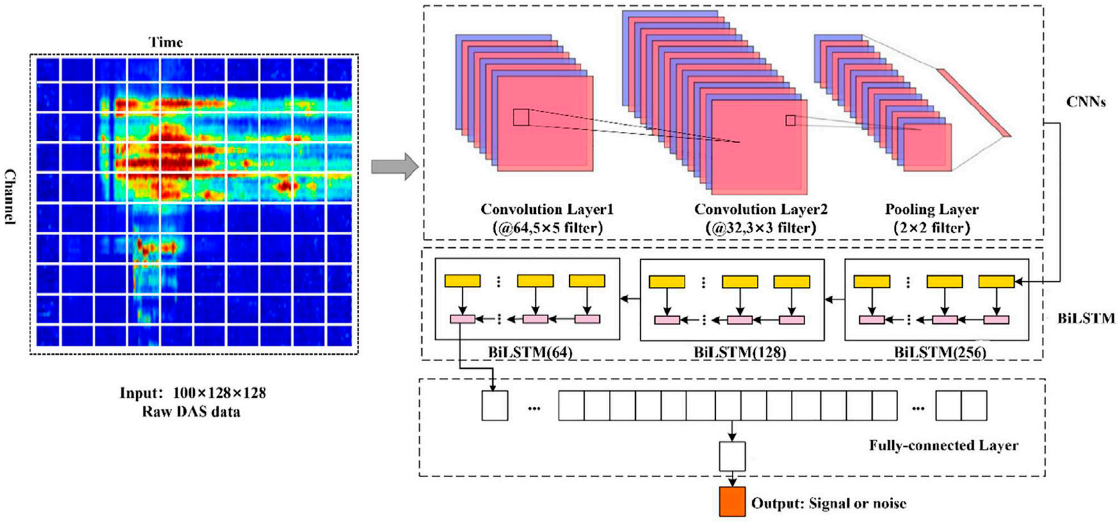

FIGURE 1
The schematic structure of the proposed network.

TABLE 1 The parameters used in the proposed network architecture.

Layer type	Parameter
INPUT LAYER	100 × 128 × 128
CONVOLUTION LAYER	64@5 × 5 (filter)
CONVOLUTION LAYER	32@3 × 3 (filter)
POOLING LAYER	2 × 2 (filter)
BILSTM LAYER	256
DROPOUT LAYER	0.5
BILSTM LAYER	128
DROPOUT LAYER	0.5
BILSTM LAYER	64
DROPOUT LAYER	0.5
FULLY-CONNECTED LAYER	100
FULLY-CONNECTED LAYER	1

technology. The fiber cable is installed permanently on the outside of a casing string and measures the vibration along the wellbore. In the DAS system, the interrogator unit transmits laser pulse along the cable, and the interferometer measures the changes in the Rayleigh back-scattering pattern associated with any deformation on the cable caused by incident waves (Mateeva et al., 2014; Spica et al., 2020). It is superior to other wellbore detection methods for real-time measurement, high spatial resolution and convenient deployment.

The high-density data recorded by the fiber cable in the injection well can directly show the fluid migration in the wellbore. Through the detailed surveillance of the fluid in the stimulation process, the design of commonly used plug-and-perf completion can be optimized. The operation parameters are chosen to achieve low-lost, high-efficiency production, such as fluid type, pumping method, injection volume, and adjustment of sand concentration (Jin et al., 2017; Richter et al., 2019). However, the manual analysis of DAS data is inefficient and prone to error. Applying machine learning or deep learning to this problem is an attractive solution. Jin et al. (2019) propose the artificial neural network (ANN) algorithm to identify fracture-hit signals from the DAS data recorded at offset monitor wells. Binder and Tura (2020) use convolutional neural networks (CNNs) to detect microseismic events in the downhole DAS data. Stork et al. (2020) shows the successful application of CNNs to microseismic event detection in DAS data. The purpose of this study is to identify the signal related to fluid injection in the borehole. The CNN is combined with Bidirectional Long Short-Term Memory Networks (BiLSTM) to extract the spatial and temporal features from the DAS data. The results demonstrate the feasibility and effectiveness of the proposed framework for large DAS data volume.

Methods

Convolutional Neural Networks (CNNs) is a class of feedforward neural networks that include convolution computation and non-linear activation operators (O'Shea and Nash, 2015). It is one of the representative algorithms of deep learning. CNNs are commonly used to analyze visual images. They are also known as motion-invariant or space-invariant

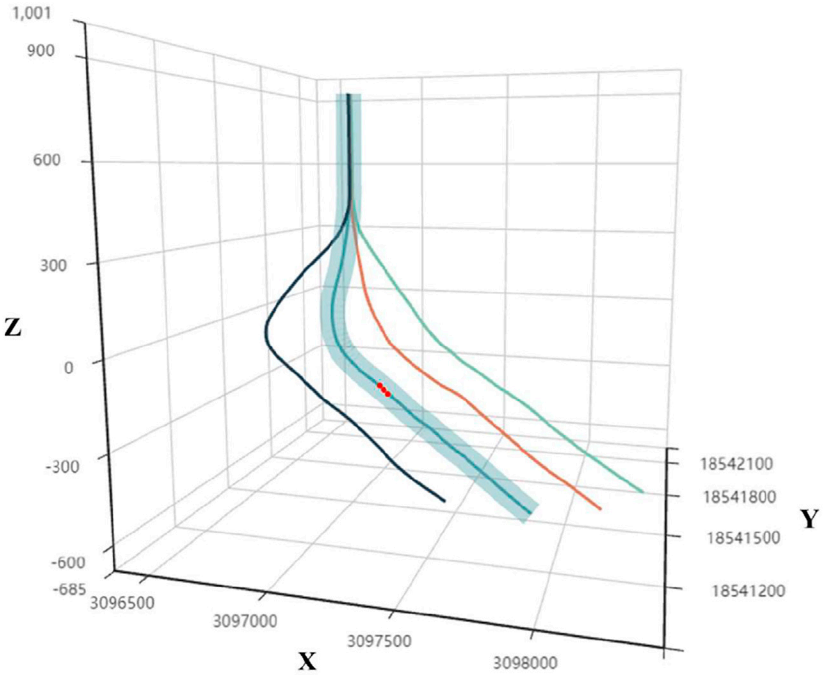

FIGURE 2
The geometry of the horizontal wells used to collect DAS data. The cable is deployed along Well 2 (blue line) and the red dots indicate the position of the data used in the application.

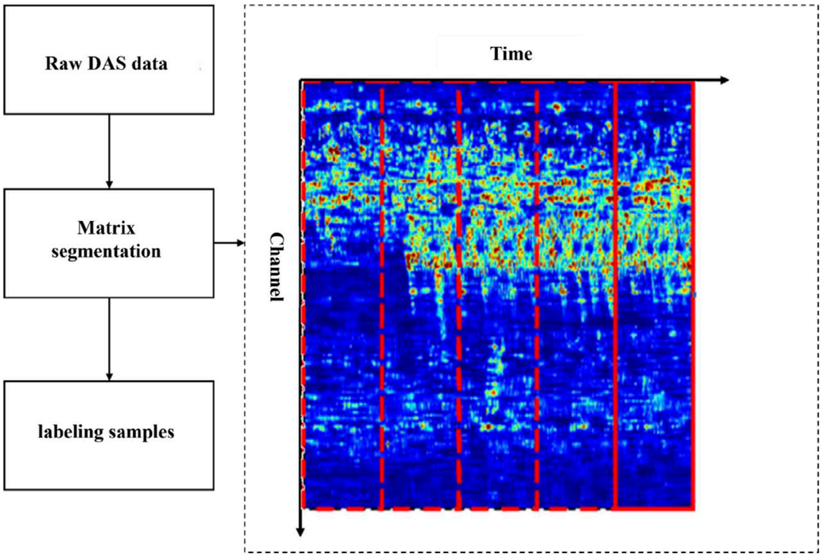

FIGURE 3
The process to generate the training and testing data sets.

artificial neural networks (SIANN) and are based on a shared weight structure of convolution kernels or filters that slide along input features and provide translation-equivalent responses. Counterintuitively, most CNNs are only equivariant to translation, not invariant. They have applications in image and video recognition, recommender systems, image

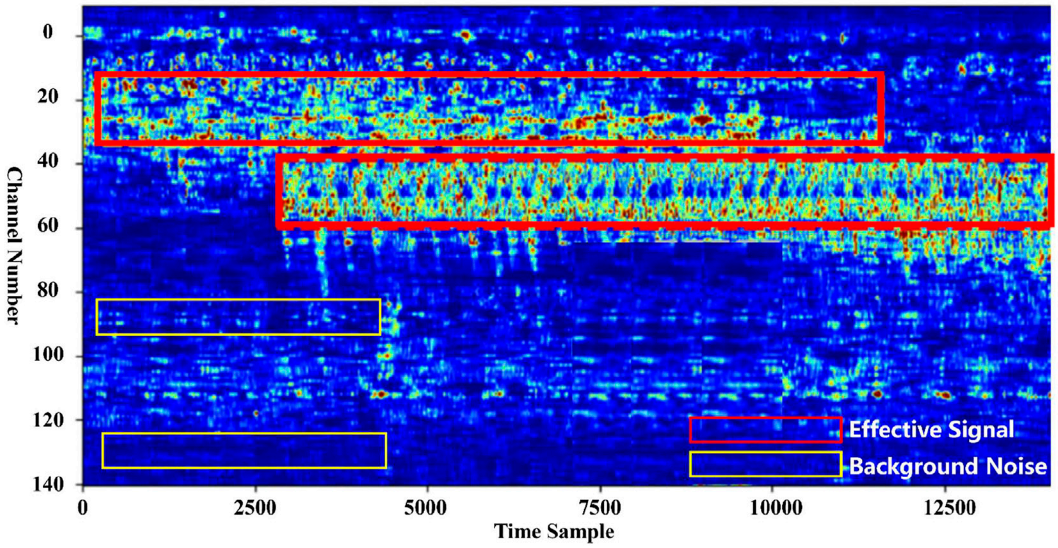

FIGURE 4
The typical labeled result of the raw data.

classification, image segmentation, medical image analysis, natural language processing, etc. (Gu et al., 2018).

As for the processing of time series data, such as the DAS data, recurrent neural networks (RNNs) is a very classic structure applied to data prediction (Medsker and Jain, 2001). It is used to find the relation of the data volume and predict the data within the corresponding context. However, due to its simple structure, RNNs suffer from gradient disappearance and gradient explosion when dealing with long-term sequence problems (Salehinejad et al., 2017). The Long Short-Term Memory (LSTM) networks are a type of neural network with stronger capability for time series prediction, which is developed from the RNNs (Hochreiter and Schmidhuber, 1997; Van Houdt et al., 2020). LSTM consists of one or more functional unit modules with forgettable and memory functions. This model is proposed to solve the problem that the traditional RNNs have the disappearance of backpropagation gradient in the long-term sequence. The core components of LSTM networks include forget, input, and output gates. LSTM networks are well suited for classification, processing and forecasting problems for time series data. Conventional RNN units and deep learning networks based on LSTM units cannot save the value of the previous time series due to the limitation of their basic structure, so they are better at predicting the next time step data with current data but lack the ability to predict a previous time step. For many sequence prediction problems, the time series data are bidirectional time-dependent. Thus RNNs and LSTM become inefficient in prediction ability. To overcome this limitation, bidirectional RNNs (BRNNs) make use of previous context by processing the data in both directions with two separate hidden layers, which are then fed forwards to the same output layer (Schuster and Paliwal, 1997). Combining BRNNs with LSTM gives bidirectional LSTM (BiLSTM), which can access long-range context in both input directions (Graves et al., 2013).

TABLE 2 The performance of the trained model on the testing dataset.

EDR	Far	F1 score	Response time (s)
0.951	0.026	0.926	1.78

CNNs is the well-known artificial neutral network and widely applied in image recognition, classification and segmentation. But it can only provide the mapping of spatial features from the input to the output. The DAS data are time series, and the temporal relations can not be learned and predicted by CNNs. RNNs are able to extract temporal dynamic characteristics but have limitations on memory cost. LSTM can be considered as an improved version of RNNs and is suitable to learn long-term dependencies. A Bidirectional LSTM (BiLSTM) is a model that consists of two LSTMs to receive the forward and backward information. It can effectively increase both preceding and subsequent information available to the network. In the processing of DAS data for signal identification, we combine the CNNs and BiLSTM to extract both the spatial and temporal features. The proposed model benefits from the advantages of CNNs and BiLSTM. The image features are captured by CNNs and the long-term dependency of the data is learned by the BiLSTM. Figure 1 shows the detailed scheme of the network architecture used in this study. The size of the input image is

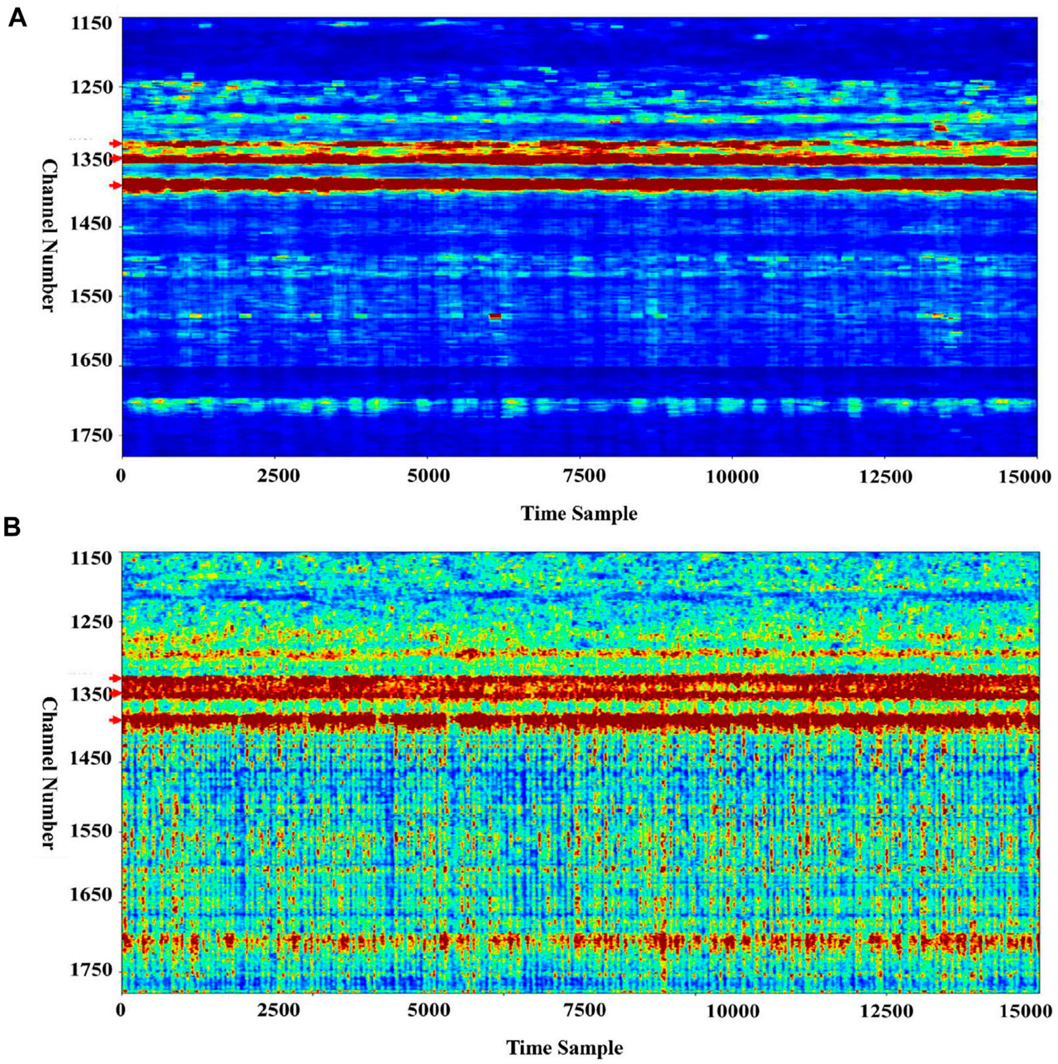

FIGURE 5
The raw DAS data with high **(A)** and low signal-to-noise ratio **(B)**.

128 x 128, as shown in Figure 1. 50% overlap is added to ensure that the continuous segmentation does not miss valid signals. The network model consists of CNN layers, BiLSTM layers and fully connected layers. The implementation of the proposed network is based on the *Python* deep learning API, Keras, which uses Tensorflow as the backend. These parameters are decided after we define the input and output, and optimized after several tests. Table 1 describes the specific structure and parameters of the network proposed in this paper in detail. The CNN layer focuses on extracting spatial feature information, the BiLSTM layer focuses on extracting time series features, and the fully connected layer is used to fuse the features extracted by the CNN layer and BiLSTM to achieve classification and recognition. The DAS data are divided into two types, effective injection signal and background noise. The input is the sequential DAS data, and the spatiotemporal characteristic is used to identify the fluid injection information. Firstly, the original data are segmented along the spatial and time axis to obtain the image with the size of 128 × 128. Then each sequence with 100 images in time are collected and used as the input. As the DAS response of fluid injection depends on the channel number and temporal step of the input DAS monitoring data, and the feature information obtained from different channels and time steps is highly correlated, the proposed network uses three BiLSTM layers successively to increase the ability of time series prediction and reduce the error in identification calculation. The problem involves the two-dimensional dynamic recognition problem both in space and time. The nonlinear conversion to linearization process

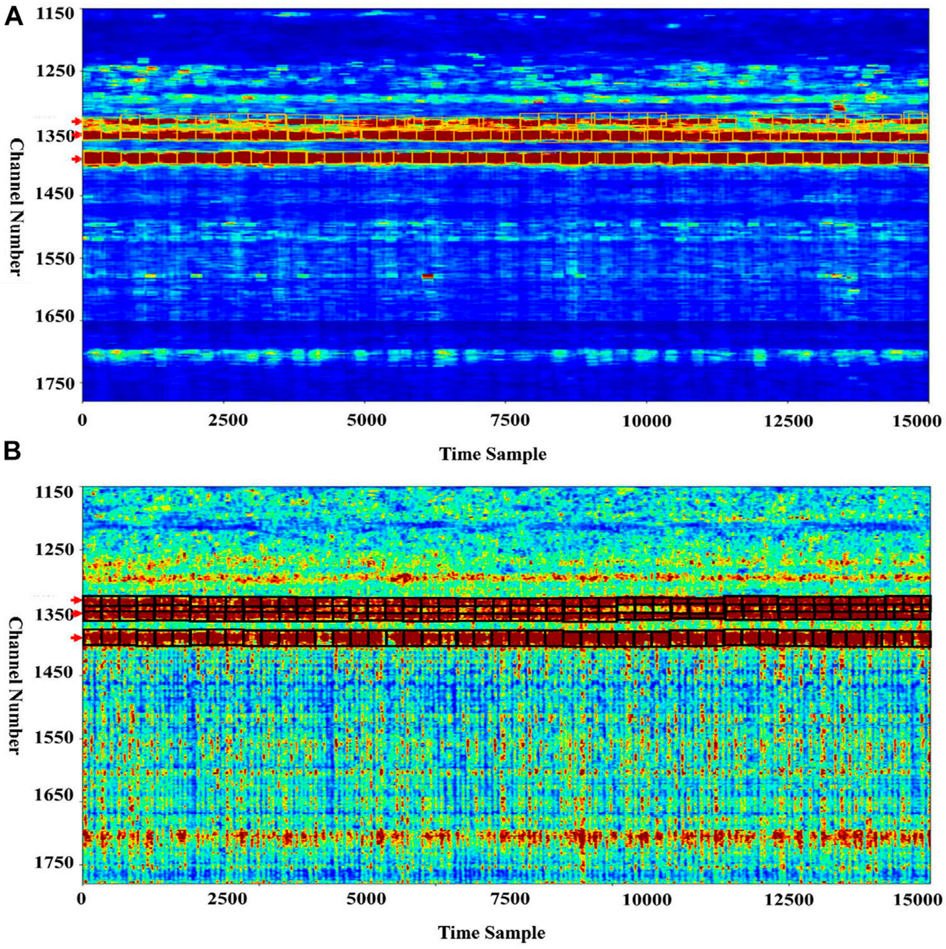

FIGURE 6
The signals related to fluid injection identified from the data shown in Figure 5.

in the fusion classification of space-time features is prone to errors (Tang et al., 2021), thus we add a fully connected network to improve the conversion performance. This modification can optimize computational efficiency and reduce the over-fitting phenomenon.

Training data

The DAS system is deployed along the injection well in the shale gas field. The monitoring geometry is shown in Figure 2. The length of the cable is approximately 2.5 km. The spatial resolution is 1 m and the temporal interval is 0.25 ms. Figure 3 shows the processing steps of the raw data. The data is segmented along the time and channel axis, respectively. The datasets are selected from the recorded data of three wells at the same site in about 1 month. With the recorded data, the data are labeled manually by visual inspection to generate the training dataset. Figure 4 shows the typical labeled result of the data slice. After the manual labeling, the dataset are separated into training dataset and testing dataset with a ratio of 8:2.

Network training

The goal of signal detection for fluid injection in hydraulic fracturing is to establish a rapid real-time evaluation and response system with high accuracy and high sensitivity. The following parameters are used to judge the performance of the trained model.

1) Effective detection rate (EDR)

The ratio of the effective signal detected, which is equal to the recall rate. It is calculated as follows:

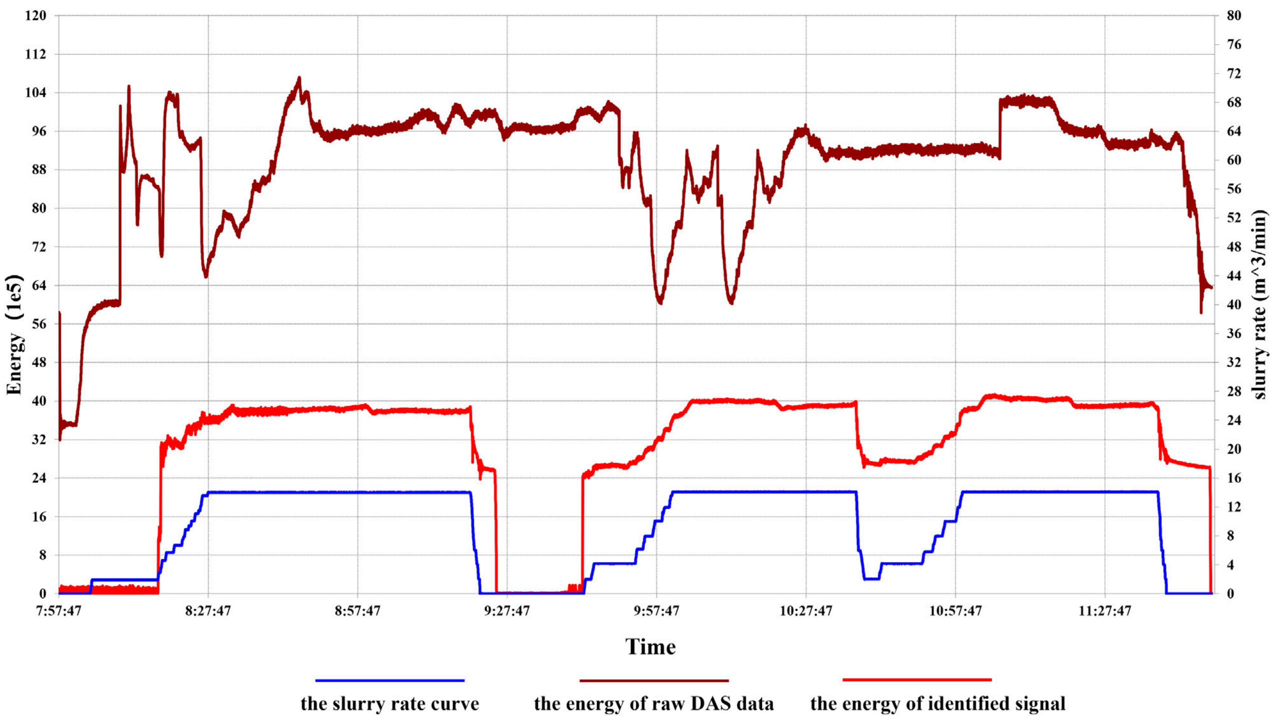

FIGURE 7
The comparison of the accumulation of DAS energy with the slurry rate curve of the well (blue line). The Red line denotes the results of the raw DAS data, and the ochre line denotes the results of the identified signals using the proposed model.

$$EDR = \frac{TP}{TP + FN}$$

where TP is the true positives, which refers to the number of correct detections for signals triggered by the trained network. FN is the false negatives, which refers to the number of wrong identifications for noise.

2) False alarm rate (FAR)

The ratio of false and correct identified signals of fluid injection, which is

$$FAR = \frac{TP}{TP + FP}$$

where FP is the false positives, which refers to the number of wrongly indication for effective injection signals.

3) F1 score

A measure that combines precision and recall, which is also the harmonic mean of precision and recall

$$F1 = \frac{2\,EDR\,(1 - FAR)}{EDR + (1 - FAR)}$$

4) Response time

This parameter is used to indicate the time consuming of the proposed workflow. It is the time difference between the time of the first sample and the output time of the first identified effective injection signal.

Using the training dataset, we obtained the proposed model and used the testing dataset to validate its performance. The results are shown in Table 2. EDR is used to evaluate the precision of the identification model, FAR is used to indicate the missing of effective signals. F1 score is the overall evaluation using evenly weighted recall and precision. The results shows the trained model can effectively identify the signal from the raw data and the processing time can meet the requirements for real-time monitoring. On the computation node with four Nvidia Titan (Pascal) GPUs, it took about 5 days for the training.

Application to field data

In the application, the collected data in different stages that are not included in the training and testing datasets are used. Figure 5 shows the data slices with relatively high and low signal-to-noise ratio, respectively. Using the trained model for identification, the results are shown in Figure 6. It can be observed from the identification results that the signals related to fluid injection are identified with high accuracy.

To further demonstrate the validity of the proposed model, the accumulated energy (the square of amplitude) of the recorded data is compared with the production curve. Figure 7 shows the results. In the conventional method of directly accumulating energy in the full record, the DAS response is inconsistent with the slurry rate curve, which is mainly due to the continuous background noise during the monitoring process. The results based on the identified DAS response can accurately fit with the slurry rate curve, as the extract DAS responses are directed related to fluid injection procedure. The model works effectively for the data collected at the same area as the validate data are similar to the training data. But it may need to be updated when the data have different characteristics. With more DAS data, the performance of the trained model can be further improved. The new deep learning algorithms developed for action recognition in video signals can also be introduced to improve the efficiency of the proposed method.

Conclusion

We propose a deep-leaning approach for real-time evaluation of raw DAS data to identify the signals related to fluid injection in hydraulic fracturing. The trained model demonstrates its effectiveness and accuracy in application to field data. The effective detection rate of injection signal is 95.1%, which enables real-time evaluation of hydraulic fracturing operation from downhole DAS data. The structure combing CNNs and BiLSTM performs reasonably well in spatiotemporal signal classification. The current models can be further improved in practical applications with more DAS data and better action recognition strategies.

Data availability statement

The data analyzed in this study is subject to the following licenses/restrictions: Data associated with this research are confidential and cannot be released. Requests to access these datasets should be directed to zhengyk@mail.iggcas.ac.cn.

Author contributions

YZ performed the data analysis. YZ and YW wrote and revised the manuscript. YW and XL provided the research ideas and supervised the findings of this work. QX, EL, SW, SA, YY, CL, and JM collected the original dataset and performed the preprocessing. All authors discussed the results and contributed to the final manuscript.

Funding

This study was funded by the CAS Project for Young Scientists in Basic Research (Grant No. YSBR-020), and the National Natural Science Foundation of China (Grant No. 42025403).

Acknowledgments

We would like to thank three reviewers for their valuable comments that improved this manuscript significantly.

Conflict of interest

Authors XL, CL and JM were employed by the company PetroChina Zhejiang Oilfield Company. Author EL was employed by the company China State Shipbuilding Corporation, Limited 715th Research Institute, Author SA was employed by the company Optical Science and Technology (Chengdu) Ltd.

The remaining authors declare that the research was conducted in the absence of any commercial or financial relationships that could be construed as a potential conflict of interest.

Publisher's note

References

Binder, G., and Tura, A. (2020). Convolutional neural networks for automated microseismic detection in downhole distributed acoustic sensing data and comparison to a surface geophone array. *Geophys. Prospect.* 68 (9), 2770–2782. doi:10.1111/1365-2478.13027

Graves, A., Mohamed, A.-r., and Hinton, G. (2013). "Speech recognition with deep recurrent neural networks," in *IEEE international conference on acoustics, speech and signal processing* (IEEE). paper presented at 2013.

Gu, J., Wang, Z., Kuen, J., Ma, L., Shahroudy, A., Shuai, B., et al. (2018). Recent advances in convolutional neural networks. *Pattern Recognit.* 77, 354–377. doi:10.1016/j.patcog.2017.10.013

Hochreiter, S., and Schmidhuber, J. (1997). Long short-term memory. *Neural Comput.* 9 (8), 1735–1780. doi:10.1162/neco.1997.9.8.1735

Jin, G., Mendoza, K., Roy, B., and Buswell, D. G. (2019). Machine learning-based fracture-hit detection algorithm using LFDAS signal. *Lead. Edge* 38 (7), 520–524. doi:10.1190/tle38070520.1

Jin, G., and Roy, B. (2017). Hydraulic-fracture geometry characterization using low-frequency DAS signal. *Lead. Edge* 36 (12), 975–980. doi:10.1190/tle36120975.1

Mateeva, A., Lopez, J., Potters, H., Mestayer, J., Cox, B., Kiyashchenko, D., et al. (2014). Distributed acoustic sensing for reservoir monitoring with vertical seismic profiling. *Geophys. Prospect.* 62 (4), 679–692. doi:10.1111/1365-2478.12116

Medsker, L. R., and Jain, L. (2001). *Recurr. neural Netw. Des. Appl.* 5, 64.

Montgomery, C. T., and Smith, M. B. (2010). Hydraulic fracturing: History of an enduring technology. *J. Petroleum Technol.* 62 (12), 26–40. doi:10.2118/1210-0026-jpt

O'Shea, K., and Nash, R. (2015). An introduction to convolutional neural networks. Available at: https://arxiv.org/abs/1511.08458 (Accessed November 26, 2015).

Richter, P., Parker, T., Woerpel, C., Wu, Y., Rufino, R., and Farhadiroushan, M. (2019). Hydraulic fracture monitoring and optimization in unconventional completions using a high-resolution engineered fibre-optic Distributed Acoustic Sensor. *First break* 37 (4), 63–68. doi:10.3997/1365-2397.n0021

Salehinejad, H., Sankar, S., Barfett, J., Colak, E., and Valaee, S. (2017). Recent advances in recurrent neural networks. Available at: https://arxiv.org/abs/1801.01078 (Accessed December 29, 2017).

Schuster, M., and Paliwal, K. K. (1997). Bidirectional recurrent neural networks. *IEEE Trans. Signal Process.* 45 (11), 2673–2681. doi:10.1109/78.650093

Spica, Z. J., Perton, M., Martin, E. R., Beroza, G. C., and Biondi, B. (2020). Urban seismic site characterization by fiber-optic seismology. *J. Geophys. Res. Solid Earth* 125 (3), e2019JB018656. doi:10.1029/2019JB018656

Stork, A. L., Baird, A. F., Horne, S. A., Naldrett, G., Lapins, S., Kendall, J.-M., et al. (2020). Application of machine learning to microseismic event detection in distributed acoustic sensing data. *Geophysics* 85 (5), KS149–KS160. doi:10.1190/geo2019-0774.1

Tang, J., Xia, H., Zhang, J., Qiao, J., and Yu, W. (2021). Deep forest regression based on cross-layer full connection. *Neural comput. Appl.* 33 (15), 9307–9328. doi:10.1007/s00521-021-05691-7

Van Houdt, G., Mosquera, C., and Nápoles, G. (2020). A review on the long short-term memory model. *Artif. Intell. Rev.* 53 (8), 5929–5955. doi:10.1007/s10462-020-09838-1

frontiers | Frontiers in Earth Science

TYPE Original Research
PUBLISHED 03 October 2022
DOI 10.3389/feart.2022.991964

EDITED BY
Yibo Wang,
Institute of Geology and Geophysics
(CAS), China

REVIEWED BY
Yikang Zheng,
Institute of Geology and Geophysics
(CAS), China
Wuqun Li,
Innovation Academy for Precision
Measurement Science and Technology
(CAS), China

*CORRESPONDENCE
Takahiro Nakajima,
tnak06@rite.or.jp

†These authors have contributed equally to this work

SPECIALTY SECTION
This article was submitted to
Solid Earth Geophysics,
a section of the journal
Frontiers in Earth Science

RECEIVED 12 July 2022
ACCEPTED 07 September 2022
PUBLISHED 03 October 2022

CITATION
Nakajima T, Miyoshi T, Hashimoto T and Xue Z (2022), Case study on amplitude and phase response comparison between DAS and 3C geophone VSP surveys at a test site in Japan.
Front. Earth Sci. 10:991964.
doi: 10.3389/feart.2022.991964

Case study on amplitude and phase response comparison between DAS and 3C geophone VSP surveys at a test site in Japan

Takahiro Nakajima[1,2*†], Takayuki Miyoshi[1,2†],
Tsutomu Hashimoto[1,2†] and Ziqiu Xue[1,2†]

[1]Geological Carbon Dioxide Storage Technology Research Association, Kyoto, Japan, [2]Research Institute of Innovative Technology for the Earth (RITE), Kyoto, Japan

Distributed acoustic sensing (DAS) is an effective tool for seismic surveys and is widely used as the preferred sensor for acquiring dense Vertical Seismic Profile (VSP). However, DAS has some disadvantages compared to conventional geophone acquisition, such as single-component data, sensor directivity pattern, low S/N, etc. To apply DAS data to VSP processing, it is important to understand the characteristics of DAS measurements. This study first examined DAS and geophone responses for a VSP survey in a 1D earth model. The relationship of signal amplitude as a function of incident angle and phase shift between wavelets was confirmed. Next, we validated this relationship in a walk-away VSP survey, which was conventionally applied to monitor geological CO_2 storage. The survey was carried out at a test site in Japan. We obtained both three-component (3C) geophone and DAS data using a single-mode fiber installed behind a casing. The observed amplitudes of the first P-waves by DAS and geophone showed very good agreement with the theoretical expectations. Finally, we performed imaging using acquired DAS data following the workflow for conventional VSP processing. These basic behaviors of DAS are useful for designing further analyses, such as VSP in deviated wells and full waveform inversion.

KEYWORDS

distributed acoustic sensing (DAS), DAS sensitivity, relationship between DAS and geophone, walk-away VSP, monitoring by DAS

1 Introduction

Fiber-optic sensors (FOS) have been developed as advanced measurement tools. Many findings in geophysical applications have been reported in the oil and gas industries, as reviewed in Fenta et al. (2021). These applications include sensing pressure, temperature, vibration, and strain. In particular, distributed acoustic sensing (DAS) has been exploited for seismic exploration surveys during the past decade.

DAS utilizes optical time-domain reflectometry (OTDR) techniques to detect seismic waves along a fiber-optic cable. A pulse of laser light is transmitted from one end of an optical fiber; coherent, back-scattered Rayleigh light is recorded by an optical interrogator at the same end of the fiber. From the observed time of arrival of the returning light, the points passing the seismic waves can be determined (Molenaar, 2013). When a second laser pulse is fired into the fiber, changes in strain are evaluated by comparing the two records (Grindei 2019).

DAS measurements have been applied in mining, geothermal studies, natural earthquake detection, and hydraulic fracturing (Ajo-Franklin et al., 2019; Bakku et al., 2014a; Bakku et al., 2014b; Li and Zhan, 2018). DAS is now used for observation in marine environments using fibers for telecommunications deployed on the seabed (Spica et al., 2021). DAS technology is also popular for seismic data acquisition, especially in wellbores (Lellouch and Biondi, 2021). P-wave observation in less noisy environments can be expected from fibers deployed in vertical wells. A Vertical Seismic Profile (VSP) survey using DAS was assessed to possibly replace conventional surveys with geophones (Mestayer et al., 2011). Reports on VSP (Barberan et al., 2012; Willis et al., 2016; Wu et al., 2017), CO_2 plume imaging by DAS-VSP (Daley et al., 2016; Miller et al., 2016; Harris et al., 2017; Cheraghi et al., 2018; Correa et al., 2018), and micro-seismic monitoring (Maxwell, 2014; Molteni et al., 2017; Karrenbach et al., 2019) have recently been published.

However, a large disadvantage of borehole DAS measurement is that only a single component can be acquired along the fiber. Moreover, DAS data on the strain or strain rate is the average over the a gauge length (Dean et al., 2016). These disadvantages introduce a sensitivity issue depending on the incident angle of a wavefield. Theoretically, the amplitude ratio of DAS over a single component of particle velocity exhibits cosine dependency as a function of the incident angle. This relationship indicates a drawback of DAS measurements of waves with large incident angles. Furthermore, comparisons of DAS and single-component geophone data have been reported in some field observations (Willis et al., 2016; Correa et al., 2017; Wu et al., 2017). In these comparisons, the basic trend followed the theoretical relationship; however, amplitude ratios in field data were very noisy. These results suggested that the relationship between DAS and geophone amplitudes in field data has not yet been fully demonstrated.

Another problem is differences in interrogator design. While some comparisons of DAS outputs among several vendors (Verliac et al., 2015; Olfsson and Martinez, 2017; Sidenko et al., 2020). Verliac et al. (2015) reported differing wavelets among three DAS datasets acquired with equipment from various suppliers, Olfsson and Martinez (2017) observed that differences among vendors were small. Sidenko et al. (2020) confirmed that the dimensions of interrogator output were deformation rate and dynamic strain, which are the output designed by the vendors. Therefore, signal directivity differed among interrogators.

Because of issues concerning differences in the averaged values or point sources and dimensional differences between DAS and conventional seismometers, it is critical to understand what is measured, and what limitations apply to those DAS measurements for a given interrogator unit. In further analysis, data conversion might be necessary to adjust data dimensions.

The present study compared DAS and conventional geophone data in a field survey conducted in Japan. In Section 2, we examine the theoretical relationship between strain rate and particle velocity that are observable by conventional geophone. In Section 3, we compute a synthetic wavefield at vertical observation points in layered models. We then compared the wavefield of direct P-waves measured by Vz and the vertical components of the strain rate. In Section 4, we introduce a test field for DAS measurements in Japan. During a walk-away VSP survey at this site, we collected both DAS and three-component (3C) geophone data at a borehole. From these data, we examined the sensitivity of the sensors against the incident angles by comparing the signal amplitudes of the direct P-waves. We also studied the resolution of imaging results obtained by standard VSP data analysis.

2 Theory of DAS measurements

In strain rate measurements for DAS output, the output is proportional to the strain rate averaged over a gauge length. This is the same as Silixa's iDAS (Willis et al., 2020). Bakku (2015) reported that this type of output can be interpreted as the difference in velocities measured by two separated geophones. We followed their method to compute the theoretical strain rate in this study.

As many have noted, DAS measurements depend on gauge length (G) and pulse width (L) (Dean et al., 2016; Correa et al., 2017). In the following analysis, we assume that the wavelength of elastic waves is several times larger than the G and L. The DAS output for an optical fiber installed in a vertical borehole is represented by the difference in the strain at the internal sampling interval (Parker et al., 2013; Daley et al., 2016).

$$\left[\boldsymbol{u_z}\left(\boldsymbol{z_0}+\frac{\boldsymbol{G}}{\boldsymbol{2}},\boldsymbol{t_0}+\boldsymbol{dt}\right)-\boldsymbol{u_z}\left(\boldsymbol{z_0}-\frac{\boldsymbol{G}}{\boldsymbol{2}},\boldsymbol{t_0}+\boldsymbol{dt}\right)\right]\Big/\boldsymbol{G}-\left[\boldsymbol{u_z}\left(\boldsymbol{z_0}+\frac{\boldsymbol{G}}{\boldsymbol{2}},\boldsymbol{t_0}\right)-\boldsymbol{u_z}\left(\boldsymbol{z_0}-\frac{\boldsymbol{G}}{\boldsymbol{2}},\boldsymbol{t_0}\right)\right]\Big/\boldsymbol{G} \tag{1}$$

where $u(z_0, t_0)$ is the dynamic displacement of the fiber at the location z_0 and measurement time t_0, respectively. When the sampling interval and gauge length are sufficiently smaller than the phenomena being considered, this output can be converted to either the strain rate of the fiber

$$\frac{\partial}{\partial \boldsymbol{t}}\left(\frac{\partial \boldsymbol{u_z}}{\partial \boldsymbol{z}}\right)_{\boldsymbol{z_0},\boldsymbol{t_0}}=\dot{\boldsymbol{\varepsilon}}_{\boldsymbol{zz}}(\boldsymbol{z_0},\boldsymbol{t_0}), \tag{2}$$

or the spatial derivative of the dynamic displacement of the fiber

$$\frac{\partial}{\partial \boldsymbol{z}}\left(\frac{\partial \boldsymbol{u_z}}{\partial \boldsymbol{t}}\right)_{\boldsymbol{z_0},\boldsymbol{t_0}}=\left(\frac{\partial \boldsymbol{v_z}}{\partial \boldsymbol{z}}\right)_{\boldsymbol{z_0},\boldsymbol{t_0}}, \tag{3}$$

where ε_{zz} is the axial strain, v is the particle velocity at a fixed point, and the dot denotes its time derivative. Eqs 2, 3 show the relationship between DAS measurements (strain rate) and standard geophone measurements (particle velocity).

We consider a primary seismic plane wave propagating in the z-direction with an apparent velocity c (or slowness $s = 1/c$) and an angular frequency ω. Then the displacement and velocity field of the seismic wave is written as

$$u_z(z,t) = ue^{-i(\omega t - k_z z)} = ue^{-i\omega t} e^{i\omega z/c}, \tag{4}$$

$$v_z(z,t) = (-i\omega) ue^{-i(\omega t - k_z z)} = (-i\omega) ue^{-i\omega t} e^{i\omega z/c}, \tag{5}$$

where u is the constant displacement equal to $u_z(0,0)$, and k_z is the vertical component of the wavenumber. From the equations with wavenumber, the relationship between the strain rate and particle velocity is represented as follows (Bakku, 2015),

$$\dot{\varepsilon}_{zz} = \frac{\partial v_z}{\partial z} = ik_z v_z = \frac{i\omega \cos\theta}{V} v_z. \tag{6}$$

where V is the inherent velocity in the medium. Thus, the amplitude of strain rate has a cosine dependency on the incident angle of the seismic wave compared to geophone data. In contrast, Daley et al. (2016) found that the dynamic strain and particle velocity could be linked from the equations with the apparent velocity:

$$\varepsilon_{zz} = -v_z/c. \tag{7}$$

This equation indicates that the strain rate amplitude depends on the apparent velocity in the z direction. Daley et al. (2016) applied this conversion to limited interval data, where the apparent velocity is a constant. This relationship suggests that the amplitude would be changed in layers with different apparent velocities. Another point in the comparison of Eqs 6, 7 is that time integration is needed as the first step to convert strain rate data to an equivalent geophone signal.

We can also derive the relationship between the strain rate and the total amplitude of the particle velocity. The sine v_z component is proportional to $|v_r|\cos\theta$; therefore, the relationship becomes

$$\varepsilon_{zz} = -|v_r|\cos^2\theta/V. \tag{8}$$

A more sophisticated transformation between DAS and geophone data was proposed by Bona et al. (2017) by considering the effects of gauge length and pulse width. Their evaluation is a kind of two-spatial averaging filter, and the amplitude ratio between DAS and geophone depends on the wavelength of the seismic field compared to the gauge length. This filter was applied to field data by Correa et al. (2017). Although the effect of gauge length is important in DAS measurement, the present study does not consider gauge length correction in its evaluation of the effect of depth-dependent apparent velocity in the DAS—geophone data conversion.

3 Comparison of DAS and geophone data using synthetic wave computation

We compared geophone and DAS data by calculating the seismic wavefield using a synthetic method. We first simulated the wavefield from a point source on layered earth models. Based on the observation points in a wellbore, the velocity fields at 5-m depth intervals were calculated. From the obtained velocity field, the strain rate $\dot{\varepsilon}_{zz}$ along a borehole was calculated as the difference in v_z between two observation points. We then compared the wavefields of the strain rates and particle velocities.

To simulate a synthetic wavefield, we used “grpnt2” developed by Hisada (1994); Hisada (1995). This code calculates the strict Green’s function theoretically in layered half-space and uses an efficient mathematical method for wavenumber integrations. The wavefield excited by a Ricker wavelet with a 20-Hz dominant frequency was obtained in the frequency domain using this code. As the time domain wavefield was a bit noisy due to the transformation from the frequency domain to the time domain, we applied a bandpass filter to reduce artificial vibrations.

We tested three earth models to compare DAS and geophone responses: homogeneous, a layer model without an impedance jump, and a layer model with an impedance jump. To simplify the comparison among models, the parameters at the upper layer were identical. The parameters of the synthetic model are summarized in Table 1.

3.1 Homogeneous model

First, we computed the wavefield in a homogeneous half-space model. Density was set to 1,400 m/s for Vp, 808 m/s for Vs, and 2.1 kg/m^3. We placed vertical sources at points 100 and 500 m horizontally from the wellbore. We introduced two source points because we encountered difficulties in following the first P-wave at shallower receivers (low incident angle). The P- and S-waves become too close to separate and were also affected by surface Rayleigh waves. These mixed waves cannot be regarded as a simple plane wave. Therefore, we excluded data from receivers shallower than 100 m in subsequent analysis. Then, the range of incident angles became limited at near offset (100 m) data. To cover the incident angle for the comparison between DAS and geophone data, we added far offset (500 m) results.

Figure 1 shows the wavefield in the synthetic homogeneous model in the case of a 500-m offset. To clearly show the wavefield, the time axis was shifted to 0.2 s using the grpnt2 function. Figures 1A,B are shot gathers for particle velocity and strain rate, respectively. The event starting about 0.55 s with a downward bent is the direct P-wave, while that starting about 0.8 s

TABLE 1 Summary of the synthetic models.

Layer	Properties	Homogeneous	No impedance jump	With impedance jump
1	Vp (km/s)	1,400	1,400	1,400
	Vs. (km/s)	808	808	808
	Density (kg/m^3)	2.1	2.1	2.1
	Thickness (m)	—	252.5	252.5
2	Vp (km/s)	—	1,500	1,500
	Vs (km/s)	—	866	866
	Density (kg/m^3)	—	1.96	2.1

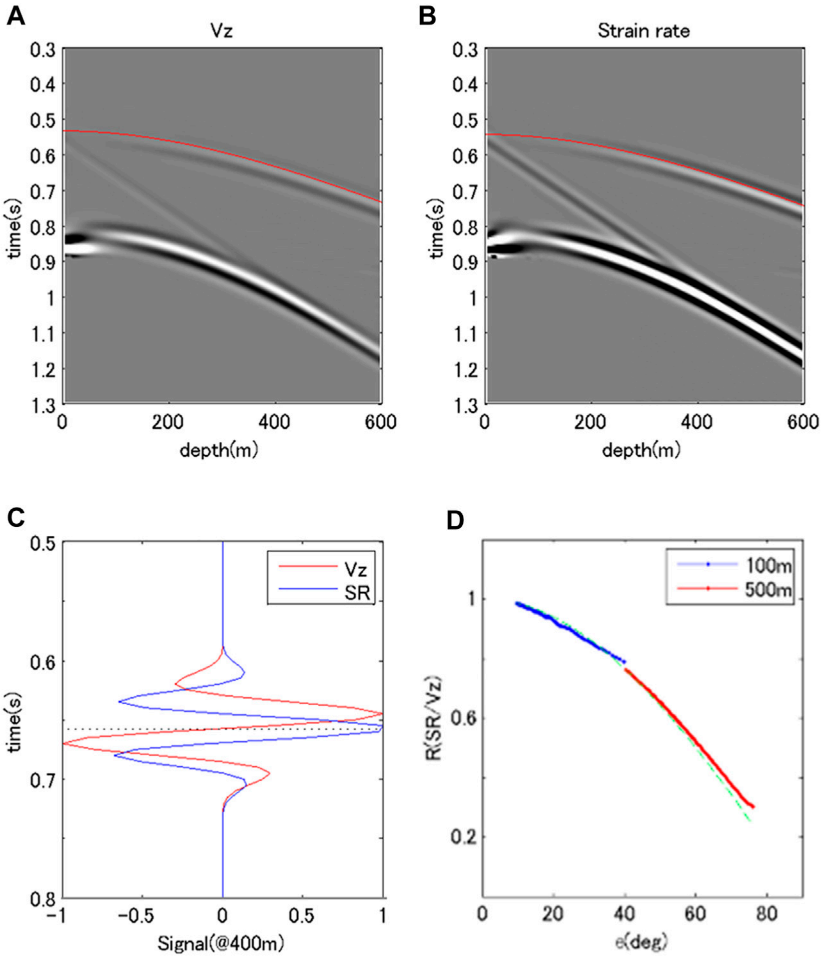

FIGURE 1
Characteristics of the synthetic wavefield in a homogeneous model. **(A,B)** show shot gather with the z components of the particle velocity and the calculated strain rate, respectively. Overlapping red lines correspond to the first P-wave. **(C)** shows the wavefields around the P-wave arrival by particle velocity (red) and calculated strain rate (blue) at a depth of 400 m. The amplitude was normalized with the maximum absolute value equal to 1. **(D)** represents the P-wave amplitude ratio of strain rate/particle velocity. The colored lines correspond to the difference in the source offset; blue: 100 m, red: 500 m. The green line is the reference of the cos θ dependency.

corresponds to the direct S-wave. The line connecting direct P- and S-waves represents the Rayleigh wave with a smaller propagation velocity than that of the S-wave excited at the surface. The directional dependency of amplitude is illustrated in this figure. The amplitude of the direct P-wave at shallower depths decreases since the wave path is close to the right angle to

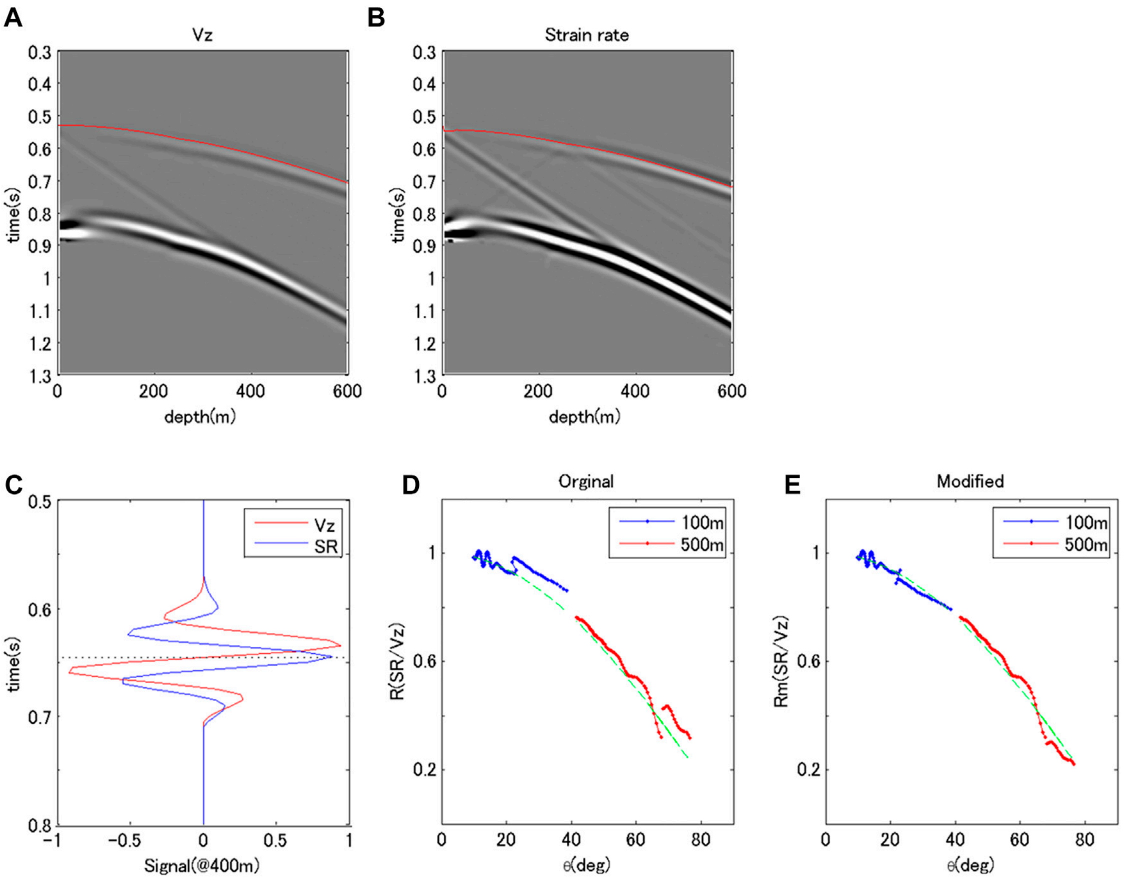

FIGURE 2
Characteristics of the synthetic wavefield in a layer mode without a difference in acoustic impedance. **(A–D)** use the same arrangement as in Figure 1. In wavefields shown in **(C)**, amplitude normalization is the same as in the homogeneous model. **(E)** shows the amplitude ratio modified by the effect of apparent velocity. The colors in **(E)** are the same as in **(D)**.

the measurement component. In contrast, the wavefield of the S-wave is perpendicular to the propagating direction; thus, the amplitude of the S-wave near the surface is larger than that of the P-wave. Figure 1C represents wavefields around the first break of the P-wave at a depth of 400 m for Vz and strain rate, although the amplitudes of the wavefields were normalized so that the maximum amplitude of the direct wave in the time domain is equal to 1. As Eq. 6 suggests, the wavelet of the particle velocity is close to the minimum phase, while that of the strain rate becomes zero phase. Figure 1D is the ratio of strain rate to particle velocity as a function of incident angle. The incident angle was simply evaluated by geometrical arrangement, and the amplitude ratio was normalized using the deepest point data to adjust the theoretical relationship ($\cos\theta$). This figure shows clear $\cos\theta$ dependencies; thus, this synthetic approach can be used to investigate the relationship between strain rate and particle velocity.

3.2 A layer model without impedance jump

Next, we computed the wavefield in a layer model without a jump in impedance. We studied this artificial case to consider the effects of differences in inherent velocity without impedance jump. Therefore, we set the parameters of the second layer to 1,500 m/s for Vp, 866 m/s for Vs, and 1.96 kg/m^3 for density at a boundary depth of 252.5 m. We also calculated the wavefield from the 100 and 500 m offsets.

Figure 2 shows the wavefields of this model for a 500-m offset. Figures 2A,B illustrate shot gathers for particle velocities and strain rates, respectively. The events in these figures are almost the same as those in Figures 1A,B. However, reflected and converted waves can be seen in Figure 2B at the point of 252.5 m and 0.6 s. These waves correspond to

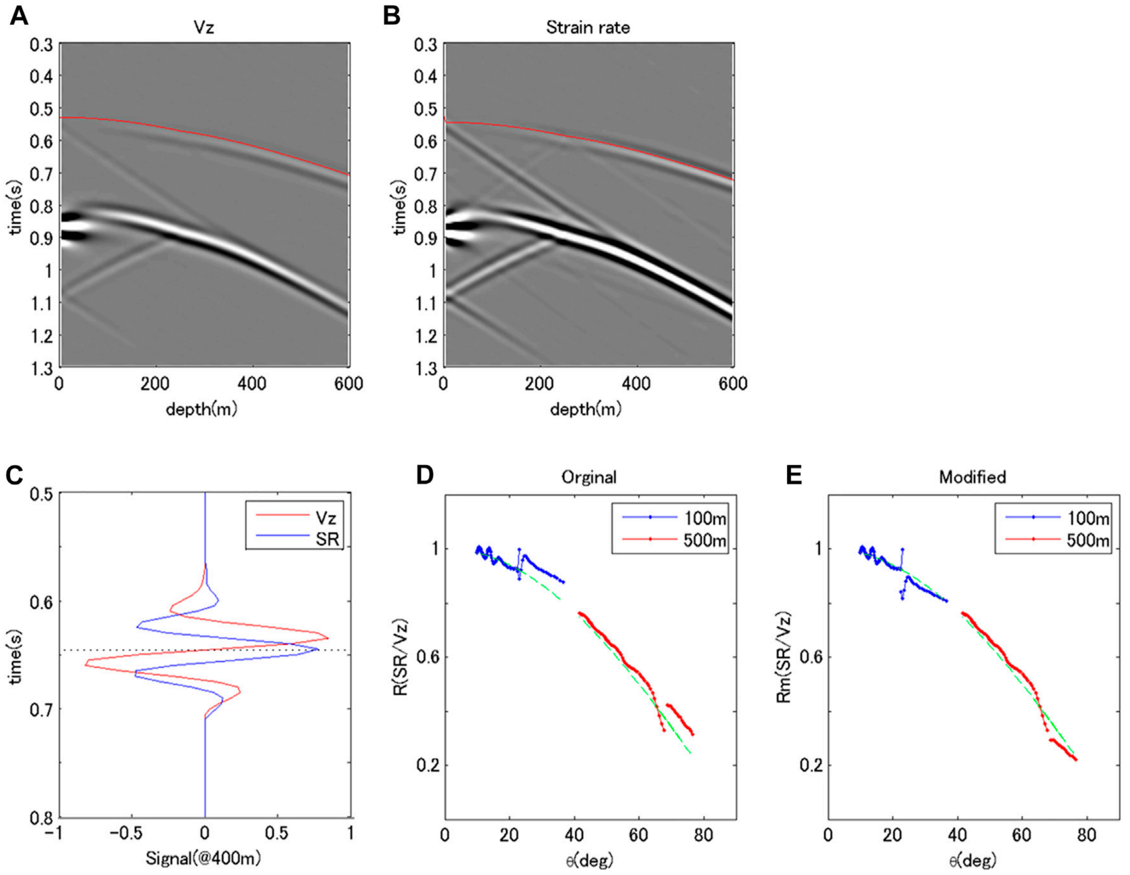

FIGURE 3
Characteristics of the synthetic wavefield in a layer mode with impedance change. **(A–E)** show the same arrangement as in Figure 2. In the wavefields shown in **(C)**, amplitude normalization is the same as in the homogeneous model.

converted P-S waves, where the properties of wave propagation were not the same as in the homogeneous model. Figure 2C shows normalized wavefields around the first P-wave (at 400 m) for strain rate and particle velocity. The features of the two wavefields are the same as those in Figure 1C. Figure 2D is the ratio of strain rate to particle velocity as a function of incident angle. The incident angle was evaluated by ray tracing between sources and receivers in the velocity model. The ratios at the two offsets differ above and below the layer boundary. From the part above the boundary, the ratios were close to the theoretical dependency, $\cos\theta$. However, for the parts below the boundary, the ratios became smaller. This difference comes from the relationship represented in Eq. 7. Thus, we modified the change of apparent velocity (Figure 2E). After the modification, the ratios were close to the theoretical dependencies.

3.3 A layer model with impedance jump

Finally, we computed the wavefield in a layer model with a jump in impedance. In this model, the amplitude of the wavefield decreased due to reflection at the layer boundaries. We used the same values as in the previous model, except for the density of the second layer (2.1 kg/m^3, as in the top layer).

Figure 3 shows the wave fields of this model for a 500-m offset. The shot gathers (A and B) show events similar to those in the previous models. Moreover, apparent reflected waves, especially S-S waves, appear at the point of 252.5 m and 0.9 s. The reflection at the surface is also evident. Figure 3C shows the normalized wavefields around the first P-wave (at 400 m) for strain rates and particle velocities. Although this reflected wave decreased the amplitude of the wavefield below the boundary, the amplitude ratio between strain ratio and particle velocity was the same, except for data near the boundary. Figures 3D,E are the ratios of strain rates to particle velocities before and after the modification of apparent velocity. The modification worked well to adjust the amplitude ratio between strain rate and particle velocity to the theoretical dependency of the incident angle.

The synthetic model confirmed the dependency of the incident angle in the amplitude ratio by modification of the apparent velocity. This was also noted by Daley et al. (2016).

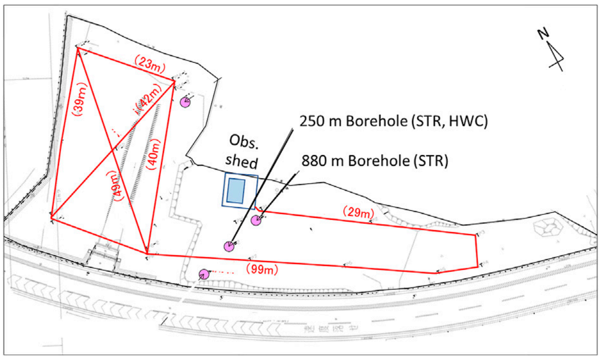

FIGURE 4
Overview of a test field for DAS field measurement in Chiba, Japan.

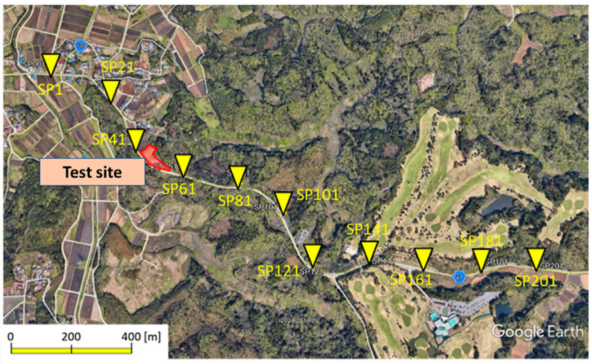

FIGURE 5
Positions of shot points and the observation site for a walk-away VSP conducted in January 2021.

However, many papers comparing the amplitude of DAS and geophone data did not consider this dependency. The next chapter introduces our field survey and shows the results using DAS.

4 A walk-away VSP survey in chiba, Japan

The results of a walk-away VSP survey at a site in Japan were used to compare DAS and geophone data. Although there was no expected subsurface change at this site, such as fluid injection, the results are a good reference for understanding the characteristics of DAS measurements and considering survey design using DAS-VSP.

4.1 Overview of the field survey

To conduct field experiments for DAS measurements, we have established a research site in Chiba Prefecture, Japan. This site has an 880-m, deep-cased borehole with a single-mode and single-end, straight, fiber-optic cable cemented behind the casing, a 250-m well in which a straight and a helically wound cable are cemented, and surface deployed cables buried in a shallow trench (Figure 4). These installed fibers were connected as a one-stroke sketch to measure the DAS signal with an interrogator located in an observation shed. This study focused on DAS data from this borehole to compare the sensitivity pattern against that of a conventional geophone.

A walk-away VSP experiment was carried out in January 2021. Eleven shot points were selected for the survey (Figure 5). Shot points up to 1,300 m away from the borehole were employed (Figure 5). At each shot point, a vibroseis truck was used, with an increased number of sweeps at far-offset points. Particle velocity was acquired *via* a 3C geophone tool with four downhole shuttles. The shuttle interval was 15 m. Therefore, with 21 deployments, we obtained data measurements every 7.5 m between depths of 100 and 700 m in the casing of the 880-m borehole. In contrast, a Silixa iDAS v2 interrogator unit was used for the DAS measurements. The data interval was set to ~1 m. Furthermore, DAS was available for data acquisition at every sweep of geophone measurements; thus, the total number of stacks at each shot point was approximately 100; 5 (sweeps) x 21 (geophone deployments). The data acquisition settings of the walk-away VSP survey are summarized in Table 2.

4.2 Comparison of observed wave data between DAS and geophone measurements

We first examined the signal-to-noise ratios (SNRs) between the DAS and geophone measurements. We simply compared the root-mean-square (RMS) between the direct P-wave signal and the duration before the first break. The seismic signal at each sweep was clearer in the geophone data. This noise floor of DAS data was higher than that of the geophone data. Figure 6 shows the SNR of DAS against stack numbers at SP121, offset 650 m, where the SNR of the geophone data was obtained by stacking five sweeps. The SNR of DAS increased when the stack number increased. When the number of stacks reached 100 for DAS at a 650-m offset and a 700-m depth, the SNRs were comparable to those of geophone data. This difference in the stack number was not disadvantageous for DAS. The geophone tool must be relocated to cover the entire length of the borehole, while DAS data can be acquired at all depths in a single sweep.

TABLE 2 VSP survey settings.

Source information

Source type	12,000 lbf EnviroVibe
Source sweep	10–100 Hz, Linear up-sweep
Sweep duration	12 s
Listing time	4 s
Force	75%, 30% (at SP1, SP21)
Source operator	OYO corporation
Number of shot points	11
Number of sweeps at one location	5, 10 (for geophone measurements)
DAS information	
Interrogator unit	Silixa iDAS v2
Fiber-optic cable	Single-mode straight fiber
Laser pulse ping rate	20 kHz
Sampling frequency	1,000 Hz
Sampling interval	1.020952 m
Pulse width	5 m (5 ns in time axis)
Gauge length	10 m
Geophone information	
Downhole tool	DS-150 (Geospace Technologies Corporation) with 4 downhole shuttles
Components in a shuttle	3 (X, Y, Z)
Center frequency of the sensor	15 Hz
Sampling frequency	1,000 Hz
Receiver step	7.5 m
Cramp to contact the casing	Magnetic

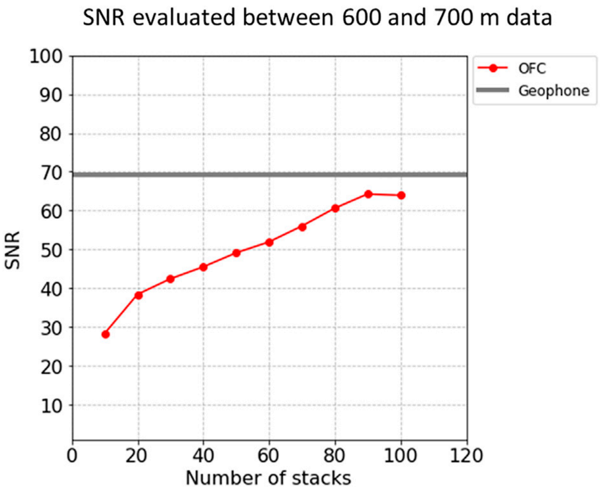

FIGURE 6
Comparison of SNR by geophone and DAS. Geophone data were evaluated by a stack of five sweeps and the effect of stacking to SNR is shown for DAS data.

Next, we compared the wavefields obtained with DAS and geophone. Figure 7 shows the wavefield and spectrum around the first P-wave at the SP121 shot point (offset 650 m) and recorded at 700 m. Unlike the results of the synthetic model, the wavelet at the direct P-wave of DAS and geophone data was close to the zero-phase case. However, the apparent first break time of the DAS data was earlier than that of the geophone data. The synthetic results and field data differences occurred due to the method of data deconvolution. The source signal was a linear sweep with a vibroseis, and the shot gathered was calculated by cross-correlation or source deconvolution. This process produces essentially zero-phase data. However, the difference in first break time may reflect the phase difference of the wavelets. As Daley et al. (2016) noted, the time integration procedure of DAS data can reduce the difference between DAS and geophone data.

After confirmation of the waveform of the direct P-wave, we compared the amplitudes of DAS and geophone data. We first evaluated the incident angle of the direct P-wave between shot points and receivers using 3C geophone data (Figure 8). This analysis did not use any special rock physics model to modify the observed amplitude. The horizontal direction and amplitude at each receiver potion were evaluated from particle motions of horizontal components of the geophone records. The incident angle was then calculated from the evaluated horizontal and vertical components of the geophone. The general trend of the

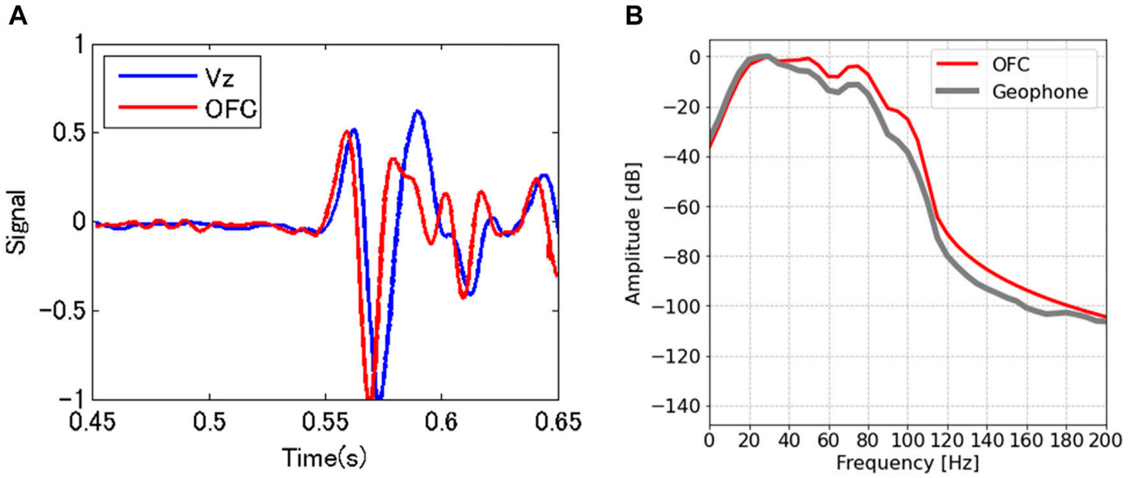

FIGURE 7
Comparison of DAS and geophone data shot at a 650-m offset and a 700-m depth. **(A)** Wavefield in the time domain. **(B)** Amplitude spectrum.

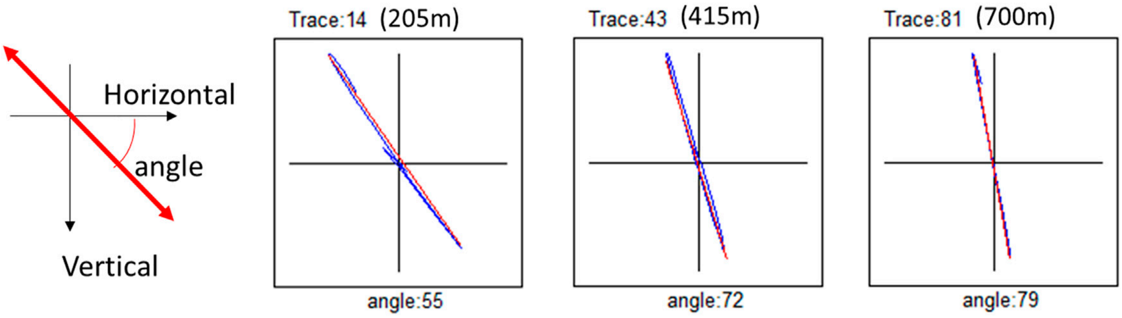

FIGURE 8
Evaluation of the incident angle evaluated by the three geophone components when the vibrator is shot at SP61. The locus is obtained from the time duration of the direct P-wave arrival.

incident angle (Figure 8) became steeper, as expected. This step provided a precise incident angle for the DAS amplitude trend against the angle and also allowed the comparison of DAS amplitude with both Vz and the total amplitude of the particle velocity. We also compensated for the difference in apparent velocity along the well, as shown in Eq. 7. Since the P-wave velocity generally increases with depth, the amplitude ratio without this modification increases at larger angles.

Figure 9 shows the ratios of DAS amplitude over Vz (A) and over the total amplitude of the particle velocity (B) against the incident angle. Dependencies are shown at all shot points against the theoretical dependencies on the incident angle; i.e., $\cos\theta$ for Vz and $\cos^2\theta$ for the total velocity field. The results show fairly good matching. At high incident angles (SP201), the data were smaller than the theoretical relationship owing to difficulties in evaluating small amplitude data from far offset data. Although there is a small inconsistency in the far offset data, we believe that this relationship is the most favorable result obtained in field DAS measurements.

4.3 Comparison of imaging results between DAS and geophone data

We evaluated imaging from DAS and geophone data, where only Vz components were used for geophone data processing.

First, we compared shot gathers of DAS and geophone stacked data. Figure 10 shows the shot gathers collected at each offset. In the near-offset geophone results, the noise was

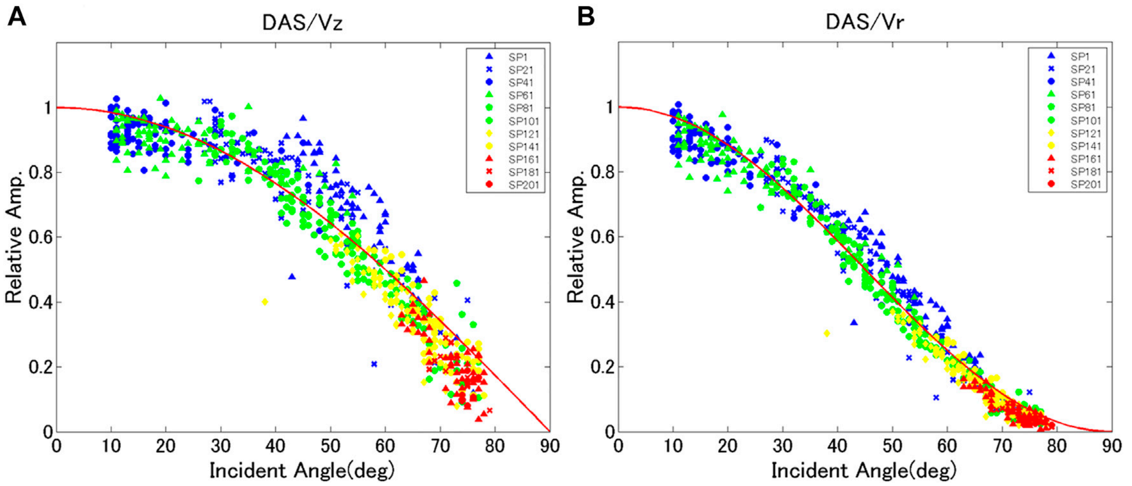

FIGURE 9
Incident angle dependency of DAS amplitude over the geophone amplitude evaluated by the direct P-wave. **(A)** Vz amplitude for geophone data. **(B)** Geophone total amplitude. The colors and markers correspond to different shot points.

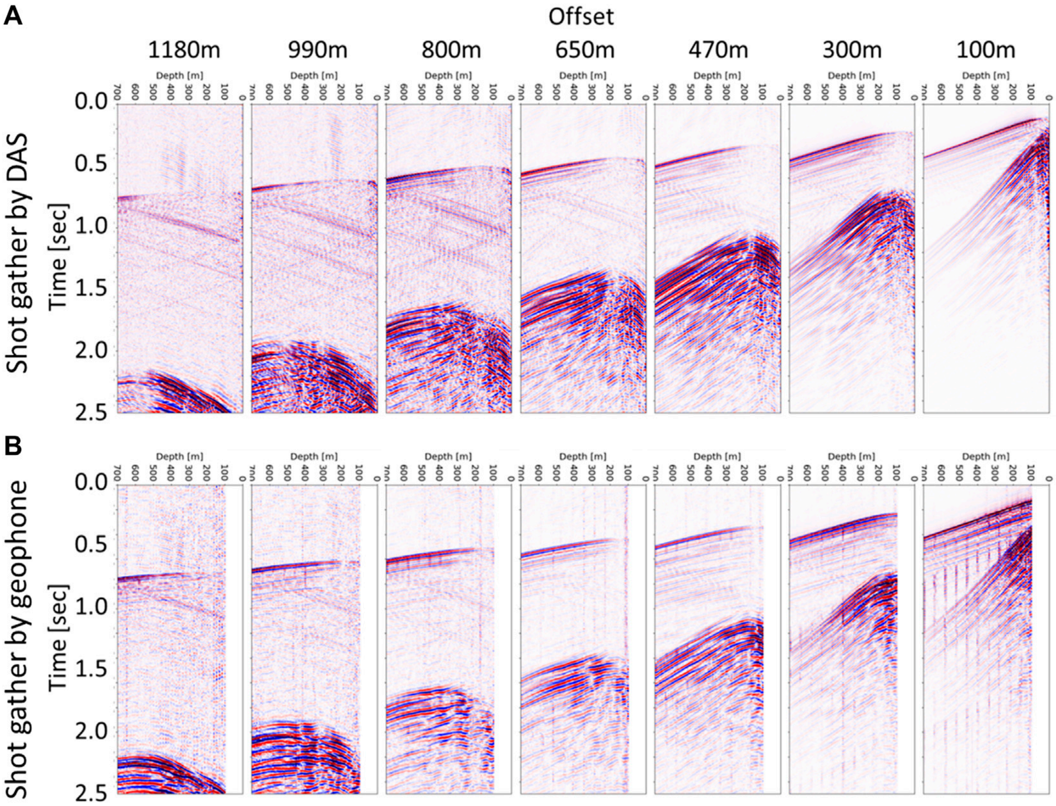

FIGURE 10
Shot gathers obtained by DAS **(A)** and geophone array **(B)** at each shot point.

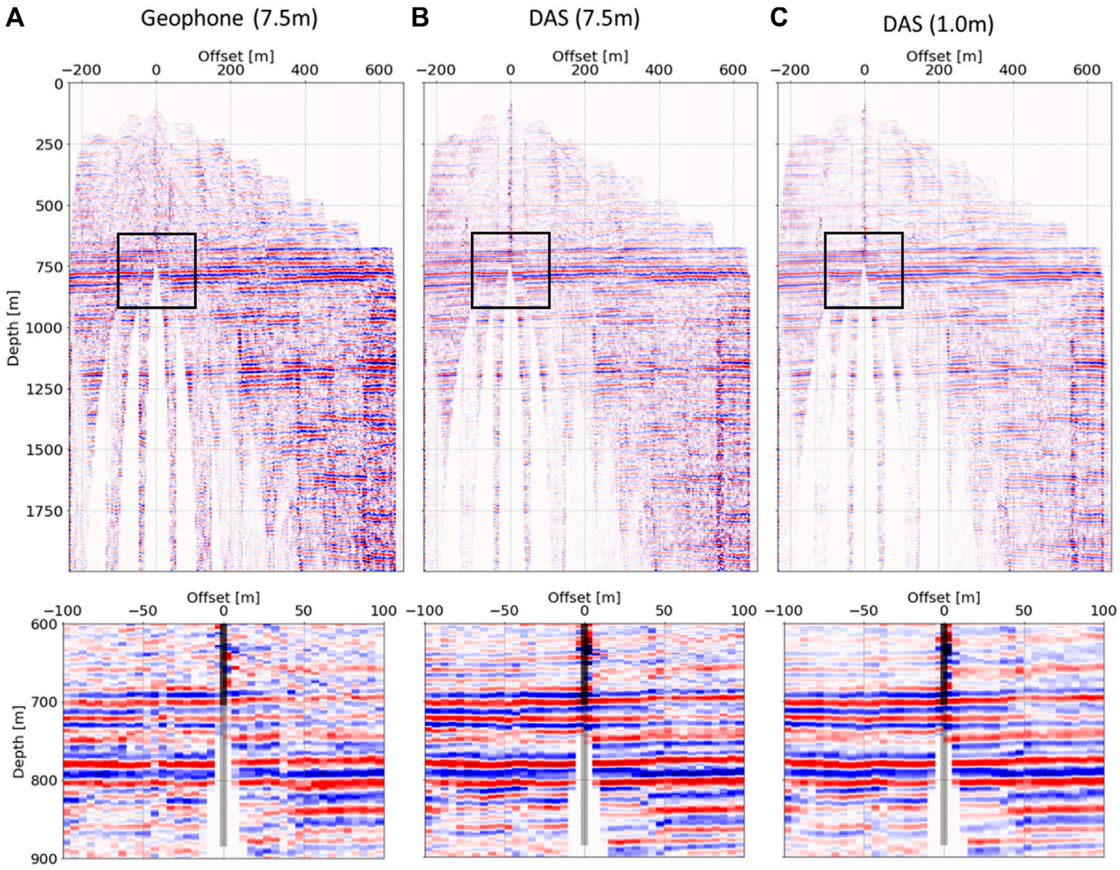

FIGURE 11
Migrated VPS images for 2-D walk away at a test site in Japan. Vz data [**(A)** 7.5-m intervals], averaged DAS data [**(B)** reduced to 7.5-m intervals], and original DAS data [**(C)** 1-m intervals] were used for migration processing. The upper raw image represents a wide area, while the lower image is the enlarged view around the well.

evenly aligned along the time axis because the sensitivity of the Vz geophone array component was not even. This effect was large in the near-offset survey. The quality of the shot gather was good in both DAS and geophone, and the direct P- and S-waves were clearly recognizable. From the first break time in the nearest offset data, we evaluated a 1-D velocity model of the site for the further analysis.

These results were used for image data processing. To image DAS data, we utilized data at 7.5-m and 1-m intervals to compare the effect of measurement density. The 7.5-m interval is the same as that of the geophone, and 1 m is the resolution of the original DAS data, although the SNR is inferior to the averaged data. The peak position of source deconvolved data from DAS measurement is about 5 ms ahead compared to that of geophone data (Figure 7). This difference can be adjusted with time integration of each trace. Signature deconvolution (Isaenkov et al., 2020), would also be useful to adjust wavelets and to obtain clear reflected events, although we did not do that in this data analysis. After preconditioning, we followed the general data processing flow for 2D-VSP. This workflow includes wavefield separation and VSP-CMP transformation. For wavefield separation, an FK-filter was used to isolate primary PP reflections. This filter is also valid to exclude diminishing S-waves. For time migration, we used normal moveout (NMO) and common mid-point (CMP) stacking techniques. Bins for migration were set at 5 m.

After time domain data processing, the time axis of the image was converted to a depth domain (Figure 11). The white area in the wide area view (upper raw) means that the reflection points cannot be visualized by the configuration of this survey. The general characteristics of the strong reflections were similar between the DAS and geophone images. However, the results looked different in the enlarged view. The reflections in geophone measurement were not clear in the right (eastern) part shallower than 800 m, while the continuity of reflections improved in DAS measurements, even in 7.5-m interval data. The coupling of the geophone at that shot point may not have been not equal to that at other shots, as the geophone tool must be relocated at each depth and shot point.

Comparison of the results of DAS data at 7.5 and 1 m intervals showed that the reflections were more clearly connected at smaller intervals. This is because the number of traces at each bin for migration was larger at 1 m intervals. This effect had advantages despite the inferior SNR at each trace. This represents another advantage of DAS-VSP with distributed sensing.

5 Discussion

To consider the observed characteristics of DAS data, we computed synthetic wavefields from a point source excitation using simple layered models. The calculated velocity field was taken as the spatial derivative to obtain the strain rate. The amplitude ratio between the strain rate and particle velocity of the direct P-wave showed that the effect of inherent velocity is more important than that of impedance, as previously suggested in DAS papers (Daley et al., 2016; Isaenkov et al., 2020), but we confirmed the compensation method for recovering the DAS amplitude. Note that the determination of wavefield amplitude near layer boundaries including the surface was difficult, even for synthetic results. This difficulty occurs because some converted waves are too close to separate near the boundaries. Therefore, we considered two shot points to cover a wide range of incident angles. This would be more severe in field surveys with observation noise.

We demonstrated a walk-away DAS-VSP using a single-mode fiber installed behind the casing of a borehole at a site in Japan. During survey comparisons, DAS and 3C geophone data were acquired at the same borehole. Using the survey data, we performed two main analyses: we compared the amplitude ratio of the direct P-wave as a function of the incident angle between DAS and geophone data. To exclude the effect of surface waves, we did not use shallow (<100 m) data. We also applied the same compensation method as in a synthetic case, in which the velocity trend was considered. Isaenkov et al. (2020) discussed the effect of rock stiffness on the amplitude ratio. This effect is essentially the same as our compensation method since both methods consider changes in medium velocity. Our results show very good agreement with the theoretical relationship. We believe that the results are the best to date among reported field results.

Field data were also imaged using DAS and geophone data. The total time of data acquisition was the same except for the wireline logging efforts to relocate the geophone array. Even though the DAS data had a lower SNR compared to that for geophone data at each trace and shot point, the connectivity of the reflected waves was better in the DAS data. One reason for this is the high-density data in DAS measurements. Many traces was more important than the quality of individual traces in the imaging analysis. Another reason is that the observation points did not change in DAS measurements and the coupling between DAS and the formation was invariant, illustrating the advantages of DAS-VPS. In contrast, signal amplitudes with high incident angles were weaker than those of the geophone (Figure 7). This is the major limitation of DAS measurements. Thus, it is better to design survey plans to exploit the sensitivity of the DAS sensor. When data with a low-sensitivity angle must be acquired, we should consider the survey time to stack the data. These limitations are important for cost-effective surveys, as in time-lapse monitoring of subsurface CO_2.

As many papers have indicated, DAS has lower sensitivity than geophone (Figure 6). However, new interrogators with high sensitivity are being developed. Moreover, the proper combination of engineered fiber and interrogator reportedly yields DAS sensitivity comparable to that of high-sensitivity seismometers (Hartog et al., 2022; Shatalin et al., 2022). This type of interrogator also has a larger dynamic range than that used in the present study. Thus, the issue of sensitivity will hopefully soon be solved.

6 Conclusion

We compared strain rates based on DAS and particle velocity data using synthetically computed data and a field survey in Japan. DAS amplitude depended on the incident angle of the acoustic waves; however, we also confirmed its dependency on the apparent velocity. The synthetic computations of artificial layered models showed that the effect of the apparent velocity in the layer is more important than that of the reflected waves. The amplitude change due to reflection was automatically adjusted by taking the ratio of the strain rate and the particle velocity, except near the boundary zone. While the effect of apparent velocity has already been suggested in the derivation of DAS measurements, it has been little discussed in the literature.

To examine the effectiveness and limitations of DAS measurements in field surveys, we conducted a walk-away VSP at a test site for DAS measurement in Japan. We acquired DAS data using a combination of a single-mode straight fiber installed behind the casing and a Silixa iDAS v2 interrogator and also obtained a conventional geophone array in the same wellbore. The amplitude ratio of DAS and geophone as a function of the incident angle agreed well with the theoretical relationship after modification of the effect of the apparent velocity. Furthermore, we compared imaging results obtained using a standard VSP analyzing workflow. The DAS image was superior at near offset owing to the high-density data and better repeatability compared to those for wireline logging. These results will guide future survey designs, such as the offset range of shot points, survey time, monitoring of small changes in physical parameters, and surveys related to the incident angle of the wavefield.

Data availability statement

The original contributions presented in the study are included in the article/Supplementary Material. Further inquiries can be directed to the corresponding author.

Author contributions

All authors listed have made substantial, direct, and intellectual contributions to the work and have approved its publication.

Acknowledgments

This article is based on results obtained from a project (JPNP18006) commissioned by the New Energy and Industrial Technology Development Organization (NEDO) and the Ministry of Economy, Trade and Industry (METI) of Japan. We thank Suncoh Ltd. for its support during the data acquisition in this study and for guidance during the processing phases.

Conflict of interest

Suncoh Ltd provided their support during the data acquisition of this study, and their guidance during processing phases. The authors declare that the research was conducted in the absence of any other commercial or financial relationships that could be construed as a potential conflict of interest.

Publisher's note

References

Ajo-Franklin, J. B., Dou, S., Lindsey, N. J., Monga, I., Tracy, C., Robertson, M., et al. (2019). Distributed acoustic sensing using dark fiber for near-surface characterization and broadband seismic event detection. *Sci. Rep.* 9, 1328. doi:10.1038/s41598-018-36675-8

Bakku, S. K. (2015). *Fracture characterization from seismic measurements in a borehole* (Massachusetts Ave, Cambridge, MA: Massachusetts Institute of Technology). Ph.D. thesis.

Bakku, S., Wills, P., Fehler, M., Mestayer, J., and Lopez, J. (2014a). "Vertical seismic profiling using distributed acoustic sensing in a hydrofrac treatment well," in *84th SEG annual international meeting*, Denver, United States, October 26–31, 2014, 5024–5028. doi:10.1117/12.2050550

Bakku, S., Wills, P., and Fehler, M. (2014b). "Monitoring hydraulic fracturing using distributed acoustic sensing in a treatment well," in *84th SEG annual international meeting* (Denver, United States, October 26–31, 2014), 5003–5008. doi:10.1190/segam2014-1559.1

Barberan, C., Allanic, C., Avila, D., Yh-Billiot, J., Hartog, A., Frignet, B., et al. (2012). "Multi-offset seismic acquisition using optical fiber behind turing," in 74th EAGE conference & exhibition incorporating SPE EUROPE 2012, Copenhagen, Denmark, 4-7 June 2012.

Bona, A., Dean, T., Correa, J., Pevzner, R., Tertyshnikov, K. V., and Van Xaanen, L. (2017). "Amplitude and phase response of DAS receivers," in 79th EAGE conference & exhibition 2017, Paris, France, June 12-15, 2017.

Cheraghi, S., White, D., Harris, K., and Roberts, B. (2018). "Initial results of time-lapse processing of VSP geophone and DAS fiber-optic cable at Aquistore CO_2 injection site," in 80th EAGE conference & exhibition, Copenhagen, Denmark, June 11-14, 2018.

Correa, J., Egorov, A., Tertyshnikov, K., Bona, K., Pevzner, R., Dean, T., et al. (2017). Analysis of signal to noise and directivity characteristics of DAS-VSP at near and far offsets – a CO2CRC Otway project data example. *Lead. Edge* 36, 994a1–994a7. doi:10.1190/tle36120994a1.1

Correa, J., Tertyshnikov, K., Wood, T., Yavuz, S., Freifeld, B., and Pevzner, R. (2018). "Time-lapse VSP with permanent seismic source and distributed acoustic sensors: CO2CRC stage 3 equipment trials, GHGT-14," in 14th International Conference on Greenhouse Gas Control Technologies, Melbourne, Australia, 21-26 October 2018.

Daley, T. M., Miller, D. E., Dodds, K., Cook, P., and Freifeld, B. M. (2016). Field testing of modular borehole monitoring with simultaneous distributed acoustic sensing and geophone vertical seismic profiles at Citronelle, Alabama. *Geophys. Prospect.* 64, 1318–1334. doi:10.1111/1365-2478.12324

Dean, T., Cuny, T., and Hartog, A. (2016). The effect of gauge length on axially incident p-wave measured using fiber optic distributed vibration sensing *Geophys. Prospect.* 65, 184–193. doi:10.1111/1365-2478.12419

Fenta, M. C., Potter, D. K., and Szanyi, L. (2021). Fibre optic methods of prospecting: A comprehensive and modern branch of Geophysics. *Surv. Geophys.* 42, 551–584. doi:10.1007/s10712-021-09634-8

Grindei, L., Kelley, M., Modroo, A., Mondanos, M., Farhadiroushan, M., and Coleman, T. (2019). "Distributed acoustic sensing (DAS) for monitoring CO2 injection into a Pinnacle-Reef reservoir," in 2nd EAGE workshop practical reservoir monitoring 2019, Amsterdam, Netherlands, April 1-4, 2019.

Harris, K., White, D., and Samson, C. (2017). Imaging the Aquistore reservoir after 36 kilotonnes of CO_2 injection using distributed acoustic sensing. *Geophysics* 82, M81–M96. doi:10.1190/geo2017-0174.1

Hartog, A. H. (2020). "Distributed sensors in the oil and gas industry," in *Optical fibre sensors*. Editors I. del Villar and U. R. Matias (Hoboken, NJ, USA: John Wiley & Sons), 151–191.

Hisada, Y. (1994). An efficient method for computing Green's functions for a layered half-space with sources and receivers at close depths. *Bull. Seismol. Soc. Am.* 84, 1456–1472. doi:10.1785/bssa0840051456

Hisada, Y. (1995). An efficient method for computing Green's functions for a layered half-space with sources and receivers at close depths (part 2). *Bull. Seismol. Soc. Am.* 85, 1080–1093. doi:10.1785/bssa0850041080

Isaenkov, R., Glubekovskikh, S., Tertyshnikov, K., Pevzner, R., and Bonna, A. (2020). "Effect on rocks stiffness on observed DAS VSP amplitude," in *EAGE Workshop on fiber optic sensing for energy applications in Asia Pacific*, Perth, Australia, November 9–11, 2020.

Karrenbach, M., Cole, S., Ridge, A., Boone, K., Kahn, D., Rich, J., et al. (2019). Fiber-optic distributed acoustic sensing of microseismicity, strain and temperature during hydraulic fracturing. *Geophysics* 84 (1), D11–D23. doi:10.1190/geo2017-0396.1

Lellouch, A., and Biondi, B. L. (2021). Seismic applications of downhole DAS. *Sensors (Basel)* 21 (9), 2897. doi:10.3390/s21092897

Li, Z., and Zhan, Z. (2018). Pushing the limit of earthquake detection with distributed acoustic sensing and template matching: A case study at the brady geothermal field. *Geophys. J. Int.* 215, 1583–1593. doi:10.1093/gji/ggy359

Maxwell, S. (2014). *Microseismic imaging of hydraulic fracturing: Improved engineering of unconventional shale reservoirs*. Denver, CO, USA: Society of Exploration Geophysics.

Mestayer, J., Cox, B., Willis, P., Kiyashchenko, D., Lopez, J., and Costello, M. (2011). "Field trials of distributed acoustic sensing for geophysical monitoring," in *81st SEG annual international meeting* (San Antonio, USA: Society of Exploration Geophysicists), 4253–4257. expanded abstract. doi:10.1190/1.3628095

Miller, D. E., Daley, T. M., White, D., Freifeld, B. M., Robertson, M., Cocker, J., et al. (2016). Simultaneous acquisition of distributed acoustic sensing VSP with multi-mode and single-mode fiber-optic cables and 3C-Geophones at the Aquistore CO_2 storage site. *Canadian Society of Exploration Geophysics* 41 (6), 28–33.

Molenaar, M. (2013). "Field cases of hydraulic fracture stimulation diagnostics using fiber-optic distributed acoustic sensing (DAS) measurements and analysis," in SPE Middle East unconventional gas conference and exhibition, Muscat, Oman, January 28–30, 2013.

Molteni, D., Williams, M. J., and Wilson, C. (2017). Detecting microseismicity using distributed vibration. *First Break* 35, 51–55. doi:10.3997/1365-2397.35.4.87841

Olofsson, B., and Martinez, A. (2017). Validation of DAS data integrity against standard geophones – DAS field test at Aquistore site *Lead. Edge* 36, 981–986.

Parker, T., Shatalin, S. V., Farhadiroishan, M., and Miller, D. (2013). "Distributed acoustic sensing : Recent field data and performance validation," in 2nd EAGE workshop on permanent reservoir monitoring 2013– Current and future trends, Stavanger, Norway, July 2–5, 2013.

Shatalin, S., Parker, T., and Farhadireoushan, M. (2022). "High definition and microseismic data acquisition using distributed and engineered fiber optic acoustic sensors," in *Distributed acoustic sensing in Geophysics, geophysical monograph series 268*. Editors Y. Li, M. Karrenbach, and J. B. Ajo-Franklin (Hoboken, NJ, USA: Jhon Wiley & Sons), 1–32.

Sidenko, E., Bonna, A., Pevzner, R., Issa, N., and Tertyshnikov, K. (2020). "Influence of interrogators' design on DAS directional sensitivity," in *EAGE workshop on fiber optic sensing for energy applications in asia pacific*, Perth, Australia, November 9–11, 2020

Spica, Z. J., Castellanos, J. C., Viens, L., Nishida, K., Akuhara, T., Shinohara, M., et al. (2022). Subsurface imaging with ocean-bottom distributed acoustic sensing and water phases reverberations. *Geophys. Res. Lett.* 49, e2021GL095287. doi:10.1029/2021GL095287

Verliac, M., Lesnikov, V., and Euriat, C. (2015). "The Rousse-1 DAS VSP experiment – observations and comparison from various optical acquisition system," in SEG 85th annual international meeting, New Orleans, United States, October 18–23, 2015, 5534–5528. doi:10.1190/segam2015-5886544.1

Willis, M. E., Barkfoot, D., Elimauthaler, A., Wu, X., Barrios, O., Erdemir, C., et al. (2016). Quantitative quality of distributed acoustic sensing vertical seismic profile data. *Lead. Edge* 35 (7), 605–609. doi:10.1190/tle35070605.1

Willis, M. E., Ellmauthaler, A., Wu, X., and Leblanc, M. J. (2020). "Important aspects of acquiring distributed acoustic sensing (DAS) data for geoscientists," in *Distributed acoustic sensing in Geophysics, geophysical monograph series 268*. Editors Y. Li, M. Karrenbach, and J. B. Ajo-Franklin (Hoboken, NJ, USA: John Wiley & Sons), 33–44.

Wu, X., Willis, M. E., Palacios, W., Ellmauthalter, A., Barrios, O., Shaw, X., et al. (2017). Compressional- and shear-wave studies of distributed acoustic sensing acquired vertical seismic profile data. *Lead. Edge* 36 (12), 987–993. doi:10.1190/tle36120987.1

frontiers | Frontiers in Earth Science

TYPE Original Research
PUBLISHED 05 January 2023
DOI 10.3389/feart.2022.991860

Multi-scale interactive network in the application of DAS seismic data processing

Hongzhou Wang[1], Jun Lin[1,2]*, Dan Shao[3], Xintong Dong[1]* and Yue Li[4]*

[1]College of Instrument Science and Electrical Engineering, Jilin University, Changchun, China, [2]Southern Marine Science and Engineering Guangdong Laboratory, Zhanjiang, Guangdong, China, [3]College of Geo-exploration Science and Technology, Jilin University, Changchun, China, [4]College of Communication Engineering, Jilin University, Changchun, China

OPEN ACCESS

EDITED BY
Yibo Wang,
Institute of Geology and Geophysics (CAS), China

REVIEWED BY
Wenchao Chen,
Xi'an Jiaotong University, China
Danping Cao,
China University of Petroleum, China

*CORRESPONDENCE
Jun Lin,
Lin_Jun@jlu.edu.cn
Xintong Dong,
18186829038@163.com
Yue Li,
liyue@jlu.edu.cn

SPECIALTY SECTION
This article was submitted to Solid Earth Geophysics,
a section of the journal
Frontiers in Earth Science

RECEIVED 12 July 2022
ACCEPTED 16 September 2022
PUBLISHED 05 January 2023

CITATION
Wang H, Lin J, Shao D, Dong X and Li Y (2023), Multi-scale interactive network in the application of DAS seismic data processing.
Front. Earth Sci. 10:991860.
doi: 10.3389/feart.2022.991860

Distributed acoustic sensing (DAS) is regarded as a novel acquisition technology for seismic data. Compared with conventional electrical geophones, DAS has a series of obvious advantages including low-cost, high spatial resolution, good coverage, and strong resistance to the harsh environment. Noise attenuation is an essential step in seismic data processing. However, there are two main difficulties faced by the denoising task of DAS seismic data. On the one hand, some background noise in DAS seismic data, such as optical low-frequency noise, horizontal noise, and fading noise, is unique and not presented in the conventional seismic data; on the other hand, the signal-to-noise ratio (SNR) of DAS seismic data is relatively low. Recently, a convolutional neural network (CNN) has shown superior denoising performance compared to the traditional method. To follow this promising trend, we propose a multi-scale interactive convolutional neural network (MSI-Net) and apply it to denoise the challenging DAS seismic data. Different from most of the existing CNN architecture used in seismic data denoising, the MSI-Net considers both coarse-scale and fine-scale features by improving the inherent serial convolution to multi-scale parallel convolution, which is beneficial to recover detailed information. Moreover, we utilize some connections to achieve the information interaction between different scales, which promotes the flow of information and enables the network to extract more informative multi-scale features from the DAS seismic data. Moreover, both synthetic and real examples demonstrate that the proposed MSI-Net can effectively attenuate a variety of unique DAS background noise and also completely recover the weak signals. Compared with conventional CNN architecture, MSI-Net exhibits better performance in global SNR and local details.

KEYWORDS

deep learning, multi-scale network, distributed acoustic sensing, DAS seismic data, noise suppression, high-resolution

Introduction

In the wake of developments in oil and gas exploration, the quality requirements for seismic data have gradually increased, finding a seismic data processing technology with higher accuracy and resolution is also a difficult problem we must face. Distributed acoustic sensing (DAS) is considered an emerging acquisition technology in seismic exploration. DAS uses changes in the phase information of the scattered optical signal to record the wavefield (Spikes et al., 2019). Compared to conventional electronic geophones, DAS has advantages in acquisition geometry, such as low cost and high-density observations. In recent years, DAS has been applied to vertical seismic profile (VSP) data acquisition (Dong et al., 2022). However, the scattered light signal with weak energy is extremely susceptible to background noise, which negatively affects the quality of the acquired seismic data (Binder et al., 2020). In addition, the in-well acquisition environment also brings new challenges to data processing, and some disturbances are not present in conventional seismic surveys, such as time-varying optical noise and coupling noise (Wang et al., 2021). The seismic data collected in the field is mixed with a wide variety of noise due to the underground geological conditions, collection conditions and environmental factors. Affected by the mixed noise, the quality of the real seismic records decreases, and the signal-to-noise ratio (SNR) and resolution of the data are relatively low, which brings difficulties to subsequent inversion, imaging and interpretation. Improving the SNR and resolution of data is of great significance to the study of underground structures and the exploration of oil, gas and mineral resources.

In seismic data processing, obtaining data with high SNR and resolution is the goal. The noise can interfere with the effective seismic information to cause a low SNR, at the same time, narrowing the effective frequency band of the seismic data and reducing the data resolution. It is a challenging problem to reduce the noise in seismic data while taking into account the resolution. Among the traditional noise reduction methods, Band-pass filtering, Wiener filtering (Mendel, 1977) and F-X deconvolution (Canales, 1984) was used earlier for seismic noise suppression. Several time-frequency attenuation algorithms have also been developed to improve the denoising capability of seismic data, including short-time Fourier transform (Lu and Li, 2013) and time-frequency peak filtering (TFPF) (Wu et al., 2011). In general, the denoising principle of these methods is based on the difference between the reflected signal and the background noise in terms of physical characteristics or frequency components to eliminate complex interference. However, the above methods cannot handle the complex DAS background noise. In addition, multi-scale denoising methods use the features of the sparse decomposition results to construct suitable filters for the purpose to suppress the noise to retain the effective signal, and typical methods include wavelet transform filtering (Mousavi et al., 2016; Anvari et al., 2017), Curvelet transform filtering (Neelamani et al., 2008; Gorszczyk et al., 2014), Shearlet transform filtering (Gan et al., 2015; Chen and Fomel 2018), empirical mode decomposition (EMD) (Bekara and van der Baan, 2009; Amezquita Sanchez et al., 2017) and variational modal decomposition (VMD) (Kesharwani et al., 2021). Unfortunately, when dealing with DAS recordings containing complex noise, researchers have difficulty in obtaining optimal filtering parameters, which leads to noise residuals and loss of amplitude of the effective signal. In addition, many other methods have been widely used in seismic data processing including singular value decomposition (SVD) (Oropeza and Sacchi, 2011), dictionary learning methods (Chen et al., 2016; Yarman et al., 2018; Wang and Ma, 2020), robust principal component analysis (RPCA) (Cheng et al., 2015; Liu et al., 2021), but the application of these methods in DAS data denoising is rarely reported. It is difficult for conventional methods to provide a better processing effect when the DAS data is seriously disturbed by noise, and give consideration to SNR and resolution. Meanwhile, it involves the manual selection of various parameters in data processing for conventional methods introduced above, which greatly increases the running time of the processing work and depends on artificial experience heavily. For the sake of high-precision seismic exploration, more intelligent and faster data processing technology is urgently needed.

In recent years, deep learning methods have become popular solutions to various seismic data processing problems. Deep learning (DL) (Lecun et al., 2015) is considered an important machine learning method that has started to be introduced into seismic data processing. And there are already some successful applications such as seismic data denoising (Chen et al., 2019; Saad and Chen, 2020), arrival picking (Tsai et al., 2018; Yuan et al., 2019; Zhang et al., 2020), fault identification (Wu et al., 2019), lithology prediction (Zhang et al., 2018) and geologic structure classification (Li, 2018). The deep learning algorithm can automatically learn highly complex nonlinear features, and it is applied to the suppression of background noise in pre-stack seismic data to achieve automatic and efficient background noise separation by automatically learning random noise features. Yu et al. (2019) proposed an intelligent CNN-based denoising method, which does not require precise modeling of signal and noise, nor optimization of parameter tuning. Wang and Chen (2019) used a deep CNN framework with residual learning for 2-D post-stack seismic random noise attenuation. Treating seismic signals as time series, Saad and Chen (2020) proposed a deep denoising autoencoder (DDAE) to attenuate seismic random noise. Li et al. (2022) proposed to leverage a deep convolutional neural network (CNN) to achieve seismic image super-resolution and denoising simultaneously. Jiang et al. (2021) proposed an improved convolutional autoencoder (CAE) method to achieve simultaneous reconstruction and denoising of seismic data. Yang et al. (2021) proposed an improved ResNet to achieve seismic random noise attenuation. Wang et al. (2022)) are applied to seismic noise attenuation tasks (Creswell et al., 2017; Wang et al., 2021), and some successful applications on ground record processing have been achieved. Furthermore, transfer learning was introduced into the training of denoising networks to enhance the generalization of the model to process the real records (Li et al., 2022; Sun et al., 2022). Supervised learning-based denoising methods need to label a large number of clean seismic data to fit the network, which will increase labor and computational costs. Therefore, some denoising models based on unsupervised learning or self-supervised learning have been proposed to address the lack of paired data in seismic signal processing (Wang et al., 2022; Yang et al., 2021; Liu et al., 2021; 2022; Qiu et al., 2022). Meanwhile, deep learning-based algorithms have also achieved good results in denoising DAS records (Zhao et al., 2022; Wang et al., 2021). In general, these denoising networks aim to establish a non-linear high-dimensional mapping relationship between noisy records and desired signals. In the training process, we can use training data to strengthen the learned mapping, and the final denoising models are obtained after training and have been proven to be effective in practical application. Notably, unlike conventional methods, the denoising network can be considered a “data-driven” approach to adaptively accomplish complex seismic noise suppression without parameter fine-tuning. If the training data is complete, CNN-based networks can always achieve more advantageous results than conventional methods. However, most of the traditional networks, such as DnCNN (Zhang et al., 2017), are based on single-scale information to extract potential features, which has reduced effectiveness and generalization when dealing with complex seismic data (Zhong et al., 2022). In addition, most existing methods transmit input through a network and reconstruct output at the last layer. Although the characterization learned by this type of network can aggregate local features with the increase of layers, it also has the characteristics of coarse scale, that is, the resolution after reconstruction is not fine enough and some detail features are ignored. As a result, it is difficult to obtain accurate prediction results in the task of seismic data processing, especially when the data is disturbed by strong noise. The stronger noise can lead to a rapid decrease in the sensitivity of the final output characterization space, a decrease in the accuracy of the reconstruction, and even some false seismic events.

Therefore, there has been an increasing interest in designing efficient denoising networks to improve the processing capability of DAS-VSP data. To solve the above problem, a multi-scale interactive deep convolutional neural network (MSI-Net) is constructed in this paper. The network builds a multi-scale framework by gradually fusing sub-networks on the main network, and repeated information interactions are performed on parallel multi-scale sub-networks to complete the repetitive information fusion between scales, which enhances the generalization ability of the network. The network can learn more abundant multi-scale characterization and reconstruct high-resolution seismic data. The experiment results show that the network can not only suppress noise effectively, but also predict effective signals accurately, it can achieve processing requirements of high SNR and resolution, and greatly reduce false seismic events. We construct a high-quality training dataset containing synthetic signals and actual DAS background noise to train the network. We also process synthetic and field DAS data to check the effectiveness of the proposed network. Compared with traditional denoising methods and recently proposed denoising networks, the proposed method in this paper has advantages in DAS background noise attenuation and weak signal amplitude retention.

Methods

DAS records often contain complex wave fields, including incident down-going waves and reflected up-going waves. The recovery of events in seismic records is very important, however, it is difficult to identify seismic events with the interference of noise, hence noise suppression is necessary. The convolutional neural network can eliminate noise, and also plays an important role in the high-resolution reconstruction of signals. To make the signal recovery more accurate, it is common practice to obtain exact semantic information through down-sampling, and then perform an up-sampling operation to restore high-resolution signal details, such as U-Net (Ronneberger et al., 2015). However, this practice leads to some loss of effective information in the continuous upsampling and downsampling. If the high-resolution transmission is maintained throughout the whole process, such as DnCNN (Zhang et al., 2017), a wider range of perceptions cannot be obtained, and some false events are often generated in the results. In this paper, a wide range of semantic information is obtained through parallel multiple resolution sub-networks and continuous information interaction between different network branches. And the proposed method achieves the purpose of recovering signal details accurately while suppressing noise effectively. To better denoise the actual DAS data, we analyzed the wave fields and complex noise in real DAS data. Then, we constructed a dedicated training set to train the model. The following sections introduce the analysis of wavefield and noise in the DAS record, the construction of the dataset, the structure of the network and the denoising principle.

Analysis of wavefield and noise in DAS-VSP

Figure 1 shows DAS-VSP data acquired from Xinjiang, western China. The horizontal coordinate represents the number of seismic traces and the vertical coordinate

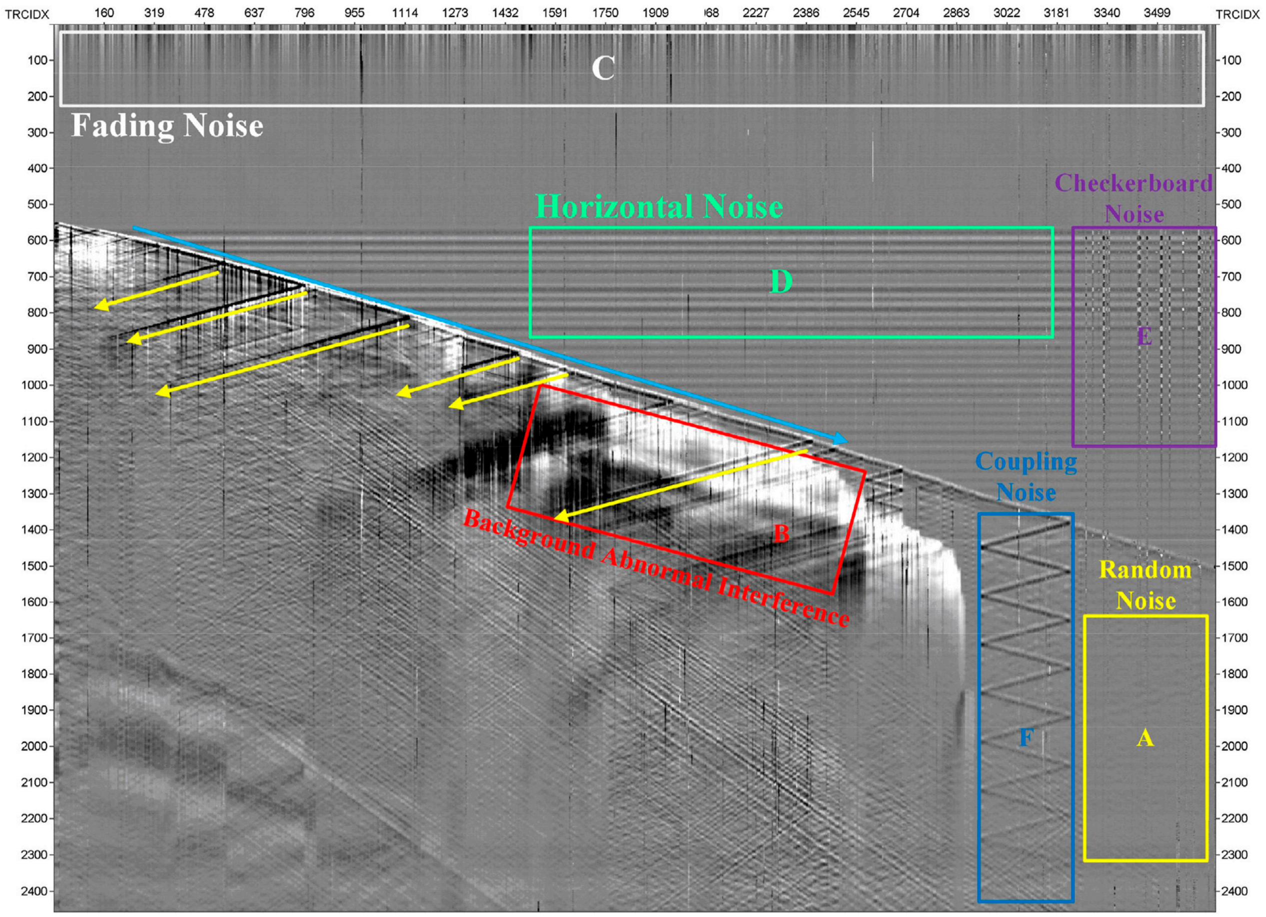

FIGURE 1
DAS VSP data with several common noises. Areas **(A–F)** are marked with random noise, background abnormal interference, fading noise, horizontal noise, checkerboard noise and coupling noise, respectively.

represents the time. The time sampling interval of the DAS data shown is 400 μs and the spatial sampling interval is 1 m. From the figure, we can observe that the data are heavily contaminated by noise, and the effective signals such as the incident down-going waves (as indicated by the blue line) and reflected up-going waves (as indicated by the yellow line) are almost covered by noise. It can be observed that the types of noise are also complex, such as random noise (as shown in region A), background abnormal interference (as shown in region B), fading noise (as shown in region C), horizontal noise (as shown in region D) and checkerboard noise (as shown in region E) and coupling noise (as shown in region F). The characteristics and causes of these noises are described as follows.

The random noise is common background noise in DAS-VSP data, with a wide frequency band and strong energy, mainly caused by vibration during data acquisition. The source of noise may come from machine vibration, underground random vibration, current disturbance, *etc.* Random noise is generally more uniformly distributed and is the main factor affecting the quality of DAS-VSP data.

The abnormal interference with low dominant frequency and very strong energy may be caused by downhole temperature anomalies. The abnormal interference tends to have large areas and high amplitudes in the records. In the presence of abnormal interference, the effective signal is completely covered and the DAS-VSP data quality is seriously affected.

The fading noise is caused by the phase canceling interference of randomly spaced backscattered light. Fading noise is mainly manifested in long periods and high amplitude. In general, the fading noise appears on the uppermost side of the record, less affecting the effective signal below the first arrival wave. It is easy to mix with horizontal noise to generate new types of noise.

The horizontal noise is caused by vibration during optical measurements. Shaking the interrogator box is probably the main trigger. The potential leakage of electronic equipment can also be another cause of horizontal noise. The horizontal

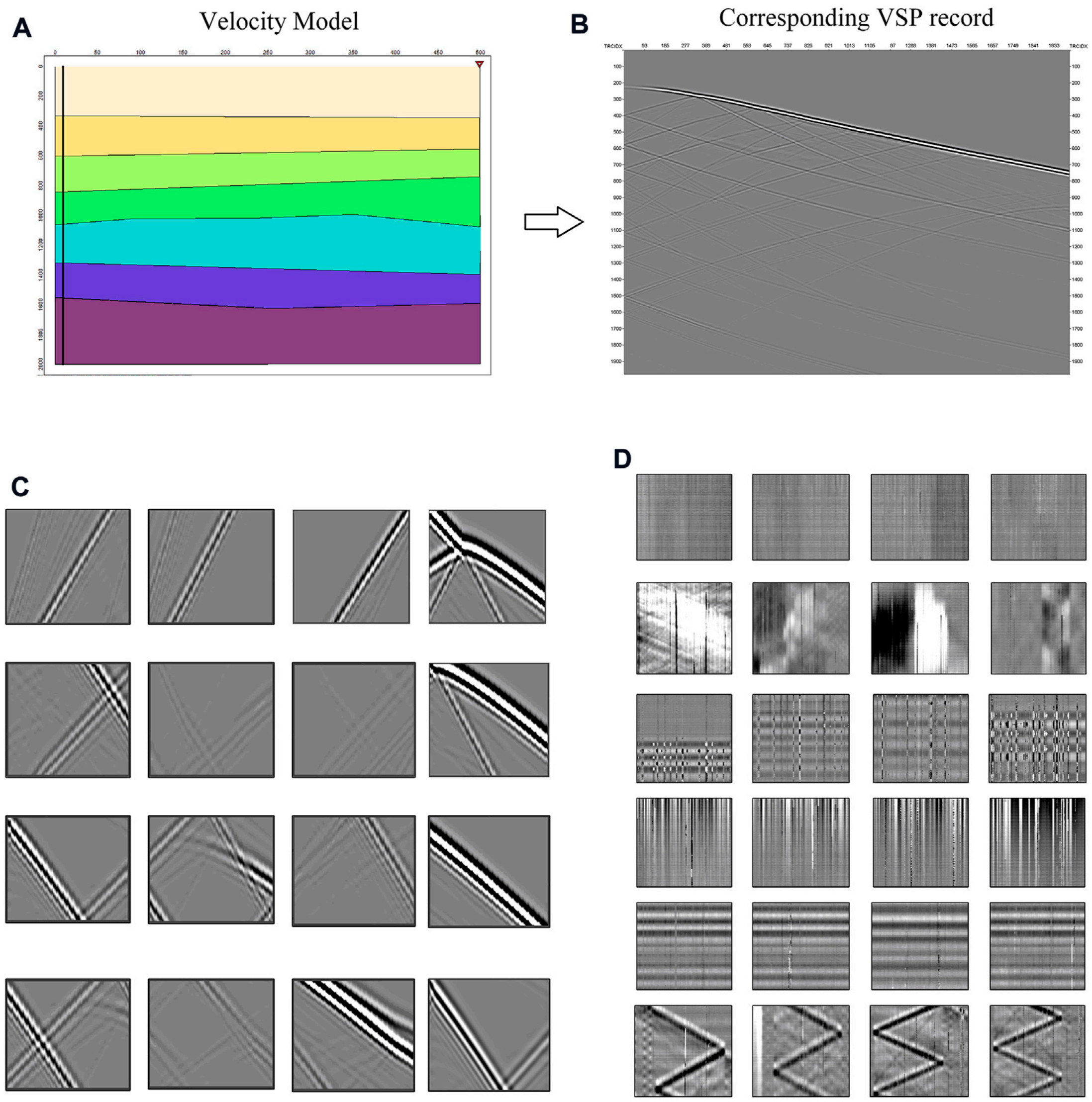

FIGURE 2
Construction of the dataset. **(A)** The velocity model. **(B)** The corresponding synthetic DAS-VSP record. **(C)** Samples of the signal dataset. **(D)** Samples of the noise dataset. These patches are the random noise, the abnormal interference, the checkerboard noise, the fading noise, the horizontal noise and the coupling noise from top to bottom.

noise usually appears as a short horizontal band with essentially the same phase in all traces and decreasing in amplitude over time.

The checkerboard noise is generally generated by a mixture of horizontal noise and fading noise. The checkerboard noise has approximately the same properties as the horizontal noise. For example, both checkerboard noise and horizontal noise have horizontal motion, and the amplitude gradually decays over time. However, checkerboard noise tends to have different phases in different traces. In general, the checkerboard noise is also more distributed before the first arrival.

The coupling noise is mainly caused by the poor coupling of the fiber and the measurement line. It often accompanies the reflected signal and is highly similar to the signal within the local view. Conventional methods are generally more difficult to distinguish between signal and coupled noise. At present, there are three ways to deploy DAS systems in wells. The first one is to permanently fix the fiber outside the casing. It maximizes the coupling between the fiber and the formation, resulting in less coupling noise in the acquired DAS data (Jiang et al., 2016). The second one is to fix the fiber to the tubing and there will still be a small amount of coupling noise. The third one is to use weights to suspend the fiber in the casing. However, the

TABLE 1 The parameters of the forward modeling.

Parameter	Value
Source number	1
The distance between the source and well	400–500 m
Receiver number	2000
Spatial sampling interval	1 m
Velocity model size	(500,2000)
Sampling time interval	4×10^{-4} s
Seismic wavelet	Ricker
Dominant frequency	50–70 Hz
Maximum traveltime	2 s

optical fiber is not in close contact with the borehole, which may produce strong coupling noise (Constantinou et al., 2016).

Construction of training set

The purpose of deep learning is to learn the feature, which can obtain hierarchical feature information adaptively through the network, solving the problem of manually designing operators for feature extraction in the past. Dataset is an important basis for deep learning algorithms, and its completeness determines the potential upper limit that the method can touch. In seismic exploration, it is difficult to obtain pure seismic signals. To obtain a more complete and realistic training set, forward modeling is used to construct a pure signal set as shown in Figure 2. For DAS-VSP, to obtain subsurface information, we usually place artificial sources to excite the seismic wave field and place receivers along the longitudinal direction to record the seismic waves. In this paper, the synthetic data are modeled based on the acoustic wave equation in the time domain, as shown in the following equation.

$$\frac{\partial^2 u(x,y,t)}{\partial t^2} = v(x,y)^2\left(\frac{\partial^2 u}{\partial x^2}+\frac{\partial^2 u}{\partial y^2}\right) + s(x,y,t) \tag{1}$$

where v represents the wave velocity and u represents the acoustic wavefield. $s(x,y,t)$ denotes the function of the source. (x,y) denotes the spatial location and t denotes time. We have built 100 velocity models with different stratigraphic configurations. The detailed parameters of the model are shown in Table 1. After preparing the velocity models, the shots of the seismic data corresponding to each velocity model are generated in the numerical simulation of the acoustic wavefield. We solve the acoustic wave equations using a staggered-grid finite-difference method in the time domain. The size of each grid is defined as 10 m × 10 m. As for the observation of each velocity model, we place a source as shown in Figure 2 to simulate the shot gathers. The source is placed at (500, 0) m. The survey line is placed along the vertical direction at x= 10 m. The recording geometry consists of 2000 receivers. In Figures 2A,B, we show a representative velocity model and the corresponding generated seismic record. By solving the wave equation, 100 simulated pure seismic records with a size of 2,000 × 2,000 are obtained, which can be used as a part of the pure signal set for network learning. To adapt to the network training, we divide the amplitude-normalized synthetic seismic records into patches with a size of 400 × 400 to obtain the pure signal set $X = \{x_1, x_2, \cdots, x_e\}$. Part of the pure signal patch is shown in Figure 2C.

A large amount of noise data is needed to synthesize the noise set. The noise in the training set should be as close as possible to the noise in field seismic data. We have selected various types of noise data collected from the actual DAS records to enrich the noisy set. A complete noise set $N = \{n_1, n_2, \cdots, n_e\}$ can be built, and Figure 2D shows a portion of the noise patch. Similarly, the noise data is divided into patches with a size of 400 × 400 and superimposed with the pure signal patches to generate a noisy set $Y = \{y_1, y_2, \cdots, y_g\}$.

The structure of network

In the denoising process, the higher the resolution of the local structure, the more conducive to the reduction of the noise, but the rich information brought by the high resolution will also produce misjudgment in processing, resulting in some false seismic events. Therefore, it is also important to grasp the overall structure of data, which requires us to use data at different resolutions. The lower-resolution data components are more conducive to the recovery of the overall signal. It is of great significance to improve the performance of the overall task by analyzing and processing signals at different resolutions. How to design a network with multi-resolution representation is a key issue for us to consider. To make the network achieve multi-scale feature extraction, the model gradually adds sub-networks with low-resolution feature maps in parallel to the main network with high-resolution feature maps to complete the feature fusion between scales. The multi-resolution interactive network shown in Figure 3A is used for noise suppression and high-resolution reconstruction of seismic data. The design idea of the proposed network takes reference from HRNet (Sun et al., 2019). In Figure 3A, the horizontal transfer process represents the representation changes with the increase of processing layers, and the vertical process represents the scale change of the feature maps. The first level (which we called stage 1) shows the main network, and its feature map is maintained at a high-resolution standard. The signal is transmitted through the main network in stage1, and more low-resolution sub-networks are gradually added in parallel in subsequent stages. The resolution of the parallel sub-network in the latter stage is composed of all previous resolutions and a new resolution, that is, in the n-th

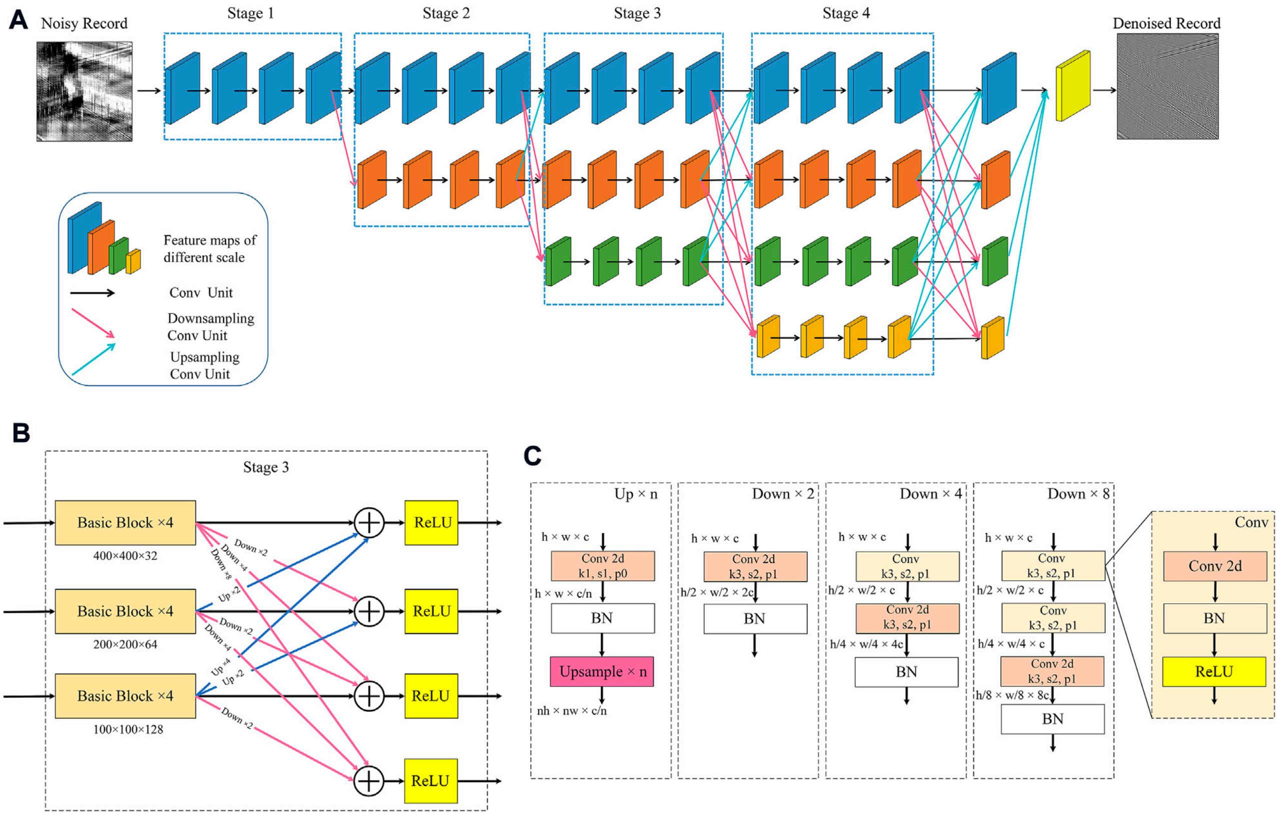

FIGURE 3
The architecture of the proposed network. **(A)** The architecture of MSI-Net. **(B)** The structure of a stage (Take the 3-th stage as an example) **(C)** Detailed structure of each part in Figure 3B.

stage, feature processing is performed in sub-networks of n resolutions in parallel. Every time a lower resolution sub-network is added, the resolution is reduced to half, and the corresponding channels are doubled.

In addition to analyzing signals in a multi-scale manner, the repeated exchange of information at various resolutions to promote multi-resolution information fusion is also an important reason for the network to maintain high performance. Similarly, it enables the network to maintain the accuracy of high-resolution reconstruction of signals under the blessing of low-resolution features. As shown in Figure 3B, taking a fusion at the 3-th stage as an example, it can be seen that the output of each resolution is related to the inputs at three different resolutions, namely $\mathrm{R}_{\tau}{}' = T_{1\to\tau}(\mathrm{R}_1) + T_{2\to\tau}(\mathrm{R}_2) + T_{3\to\tau}(\mathrm{R}_3)$. At the same time, a new output at a lower resolution is produced, that is, $\mathrm{R}_4{}' = T_{1\to 4}(\mathrm{R}_1) + T_{2\to 4}(\mathrm{R}_2) + T_{3\to 4}(\mathrm{R}_3)$, where R_i represents the input feature map of different resolutions, $R_i^{'}$ represents the output feature map of different resolutions, and $T_{i\to\tau}$ is an operator to process features between different resolutions. The operator is a down-sampling operation from high to low resolution, an up-sampling operation from low to high resolution, and the identity during the same resolution, respectively. In this way, while the parallel convolutional operations move forward synchronously, the network also carries out feature interaction between scales, to realize multi-scale feature fusion and extraction. Among them, the basic block adopts the structure of ResNet (He et al., 2016). The detailed introduction of each module is shown in Figure 3C. The introduction of each functional module can be obtained in

TABLE 2 The specific description of the layers or functions.

Layers	Description	Function
Conv 2d	Convolution	$y = W^{*}x + b$
BN	Batch Normalization	Normalize all samples for the entire batch
ReLU	Rectified Linear Unit	$y = max(0, x)$
Upsample	Upsample function	Upsample feature maps

TABLE 3 The details of training the proposed network.

Hyperparameter	Value
Batch size	16
Epochs	200
Learning rate range	$[1 \times 10^{-4}; 1 \times 10^{-3}]$
Patch size	400×400
Optimizer	Adam

Table 2. The designed network consists of four stages, and the feature extraction of each resolution in every stage is completed by four residual convolution operations. With the final integration of the feature maps obtained on each resolution, noise suppression and high-resolution signal reconstruction can be completed.

The denoising principle

In this paper, the DAS-VSP record disturbed by noise can be expressed as:

$$y = x + n \tag{2}$$

among them, x refers to the potential pure seismic signal and n refers to noise interference. In the proposed structure, the constructed high-resolution reconstruction network aims to learn the end-to-end mapping function between the noisy signal y and the pure signal x, and the predicted pure signal can be expressed as:

$$\tilde{x} = \mathrm{H}(y; \Theta) \tag{3}$$

In Equation 3, H represents the multi-scale interactive reconstruction network, $\Theta = \{W, b\}$ is the network optimized parameters with weights W and biases b.

Figure 4 shows the workflow of the DL-based denoising algorithm. During the training process, we can calculate the error between the network output $\tilde{x}$ and the pure record x, and update the network parameters by gradient backpropagation. After several iterations, the error will converge to a small enough value and the network parameters can be determined. In the inference process, given the seismic data, the denoised DAS data can be predicted by the network. In this paper, the $L2$ loss function is used as the cost function to guide the training process of the model, and the equation is given as follows:

$$L = \frac{1}{2N}\sum_{i=1}^{N}\left\|\mathrm{H}(y_i; \Theta) - x_i\right\|_F^2 \tag{4}$$

where $\mathrm{H}(y_i; \Theta)$ represents the denoising result of the training sample y_i, and x_i represents the pure signal which we called the label, that is, the output we expect from the network. i is the index of the sample and N is the batch size. The gradient descent method is used to minimize the loss function. To improve the reconstruction ability for seismic signals, the network adjusts the weight parameters reversely layer by layer and performs frequent iterative training. Specifically,

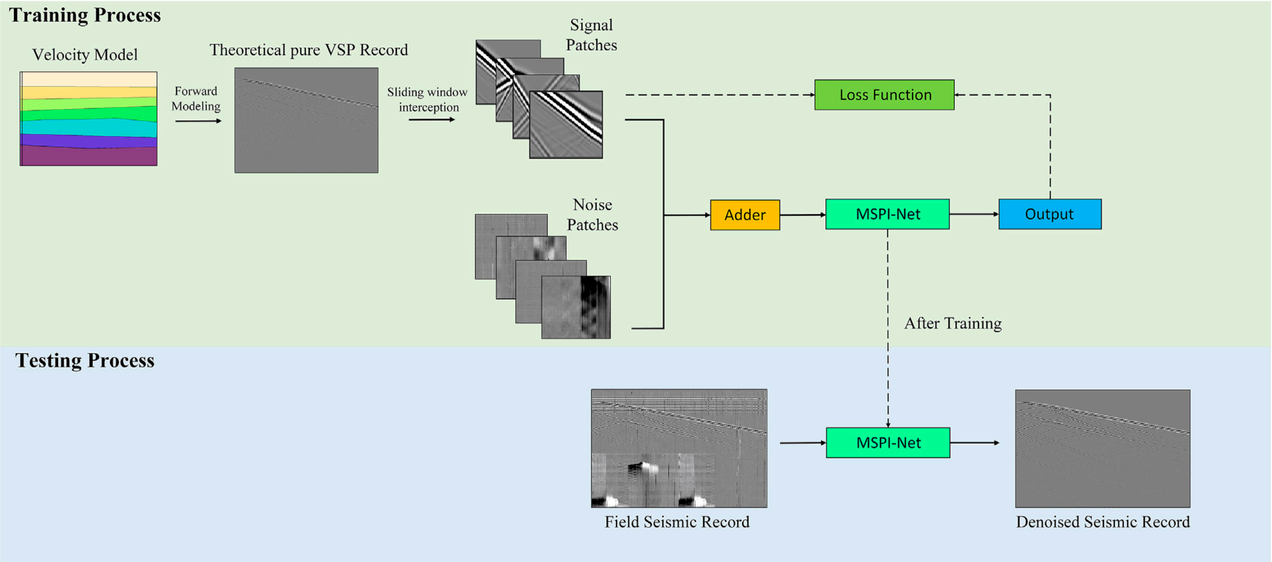

FIGURE 4
The flowchart of MSI-Net denoising procedures.

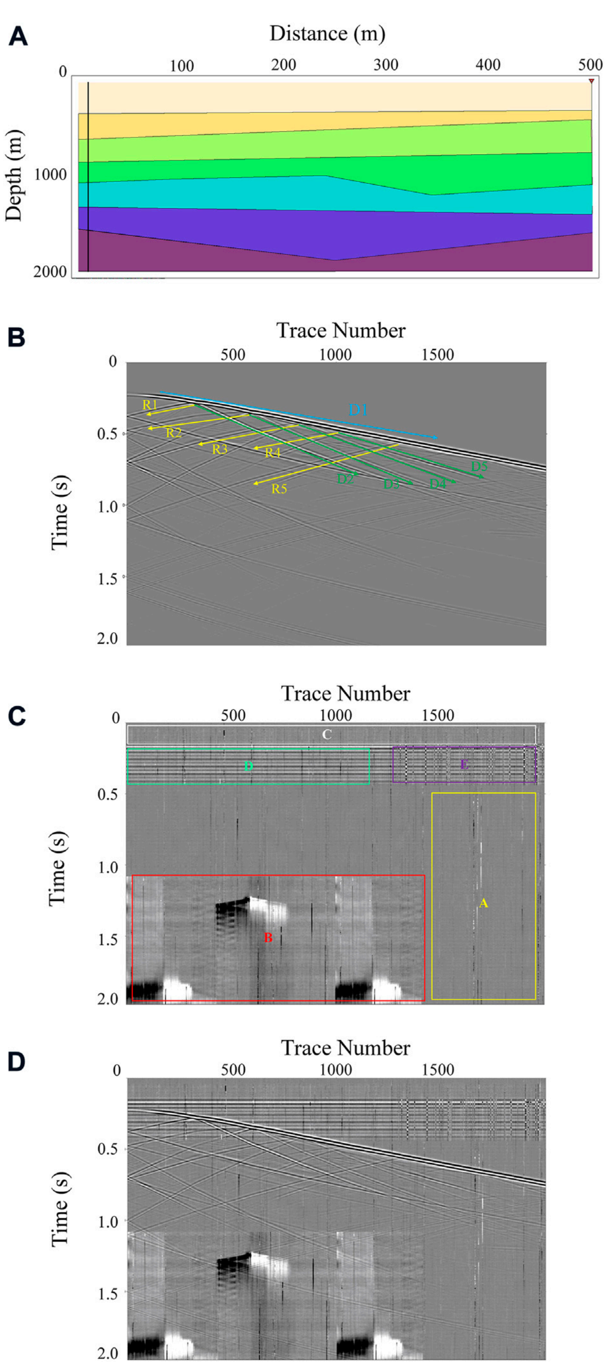

FIGURE 5
Construction of the noisy synthetic DAS-VSP record. **(A)** The velocity model. **(B)** The theoretical pure DAS-VSP record. **(C)** The added field noise. **(D)**The synthetic noisy record with the SNR of -0.5132 dB.

we use Adam optimizer to optimize the network. More network training parameters can be found in Table 3. After the training, we use the trained network to process the noisy DAS records.

Results

Experiment settings

Synthetic DAS-VSP data were generated by forward modeling, and a seven-layer 2D geological model is shown in Figure 5. The horizontal coordinates indicate the horizontal distance and the vertical coordinates indicate the depth. The velocities of the P-wave from the top to the bottom are 2,000, 2,250, 2,500, 2,750, 3,000, 3,250, and 3,500 m/s. And the media densities from the top to the bottom are 2,050, 2,100, 2,150, 2,200, 2,250, and 2,300 kg/m^3. Next, we set up the acquisition geometry. As shown in Figure 5, the inverted triangle represents the source and the vertical black line represents the measurement line formed by the fiber optic sensor. The time sampling interval is 400 μs, and the spatial sampling interval is 1 m. By solving the elastic wave equation, we can obtain the synthetic clean DAS -VSP data as shown in Figure 5B, where D1 is the direct wave, R1-R5 are the reflected up-going wave, and D2-D5 are the incident down-going waves. Common noises in DAS, such as random noise (as shown in region A), background anomalous interference (as shown in region B), fading noise (as shown in region C), horizontal noise (as shown in region D), and checkerboard noise (as shown in region E) are added as shown in Figure 5C. Because the generation mechanism of coupling noise is not yet clear, in the simulation experiment, it is not considered to add coupling noise to the simulation DAS record. The remade simulated pure signals and the noise collected together form synthetic noisy records and are used as a test. Figure 5D shows the synthesized noisy DAS-VSP data. We synthesized 10 noise-bearing records as the test set. The effect of the proposed method on the signal reconstruction task is evaluated on the test data set. The data used for testing and the data used for training are independent of each other. Experiments were carried out by the Pytorch framework for network training and testing in the Python environment and deployed on a computer equipped with Inter Xeon CPU E5-2620 and double Nvidia GeForce GTX 1080Ti GPUs. The proposed method is used to process synthetic and field noisy records. Meanwhile, some competitive methods are also used to process records, including the conventional method—band-pass filtering, wavelet transform filtering, weighted nuclear norm minimization (WNNM) and the deep learning common models—DnCNN and U-Net. For the convenience of description, the proposed method in this paper is called MSI-Net.

Synthetic data denoising results

Taking a synthetic DAS-VSP record containing complex noise as an example in Figure 5D, this paper shows the signal reconstruction results and removed noise in Figure 6 of different methods. The SNR of the synthesized noisy record is −0.5132 dB.

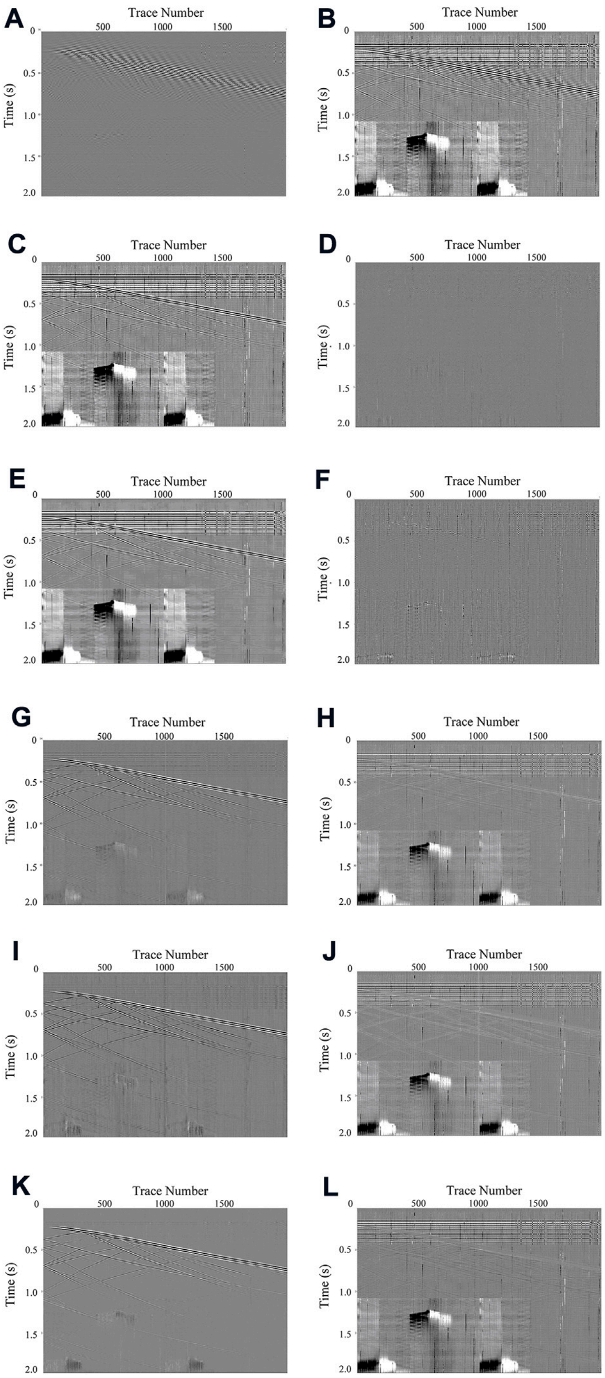

FIGURE 6
Comparisons for denoising results of different methods. **(A–B)** The denoising result with the SNR of 1.9371 dB and predicted noise of Band-pass filtering. **(C–D)** The denoising result with the SNR of 1.0421 dB and predicted noise of Wavelet transform filtering. **(E–F)** The denoising result with the SNR of 0.5712 dB and predicted noise of WNNM. **(G–H)** The denoising result with the SNR of 18.3209 dB and predicted noise of DnCNN. **(I–J)** The denoising result with the SNR of 18.4935 dB and predicted noise of U-Net **(K–L)** The denoising result with the SNR of 19.0062 dB and predicted noise of MSI-Net.

We can observe that MSI-Net can suppress many common noises at one time, and the denoising process is more efficient and faster. The results are shown in Figures 6K,L, where Figure 6K is the denoising result and Figure 6L is the difference between noisy input and the predicted pure signal, which can also be considered as the noise predicted by the method. From the quantitative analysis, on the whole, the SNR of the results of the three deep learning methods is much higher than that of the traditional methods. In deep learning methods, the SNR of the result of the MSI-Net (19.0062 dB) is the highest, which is higher than that of DnCNN (18.3209 dB) and U-Net (18.4935 dB). From the point of view of signal recovery, all kinds of signals in the wave field are recovered, and the direct wave, reflected up-going wave and incident down-going waves which were originally polluted by noise can be observed, which will be beneficial to the subsequent inversion and imaging. From the point of view of noise suppression, all noises are suppressed. In contrast, the denoising effect of the conventional method for DAS-VSP records does not meet the requirements of seismic exploration. The analysis of the processing results shows that band-pass filtering can only attenuate noise in a defined frequency band in Figure 6A, which not only fails to suppress the noise but also damages the signal. Wavelet transform filtering can only remove a part of random noise, and most of the noise is still retained in the denoised record in Figure 6C. The filtering effect of WNNM is poor, only part of the noise can be removed mechanically, there is still a large amount of noise residue in the record in Figure 6E, and obvious signal leakage can also be observed in the removed noise result in Figure 6F, which is unacceptable for reconstruction. Compared with the three traditional methods, DnCNN, U-Net and MSI-Net have better denoising effects, the noise suppression is more uniform and thorough, and there is no obvious signal leakage in the removed noise results.

The comparison results of the three deep learning methods are more focused on the high-resolution reconstruction of the signal structure. For MSI-Net, the idea of multi-scale analysis is adopted, and the suppression effect of noise is better than that of DnCNN (only at a single scale). At the same time, we can see that MSI-Net has the highest resolution in denoised recovery, and the recovery effect of weak signals is better than DnCNN and U-net, which shows that MSI-Net is more suitable for the high-resolution requirements of seismic exploration. We also analyze the signals and differences of various methods in the frequency domain as shown in Figure 7, and mainly expect to observe whether the signals leaked by various methods through the frequency spectrum. From the frequency domain, it can be seen that the traditional method does not recover the signal well. At the same time, there are different degrees of signal leakage in their differences. In contrast, the results of the three deep learning methods are closer to the original record. And it is difficult to see the leakage of the signal in the difference between the three methods. The three deep learning methods are not significantly different in the frequency domain. The comparison of the three kinds of deep learning relies more on quantitative analysis.

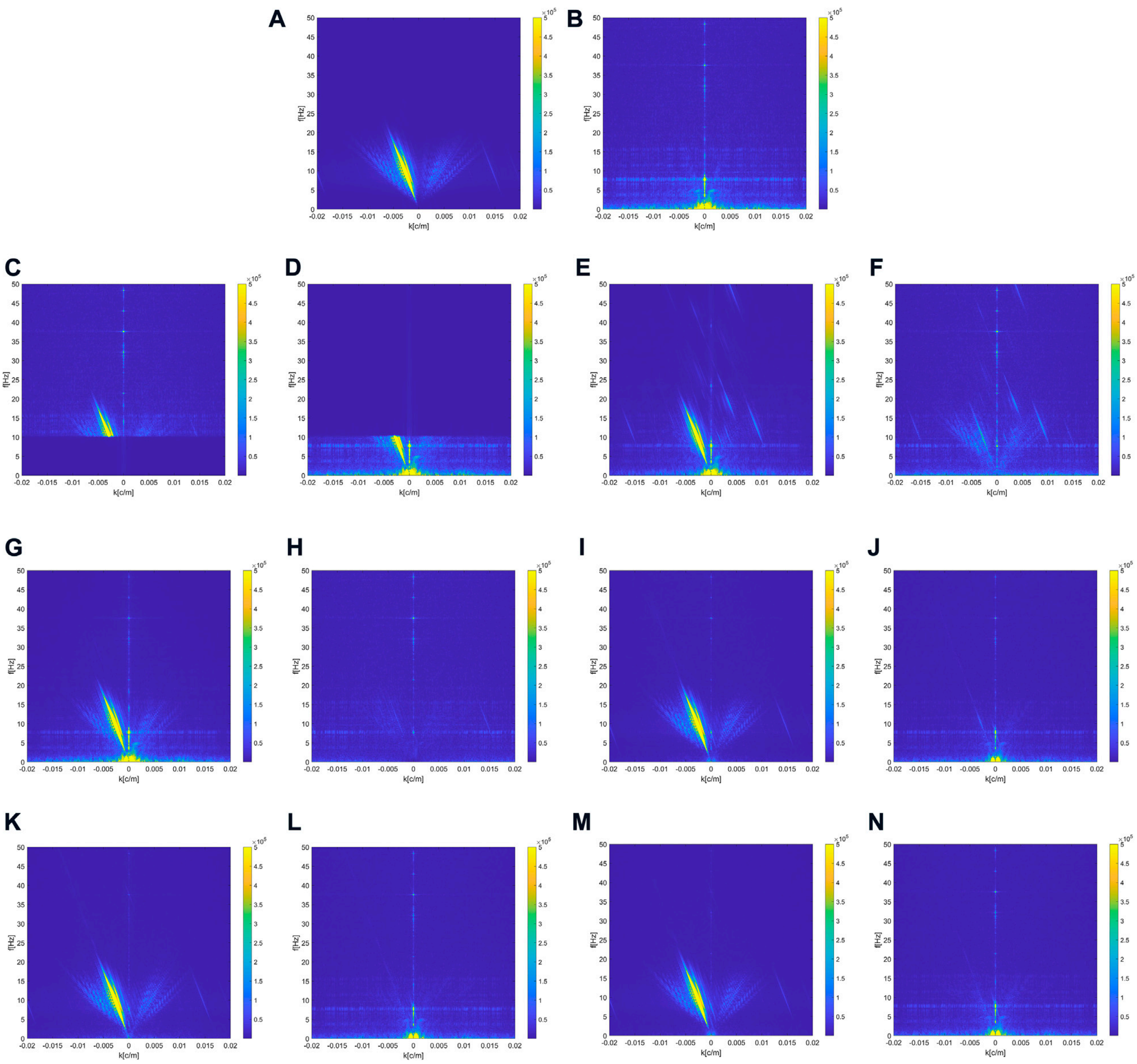

FIGURE 7
F-K domain analysis for the denoising results of different methods. **(A,B)** F-K spectrum of the pure record and noise data. **(C,D)** F-K spectra of the denoising results and predicted noise of Band-pass filtering. **(E,F)** F-K spectra of the denoising results and predicted noise of Wavelet Transform filtering. **(G,H)** F-K spectra of the denoising results and predicted noise of WNNM. **(I,J)** F-K spectra of the denoising result and predicted noise of DnCNN **(K,L)** F-K spectra of the denoising result and predicted noise of U-Net **(M,N)** F-K spectra of the denoising result and predicted noise of MSI-Net.

The signal-to-noise ratio (SNR) is one of the important indexes to measure the quality of seismic data, and the improvement of SNR is an important index to evaluate the performance of denoising methods. According to the size of the calculation, SNR can be divided into global SNR and local SNR. Global SNR is usually used to measure the overall quality of seismic data. Besides, mean absolute error (MAE), mean square error (MSE) and structural similarity (SSIM) (Wang et al., 2004) are commonly used measures. In this paper, SNR, MAE, MSE and SSIM are used to quantitatively evaluate several methods.

Generally speaking, higher SNR, SSIM and smaller MAE, MSE represent better denoising results. The denoising results of different methods are shown in Table 4, from which it can be seen that MSI-Net has the highest performance in the evaluation of four indexes. We also realize that the global SNR may not be sensitive to the quality of local data. There may be some cases

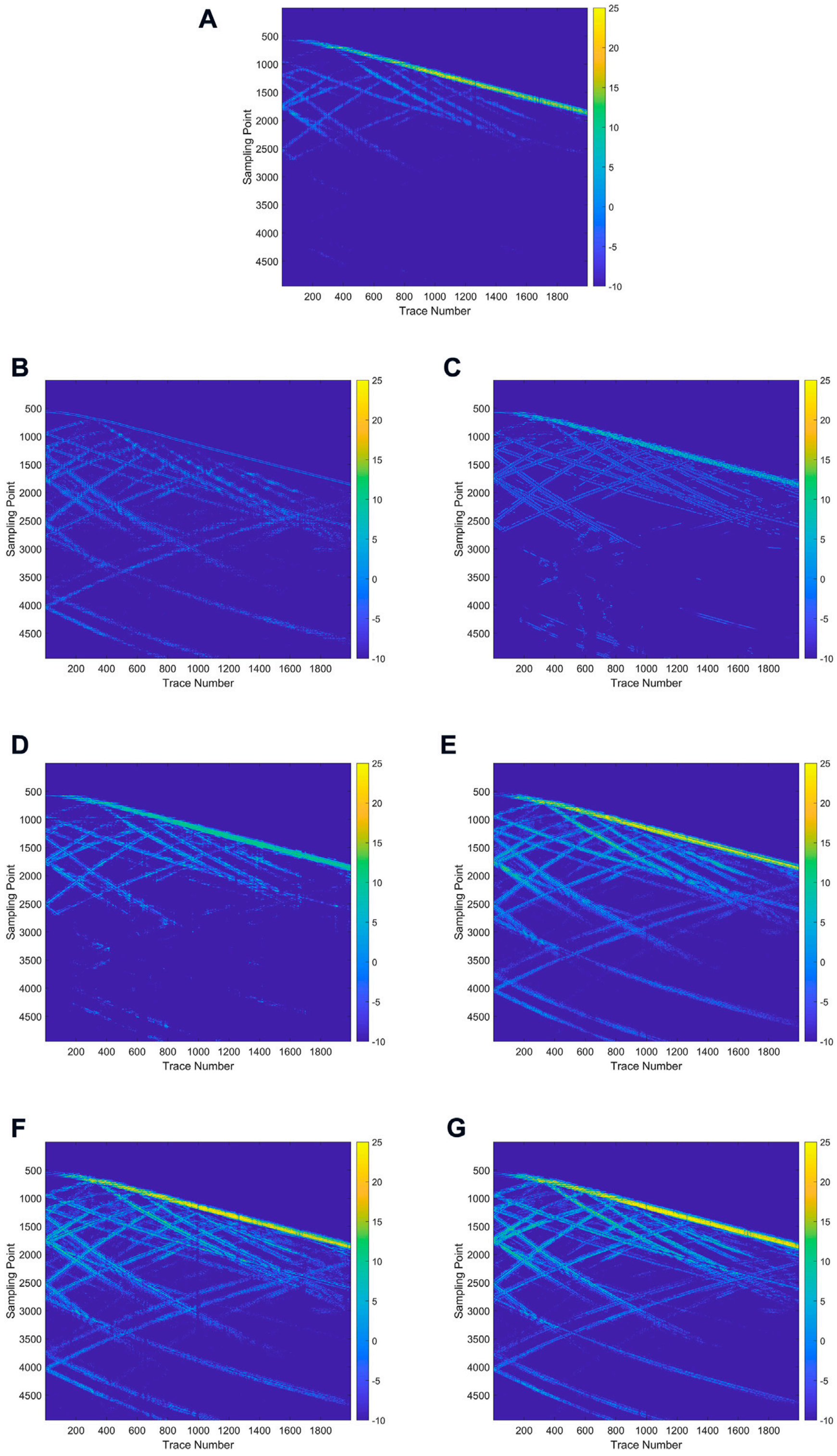

FIGURE 8
Local SNR analysis. **(A)** Local SNR of the synthetic noisy DAS-VSP data. **(B–G)** Local SNR of the denoised result of Band-pass filtering, Wavelet transform filtering, WNNM, DnCNN, U-Net, MSI-Net, respectively.

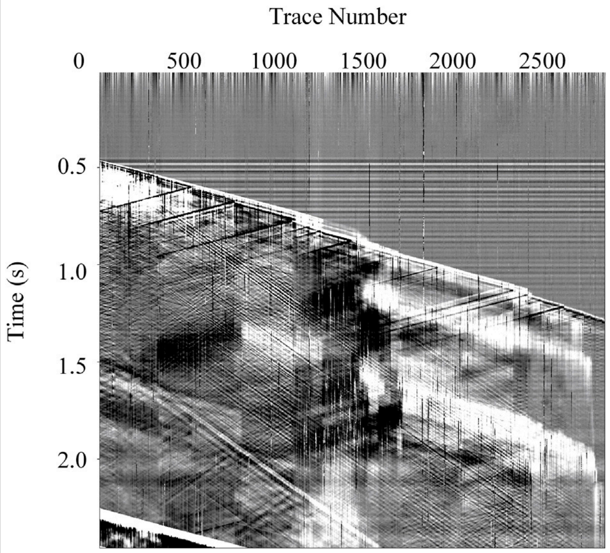

FIGURE 9
Field DAS-VSP data.

TABLE 4 Performance statistics of different denoising methods on the test sets.

Metric	MAE	MSE	SNR	SSIM
The original record	0.18832	0.12074	−0.4005	0.0516
Bandpass filtering	0.0947	0.0728	1.8221	0.1495
Wavelet transform filtering	0.1565	0.0907	0.8423	0.0518
WNNM	0.1611	0.0991	0.4593	0.0881
DnCNN	0.0293	0.0016	18.3303	0.3641
U-Net	0.0278	0.0016	18.4876	0.4081
MSI-Net	0.0274	0.0014	19.0006	0.4127

where the local data quality is poor, but the overall SNR is high, which is unacceptable for DAS records with large differences in global. The local SNR can describe the quality of local seismic data in detail, so it is used to quantitatively analyze the denoising performance of the proposed method. A moving window with a size of 5 × 5 and a step of one is used to segment DAS-VSP data, and the local SNR is calculated in the moving window. The local SNR of the data at (t, x) can be expressed as

$$\mathrm{SNR}(t,x) = 10\log_{10}\frac{\sum_{i=t-(w-1)/2}^{t+(w-1)/2}\sum_{j=x-(w-1)/2}^{x+(w-1)/2}\left(S(i,j)-\bar{S}(i,j)\right)^2}{\sum_{i=t-(w-1)/2}^{t+(w-1)/2}\sum_{j=x-(w-1)/2}^{x+(w-1)/2}\left(Dn(i,j)-\overline{Dn}(i,j)\right)^2} \tag{5}$$

where $S$is the pure signal and $Dn$is the denoised data. $\bar{S}$and $\overline{Dn}$ is the mean of $S$and Dn, respectively. And w is the window length. The local SNR of the result of the MSI-Net and the methods for comparison is shown in Figure 8, where the abscissa is the number of seismic traces, the ordinate is the sampling point and the number in the color bar is the SNR (dB). Figure 8A shows the local SNR of synthetic noisy DAS-VSP data. We can see that the local SNR of areas affected by different noises is low, which is consistent with the actual situation. Figure 8G shows the local SNR of the results processed by the proposed method. It can be seen that the method proposed in this paper has the best performance in improving the local SNR.

Denoising results of field DAS-VSP data

To verify the practicability and generalization performance of the network, the field DAS-VSP data was processed through the proposed method and other competitive methods. The time sampling interval of the DAS data shown is 400 μs and the spatial sampling interval is 1 m. The processing results are shown in Figure 9. From the field seismic records, it can be observed that there is a lot of noise in the records, and the SNR is generally low. Some random noise interferes with the presentation of effective signals seriously and even submerges the seismic events completely. Traditional methods are less effective in denoising the actual records. Band-pass filtering makes a rough distinction between signal and noise, greatly destroying the valid signal in Figure 10A. The reconstructed result of wavelet transform filtering still retains some random noise, and the recovery of the effective signal is also poor in Figure 10B. The suppression effect of WNNM on various kinds of noise is not obvious, and the result after denoising still retains a large number of various kinds of noise in Figure 10C. It can be seen that, compared with the traditional denoising methods, the MSI-Net is effective for signal recovery and noise suppression in actual records. As shown in the blue area in Figure 10F, the reflected up-going wave and the converted wave, which were originally seriously affected by noise, become clearer and more continuous after denoising, which proves that MSI-Net has a good ability to recover the signals in DAS-VSP. As shown in the red area in Figure 10F, the reflected up-going wave with weak energy can hardly be observed under the influence of noise. After being treated by the MSI-Net, it is obviously recovered. Compared with DnCNN and U-Net, the amplified signal leakage of the method proposed in this paper is obviously less. It proves that MSI-Net has a better ability to retain valid signals. This makes the MSI-Net better meet the high amplitude-preserving requirements of DAS-VSP data processing. For the actual records after processing, we also observe that the first arrival of the processed direct wave is discontinuous. The first arrival wave in the original record may be discontinuous due to the poor coupling of the optical fiber during the data acquisition. The neural network not only removes noise but also restores weak signals. This also causes the discontinuity of the first arrivals to be more prominent. This problem can be resolved during acquisition.

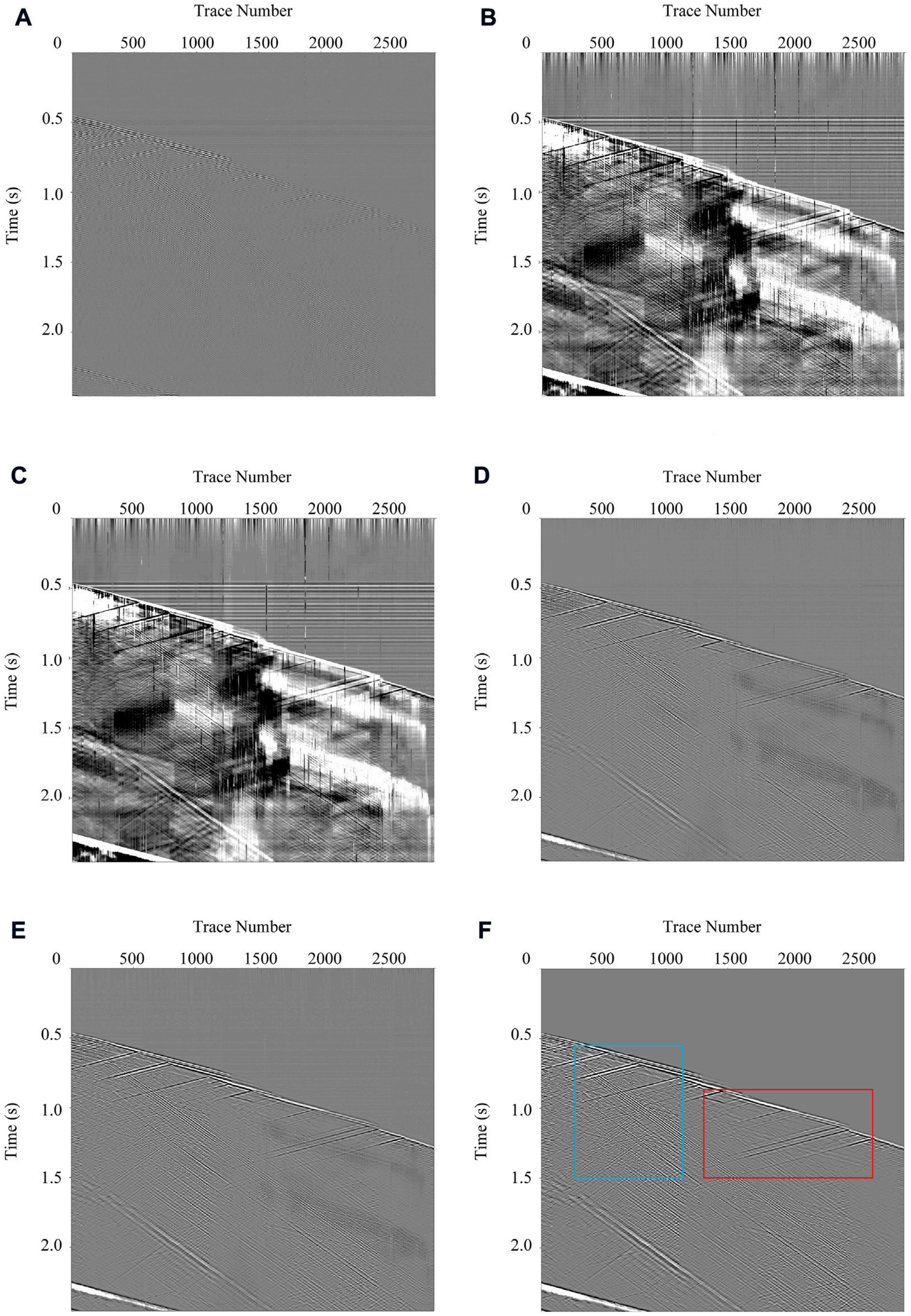

FIGURE 10
Comparisons for the denoising results of the field DAS-VSP record. **(A–F)** The denoising results for Band-pass filtering, Wavelet transform filtering, WNNM, DnCNN, U-Net, and MSI-Net, respectively.

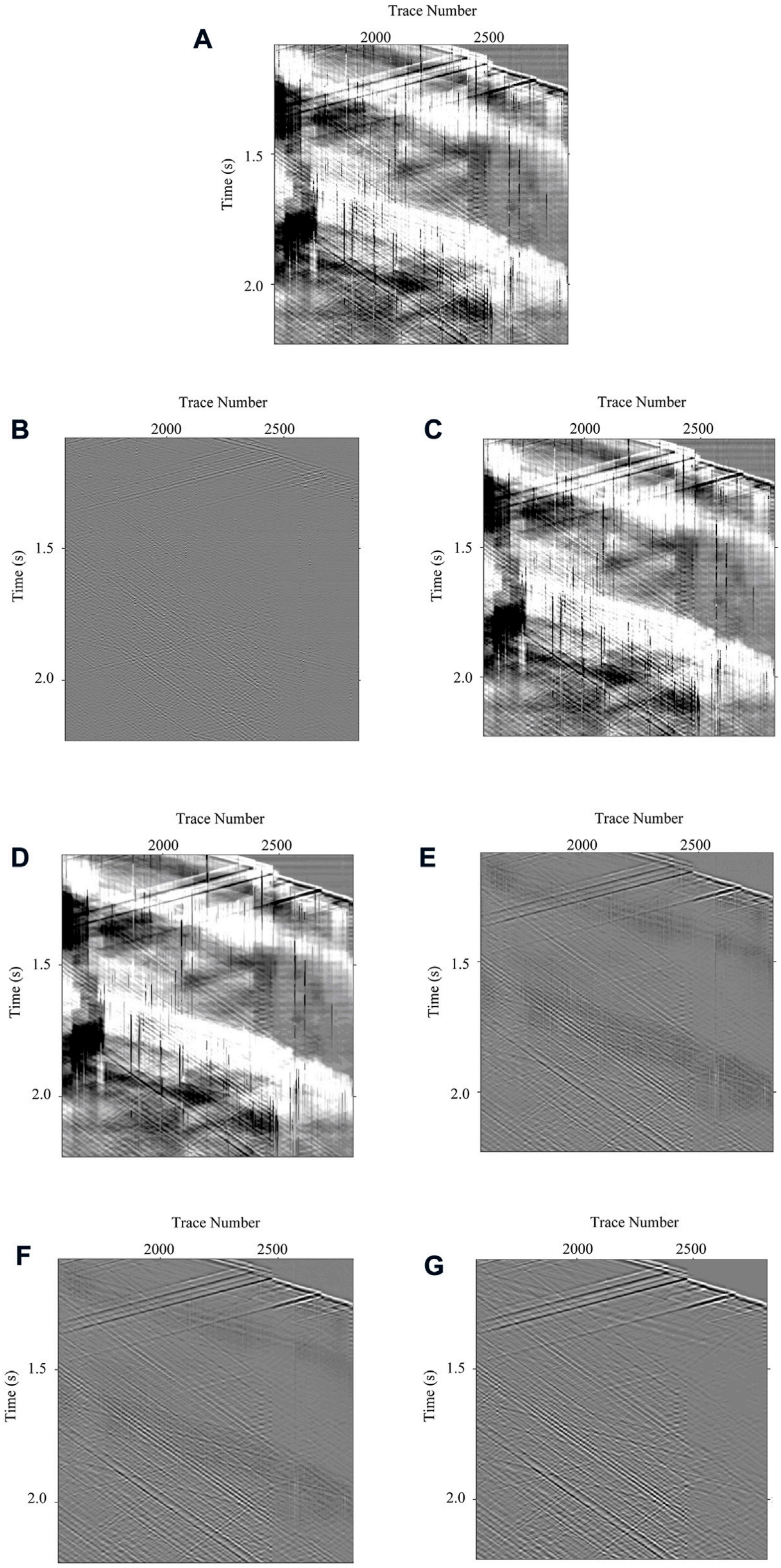

FIGURE 11
Local enlargements for the denoising results of different methods. **(A)** Local enlargements of the field noisy DAS-VSP data. **(B–G)** Local enlargements of denoising results by utilizing Band-pass filtering, Wavelet transform filtering, WNNM, DnCNN, U-Net, and MSI-Net, respectively.

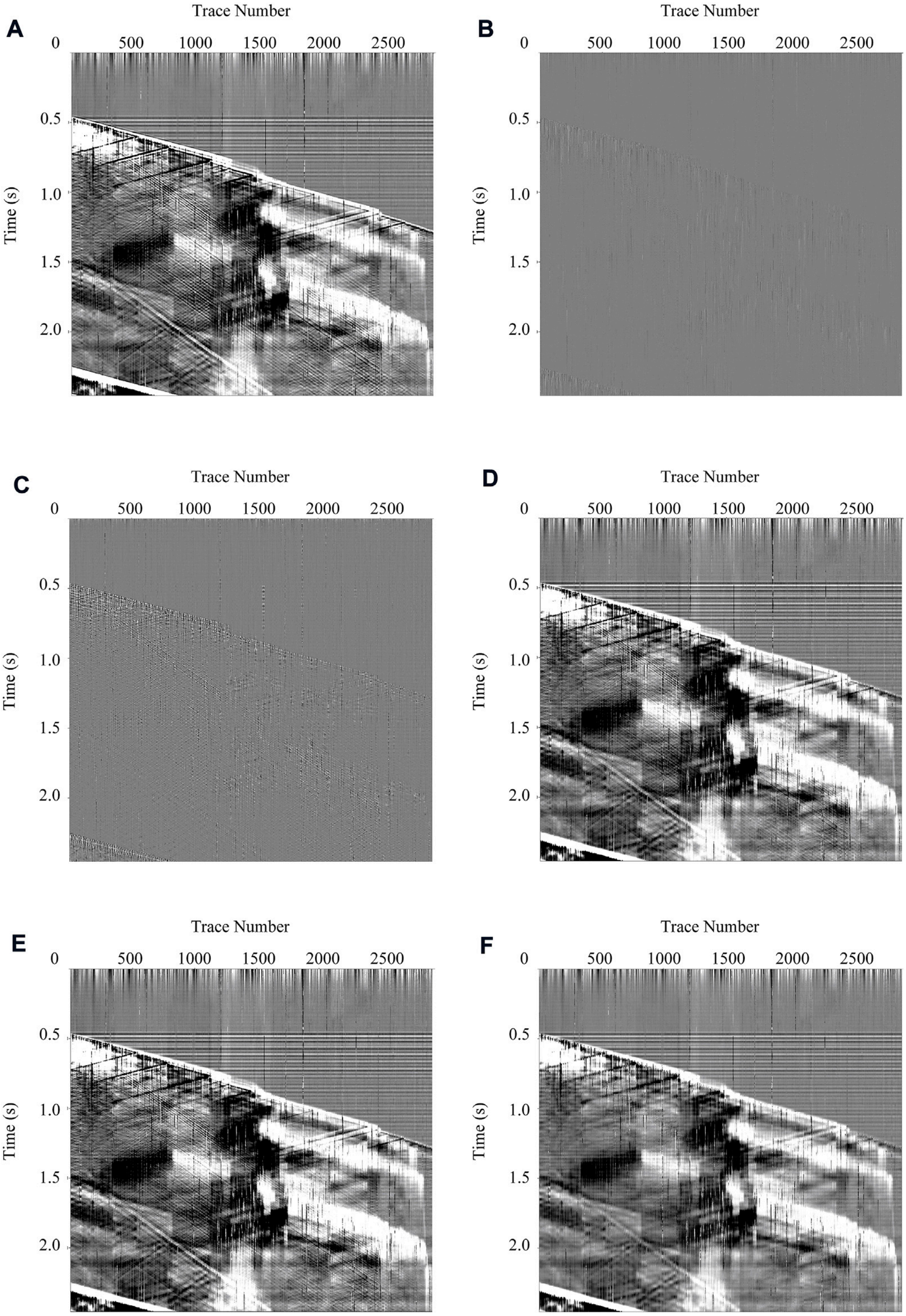

FIGURE 12
Comparisons for the predicted noise of different methods. **(A–F)** The predicted noise for Band-pass filtering, Wavelet transform filtering, WNNM, DnCNN, U-Net, and MSI-Net, respectively.

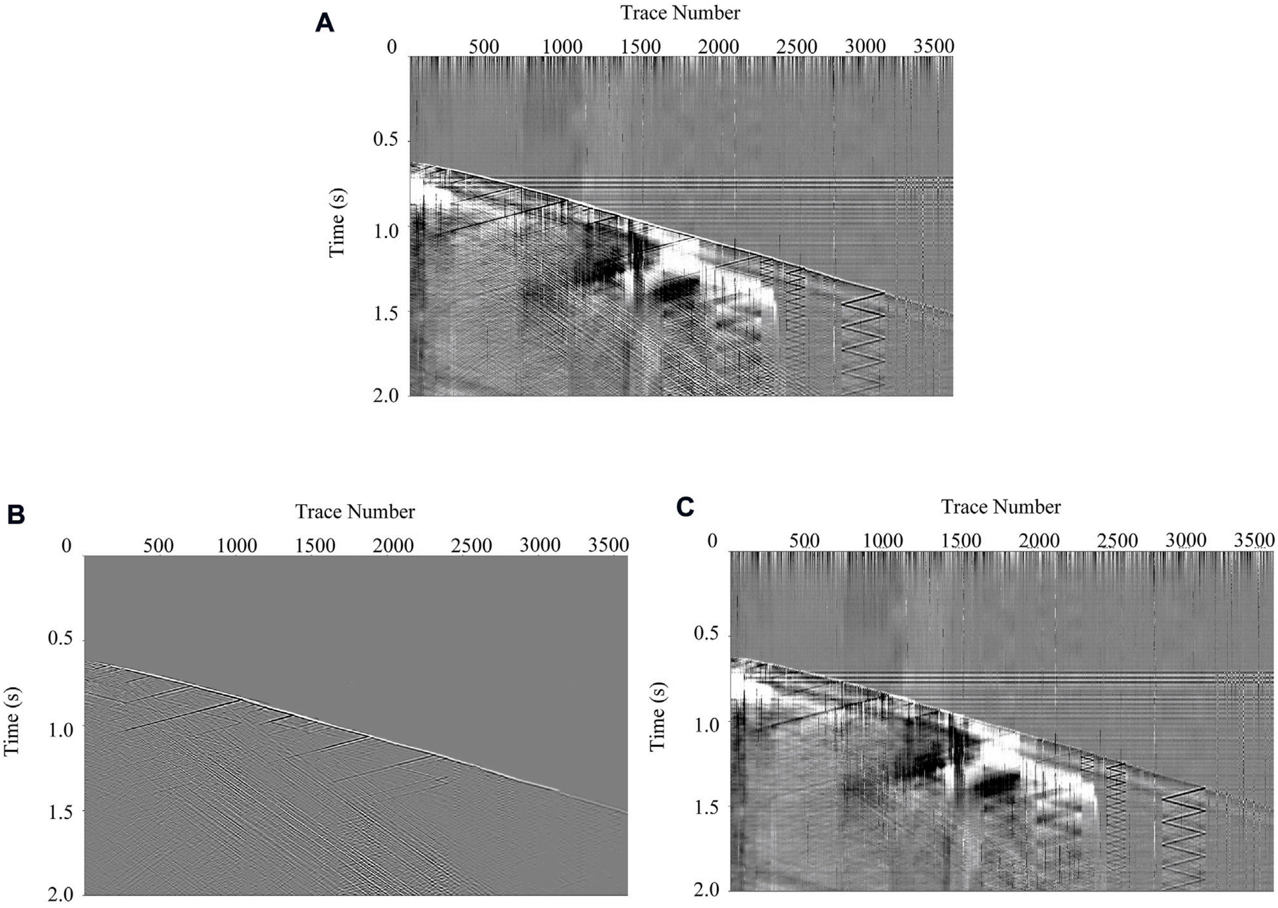

FIGURE 13
The denoising result of another field DAS-VSP record. **(A)** The new field DAS-VSP data. **(B)** The denoising results for the proposed method. **(C)** The predicted noise of the proposed method.

To further illustrate the denoising ability of different methods, we selected a representative local enlargement to evaluate them in detail in Figure 11. Though the interference of random noise can be eliminated basically, the three deep learning methods have different performances in the recovery of signals. Observing the magnified partial processing results, it can be found that the recovered signals recovered by DnCNN shown in Figure 11E are not continuous due to the relatively small receptive field. In DnCNN, the features are only based on single-scale analysis, and the expansion of the receptive field can only depend on the increase of the number of layers, which makes it difficult to expand the receptive field of DnCNN too much.

The continuity of reconstructed signals by U-Net shown in Figure 11F is relatively better, but some details of the signals are still missing. On the whole, the MSI-Net has more advanced effects on the high-resolution reconstruction of signals, whether in the maintenance of events continuity or the recovery of signal details as shown in Figure 11G. From the local view, the method proposed in this paper is obviously better for signal recovery. Specifically, DnCNN is always maintained in high-resolution representation, so the prediction of the signal may be limited by the local receptive field, which is often vague. U-Net adopts the processing mode of downsampling before upsampling, and its recovery effect for high resolution is not as good as that of MSI-Net. The MSI-Net adopts a multi-scale processing method, and it also frequently uses information exchange among scales, which better fuses multi-scale signals, so it has a better effect on high-resolution restoration.

In addition, the difference between each method is shown in Figure 12. From the difference, we can observe that there is often some residual signal in the results processed by the conventional method. For example, the leakage of the signal can be clearly observed in the difference in the band-pass filtering. In contrast, it can be seen that the signal leakage in the difference between the three deep learning-based methods is very small. Among them, there is basically no signal leakage in the difference between the MSI-Net. It proves that the method proposed in this paper basically does not damage the effective signal.

The generalization ability is a crucial evaluation criterion for a denoising network in practice applications. The main purpose of training the network is to obtain capture features and learns the laws from the training data. The model should have the generalization ability that can make the trained model perform well when processing different data with a similar pattern. To test the generalization performance of MSI-Net, we utilize MSI-Net to process more records. Figure 13A shows other DAS records that contain various types of noise. It was collected from other wells in the same region as the record shown in Figure 9. Figure 13B shows the result processed by MSI-Net, and Figure 13C shows the difference after denoising. It can be seen that for each DAS record, the effective signal has been completely restored. The MSI-Net can still maintain good performance in the denoising of other records, indicating that our model has a good generalization ability for DAS records. At the same time, the different kinds of noise in the DAS-VSP record were completely predicted. In particular, the trained network can also accurately predict the coupled noise in the record. This is even more important for the high-resolution reconstruction of the DAS record.

Conclusion

In this paper, we proposed a network for high-resolution reconstruction of DAS-VSP records. With the help of multi-scale feature learning and frequent information interaction between scales, the network can successfully acquire abundant multi-resolution characterizations. The low-resolution information of different scales is used to supplement the high-resolution information at the same time, to realize accurate high-resolution reconstruction. The proposed method achieves an excellent reconstruction effect in processing synthetic and field DAS-VSP records, especially improving the SNR and resolution. Benefiting from multi-scale analysis, the network recovers local details better than previous general network architectures. High-resolution reconstructed records can have positive implications for subsequent imaging. In addition, the multi-scale analysis also inevitably increases the computational cost, so more efficient multi-scale strategies will be explored in the future.

Data availability statement

The raw data supporting the conclusions of this article will be made available by the authors, without undue reservation.

Author contributions

HW (First Author): Conceptualization, Methodology, Software, Investigation, Formal Analysis, Writing—Original Draft; JL (Corresponding Author): Data Curation, Funding Acquisition, Resources, Supervision; DS: Software, Validation; XD (Corresponding Author): Data Curation, Visualization, Investigation; YL (Corresponding Author): Conceptualization, Funding Acquisition, Resources, Supervision, Writing—Review and Editing.

Funding

This work was supported by the National key research and development program of China under Grant 2021YFA0716800 and National Science Foundation of China under Grant 42230805, 42074123. Besides, this work was also supported by Key project of Guangdong Province for Promoting High-quality Economic Development (Marine Economic Development) in 2022: Research and development of key technology and equipment for Marine vibroseis system (GDNRC(2022)29).

Conflict of interest

The authors declare that the research was conducted in the absence of any commercial or financial relationships that could be construed as a potential conflict of interest.

Publisher's note

References

Amezquita Sanchez, J. P., Chavez Alegria, O., Valtierra Rodriguez, M., Abeyro, Lopez Cruz, Jose, Antonio, Millan Almaraz, J. R., et al. (2017). Detection of ULF geomagnetic anomalies associated to seismic activity using EMD method and fractal dimension theory. *IEEE Lat. Am. Trans.* 15 (2), 197–205. doi:10.1109/tla.2017.7854612

Anvari, R., Siahsar, M. A. N., Gholtashi, S., Roshandel Kahoo, A., and Mohammadi, M. (2017). Seismic random noise attenuation using synchrosqueezed wavelet transform and low-rank signal matrix approximation. *IEEE Trans. Geosci. Remote Sens.* 55 (11), 6574–6581. doi:10.1109/tgrs.2017.2730228

Binder, G., Titov, A., Liu, Y., Simmons, J., Tura, A., Byerley, G., et al. (2020). Modeling the seismic response of individual hydraulic fracturing stages observed in a time-lapse distributed acoustic sensing vertical seismic profiling survey. *Geophysics* 85 (4), T225–T235. doi:10.1190/geo2019-0819.1

Bekara, M., and Van der Baan, M. (2009). “Random and coherent noise attenuation by empirical mode decomposition. *Geophysics* 74 (5), V89–V98

Canales, L. L. (1984). “Random noise reduction,” in 54th Annual International Meeting, SEG, Expanded Abstracts, 525–527.

Chen, Y., and Fomel, S. (2018). EMD-seislet transform. *Geophysics* 83 (1), A27–A32. doi:10.1190/geo2017-0554.1

Chen, Y., Jianwei, M., and Fomel, S. (2016). Double-sparsity dictionary for seismic noise attenuation. *Geophysics* 81 (2), V103–V116. doi:10.1190/geo2014-0525.1

Chen, Y., Zhang, M., Bai, M., and Chen, W. (2019). Possible site effects revealed by regional earthquake records in the qaidam basin, China. *Seismol. Res. Lett.* 90, 280–293. doi:10.1785/0220180095

Cheng, J., Chen, K., and Sacchi, M. D. (2015). *Application of robust principal component analysis (RPCA) to suppress erratic noise in seismic records*, 4646.

Constantinou, A., Farahani, A., Cuny, T., and Hartog, A. (2016). “Improving DAS acquisition by real-time monitoring of wireline cable coupling”, in Proc. SEG Tech. Program Expanded Abstracts, 5603–5607 10.1190/segam2016-13950092.1

Creswell, A., White, T., Dumoulin, V., Arulkumaran, K., Sengupta, B., and Bharath, A. A. (2017). Generative adversarial networks: An overview. *IEEE Signal Process. Mag.* 35 (1), 53–65. doi:10.1109/msp.2017.2765202

Dong, X., Li, Y., Zhong, T., Wu, N., and Wang, H. (2022). Random and coherent noise suppression in DAS-VSP data by using a supervised deep learning method. *IEEE Geosci. Remote Sens. Lett.* 19, 1–5. doi:10.1109/lgrs.2020.3023706

Gan, S., Wang, S., Chen, Y., Zhang, Y., and Jin, Z. (2015). Dealiased seismic data interpolation using seislet transform with low-frequency constraint. *IEEE Geosci. Remote Sens. Lett.* 12 (10), 2150–2154. doi:10.1109/lgrs.2015.2453119

Goodfellow, I. J., Pouget-Abadie, J., Mirza, M., Xu, B., Warde-Farley, D., Ozair, S., et al. (2020). Generative adversarial networks. *Communications of the ACM* 63 (11), 139–144.

Gorszczyk, A., Adamczyk, A., and Malinowski, M. (2014). Application of curvelet denoising to 2D and 3D seismic data; practical considerations. *J. Appl. Geophys.* 105, 78–94. doi:10.1016/j.jappgeo.2014.03.009

He, K., Zhang, X., Ren, S., and Sun, J. (2016). “Deep residual learning for image recognition,” in 2016 IEEE Conference On Computer Vision And Pattern Recognition (Cvpr), 770. doi:10.1109/CVPR.2016.90

Jiang, J., Ren, H., and Zhang, M. (2021). A Convolutional Autoencoder Method for Simultaneous Seismic Data Reconstruction and Denoising. *IEEE geoscience and remote sensing letters* 19, 1–5.

Jiang, T., Zhan, G., Hance, T., Sugianto, S., Soulas, S., and Kjos, E. (2016). “Valhall dual-well 3D DAS VSP field trial and imaging for active wells”, in Proc. SEG Tech. Program Expanded Abstracts, 5582–5586 10.1190/segam2016-13871754.1.

Kesharwani, A., Aggarwal, V., Singh, S. B. R, R., and Kumar, A. (2021). Marine seismic signal denoising using VMD with Hausdorff distance and wavelet transform. *J. Def. Model. Simul.* 19 (4). doi:10.1177/15485129211036044

Lecun, Y., Bengio, Y., and Hinton, G. (2015). Deep learning. *Nat. Lond.* 521 (7553), 436–444. doi:10.1038/nature14539

Li, W. (2018). *Classifying geological structure elements from seismic images using deep learning*. SEG Technical Program, Expanded Abstracts, 4643–4648. doi:10.1190/segam2018-2998036.1

Li, J., Wu, X., and Hu, Z. (2022). Deep Learning for Simultaneous Seismic Image Super-Resolution and Denoising. *IEEE transactions on geoscience and remote sensing* 60, 1–11.

Liu, X., Chen, X., Li, J., and Chen, Y. (2021). Nonlocal weighted robust principal component analysis for seismic noise attenuation. *IEEE Trans. Geosci. Remote Sens.* 59 (2), 1745–1756. doi:10.1109/tgrs.2020.2996686

Liu, D., Deng, Z., Wang, C., Wang, X., and Chen, W. (2022). An Unsupervised Deep Learning Method for Denoising Prestack Random Noise. *IEEE geoscience and remote sensing letters* 19, 1–5.

Lu, W., and Li, F. (2013). Seismic spectral decomposition using deconvolutive short-time Fourier transform spectrogram. *Geophysics* 78, V43–V51. doi:10.1190/geo2012-0125.1

Mendel, J. (1977). White-noise estimators for seismic data processing in oil exploration. *IEEE Trans. Autom. Contr.* 22 (5), 694–706. doi:10.1109/tac.1977.1101597

Mousavi, S. M., Langston, C. A., and Horton, S. P. (2016). Automatic microseismic denoising and onset detection using the synchrosqueezed continuous wavelet transform. *Geophysics* 81 (4), V341–V355. doi:10.1190/geo2015-0598.1

Neelamani, R., Baumstein, A. I., Gillard, D. G., Hadidi, M. T., and Soroka, W. L., (2008). Coherent and random noise attenuation using the curvelet transform. *Lead. Edge* 27 (2), 240–248. doi:10.1190/1.2840373

Oropeza, V., and Sacchi, M. D. (2011). Simultaneous seismic data denoising and reconstruction via multichannel singular spectrum analysis. *Geophysics* 76 (3), V25–V32. doi:10.1190/1.3552706

Qiu, C., Wu, B., Liu, N., Zhu, X., and Ren, H. (2022). Deep Learning Prior Model for Unsupervised Seismic Data Random Noise Attenuation. *IEEE geoscience and remote sensing letters* 19, 1–5.

Ronneberger, O., Fischer, P., and Brox, T. (2015). *U-net: Convolutional networks for biomedical image segmentation*. 234.

Saad, O., and Chen, Y. (2020). Deep denoising autoencoder for seismic random noise attenuation. *Geophysics* 85 (4), V367–V376. doi:10.1190/geo2019-0468.1

Saad, O. M., Oboue, Yapo Abole Serge Innocent, Bai, M., Samy, L., Yang, L., and Chen, Y. (2021). Self-Attention Deep Image Prior Network for Unsupervised 3-D Seismic Data Enhancement. *IEEE transactions on geoscience and remote sensing* 60, 1–14.

Spikes, K. T., Tisato, N., Hess, T. E., and Holt, J. W. (2019). Comparison of geophone and surface-deployed distributed acoustic sensing seismic data. *Geophysics* 84 (2), A25–A29. doi:10.1190/geo2018-0528.1

Sun, K., Xiao, B., Liu, D., and Wang, J. (2019). *Deep high-resolution representation learning for human pose estimation*, 5686.

Sun, H., Yang, F., and Ma, J. (2022). Seismic Random Noise Attenuation via Self-Supervised Transfer Learning. *IEEE geoscience and remote sensing letters* 19, 1–5.

Tsai, K. C., Hu, W., Wu, X., Chen, J., and Han, Z. (2018). *First-break automatic picking with deep semisupervised learning neural network*. SEG Technical Program, Expanded Abstracts, 2181–2185. doi:10.1190/segam2018-2998106.1

Wang, F., and Chen, S. (2019). Residual Learning of Deep Convolutional Neural Network for Seismic Random Noise Attenuation. *IEEE geoscience and remote sensing letters* 16 (8), 1314–1318.

Wang, H., Li, Y., and Dong, X. (2021). Generative adversarial network for desert seismic data denoising. *IEEE Trans. Geosci. Remote Sens.* 59 (8), 7062–7075. doi:10.1109/tgrs.2020.3030692

Wang, S., Li, Y., and Zhao, Y. (2022). Attribute-guided target data separation network for DAS VSP data. *IEEE Trans. Geosci. Remote Sens.* 60, 1–16. doi:10.1109/tgrs.2021.3126022

Wang, X., and Ma, J. (2020). Adaptive dictionary learning for blind seismic data denoising. *IEEE Geosci. Remote Sens. Lett.* 17 (7), 1273–1277. doi:10.1109/lgrs.2019.2941025

Wang, Z., Bovik, A. C., Sheikh, H. R., and Simoncelli, E. P. (2004). Image quality assessment: From error visibility to structural similarity. *IEEE Trans. Image Process.* 13 (4), 600–612. doi:10.1109/tip.2003.819861

Wu, N., Li, Y., and Yang, B. (2011). Noise attenuation for 2-D seismic data by radial-trace time-frequency peak filtering. *IEEE Geosci. Remote Sens. Lett.* 8 (5), 874–878. doi:10.1109/lgrs.2011.2129552

Wu, X., Liang, L., Shi, Y., and Fomel, S. (2019). FaultSeg3D: Using synthetic datasets to train an end-to-end convolutional neural network for 3D seismic fault segmentation. *Geophysics* 84 (3), IM35–IM45. doi:10.1190/geo2018-0646.1

Yarman, C. E., Kumar, R., and Rickett, J. (2018). A model-based data-driven dictionary learning for seismic data representation. *Geophys. Prospect.* 66 (1), 98–123. doi:10.1111/1365-2478.12533

Yang, L., Wang, S., Chen, X., Saad, O. M., Chen, W., Oboue, Yapo Abole Serge Innocent, et al. (2021). Unsupervised 3-D Random Noise Attenuation Using Deep Skip Autoencoder. *IEEE transactions on geoscience and remote sensing* 60, 1–16.

Yu, S., Ma, J., and Wang, W. (2019). Deep learning for denoising. *Geophysics* 84 (6), V333–V350. doi:10.1190/geo2018-0668.1

Yuan, P., Hu, W., Wu, X., Chen, J., and Van Nguyen, H. (2019). *First arrival picking using U-net with lovasz loss and nearest point picking method*. SEG Technical Program, Expanded Abstracts, 2624–2628. doi:10.1190/segam2019-3214404.1

Zhang, G., Lin, C., and Chen, Y. (2020). Convolutional neural networks for microseismic waveform classification and arrival picking. *Geophysics* 85 (4), WA227–WA240. doi:10.1190/geo2019-0267.1

Zhang, G., Wang, Z., and Chen, Y. (2018). Deep learning for seismic lithology prediction. *Geophys. J. Int.* 215, 1368–1387. doi:10.1093/gji/ggy34

Zhang, K., Zuo, W., Chen, Y., Meng, D., and Zhang, L. (2017). Beyond a Gaussian denoiser: Residual learning of deep CNN for image denoising. *IEEE Trans. Image Process.* 26 (7), 3142–3155. doi:10.1109/tip.2017.2662206

Zhao, Y., Li, Y., and Wu, N. (2022). Distributed acoustic sensing vertical seismic profile data denoiser based on convolutional neural network. *IEEE Trans. Geosci. Remote Sens.* 60, 1–11. doi:10.1109/tgrs.2020.3042202

Zhong, T., Cheng, M., Dong, X., and Wu, N. (2022). Seismic random noise attenuation by applying multiscale denoising convolutional neural network. *IEEE Trans. Geosci. Remote Sens.* 60, 1–13. doi:10.1109/tgrs.2021.3095922

frontiers | Frontiers in Earth Science

TYPE Original Research
PUBLISHED 06 January 2023
DOI 10.3389/feart.2022.986470

OPEN ACCESS

EDITED BY
Ge Jin,
Colorado School of Mines, United States

REVIEWED BY
Jianyong Xie,
Chengdu University of Technology, China
Xiaoyue Cao,
Ministry of Education, China

*CORRESPONDENCE
Xingguo Huang,
xingguohuang@jlu.edu.cn

SPECIALTY SECTION
This article was submitted to Solid Earth Geophysics,
a section of the journal
Frontiers in Earth Science

RECEIVED 05 July 2022
ACCEPTED 05 September 2022
PUBLISHED 06 January 2023

CITATION
Wang C, Huang X, Li Y and Jensen K (2023), Removing multiple types of noise of distributed acoustic sensing seismic data using attention-guided denoising convolutional neural network.
Front. Earth Sci. 10:986470.
doi: 10.3389/feart.2022.986470

Removing multiple types of noise of distributed acoustic sensing seismic data using attention-guided denoising convolutional neural network

Cong Wang[1], Xingguo Huang[1]*, Yue Li[2] and Kristian Jensen[3]

[1]College of Instrumentation and Electrical Engineering, Jilin University, Changchun, China, [2]College of Communication Engineering, Jilin University, Changchun, China, [3]Metis Privatistskole, Bergen, Norway

In recent years, distributed optical fiber acoustic sensing (DAS) technology has been increasingly used for vertical seismic profile (VSP) exploration. Even though this technology has the advantages of high spatial resolution, strong resistance to high temperature and pressure variations, long sensing distance, DAS seismic noise has expanded from random noise to optical abnormal noise, fading noise and horizontal noise, etc. This seriously affects the quality of the seismic data and brings huge challenges to subsequent imaging, inversion and interpretation. Moreover, the noise is more complex and more difficult to simultaneously suppress using traditional methods. Therefore, for the purpose of effectively improving the signal-to-noise ratio (SNR) of DAS seismic data, we introduce a denoising network named attention-guided denoising convolutional neural network (ADNet). The network is composed of four blocks, including a sparse block (SB), a feature enhancement block (FEB), an attention block (AB) and a reconstruction block (RB). The network uses different kinds of convolutions alternately to enlarge the receptive field size and extract global feature of the input. Meanwhile, the attention mechanism is introduced to extract the hidden noise information in the complex background. The network predicts the noise, and denoised data are obtained by subtracting the predicted results from the noisy inputs. In addition, we uniquely construct a large number of complex forward models for pure seismic data training set to enhance the network suitability. The combination design improves the denoising performance and reduces computational cost and memory consumption. The results obtained from both synthetic- and field data illustrate that the network has the ability to denoise the seismic images and retrieve weak effective signals better than conventional methods and common networks.

KEYWORDS

deep learning, convolutional neural network, distributed optical fiber acoustic sensing, attention mechanism, noise suppression

1 Introduction

As an emerging signal detection technology, distributed optical fiber acoustic sensing (DAS) has been used to detect seismic signals. DAS records seismic waves using fiber optic cables that are continuously distributed from well head to bottom of the drill hole (Kobayashi et al., 2020). Compared to conventional seismic geophones, DAS has many advantages such as wide detection range, high spatial resolution, strong resistance to harsh environments, convenient layout (Ma et al., 2018). However, many challenges also result from the application of the method when it is used in seismic exploration from wells. The seismic data acquired by DAS technology have different types of effective signals and high-level noise with complex properties. The signals contain down-going direct waves, and up- and down-going reflected waves, which frequently suffer from a large amount of noise, including random noise, optical abnormal noise, fading noise and horizontal noise (Mateeva et al., 2014; Correa et al., 2017; Olofsson and Martinez, 2017). The noise may seriously decrease the signal-to-noise (SNR) of DAS seismic data, and subsequently leads to huge difficulties in imaging, inversion and interpretation. Methods for suppressing complex noise and improving SNR in geophysical data obtained from DAS are therefore desired.

In the past years, many denoising methods have been proposed and developed successively to suppress noise in seismic data. Examples include wavelet transform (Alali et al., 2018), band-pass filtering (Stein and Bartley, 1983), f-x deconvolution (Gulunay, 2017), median filtering (Huo et al., 2017; Chen et al., 2019), curvelet transform (Naghizadeh and Sacchi, 2018; Li et al., 2020), empirical mode decomposition (Gomez and Velis, 2016; Xue et al., 2019), variational mode decomposition (Yu and Ma, 2018; Feng et al., 2022) and singular value decomposition (Gan et al., 2015; Wang and Wang, 2021). These methods are effective when dealing with some random noise or Gaussian noise, but they all have limitations for DAS noise. For instance, band-pass filtering cannot separate the effective signals and noise in the same frequency bands. The sparse representation methods such as wavelet transform and curvelet transform depend on threshold functions and the need for choosing the threshold value manually. In recent years, some denoising methods have been proposed to suppress specific DAS data noise. For example, optical abnormal noise can be suppressed by median filtering and horizontal noise can be removed by dip filtering (Binder et al., 2020). However, these denoising methods have only achieved good denoising results for one or two types of noise. In addition, their application is limited by noise level and the effective signals are easy loss. When multiple types of noise exist together, the denoising results are usually unsatisfactory.

Deep learning has great potential and remarkable performance in many fields owing to its flexible modular architectures and strong representation capability. A common deep learning algorithm, convolutional neural network (CNN), is a feed forward neural network that has great feature extract ability. Many CNN-based deep learning methods have been applied for seismic exploration fields, such as seismic event detection (Wu H. et al., 2019; Binder and Tura, 2020; Yang et al., 2021), first-arrival picking (Wu Y. et al., 2019; Yuan et al., 2020; Guo et al., 2021) and seismic inversion (Feng, 2020; Wang et al., 2020; Aleardi and Salusti, 2021). Furthermore, it is also an effective tool for seismic noise suppression. Zhao et al. (2019) applied denoising convolutional neural networks (DnCNNs) to suppress low-frequency random noise. Other recently proposed noise suppressing algorithms include deep residual encoder-decoder networks (Yao et al., 2022), deep-denoising autoencoders (Saad and Chen, 2020), and the use of a CNN framework with learned noise prior to random noise suppression (Cui et al., 2022). However, the existing CNN-based denoising methods still have drawbacks. The full convolution networks ignore the connection between shallow layers and deep layers, which is disadvantageous for sufficient feature extraction. Furthermore, if networks are too deep, they cannot make full use of the effects from the shallow layers on the deep layers. This leads to increased difficulty in achieving proper training of the network. Additionally, DAS data typically contain weak reflected signals and more complex multiple noise. Thus, the requirements for proper noise suppression and signal recovery are higher.

Attention mechanism has attracted a lot of attention in the current deep learning research field and the method is widely applied to image denoising tasks. Tian et al. (2020) proposed attention-guided denoising convolutional neural networks (ADNet) for suppressing blind noise and real noise of images and showed excellent deoising effect. However, the application of attention mechanism in seismic data processing is limited. Inspired by this, we apply ADNet for DAS seismic noise suppression. The denoising network ADNet utilizes different convolutions to learn noise and signal features from the noisy input data. This allows for discrimination between the effective signals and different types of noise, which improves the training efficiency and the denoising performance. The network fuses global and local features to enhance the expressive ability of network. The complex noise background of the input DAS data frequently hides features, which increases the difficulty of training the network. Thus, we employ an attention mechanism to extract noise information present in the complex noisy data background. Additionally, to train the network, we construct a great number of synthetic DAS training sets through forward modelling using different theoretical parameters, such as main frequency of the seismic signals, well depth, trace interval, and so on. Both synthetic and field experimental results show that the proposed network can suppress different types of noise and recover the seismic signals without almost any loss of DAS seismic data.

The structure of this paper is as follows. In Section 2 we introduce the architecture of ADNet, the construction of training

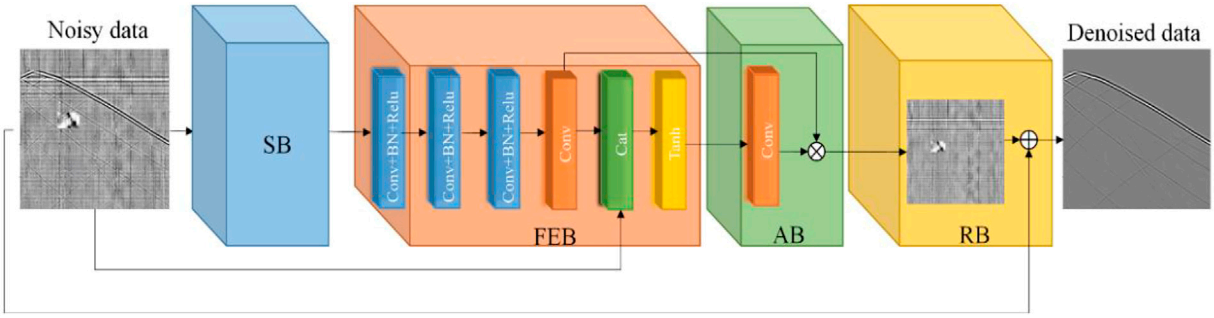

FIGURE 1
Architecture of ADNet (According to Tian et al. (2020), we modified Figure 1).

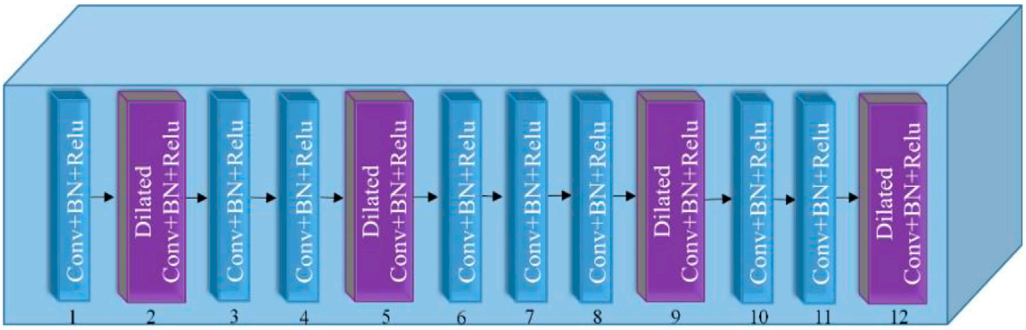

FIGURE 2
Architecture of the SB (According to Tian et al. (2020), we modified Figure 1).

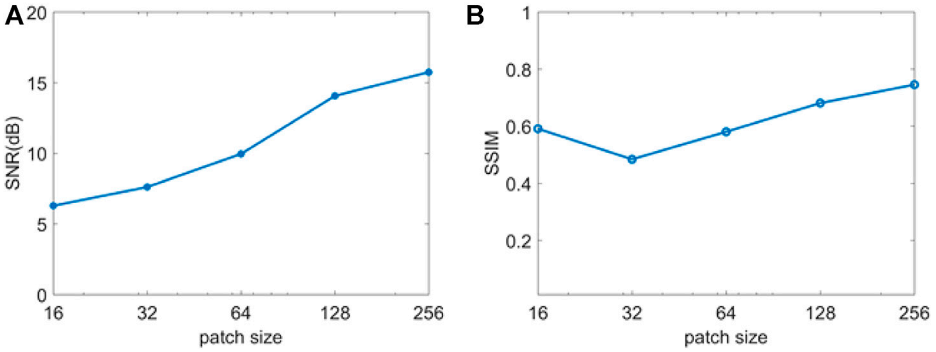

FIGURE 3
Comparison of denoised results when training the network with different patch sizes. **(A)** SNR comparison of denoised results, **(B)** SSIM comparison of denoised results.

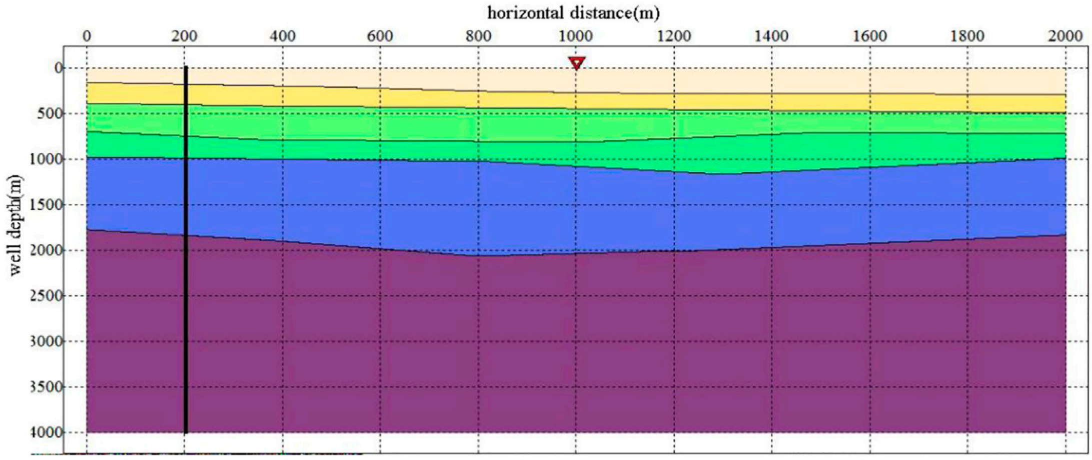

FIGURE 4
2-D geological model.

TABLE 1 Wave velocities and media densities of 2-D geological model.

Layer (from top to bottom)	1	2	3	4	5	6
P-wave velocity (m/s)	2,000	2,250	2,500	2,700	3,000	3,300
S-wave velocity (m/s)	1,000	1,125	1,250	1,350	1,530	1,800
Media density (kg/m^3)	2,010	2,105	2,200	2,200	2,200	2,245

sets and optimization of network parameters. In Section 3 we process the synthetic DAS seismic data and compared it with data obtained *via* traditional methods and a common network approach. Moreover, we process a field seismic record to verify the denoising performance of the network. Finally, Section 4 includes a discussion and conclusion of the paper.

2 Theory and methodology

2.1 Network architecture

In this section, we introduce the architecture of ADNet composed of 17 layers, and illustrated in Figure 1 It contains a sparse block (SB), a feature enhancement block (FEB), an attention block (AB) and a reconstruction block (RB). The SB is used to extract features from the noisy data to learn and distinguish between effective signals and noise. The FEB fuses the global and local features to enhance the robustness of the denoising model. The AB is used to mine noise information hidden in the complex background. And the RB predicts noise and constructs the denoised results.

The 12 forward layers are SB, and the architecture is shown in Figure 2. It consists of standard and dilated convolutions layers. The standard convolution layer contains convolution (Conv), batch normalization (BN), and activation function for a linear rectification function (Relu). BN can ensure that the input of each layer has an approximate distribution and accelerate the convergence speed of network loss function. Relu can implement gradient descent and back propagation. The standard convolution layers are set at the first, third, fourth, sixth, seventh, eighth, tenth, and eleventh layer in the SB. The dilated convolution layer includes dilated convolution with a dilated factor of 2, BN, and Relu. The dilated convolution layers are set at the second, fifth, ninth, and twelfth layer. All the convolution filter sizes of the SB are 3 × 3. The input channel of the first layer is 1, whereas other eleven layers are 64. Dilated convolution can enlarge the receptive field size and extract global input features, which is beneficial to reduce the complexity of network. The combination of two kinds of convolutions can improve the denoising performance and cut down the computational cost and memory consumption.

To reduce the influence of the shallow layers on the deep layers and mine the robust features, an FEB is designed in the network. It consists of three standard convolution layers, a Conv and activation function Tanh. The standard convolutions are installed from 13 to 15 layers and the filter sizes are 64 × 3 × 3 × 64. The Conv is fitted at the sixteenth layer and its filter size is 64 × 3 × 3 × 1. The 4-layer FEB can enhance feature learning to better restore weak effective signals. Additionally, a concatenation operation is added to fuse the input noisy data and the output of the sixteenth layer to enhance the representation ability of the denoising model. It can merge the

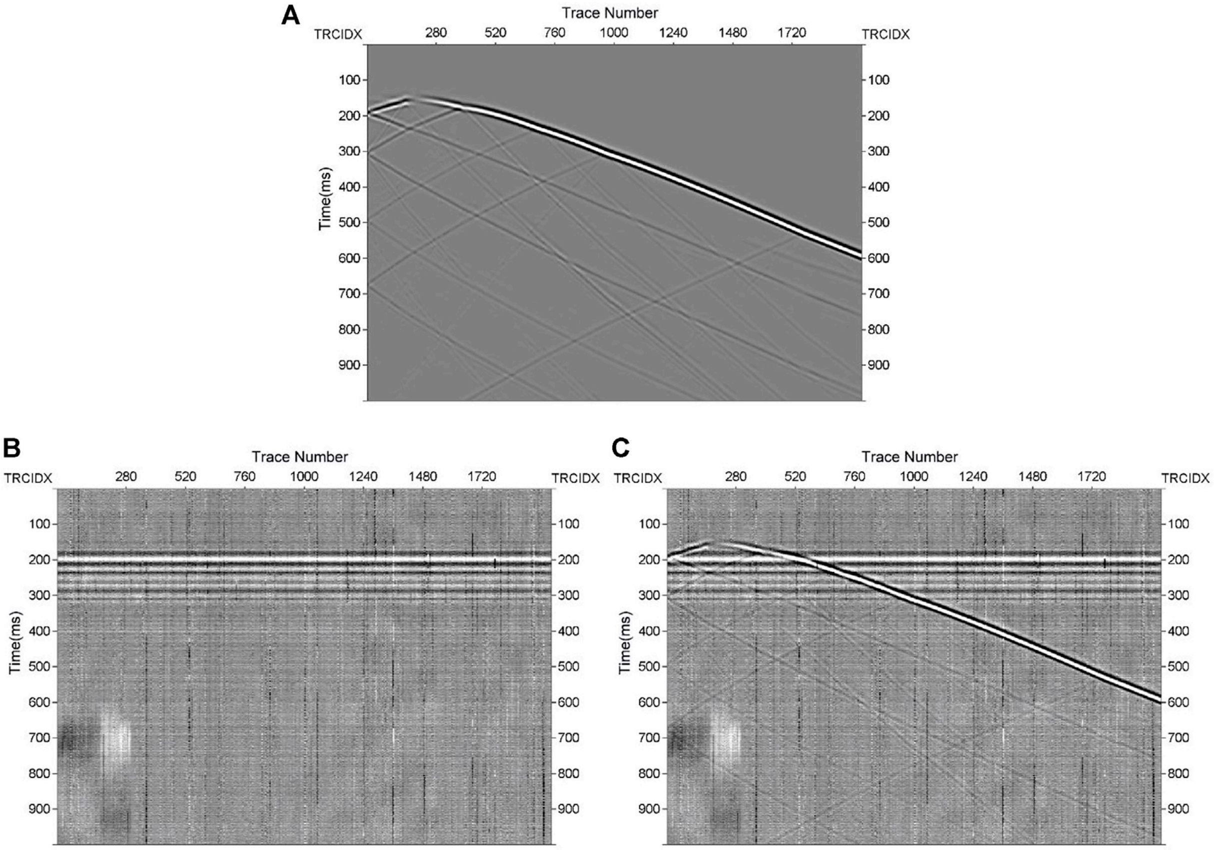

FIGURE 5
Synthetic DAS records. **(A)** Synthetic pure DAS record, **(B)** real noise record and **(C)** synthetic noisy DAS record.

features extracted from the input into new features for enhancing the expressive ability of the denoising network. And Tanh is used to convert the obtained features into nonlinearity.

As mentioned earlier, DAS data have complex noise. The effective signals are frequently covered by noise and cannot be identified. Distinguishing between noise and effective signals is a prerequisite for noise suppression tasks. Therefore, an AB is added to the network to guide the denoising model training. It includes a Conv and the filter size is $2 \times 1 \times 1 \times 1$. This is used to guide the previous stage for learning the noise information and to better distinguish between noise and effective signals. The convolution of size 1×1 from the seventeenth layer compresses the obtained features into a vector as the weights to adjust the previous stage. Then AB utilizes the obtained weights to multiply the output of the sixteenth layer for extraction of more noise features.

Finally, an RB predicts the residual data and reconstructs the denoised data. The network adjusts network parameters by predicted residual results and actual noise data when training.

2.2 Network denoising principle

The optimization of deep learning methods is principally driven by the loss function. Noisy DAS data can be regarded as a linear superposition of pure data and noise (Li et al., 2017).

$$\boldsymbol{y} = \boldsymbol{s} + \boldsymbol{n} \tag{1}$$

where $\boldsymbol{y}$, $\boldsymbol{s}$, and $\boldsymbol{n}$ stand for the noisy data, the pure data and noise. All types of noise can be represented as $\boldsymbol{n}$. The denoising model is to recover the pure data $\boldsymbol{s}$ from the noisy data $\boldsymbol{y}$. The ADNet predicts the noise through residual learning to get the predicted denoised data:

$$\hat{\boldsymbol{s}} = \boldsymbol{y} - \hat{\boldsymbol{n}} = \boldsymbol{y} - \mathbf{A}(\boldsymbol{y}; \boldsymbol{\theta}) \tag{2}$$

where $\hat{\boldsymbol{s}}$ and $\hat{\boldsymbol{n}}$ are the predicted denoised data and predicted noise, $\boldsymbol{\theta}$ is a set of learnable parameters, and $\mathbf{A}(\cdot)$ is the ADNet model. We use the mean square error (MSE) (Ephraim and Malah, 1984) to train the denoising model, so the loss function can be expressed as

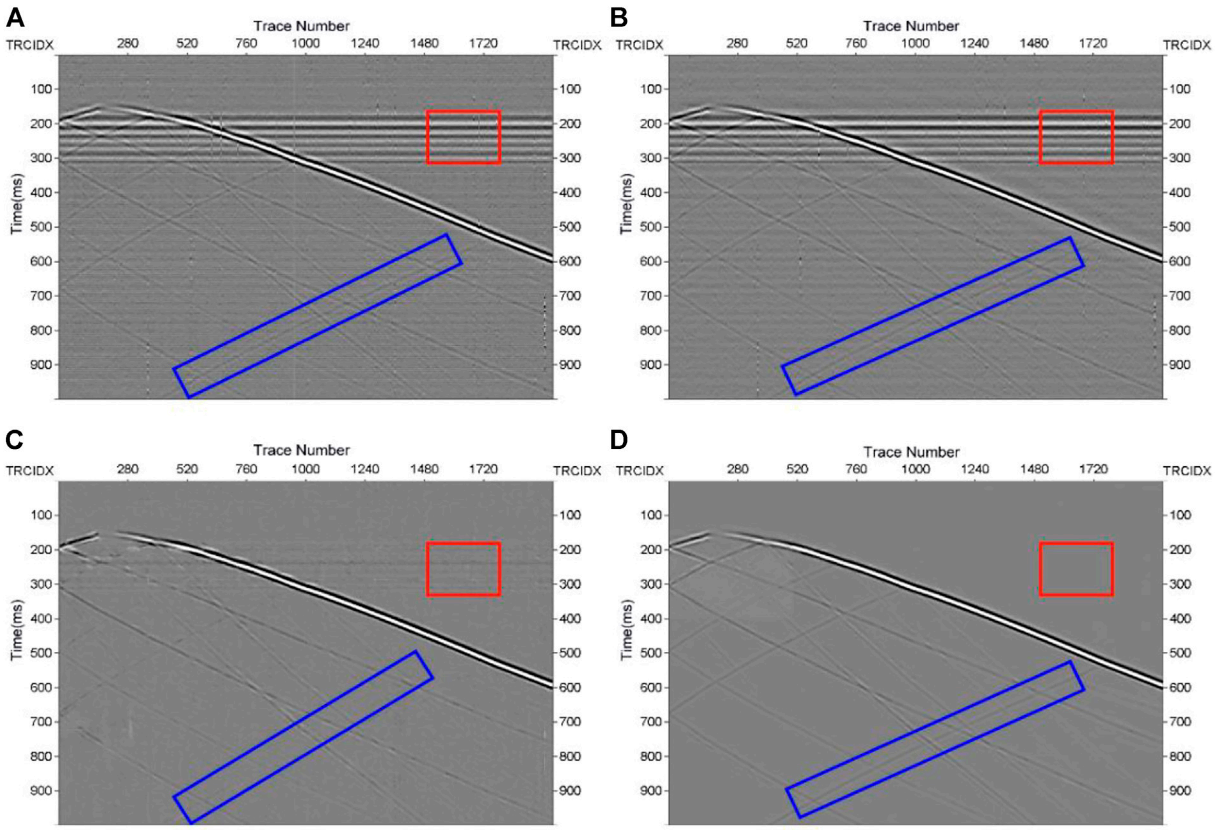

FIGURE 6
Comparison of different methods for synthetic denoising. **(A)** Denoised result of VMD, **(B)** denoised result of band-pass filtering, **(C)** denoised result of DnCNNs, **(D)** denoised result of ADNet.

$$l(\theta) = \frac{1}{2N}\sum_{i=1}^{N}\left\|A(y_i;\theta) - (y_i - s_i)\right\|_F^2 \tag{3}$$

where y_i and s_i are i^{th} pair of noisy and pure training pairs.

2.3 Quantitative analysis of denoising performance

SNR and structural similarity index (SSIM) (Wang et al., 2004) are important indicators to measure the quality of seismic data. To evaluate the denoising performance, we use SNR and SSIM to analyze the denoised results. The formula for SNR is as follows:

$$SNR = 10\log_{10}\left(\frac{\sum_{i=1}^{M}\sum_{j=1}^{N}\left(S(i,j) - \bar{S}(i,j)\right)^2}{\sum_{i=1}^{M}\sum_{j=1}^{N}\left(D(i,j) - S(i,j)\right)^2}\right) \tag{4}$$

where S represents the pure record, $\bar{S}$ represents the mean of S, and D represents the noisy record or denoised record. M and N represents the trace number and the number of sampling points, respectively. Lastly, i represents the ith trace and j represents the jth sampling point. The definition of SSIM (Wang et al., 2004) is:

$$SSIM = [l(S,D)]^{\alpha} \cdot [c(S,D)]^{\beta} \cdot [s(S,D)]^{\gamma} \tag{5}$$

here $l(S,D)$ represents the luminance comparison function, $c(S,D)$ is the contrast comparison function, and $s(S,D)$ is the structure comparison function. The definition of $l(S,D)$ is:

$$l(S,D) = \frac{2\bar{S}\bar{D} + C_1}{\bar{S}^2 + \bar{D}^2 + C_1} \tag{6}$$

where $\bar{D}$ represents the mean of D. The constant C_1 is included to avoid instability when $\bar{S}^2 + \bar{D}^2$ is very close to zero. $C_1 = (K_1 L)^2$, where L is the maximum value of the data matrix, $K_1 \ll 1$. Furthermore, $c(S,D)$ and $s(S,D)$ are defined as:

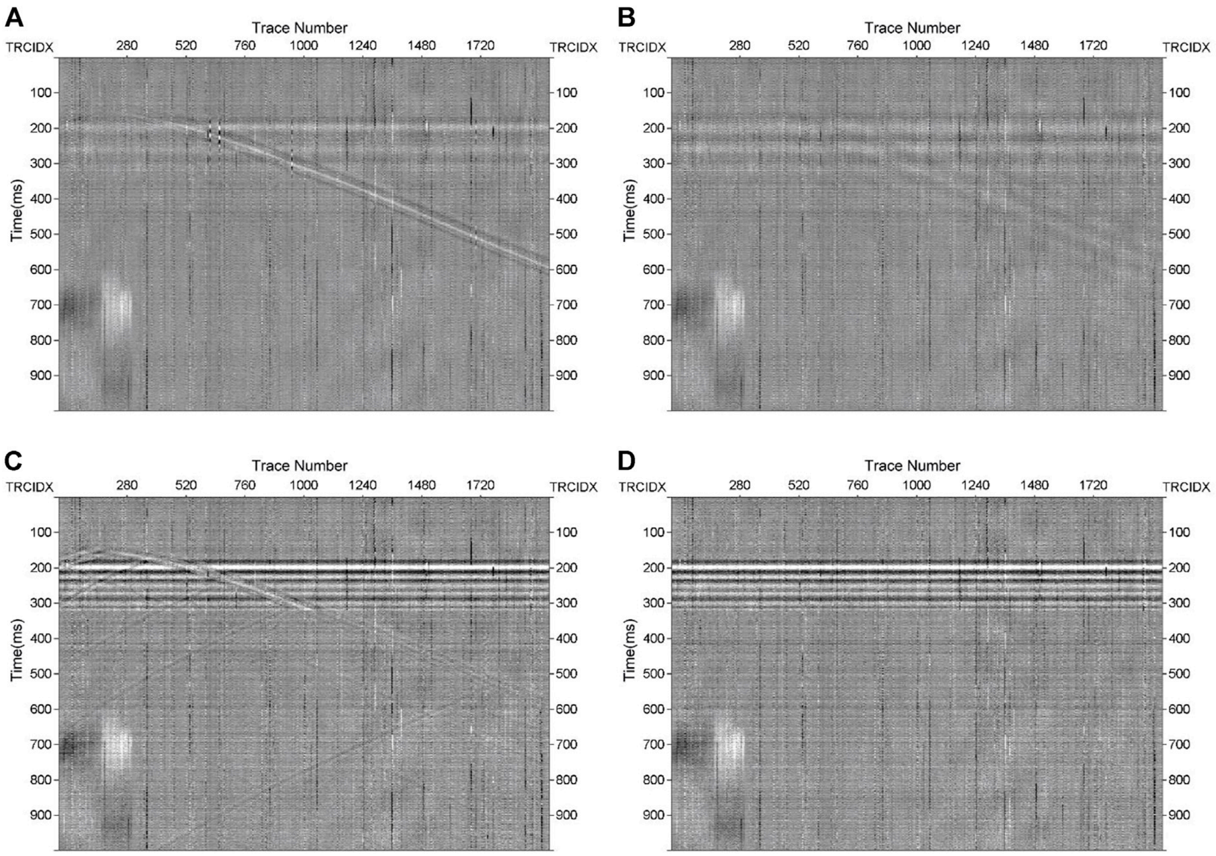

FIGURE 7
Difference maps from the four denoised results. **(A)** Difference map from VMD, **(B)** difference map from band-pass filtering, **(C)** difference map from DnCNNs, **(D)** difference map from ADNet.

$$c(S,D) = \frac{2\bar{S}\bar{D} + C_2}{\bar{S}^2 + \bar{D}^2 + C_2} \tag{7}$$

$$s(S,D) = \frac{\sigma_{SD} + C_3}{\sigma_S \sigma_D + C_3} \tag{8}$$

where $\sigma_{SD} = \frac{1}{M \times N-1}\sum_{i=1}^{M}\sum_{j=1}^{N}[S(i,j) - \bar{S}(i,j)][D(i,j) - \bar{S}(i,j)]$, and $\sigma_S = (\frac{1}{M \times N-1}\sum_{i=1}^{M}\sum_{j=1}^{N}[S(i,j) - \bar{S}(i,j)]^2)^{\frac{1}{2}}$. We also define $C_2 = (K_2L)^2$, $K_2 \ll 1$, $C_3 = C_2/2$. Larger SNR and SSIM values indicate better denoising effect.

2.4 Training set construction and network parameter optimization

Adequate and accurate training sets can improve the performance of networks. The training sets of ADNet include a pure data set and a noisy data set. As there are no existing training sets for DAS data, we performed forward velocity modelling with many types of layers (flat, inclined, concave, convex, and so on) to generate ten models. The models were obtained through an implementation of the elastic wave equation utilizing seismic wavelet source functions. From the ten models, a pure DAS data set was generated based on analysis of the signal dominant frequency, apparent velocity, and wavelet type. The dominant signal frequencies ranged from 40 Hz to 80 Hz. The apparent velocities were 1,000 m/s–3,000 m/s and the velocities increased with formation depth. The wavelet type was a standard Ricker wavelet with a sampling frequency of 2,500 Hz and a sampling interval of 1 m. A 256 × 256 moving window was used to segment the records to generate 5,000 patches of the pure data samples.

The noisy data set are made by adding DAS noise to synthetic pure records randomly. To estimate noise accurately, and to separate signals and noise well, noise in the noisy data set must be as abundant as possible. Random noise and fading noise were acquired from passive DAS data. Horizontal noise and optical abnormal noise were taken from some real noisy DAS records. We randomly added different

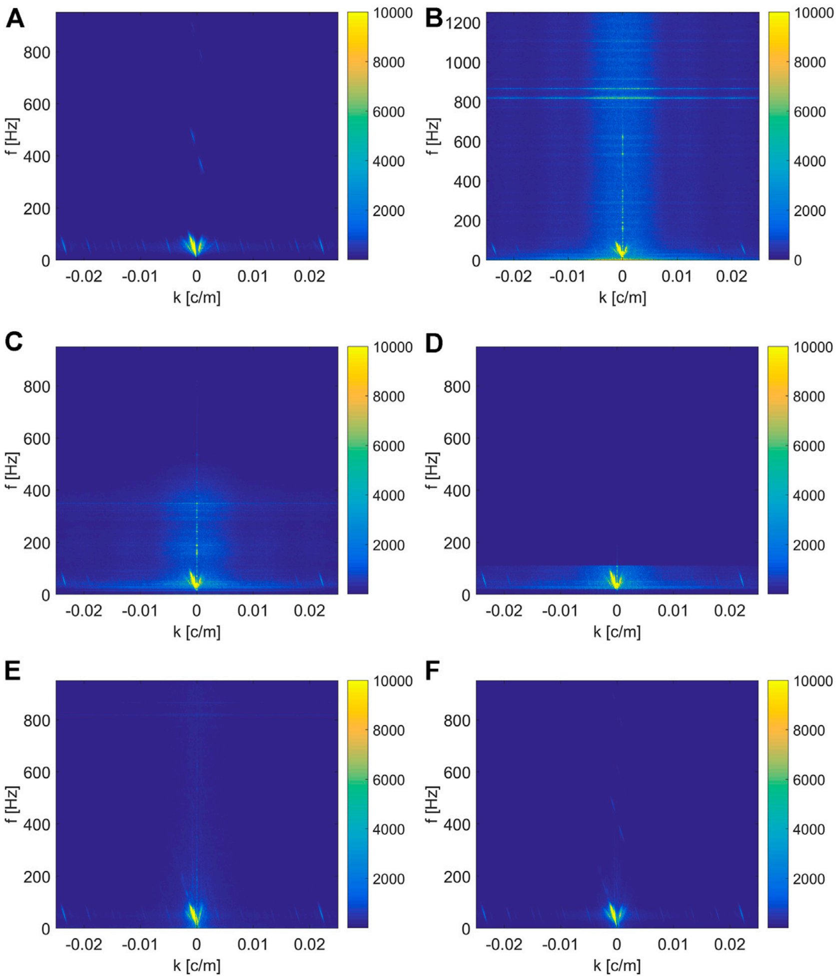

FIGURE 8
F-k spectra comparisons of denoised results. **(A)** F-k spectrum of Figure 5A, **(B)** f-k spectrum of Figure 5C, **(C–F)** f-k spectra of denoised results in Figure 6.

types and levels of noise to the synthetic pure records. The datasets were then divided into 5,000 patches noisy data samples by a 256 × 256 moving window.

The network randomly takes noisy data samples as the input and the corresponding pure data samples are regarded as labels of the network. The initial learning rate was 1e-3 and the number of epochs were 1,000. The learning rates of the 200th–500th epochs were 1e-4 and the learning rates of the final 500 epochs were 1e-5. Additionally, an Adam optimizer (Kingma and Ba, 2015) was implemented to optimize the network.

In the experiment, we verified the influence of different patch sizes for denoised results. The patch sizes were set to 16, 32, 64, 128, and 256, respectively, to train the network. We utilized a synthetic noisy dataset to verify the denoising performance, and a comparison of the results acquired through SNR and SSIM are showed in Figure 3. From the results, we can see that the network with patch size of 256 achieved the best denoising result. Thus, a patch size of 256 is an optimal choice for DAS seismic data denoising.

We applied Tensorflow 1.8.0 and Python 3.6.1 to train and test the ADNet. All the experiments were conducted on a PC with Intel Core i5-7500 CPU at 3.40 GHz and an NVIDIA GeForce GTX 1050 Ti GPU.

3 Experiment results

3.1 Denoised results comparison of synthetic DAS data

In this section, we illustrate the results from the denoising performance of ADNet by processing the synthetic DAS data generated by a six-layer forward modeling. The 2-D geological

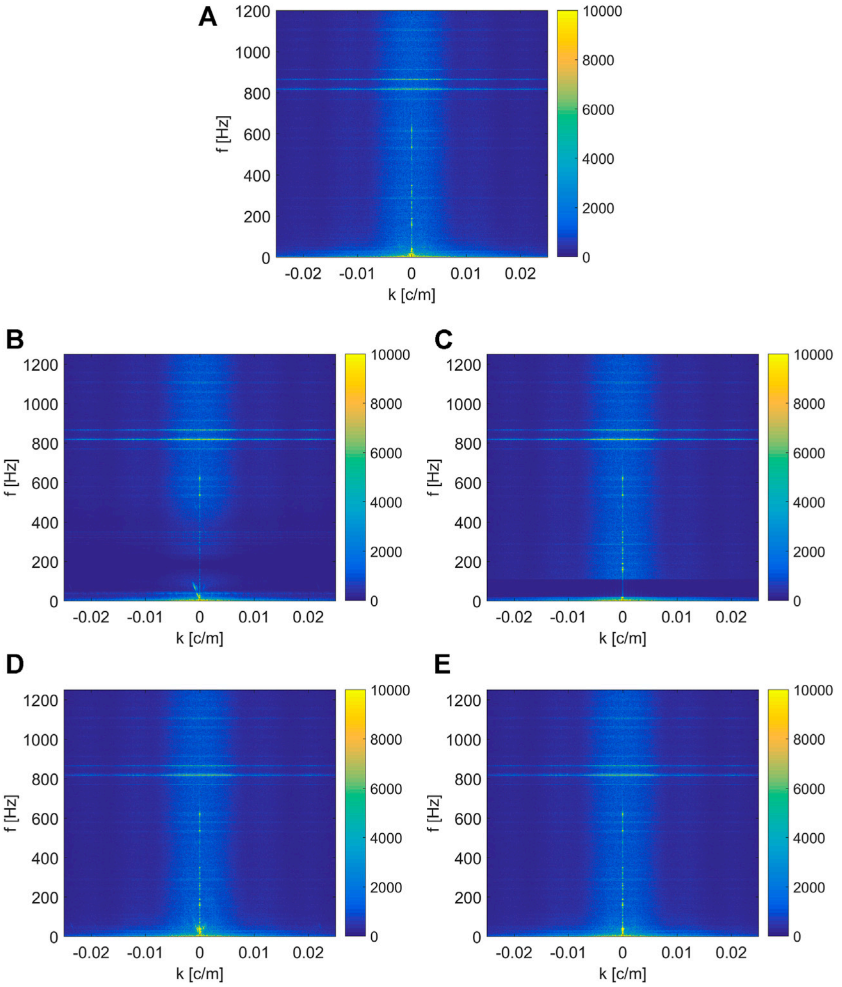

FIGURE 9
F-k spectra of difference maps. **(A)** F-k spectrum of Figure 5B, **(B–E)** F-k spectra of the difference maps in Figure 7.

model is shown in Figure 4, where the horizontal distance is 2,000 m, the well depth is 4,000 m, the inverted triangle represents the seismic source, and the vertical black line represents the fiber optic sensor. And the detailed parameters of the geological model are shown in Table 1. We constructed a synthetic DAS record with 2,000 traces and 1,000 ms, shown in Figure 5A. The wavelet type used is a zero-phased Ricker wavelet with a dominant frequency of 50 Hz. The trace interval was set to 1 m and the sampling frequency to 2,500 Hz.

The synthetic noisy record was constructed by adding noise to the synthetic pure record. Figure 5B shows the real DAS noise record and Figure 5C shows the synthetic DAS record with added noise. We can see that most of effective signals are contaminated by noise and cannot be identified easily.

To verify the denoising performance of our method, we compare the ADNet-approach with variational mode decomposition (VMD), band-pass filtering, and DnCNNs. The denoised results are shown in Figure 6. VMD has four modes. Band-pass filtering is from 20 Hz to 110 Hz. The DnCNNs used the same network layers and basic parameters as the ADNet, as well as the same training sets. As shown in Figures 6A,B, VMD and band-pass filtering cannot suppress horizontal noise and fading noise well, which is marked with red box. Compared to conventional methods, DnCNNs has better noise suppression ability. However, there is a reflected signal lost in part of the image highlighted with the blue box, and some optical abnormal noise remains, as seen in Figure 6C. By contrast, ADNet can suppress almost all the noise, and the denoised result is closest to synthetic pure record seen in Figure 5A.

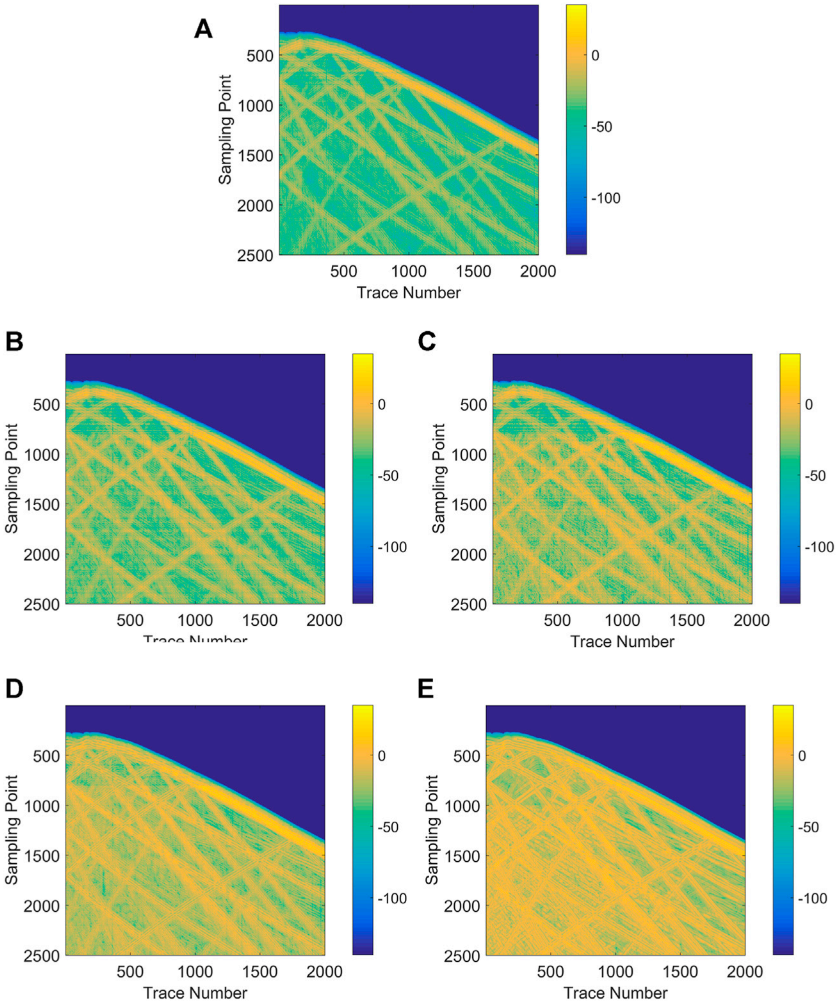

FIGURE 10
Local SNR comparison of denoised results. **(A)** Local SNR of Figure 5C, **(B–E)** local SNR of denoised results in Figure 6.

TABLE 2 Comparison of denoising performance of different methods.

	Noisy record	VMD	Band-pass filtering	DnCNNs	ADNet
SNR (dB)	−2.9260	2.3098	2.8239	11.9488	15.3275
SSIM	0.0286	0.1799	0.3406	0.6231	0.7864
Training time (hr)	—	—	—	52.00	34.33

To verify the signal recovery ability, we compared the differences between the noisy record and the denoise results obtained via the four denoising methods. The results are shown in Figure 7. In Figures 7A,B, the direct waves are muted. The difference map obtained from DnCNNs has a great number of reflected waves, which is shown in Figure 7C. Thus, all three methods lose effective signals, whereas in Figure 7D, we can see that difference map obtained via ADNet has almost no effective signal residual. This result is also closest to the noise example illustrated in Figure 5B. That demonstrates that ADNet has better noise suppression ability and stronger effective signals restoration ability.

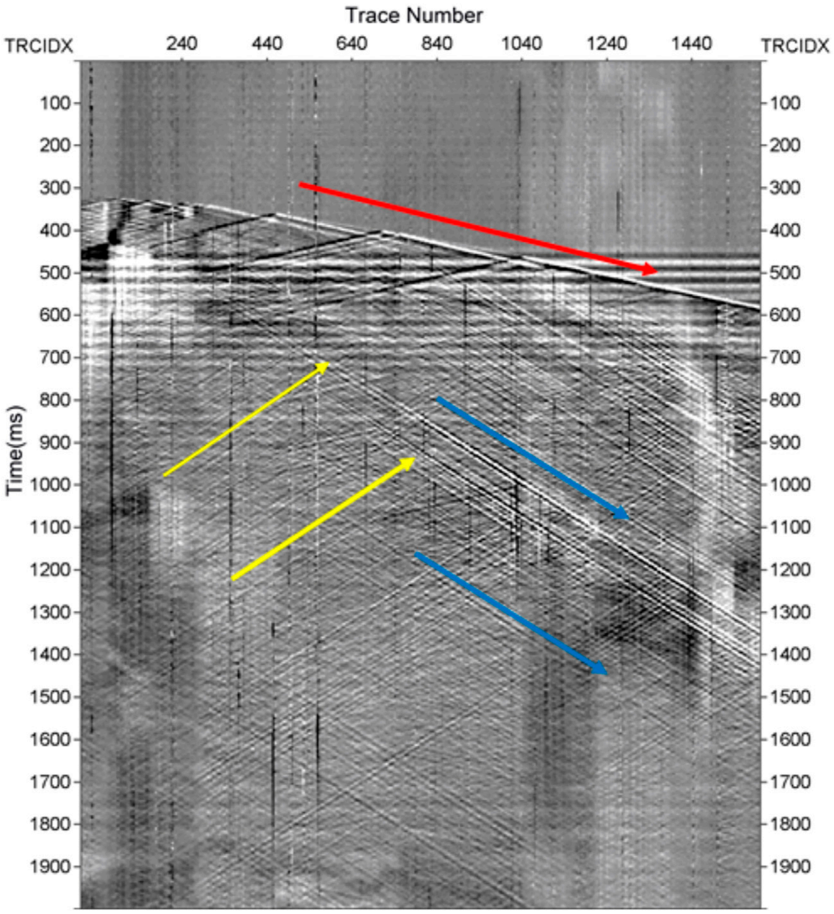

FIGURE 11
Real DAS record.

Additionally, we analyzed the denoised results in the frequency domain. The f-k spectra of the denoised results are illustrated in Figure 8. From the f-k spectra shown in Figures 8C,D, we observe that the noise has a wide frequency band compared to the effective signals. The denoised results from VMD and band-pass filtering have plenty of noise residual. By contrast, the f-k spectra in Figures 8E,F are closer to the pure record spectrum. Furthermore, the f-k spectra of the difference maps are plotted in Figure 9. We see here that part of effective signals is left in Figures 9B,D. This again indicates the ADNet has the best denoising effect.

To compare the denoising results in even more detail, we show the local SNR in Figure 10. The local SNR and global SNR have the same formula. From the results, we can see that local SNR of ADNet is closer to yellow, which indicates higher SNR. Additionally, to quantitatively analyze the denoising performance, we compare SNR, SSIM and training time in the Table 2. The denoised results from ADNet increases approximately 18 dB. The higher SNR and SSIM values indicate better denoising performance than the results obtained with the three other methods. In addition, the training time of ADNet is shorter than that of DnCNNs.

3.2 Field DAS data denoised results

Next, we processed a field DAS record from the Tarim Basin of Xinjiang located in the northwest China to test the denoising performance of ADNet and compare the result with the denoised results of VMD, band-pass filtering and DnCNNs. Figure 11 shows the real DAS record. The red arrow represents the direct wave, and the yellow and blue arrows represent up-going reflected waves and down-going reflected waves, respectively. The record contains multiple types of noise and effective signals cannot be easily identified.

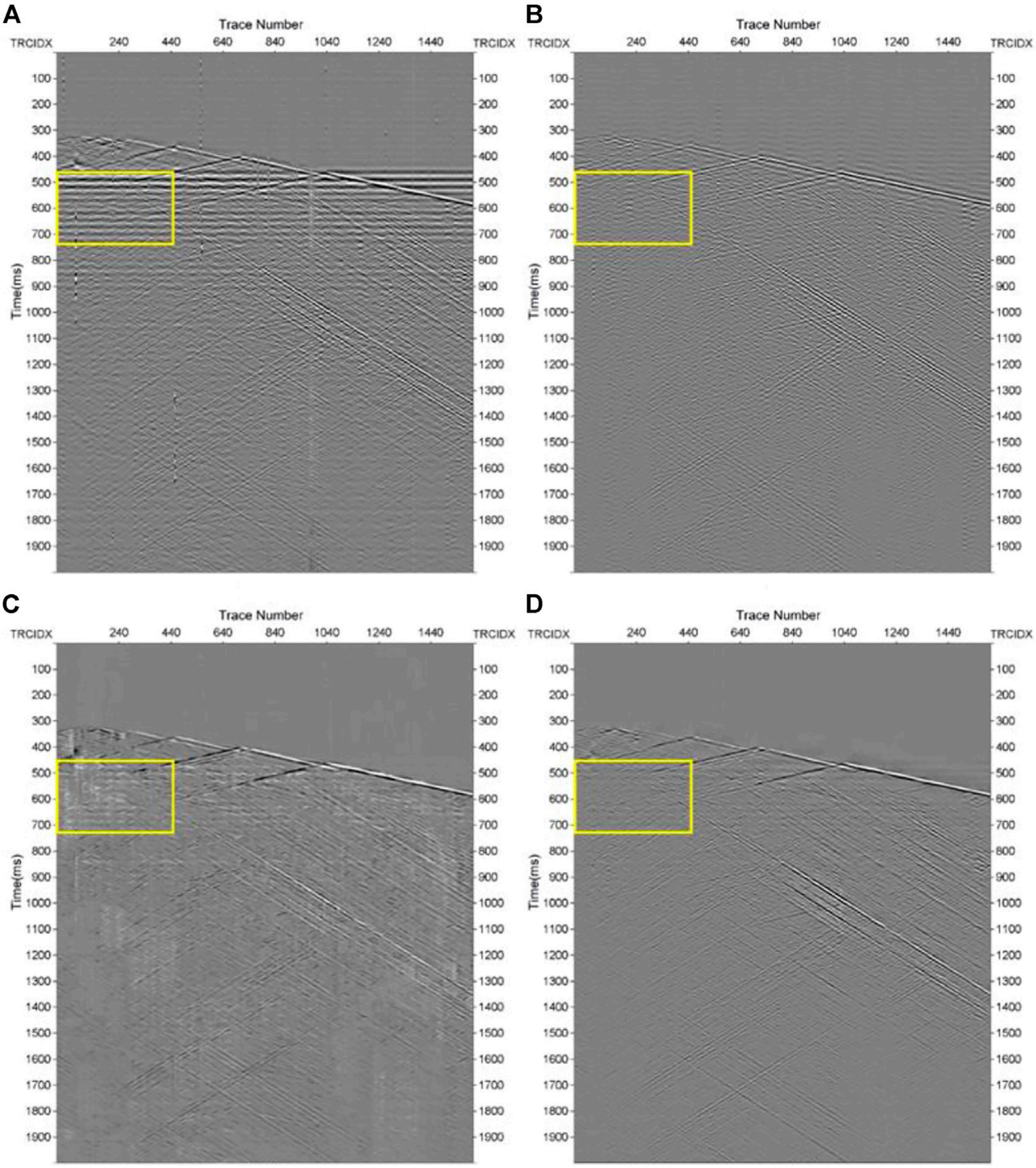

FIGURE 12
Field data: Denoising results. **(A)** Denoised result from VMD, **(B)** denoised result from band-pass filtering, **(C)** denoised result from DnCNNs, **(D)** denoised result from ADNet.

Figure 12 shows the denoised results from the four methods, and Figure 13 displays the corresponding difference maps. From Figure 12A, we can see that a large amount of noise is suppressed, but horizontal noise can still be seen, particularly within the yellow box. In Figure 12B, the continuity of the effective signals is poor, and the difference map obtained after band-pass filtering obtains many reflected waves. The denoised result of DnCNNs still contains horizontal noise and optical abnormal noise residual, which influences the effective signal identification. Besides, the difference map has plenty of effective signal loss, as illustrated in Figure 13C. On the contrary, the denoised result from ADNet contains very little noise residual, and the direct wave and reflected waves can be seen clearly. This indicates that ADNet is more suitable for DAS seismic data denoising and has better effective signal recovery ability.

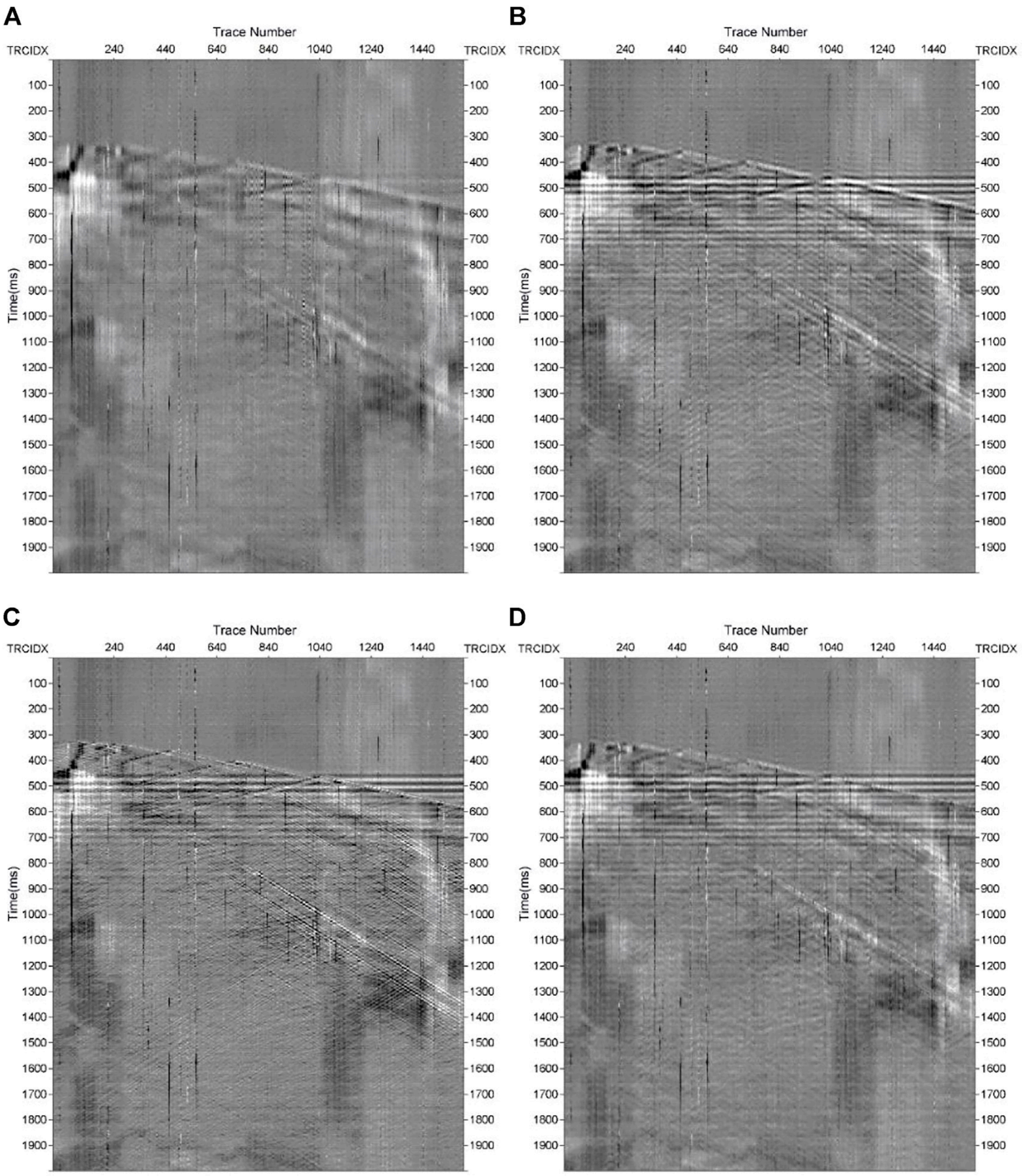

FIGURE 13
Difference maps from denoised results in Figure 12. **(A)** Difference map from real DAS record and denoised result from VMD, **(B)** difference map from real DAS record and denoised result from band-pass filtering, **(C)** difference map from real DAS record and denoised result from DnCNNs, **(D)** difference map from real DAS record and denoised result from ADNet.

4 Conclusion and discussion

DAS seismic data include multiple types of noise and this affects the identification of effective signals, such as the direct wave and reflected waves. In this paper we have introduced a CNN denoising network with attention mechanism to suppress DAS seismic noise. The ADNet can extract effective signals and noise features. This allows for accurate prediction of data noise. The attention block can furthermore guide the network to learn more noise information and adjust the training parameters of the network. The results illustrate that ADNet can suppress complex noise and recover weak reflected signals clearly. Comparisons of denoised results obtained from ADNet and DnCNNs, reveal that attention mechanism is vital to DAS noise suppression. It enhances the denoising performance and the quality of DAS seismic data.

However, the network cannot eliminate ringing noise well due to the high similarity between ringing noise and weak reflected noise. Future improvements in the network architecture and training sets may mitigate this problem.

Data availability statement

The original contributions presented in the study are included in the article/supplementary material, further inquiries can be directed to the corresponding author.

Author contributions

CW contributed to the conception and investigation of the study and wrote the first draft of the manuscript. YL provided field data for the paper. All authors contributed to manuscript revision, read, and approved the submitted version.

Funding

This research is supported by the National Natural Science Foundation of China (Under Grant 41974143).

Acknowledgments

The authors express their gratitude for the support. And thanks to Tessaral software for helping us.

Conflict of interest

The authors declare that the research was conducted in the absence of any commercial or financial relationships that could be construed as a potential conflict of interest.

Publisher's note

References

Alali, A., Machado, G., and Marfurt, K. J. (2018). Attribute-assisted footprint suppression using a 2D continuous wavelet transform. *Interpret. (Tulsa)* 6 (2), T457–T470. doi:10.1190/INT-2017-0175.1

Aleardi, M., and Salusti, A. (2021). Elastic prestack seismic inversion through discrete cosine transform reparameterization and convolutional neural networks. *Geophysics* 86 (1), R129–R146. doi:10.1190/geo2020-0313.1

Binder, G., Titov, A., Liu, Y., Simmons, J., Tura, A., Byerley, G., et al. (2020). Modeling the seismic response of individual hydraulic fracturing stages observed in a time-lapse distributed acoustic sensing vertical seismic profiling survey. *Geophysics* 85 (4), T225–T235. doi:10.1190/geo2019-0819.1

Binder, G., and Tura, A. (2020). Convolutional neural networks for automated microseismic detection in downhole distributed acoustic sensing data and comparison to a surface geophone array. *Geophys. Prospect.* 68 (9), 2770–2782. doi:10.1111/1365-2478.13027

Chen, Y., Zu, S., Wang, Y., and Chen, X. (2019). Deblending of simultaneous source data using a structure-oriented space-varying median filter. *Geophys. J. Int.* 216 (2), 1214–1232. doi:10.1093/gji/ggy487

Correa, J., Egorov, A., Tertyshnikov, K., Bona, A., Pevzner, R., Dean, T., et al. (2017). Analysis of signal to noise and directivity characteristics of DAS VSP at near and far offsets; a CO2CRC otway project data example. *Lead. Edge* 36 (12), 994a1–994a7. doi:10.1190/tle36120994a1.1

Cui, M., Fu, L., and Fang, W. (2022). Seismic noise attenuation via convolution neural network with learningnoise prior. *Explor. Geophys. Melb.* 53 (1), 38–51. doi:10.1080/08123985.2021.1886853

Ephraim, Y., and Malah, D. (1984). Speech enhancement using a minimum-mean square error short-time spectral amplitude estimator. *IEEE Trans. Acoust.* 32 (6), 1109–1121. doi:10.1109/TASSP.1984.1164453

Feng, J., Liu, X., Li, X., Xu, W., and Liu, B. (2022). Low-rank tensor minimization method for seismic denoising based on variational mode decomposition. *IEEE Geosci. Remote Sens. Lett.* 19, 1–5. doi:10.1109/LGRS.2021.3100262

Feng, R. (2020). Estimation of reservoir porosity based on seismic inversion results using deep learning methods. *J. Nat. Gas Sci. Eng.* 77, 103270. doi:10.1016/j.jngse.2020.103270

Gan, S., Chen, Y., Shaohuan, Z., Shan, Q., and Wei, Z. (2015). Structure-oriented singular value decomposition for random noise attenuation of seismic data. *J. Geophys. Eng.* 12 (2), 262–272. doi:10.1088/1742-2132/12/2/262

Gomez, J. L., and Velis, D. R. (2016). A simple method inspired by empirical mode decomposition for denoising seismic data. *Geophysics* 81 (6), V403–V413. doi:10.1190/geo2015-0566.1

Gulunay, N. (2017). Signal leakage in f-x deconvolution algorithms. *Geophysics* 82 (5), W31–W45. doi:10.1190/geo2017-0007.1

Guo, C., Zhu, T., Gao, Y., Wu, S., and Sun, J. (2021). AEnet: Automatic picking of P-wave first arrivals using deep learning. *IEEE Trans. Geosci. Remote Sens.* 59 (6), 5293–5303. doi:10.1109/TGRS.2020.3010541

Huo, S., Zhu, W., and Taikun, S. (2017). Iterative dip-steering median filter. *J. Appl. Geophys.* 144, 151–156. doi:10.1016/j.jappgeo.2017.05.012

Kingma, D. P., and Ba, J. L. (2015). Adam: A method for stochastic optimization, in 3rd International Conference on Learning Representations (ICLR), San Diego, CA, USA, May 7-9, 2015. doi:10.48550/arXiv.1412.6980

Kobayashi, Y., Uematsu, Y., Mochiji, S., and Xue, Z. (2020). A field experiment of walkaway distributed acoustic sensing vertical seismic profile in a deep and deviated onshore well in Japan using a fibre optic cable deployed inside coiled tubing. *Geophys. Prospect.* 68 (2), 501–520. doi:10.1111/1365-2478.12863

Li, G., Li, Y., and Yang, B. (2017). Seismic exploration random noise on land: Modeling and application to noise suppression. *IEEE Trans. Geosci. Remote Sens.* 55 (8), 4668–4681. doi:10.1109/TGRS.2017.2697444

Li, M., Li, Y., Wu, N., and Tian, Y. (2020). Desert seismic data denoising based on energy spectrum analysis in empirical curvelet domain. *Stud. Geophys. Geod.* 64 (3), 373–390. doi:10.1007/s11200-019-0476-4

Ma, G., Zhou, H., Shi, C., Li, Y., Zhang, Q., Li, C., et al. (2018). Distributed partial discharge detection in a power transformer based on phase-shifted FBG. *IEEE Sens. J.* 18 (7), 2788–2795. doi:10.1109/JSEN.2018.2803056

Mateeva, A., Lopez, J., Potters, H., Mestayer, J., Cox, B., Kiyashchenko, D., et al. (2014). Distributed acoustic sensing for reservoir monitoring with vertical seismic profiling: Distributed acoustic sensing (DAS) for reservoir monitoring with VSP. *Geophys. Prospect.* 62 (4), 679–692. doi:10.1111/1365-2478.12116

Naghizadeh, M., and Sacchi, M. D. (2018). Ground-roll attenuation using curvelet downscaling. *Geophysics* 83 (3), V185–V195. doi:10.1190/geo2017-0562.1

Olofsson, B., and Martinez, A. (2017). Validation of DAS data integrity against standard geophones; DAS field test at aquistore site. *Lead. Edge* 36 (12), 981–986. doi:10.1190/tle36120981.1

Saad, O. M., and Chen, Y. (2020). Deep denoising autoencoder for seismic random noise attenuation. *Geophysics* 85 (4), V367–V376. doi:10.1190/geo2019-0468.1

Stein, R. A., and Bartley, N. R. (1983). Continuously time-variable recursive digital band-pass filters for seismic signal processing. *Geophysics* 48 (6), 702–712. doi:10.1190/1.1441500

Tian, C., Xu, Y., Li, Z., Zuo, W., Fei, L., and Liu, H. (2020). Attention-guided CNN for image denoising. *Neural Netw.* 124, 117–129. doi:10.1016/j.neunet.2019.12.024

Wang, C., and Wang, Y. (2021). Robust singular value decomposition filtering for low signal-to-noise ratio seismic data. *Geophysics* 86 (3), V233–V244. doi:10.1190/geo2020-0169.1

Wang, Y., Ge, Q., Lu, W., and Yan, X. (2020). Well-logging constrained seismic inversion based on closed-loop convolutional neural network. *IEEE Trans. Geosci. Remote Sens.* 58 (8), 5564–5574. doi:10.1109/TGRS.2020.2967344

Wang, Z., Bovik, A. C., Sheikh, H. R., and Simoncelli, E. P. (2004). Image quality assessment: From error visibility to structural similarity. *IEEE Trans. Image Process.* 13 (4), 600–612. doi:10.1109/TIP.2003.819861

Wu, H., Zhang, B., Li, F., and Naihao, L. (2019). Semiautomatic first-arrival picking of microseismic events by using the pixel-wise convolutional image segmentation method. *Geophysics* 84 (3), V143–V155. doi:10.1190/geo2018-0389.1

Wu, Y., Lin, Y., Zhou, Z., Bolton, D. C., Liu, J., and Johnson, P. (2019). DeepDetect: A cascaded region-based densely connected network for seismic event detection. *IEEE Trans. Geosci. Remote Sens.* 57 (1), 62–75. doi:10.1109/TGRS.2018.2852302

Xue, Y., Cao, J., Wang, X., Li, Y., and Du, J. (2019). Recent developments in local wave decomposition methods for understanding seismic data: Application to seismic interpretation. *Surv. Geophys.* 40 (5), 1185–1210. doi:10.1007/s10712-019-09568-2

Yang, S., Hu, J., Zhang, H., and Liu, G. (2021). Simultaneous earthquake detection on multiple stations via a convolutional neural network. *Seismol. Res. Lett.* 92 (1), 246–260. doi:10.1785/0220200137

Yao, H., Ma, H., Li, Y., and Feng, Q. (2022). DnResNeXt network for desert seismic data denoising. *IEEE Geosci. Remote Sens. Lett.* 19, 1–5. doi:10.1109/LGRS.2020.3044036

Yu, S., and Ma, J. (2018). Complex variational mode decomposition for slop-preserving denoising. *IEEE Trans. Geosci. Remote Sens.* 56 (1), 586–597. doi:10.1109/TGRS.2017.2751642

Yuan, P., Wang, S., Hu, W., Wu, X., Chen, J., and Nguyen, H. V. (2020). A robust first-arrival picking workflow using convolutional and recurrent neural networks. *Geophysics* 85 (5), U109–U119. doi:10.1190/geo2019-0437.1

Zhao, Y., Li, Y., Dong, X., and Yang, B. (2019). Low-frequency noise suppression method based on improved DnCNN in desert seismic data. *IEEE Geosci. Remote Sens. Lett.* 16 (5), 811–815. doi:10.1109/LGRS.2018.2882058

frontiers | Frontiers in Earth Science

TYPE Brief Research Report
PUBLISHED 09 January 2023
DOI 10.3389/feart.2022.993465

EDITED BY
Baoshan Wang,
University of Science and Technology of China, China

REVIEWED BY
Yichuan Wang,
University of Calgary, Canada
Yaxing Li,
University of Science and Technology of China, Hefei, China

*CORRESPONDENCE
Weijian Mao,
wjmao@whigg.ac.cn

SPECIALTY SECTION
This article was submitted to Solid Earth Geophysics,
a section of the journal
Frontiers in Earth Science

RECEIVED 13 July 2022
ACCEPTED 16 September 2022
PUBLISHED 09 January 2023

CITATION
Tang H, Cheng S, Li W and Mao W (2023), Simultaneous reconstruction and denoising for DAS-VSP seismic data by RRU-net.
Front. Earth Sci. 10:993465.
doi: 10.3389/feart.2022.993465

Simultaneous reconstruction and denoising for DAS-VSP seismic data by RRU-net

Huanhuan Tang, Shijun Cheng, Wuqun Li and Weijian Mao*

State Key Laboratory of Geodesy and Earth's Dynamics, Research Center for Computational and Exploration Geophysics, Innovation Academy for Precision Measurement Science and Technology, Chinese Academy of Science, Wuhan, China

Distributed acoustic sensing in vertical seismic profile (DAS-VSP) acquisition plays an important role in reservoir monitoring. But the field data can be noisy and associated with missing traces which affects the seismic imaging and geological interpretation. Therefore, the DAS-VSP seismic data reconstruction with a high signal-to-noise ratio (SNR) is worth studying. There are no exact relationships between signals and noise in the t-x domain DAS-VSP seismic data, which means that reconstructing signals and suppressing noise simultaneously by the deep neural network is difficult. We develop a novel algorithm based on U-net in combination with the Hankel matrix as input/output, rather than t-x domain seismic data. The frequency domain Hankel matrix of the seismic data is proposed to facilitate the reconstruction and denoising of DAS-VSP seismic data as a rank reduction problem of the high-rank matrix. The Hankel matrices of incomplete data with noise are high-rank ones while those of complete data without noise are low-rank ones, which is beneficial to the network learning. In our proposed rank reduction U-net (RRU-net), two-channel input/output layers are designed for the real and the imaginary parts of the Hankel matrix in the frequency domain. Thus, reconstructed data with high precision and high SNR could be obtained using a trained RRU-net. Meanwhile, we tested our RRU-net algorithm on two synthetic data and one field data, and the results show the effectiveness and the feasibility of the method. Our algorithm performs better than both the U-net-based method that uses $t-x$ domain data as input/output and the rank reduction approach.

KEYWORDS

DAS-VSP, reconstruction, denoising, RRU-net, Hankel matrix

Introduction

Recently, DAS has been used in vertical seismic profile (VSP) acquisition for permanent reservoir monitoring due to its advantages of full vertical coverage, low cost, repeatability, adaptability to high-temperature and high-pressure environment, and long-term deployment (Miller et al., 2012). However, the quality of DAS seismic data is poor for the following three reasons: first, the low sensitivity of DAS results in the weakly received upward-reflected signal, worsened by a large amount of environmental noise, optical noise, and "ringing" noise. Second, the obstacles in the acquisition area and the pressure of economic costs for long-term monitoring result in low-density shot arrangement and sparsely acquired data. Third, the perforation operation can easily destroy the fiber in the well, making the signals hardly recordable at this point. Additionally, the storage cost for time-lapse DAS-VSP seismic data is usually measured in TB, which is a challenge for data processing. Briefly, the DAS-VSP seismic data have the characteristics of low SNR, sparseness, and big data. Therefore, it is necessary to research the reconstruction and denoising of the DAS-VSP seismic data in high precision and real time.

Thanks to the rapid development of deep learning technology in the field of image processing in recent years (Krizhevsky et al., 2012; Ronneberger et al., 2015; Liu et al., 2018), intelligent processing has been widely used in the field of massive seismic data reconstruction (Jia and Ma, 2017; Jia et al., 2018; Mandelli et al., 2018). Among those methods, the convolutional neural network (CNN) is the most widely used method. The local perception capability of the CNN could extract more detailed intrinsic features of data. At the same time, the number of CNN parameters could be reduced by weight-sharing, which improves the training speed of the network. This kind of method (deep learning methods, including the aforementioned CNN) extracts the inherent high-dimensional features of the data adaptively through massive datasets and does not rely on prior conditions and artificial experience. Moreover, the trained net takes less than a few milliseconds to predict 1024 × 112 data (Chai et al., 2020). Therefore, deep learning could be a potential method to solve the problem of massive DAS-VSP seismic data reconstruction. Currently, many researchers have applied deep learning methods to seismic data reconstruction and denoising. In these studies, seismic data reconstruction and denoising are always discussed separately. For example, Liu et al. (2018) proposed the use of partial convolution methods to improve the blur problem of reconstructed images. Siahkoohi et al. (2019) accomplished the accurate reconstruction of the common shot records by the CNN, which is trained by the common receiver records in the FK domain based on the reciprocity theorem. Chen and Wang, (2021) proposed a method to enrich the training set by sampling at different scales and image flipping to improve the generalization ability of CNN in seismic data reconstruction. Furthermore, different nets based on CNN, such as residual net (ResNet) (Wang et al., 2019), generative adversarial neural network (GAN) (Oliveira et al., 2018), and U-net (Chai et al., 2020; Fang et al., 2021), were applied to data reconstruction. In the seismic data noise suppression problem, learning data augmentation strategies are also adopted to train the CNN (Wang et al., 2019). Dong et al. (2020) combined the denoising convolutional neural network (DnCNN) with robust principal component analysis to learn the noise characteristics in the noisy desert seismic data and realized the effective suppression of irregular random noise and regular surface waves. Then, based on the CNN, an energy ratio factor is used to adjust the energy ratio of the effective signal patch and noise patch in the training process to improve the generalization ability of the CNN denoising model to different SNRs (Dong et al., 2021). Feng and Li, (2022) designed a denoising neural network based on spectral decomposition analysis (SVDDCNN), and the net extracted DAS-VSP data features from a singular spectrum instead of the time-domain data, which can represent geophysical features more accurately. In addition, cycle generative adversarial networks (Cycle-GANs) and residual encoding–decoding neural networks (RED-Nets) are also used in random noise suppression (Li and Wang, 2021; Zhong et al., 2021). The aforementioned methods achieved high-precision reconstructed data and effective noise suppression data, respectively. However, noise and missing data coexist in the field records, and only a few studies have applied a simultaneous reconstruction and denoising of seismic data by the deep learning method (Wang, 2020; Jiang et al., 2021). In Wang's research (2020), the CNN-based 3D data reconstruction and denoising method first trained the network for denoising and then trained the network for reconstruction, separately. Jiang et al. (2021) proposed an improved convolutional auto-encoder (CAE) method to achieve simultaneous reconstruction and denoising of seismic data; however, the noise was residual in the field data testing. For noisy incomplete DAS-VSP seismic data, when the neural network is trained to implement one of the tasks (reconstruction/denoising), the other factor (noise/missing data) will adversely affect the neural network. Therefore, it is a difficult problem to realize the simultaneous reconstruction and denoising of DAS-VSP seismic data based on deep learning.

Among the traditional simultaneous reconstruction and denoising methods of seismic data, the rank reduction based on the Hankel matrix is one of the effective methods (Gao et al., 2011; Oropeza and Sacchi, 2011; Chen et al., 2016). The principle is that the seismic data will repeatedly record the information of the same or adjacent underground locations, so that the seismic data have a low-rank structure. The absence of data or the noise will increase the rank; therefore, seismic data reconstruction and noise suppression can be regarded as the rank reduction problem of the high-rank matrix. However, the data in some columns are all zero in the incomplete seismic data gather, which will lead to instability in the rank reduction process. Generally, the incomplete seismic data need to be transformed into a Hankel matrix and then the rank of which will be reduced by singular value decomposition (SVD) (Cadzow, 1988; Trickett, 2008; Gao et al., 2011; Popa et al., 2021). The disadvantage of the rank reduction method is that the SVD of large Hankel matrices requires a huge amount of computational cost, which makes it unsuitable for massive DAS-VSP monitoring data. In addition, it is difficult to determine the number of retained eigenvalues in the SVD process, which will lead to insufficient noise suppression or signal leakage.

In this article, we propose a simultaneous reconstruction and denoising method for DAS-VSP seismic data under the framework of deep learning based on rank reduction. When using a U-net instead of the SVD process of the Hankel matrix, the U-net is trained to learn the mapping relationship between the high-rank Hankel matrix (noisy missing data) and the low-rank Hankel matrix (noise-free complete data) adaptively, which neatly avoids the shortcomings of the rank reduction method. First, the $t-x$-domain training data are transformed into the Hankel matrices in the frequency domain. So, the two different tasks of data reconstruction and noise suppression are unified into a reduced-rank learning task, which could improve the reconstruction accuracy and efficiency. Second, two-channel input/output layers are designed for the real and imaginary parts of the frequency-domain Hankel matrix. Meanwhile, different types of noise and signal data with different missing percentages are added to the training set to improve the generalization ability of the network. In this article, synthetic examples and field data are provided to prove the effectiveness of the proposed method. Furthermore, the results of the rank reduction method, the U-net trained in the $t-x$ domain, and the RRU-net are compared to show the superiority of the RRU-net in simultaneous reconstruction and denoising of DAS-VSP seismic data.

Methodology

Rank reduction method

Fully sampled seismic data can be represented by a low-rank matrix. Missing trace or noise will increase the rank of the data. Therefore, the reconstruction and denoising of DAS-VSP seismic data can be regarded as a rank reduction problem of a high-rank matrix (Sacchi, 2009; Oropeza and Sacchi, 2011). When approximated, seismic data are linear within the $t-x$ window, and then the seismic data d with one event can be expressed as

$$d(t,x_n) = w(t_0 + px_n), \tag{1}$$

where t is the time, t_0 is the time intercept of the first trace in the time–space window, x_n is the offset of the n^{th} trace, w is the wavelet, and p is the dip of the event. In the frequency domain, Eq. 1 becomes

$$D(\omega,x_n) = W(\omega)e^{i\omega p x_n}. \tag{2}$$

For regularly sampled seismic data, $x_n = (n-1)\Delta x$, where $n = 1,2,...,N$, N is the number of geophones on a receiver line, and Δx is the spacing of geophones within lines. The seismic data of adjacent traces have the following recurrence relation in the frequency domain:

$$\begin{aligned} D(\omega,x_{n+1}) &= W(\omega)e^{i\omega p x_{n+1}}, \\ &= W(\omega)e^{i\omega p n\Delta x}, \\ &= D(\omega,x_n)e^{i\omega p\Delta x}, \end{aligned} \tag{3}$$

where $e^{i\omega p\Delta x}$ is constant for seismic data with certain frequency ω and dip p. By denoting $e^{i\omega p\Delta x}$ as λ_ω and $D(\omega,x_n)$ as D_n, Eq. 3 is simplified to

$$D_{n+1} = \lambda_\omega D_n. \tag{4}$$

The equation for constructing the Hankel matrix with seismic data in the frequency domain is

$$H = \begin{bmatrix} D_1 & D_2 & \cdots & D_k \\ D_2 & D_3 & \cdots & D_{k+1} \\ \vdots & \vdots & \ddots & \vdots \\ D_l & D_{l+1} & \ldots & D_N \end{bmatrix}, \tag{5}$$

where $k+l-1 = N$. Based on Eq. 4, the Hankel matrix in Eq. 5 can be further expressed as

$$H = \begin{bmatrix} D_1 & \lambda D_1 & \cdots & \lambda^{(k-1)}D_1 \\ D_2 & \lambda D_2 & \cdots & \lambda^{(k-1)}D_2 \\ \vdots & \vdots & \ddots & \vdots \\ D_l & \lambda D_l & \ldots & \lambda^{(k-1)}D_l \end{bmatrix}. \tag{6}$$

From Eq. 6, there is a linear relationship among the columns of the Hankel matrix, that is, the rank of the matrix is 1. Similarly, it can be proved that when the seismic data contain multiple dip events, the rank of the Hankel matrix is equal to the number of dips. Therefore, the Hankel matrix constructed with the seismic data in the frequency domain is a low-rank Hankel matrix. When there are missing traces or noise, Eq. 6 becomes non-linear; thus, the rank of H will increase. The signal reconstruction and the noise suppression can be effectively achieved by performing SVD on the Hankel matrix H and reducing its rank. The SVD of the Hankel matrix is

$$H = U\Sigma V^T. \tag{7}$$

In Eq. 7, U and V are the unitary matrices with sizes $l \times l$ and $k \times k$, respectively, and they are the eigenvector matrices of H. Σ is a diagonal matrix, and its diagonal elements are the singular values of H. Σ can be presented as

$$\Sigma = \begin{bmatrix} \sigma_{1,1} & \cdots & 0 \\ \vdots & \ddots & \vdots \\ 0 & \cdots & \sigma_{l\times k} \end{bmatrix}, \tag{8}$$

where $\sigma_1 \geq \sigma_2 \geq \cdots \sigma_i \geq 0$. We reduce the rank of the Hankel matrix by keeping the first r eigenvalues:

$$\Sigma = \begin{bmatrix} \Sigma_r & 0 \\ 0 & 0 \end{bmatrix}, \tag{9}$$

where $\Sigma_r = diag(\sigma_1,\cdots,\sigma_r)$. Then, the rank-reduced Hankel matrix $\tilde{H}$ is calculated as

$$\tilde{H} = U_r\Sigma_r V_r^T. \tag{10}$$

Next, the elements along the anti-diagonal of the matrix $\tilde{H}$ are averaged to obtain $\tilde{D}_n$, and $\tilde{D}_n$ is the reconstructed and denoised seismic data in the frequency domain. There are two shortcomings in the aforementioned process of simultaneous reconstruction and denoising of seismic data based on rank reduction. One, for field seismic data, the rank of seismic data in different time–space windows is different, and it is difficult to determine how many ranks are needed to be retained. The other

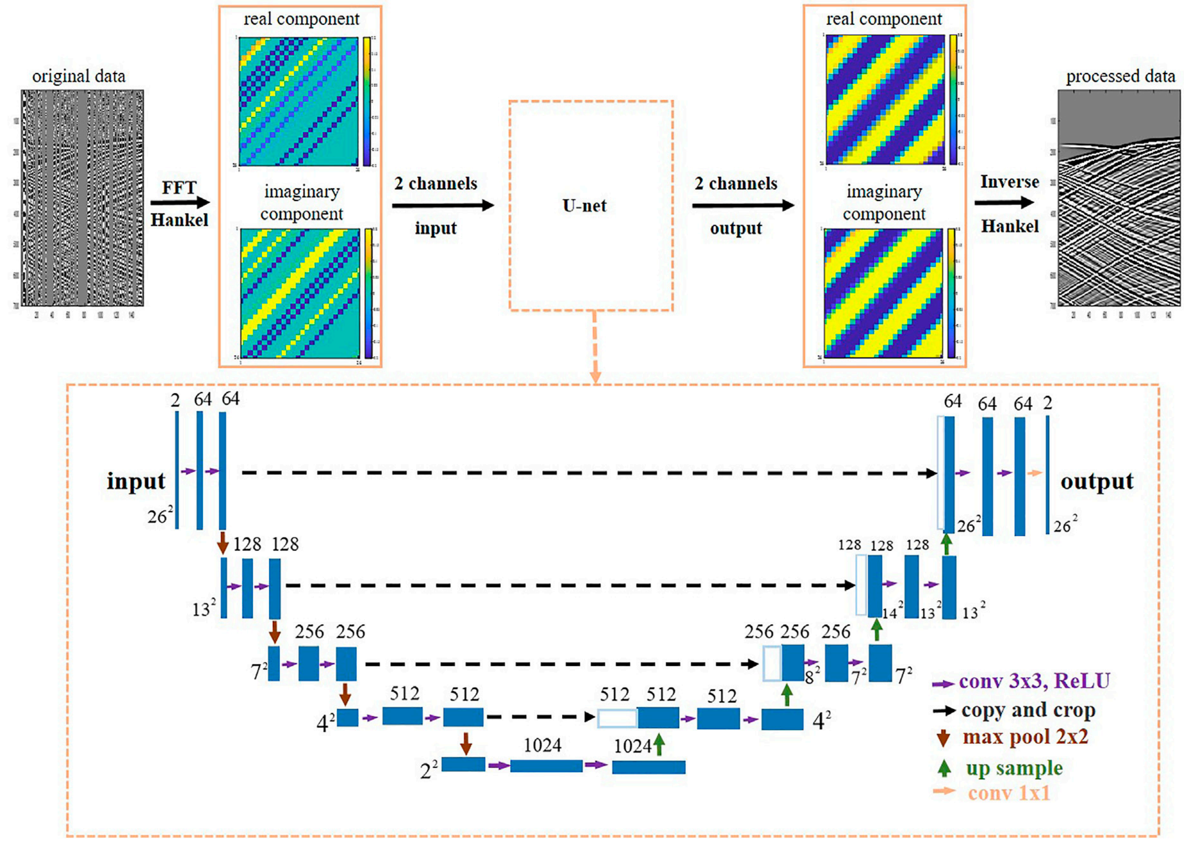

FIGURE 1
Architecture of the RRU-net.

problem is that both the SVD of the matrix H and the rank-reduced matrices $\tilde{H}$ require huge computations. Therefore, we propose to use a U-net to adaptively learn the mapping relationship between the high-rank Hankel matrix (noisy missing data) and the low-rank Hankel matrix (noise-free complete data), instead of relying on artificial experience to determine the number of the retained rank. Moreover, once the training of one net has been carried out, the prediction will be highly efficient.

The architecture of the rank reduction U-net

The architecture of the RRU-net proposed in this article is shown in Figure 1. The main part of this network is a U-net with 27 layers, which is a symmetric structure based on CNNs (Falk et al., 2019). The input of the RRU-net is the Hankel matrix of seismic data in the frequency domain. Since the elements in the Hankel matrix are complex, the real convolution neural network cannot process the data directly. We design the U-net with two-channel input/output layers, which correspond to the real and imaginary parts of the Hankel matrix, respectively. In this way, the RRU-net can extract signal features from both the real and imaginary parts of the input data. The U-net has three important components. One is the encoder (left side) composed of the repeated operators of two 3 × 3 convolutions (purple arrow) that are followed by batch normalization (BN), a rectified linear unit (ReLU), and a 2 × 2 max-pooling (red arrow) for down-

TABLE 1 Parameters setting of the RRU-net.

Parameter	Value
Patch size	26 × 26
Convolution kernel size	3 × 3
Batch size	25
Learning rate	3×10^{-4}
Optimizer	Adam
Loss function	MSE
Epochs	50

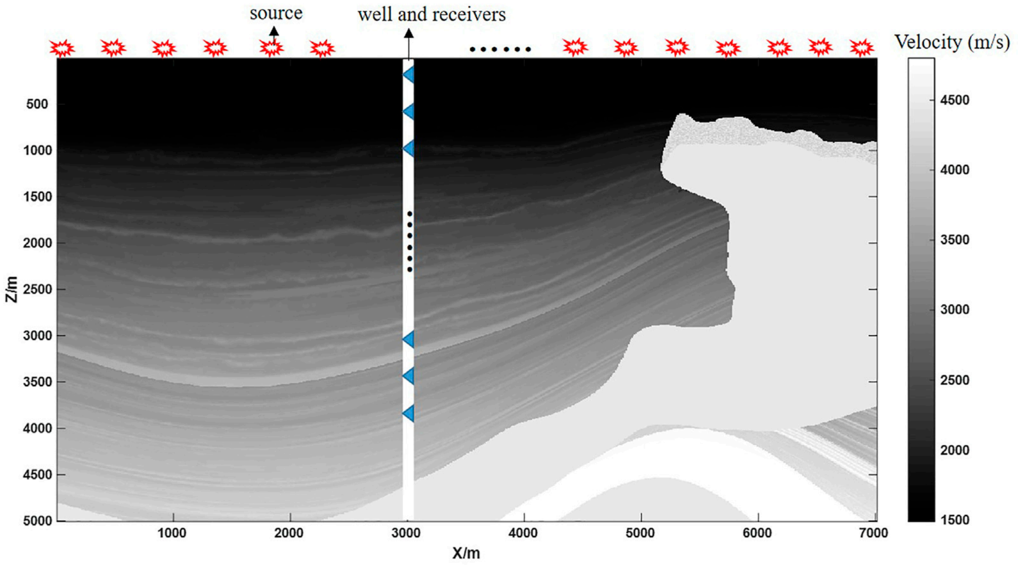

FIGURE 2
Two-dimensional profile of the SEAM model and the acquisition geometry.

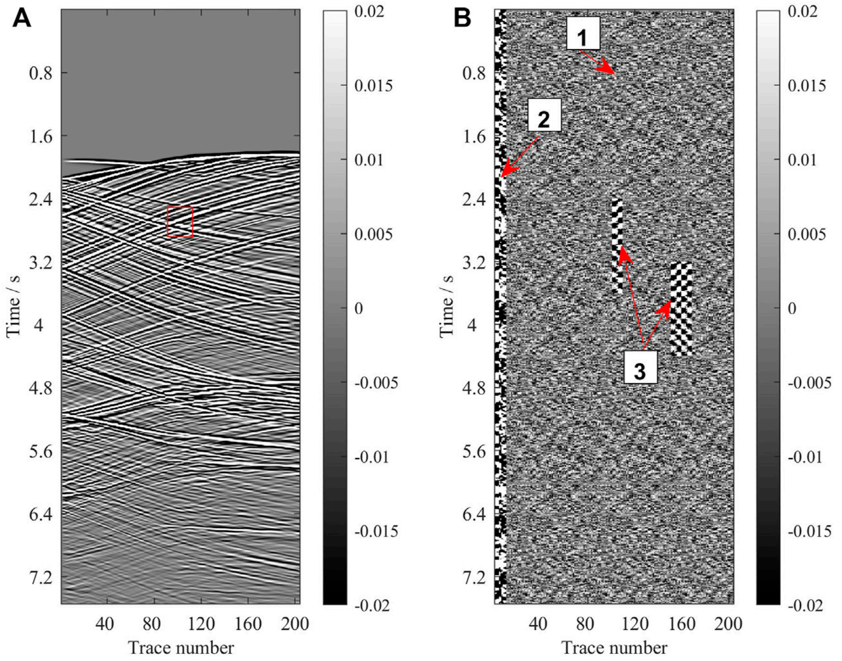

FIGURE 3
(A) Synthetic noise-free complete signal data and the shot is located at x = 0 m. **(B)** Noise data from the field DAS-VSP records.

sampling. After the down-sampling step, the effective receptive field of the network increases as the size of the feature maps decreases. Meanwhile, the amounts of feature channels are generally doubled. For the simultaneous seismic data reconstruction and denoising task, the encoding process is responsible for extracting features in different scales of the

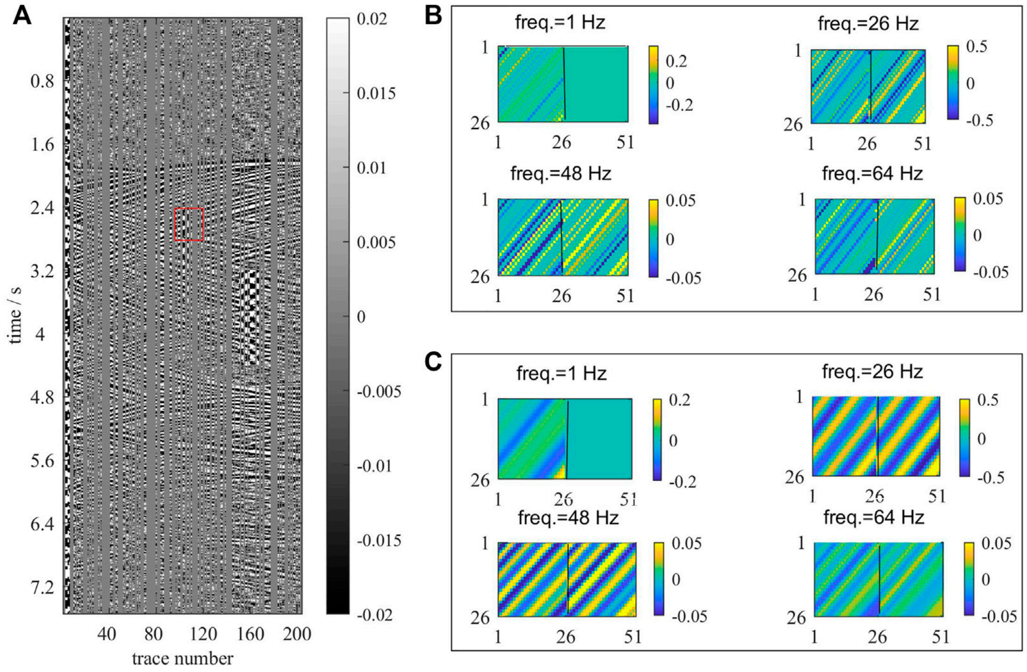

FIGURE 4
(A) Synthetic noisy incomplete data based on Figure 3 and the missing trace percentage is 56.4%. **(B)** Hankel matrices in different frequencies of the noise incomplete data in the red rectangle of Figure 4A; each Hankel matrix contains a real part (left side) and an imaginary part (right side). **(C)** Hankel matrices in different frequencies of the noise-free complete data in the red rectangle of Figure 3A; each Hankel matrix contains a real part (left side) and an imaginary part (right side).

input noisy missing data. The second component is the decoder (right side) with an expansive path, in which the feature maps are first up-sampled by bilinear interpolation (green arrow) to halve the number of feature channels at each step. In the decoding process, the size of the feature maps increases after each up-sampling step, which leads to the reduction of the effective receptive field of the network. The decoding process is used to decode the low-dimensional features to the original size, obtaining the location information. The last layer uses a 1 × 1 convolution to map the multi-channel features to the desired number of classes. The third component is a skip connection (black dotted arrows) combining the deep feature maps from the decoder network with the shallow feature maps from the encoder network, which is useful to learn the rank reduction theory of the Hankel matrix with noisy missing data and then implement two 3 × 3 convolutions, each followed by BN and ReLU.

In Eq. 11, L is the loss function of the RRU-net, and it is defined as

$$L(\theta) = \frac{1}{M}\sum_{j=1}^{M}\left(f\left(\theta, H_{sample}{}^{j}\right) - H_{label}{}^{j}\right)^2, \tag{11}$$

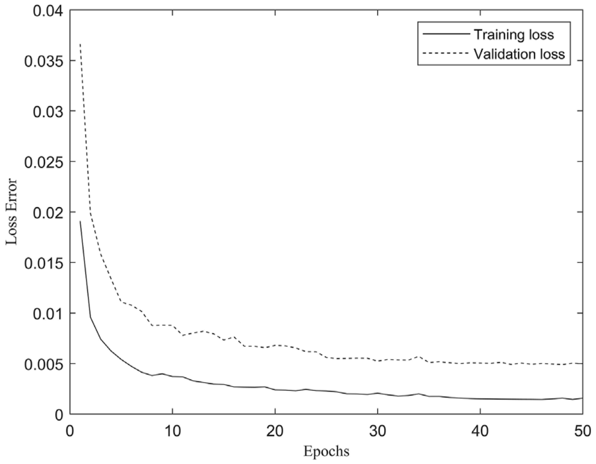

FIGURE 5
Training loss and validation loss of the RRU-net.

where M is the batch size in the training process, f is the U-net described in Figure 1, θ represents the parameters of the convolution kernel, $H_{sample}{}^{j}$ is the Hankel matrix with noisy missing data in the training set, and $H_{label}{}^{j}$ is the label (noise-free complete data) in the training set. The RRU-net is trained to minimize the loss function L to obtain the best value of θ under the framework of 1.7 PyTorch version. The other parameters of the RRU-net such as convolution, max-pooling, and bilinear interpolation are shown in Table 1. In addition, the patch size of the training data, the layers of the net, and the convolution kernel size all have an impact on the result of deep learning as established in other research studies (Wang et al., 2019; Chai et al., 2020; Feng and Li, 2022). Therefore, this article does not repeat the analysis, but we refer to the relevant research in the selection of these parameters.

Training datasets

We prepare the training data with the synthetic signals by forward modeling and the noises from the field DAS-VSP seismic data. The synthetic signals are simulated by forward modeling using the finite difference method for a 2D profile of the SEAM model (Figure 2). The model has 70 km width and 5 km depth, and the velocity range is distributed from 1,490 m/s to 4,800 m/s. The well is located at 3 km (the white stripe in Figure 2) and

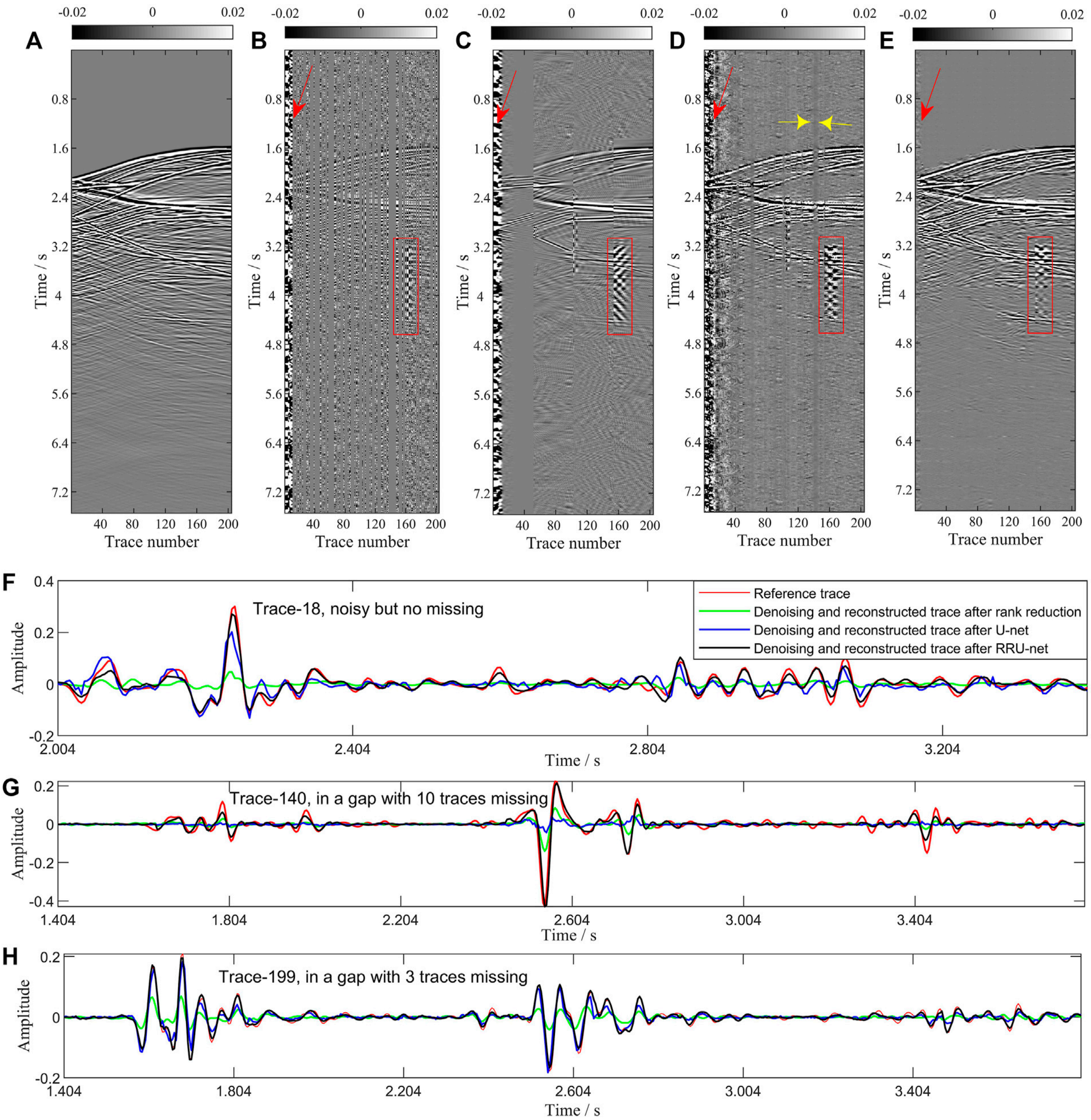

FIGURE 6
Simultaneous reconstruction and denoising results of the three methods on synthetic data generated with the SEAM model. **(A)** Synthetic noise-free complete signal data and the shot is located at $x = 6400$ m. **(B)** Original gather with noise and the missing trace percentage is 63%. **(C)** Result by rank reduction. **(D)** Result by U-net. **(E)** Result by RRU-net. **(F–H)** One-dimensional waveform comparison.

equipped with 401 receivers (the blue triangle in Figure 2) spaced at 10-m intervals and has a depth range from 0 to 4,000 m. There are 176 sources spaced at 40-m intervals (the red circle in Figure 2) at the surface. A 30-Hz Ricker wavelet is used in the simulation. The size of the synthetic data is $1905 \times 401 \times 176$, that is, the size of the time axis (0.004 s interval), receiver axis, and shot axis, respectively. In the 176 common shot gathers, 150 shot gathers are randomly selected for training and the rest for testing. One of the common shot gathers is shown in Figure 3A. The noise records including the background noise (arrow 1), ringing noise (arrow 2), and horizontal noise (arrow 3) are obtained from the real DAS-VSP data as shown in Figure 3B. Approximately, 40%–70% of the traces are randomly deleted in different gathers. The noise records from the real data are added to the incomplete signal records to obtain the noisy incomplete data as shown in Figure 4A. So, the noisy incomplete data and the noise-free complete data are transformed into the Hankel matrix separately, before all the needed data are normalized to $[-1, 1]$ and windowed to patches with size 51×51. There are 266400 pairs of samples in the training dataset, each sample with size 26×26, and parts of them are shown in Figures 4B,C.

The training environment is in the PyTorch framework with GPU (8 cores) in the Linux system. The total training cost is about 25 h, and the loss error in epochs is shown in Figure 5.

Numerical examples

The reconstruction and denoising effectiveness of the trained RRU-net is validated by two synthetic datasets and one field dataset. One of the synthetic datasets is modeled by the same velocity model as the training dataset (Figure 4) with different source positions. The other is from the Marmousi2 model. The field DAS-VSP records are employed to test the generalization capacity of the RRU-net. Moreover, to prove the superiority of the RRU-net in handling simultaneous reconstruction and denoising of the DAS-VSP data, we compare the results of the RRU-net with those of the rank reduction method and U-net trained with t-x-domain data.

Synthetic records

There are 26 shot gathers in the first synthetic records to be tested. One of the processed gathers by the rank reduction method, U-net, and RRU-net is presented in Figures 6C,D,E, respectively. The original data are shown in Figures 6A,B. These figures show data with 65% missing traces. Figures 6C,D show that the rank reduction method and U-net cannot suppress the strong ringing noise as marked by the red arrows, while the RRU-net is able to suppress it more entirely as seen in Figure 6E. Meanwhile, the signals divided in the window with the strong ringing noise also are suppressed by the rank reduction method (Figure 6C) because in the SVD process for the near traces, ringing noise dominates the eigenvalues. As we can see in Figures 6D,E, the RRU-net suppressed the horizontal noise (red rectangle) more efficiently than the other two methods. In addition, the RRU-net performs the best in suppressing the background noise. For the missing signal reconstruction, the near traces are barely reconstructed by the rank reduction method as shown in Figure 6C, while the U-net method has poor effectiveness for the big gap as marked by the yellow arrow in Figure 6D. Contrary to the rank reduction method and U-net, the reconstructed signal by the RRU-net is complete, and the event continuity is the best as shown in Figure 6E.

To prove the accuracy of the reconstructed signals and to confirm whether the studied method harms the signal in the denoised results, we carry out a detailed 1D waveform comparison. Three traces are shown in Figures 6F–H, respectively. Figure 6F is the denoised results of the 18th trace in Figure 6B. Figures 6G,H are the reconstructed signals of the 140th and 199th trace, respectively, which are in different gaps. The 1D waveform comparison shows that the RRU-net method best fits the single trace and yields fewer reconstruction errors. Additionally, the SNR of the 26 shot gathers processed by the three methods is presented in Figure 7. It is obvious that the SNR of the proposed network is much higher than that of the other two methods. To complete the processing of the 26 shot gathers, the rank reduction method takes 44 s, and the U-net and RRU-net take less than 5s, which demonstrates the efficiency of the deep learning method. All these analyses affirm that the proposed RRU-net can suppress the noise and reconstruct the missing signal effectively. However, for weak signals below 4s, none of these three methods can obtain satisfactory reconstruction results as the weak signal is completely buried in the strong background noise as shown in Figure 6B. In addition, the cross term between the real part and imaginary part of the Hankel

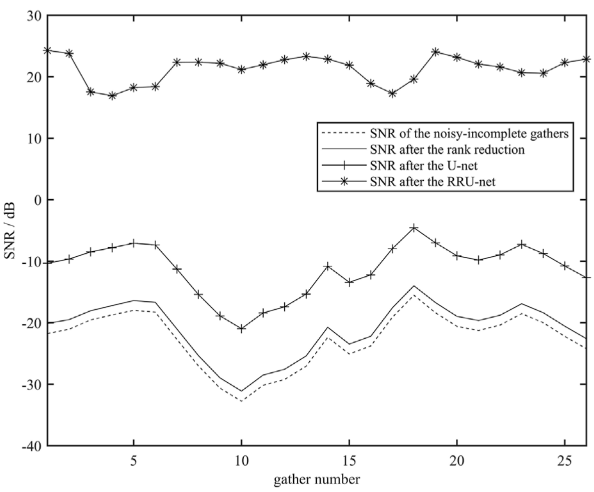

FIGURE 7
SNRs of the 26 shot gathers processed by three methods.

matrix in the frequency domain is ignored as we apply the real neural network, which may affect the effectiveness of the proposed method.

To test the effect of the trained network on other synthetic data, we use the RRU-net to reconstruct and denoise the DAS-VSP data generated using the Marmousi2 model. The data include a total of 21 shots and 255 receivers per shot, and every trace has 1,000 temporal sampling points. One of the processed gathers by the three methods is presented in Figure 8. As highlighted by the arrows and the boxes (Figures 8B–E), the RRU-net yields the best denoising results, and the 1D waveform comparison of different traces (Figures 8F–H) shows the accuracy of the reconstructed signals by our method. The average SNR value of gathers with noise and 65% missing traces is −17.09 dB, which is increased to 25.69 dB after reconstruction by the RRU-net.

Field data application

To further prove the effectiveness of the proposed method, two real DAS-VSP gathers are tested. The data contain 5001 samples along the time axis with a 1-ms time interval and 204 receivers along the well with a 0.1-m space interval as shown in Figures 9Ai,Ei. The signal in Figures 9Ai,Ei is

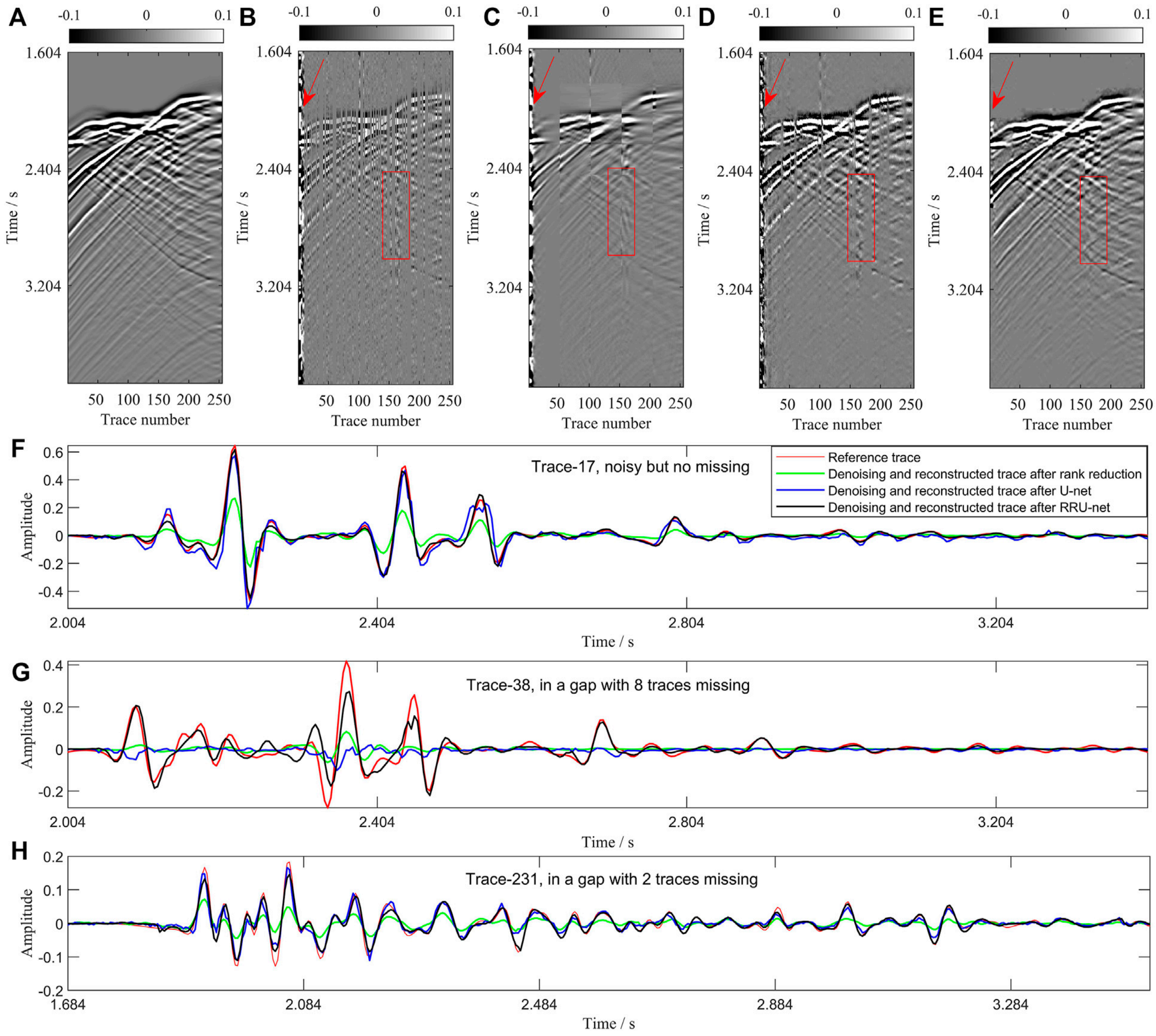

FIGURE 8
Simultaneous reconstruction and denoising results of the three methods on synthetic data generated using the Marmousi2 model. **(A)** Synthetic noise-free complete signal data. **(B)** Original gather with noise and the trace missing percentage is 63%. **(C)** Result by rank reduction. **(D)** Result by U-net. **(E)** Result by RRU-net. **(F–H)** One-dimensional waveform comparison.

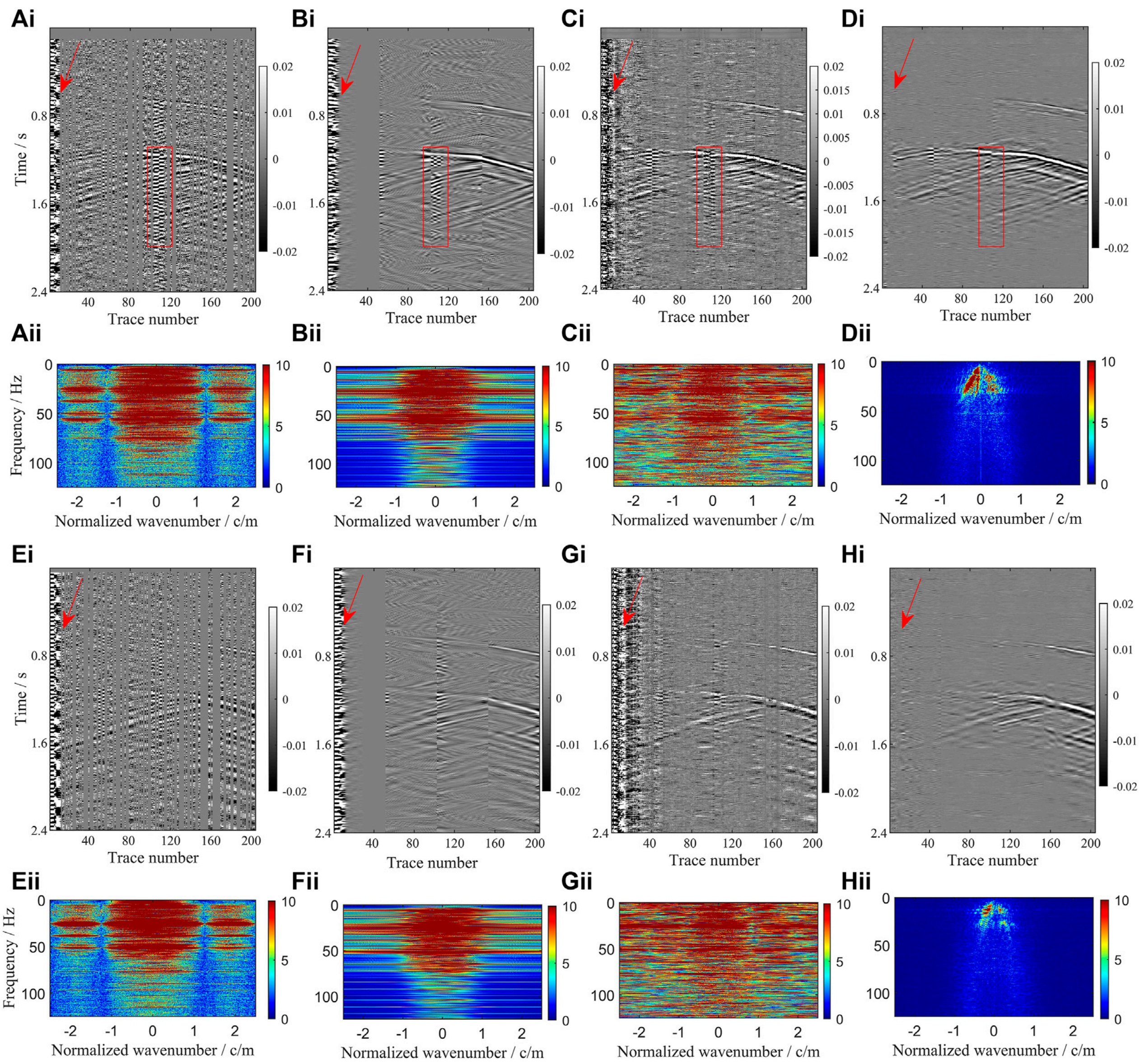

FIGURE 9
Simultaneous reconstruction and denoising results of the three methods in field DAS-VSP data. **(Ai)** Original field DAS-VSP data, shot1. **(Bi)** Result of **(Ai)** by rank reduction. **(Ci)** Result of **(Ai)** by U-net. **(Di)** Result of **(Ai)** by RRU-net. **(Aii–Dii)** FK spectrum of **(Ai–Di)**, respectively. **(Ei)** Original field DAS-VSP data, shot1. **(Fi)** Result of **(Ei)** by rank reduction. **(Gi)** Result of **(Ei)** by U-net. **(Hi)** Result of **(Ei)** by RRU-net. **(Eii–Hii)** FK spectrum of **(Ei–Hi)**, respectively.

strongly contaminated by several types of noise, and nearly 50% of the traces are missing. The denoised and reconstructed results by rank reduction, U-net, and RRU-net are presented in Figures 9Bi–Di, Fi–Hi, respectively. The rank reduction method in Figures 9Bi,Fi shows the ability to suppress the background noise but fails to preserve the signal events. The RRU-net could suppress the strong ringing noise (red arrows) and the horizontal noise (red rectangles) in Figures 9Di,Hi, while the other two methods could not (Figures 9Bi,Ci,Fi,Gi). At the same time, the RRU-net method also performs very well in recovering the missing signals. The FK spectrum in Figures 9Aii–Dii,Eii–Hii further illustrates the validity of this algorithm.

Testing the trained RRU-net on both synthetic and field data indicates its ability to reconstruct randomly missing data with high accuracy on different datasets, which validates the feasibility and generalization capacity of the proposed method.

Conclusion

We proposed the RRU-net to simultaneously pursue the reconstruction and denoising of the massive DAS-VSP seismic data. It is difficult for training the U-net directly with $t-x$-domain data to extract the mapping relationship between noisy incomplete data and noise-free complete data, but the RRU-net proposed in this article can achieve this. Compared with the traditional rank reduction method, the RRU-net avoids the difficulties of selecting the rank parameters and a large amount of computation for SVD. These advantages enable the RRU-net to achieve better results in simultaneous reconstruction and denoising of DAS-VSP seismic data with higher efficiency. Both synthetic data and real DAS-VSP seismic data demonstrate the effectiveness of RRU-net in noise suppression (background noise, ringing noise, and horizontal noise) and signal reconstruction.

There are still issues that require further investigation in the simultaneous reconstruction and denoising of DAS-VSP seismic data. Issues, such as preserving the weak signals, and the application of the neural network with complex convolution for seismic data in the frequency domain also need further investigation.

Data availability statement

The original contributions presented in the study are included in the article/Supplementary Material; further inquiries can be directed to the corresponding authors.

Author contributions

HT contributed to the original conception, algorithm implementation, and method validation; HT wrote the original draft of the manuscript; WM provided suggestions; and SC and WL assisted with the algorithm. All authors contributed to the study and improved the manuscript.

Funding

This work was supported by the National Key Research and Development Program of China under grant 2021YFA0716802 and the National Natural Science Foundation of China under grants 42130808 and 41974163.

Acknowledgments

The authors appreciate the valuable suggestions and comments from Qianru Xu, Lingli Gao, Huan Song, and E. I. Evinemi. The authors thank the developers of PyTorch on which they implemented this work.

Conflict of interest

The authors declare that the research was conducted in the absence of any commercial or financial relationships that could be construed as a potential conflict of interest.

Publisher's note

References

Cadzow, J. (1988). Signal enhancement-A composite property mapping algorithm. *IEEE Trans. Acoust.* 36 (1), 49–62. doi:10.1109/29.1488

Chai, X., Tang, G., Wang, S., Lin, K., and Peng, R. (2020). Deep learning for irregularly and regularly missing 3-D data reconstruction. *IEEE Trans. Geosci. Remote Sens.* 99, 6244–6265. doi:10.1109/TGRS.2020.3016343

Chen, R., and Wang, Q. (2021). Seismic data reconstruction with data augmentation-based convolutional neural network. *Chin. J. Eng. Geophys.* 18 (4), 471–478. doi:10.3969/j.issn.1672-7940.2021.04.009

Chen, Y., Zhang, D., Jin, Z., Chen, X., Zu, S., Huang, W., et al. (2016). Simultaneous denoising and reconstruction of 5-D seismic data via damped rank-reduction method. *Geophys. J. Int.* 206 (3), 1695–1717. doi:10.1093/gji/ggw230

Dong, X., Li, Y., Liu, F., Feng, Q., and Zhong, T. (2021). New suppression technology for the random noise in the DAS seismic data based on convolutional neural network. *Chin. J. Geophys.* 64 (7), 2554–2565. doi:10.6038/cjg2021O0274

Dong, X., Zhong, T., and Li, Y. (2020). New suppression technology for low-frequency noise in desert region: The improved robust principal component analysis based on prediction of neural network. *IEEE Trans. Geosci. Remote Sens.* 58 (7), 4680–4690. doi:10.1109/TGRS.2020.2966054

Falk, T., Mai, D., Bensch, R., Cicek, O., Abdulkadir, A., Marrakchi, Y., et al. (2019). U-Net: deep learning for cell counting, detection, and morphometry. *Nat. Met.* 16, 67–70. doi:10.1038/s41592-018-0261-2

Fang, W., Fu, L., Zhang, M., and Li, Z. (2021). Seismic data interpolation based on U-net with texture loss. *Geophysics* 86 (1), 41–54. doi:10.1190/geo2019-0615.1

Feng, Q., and Li, Y. (2022). Denoising deep learning network based on singular spectrum analysis-DAS seismic data denoising with multichannel SVDDCNN. *IEEE Trans. Geosci. Remote Sens.* 60, 1–11. doi:10.1109/TGRS.2021.3071189

Gao, J., Sacchi, M., and Chen, X. (2011). "A fast rank reduction method for the reconstruction of 5D seismic volumes," in *SEG technical Program expanded abstracts 2011* (San Antonio, Texas: Society of Exploration Geophysicists), 3622–3626. doi:10.1190/1.3627953

Jia, Y., and Ma, J. (2017). What can machine learning do for seismic data processing? An interpolation application. *Geophysics* 82 (3), 163–177. doi:10.1190/geo2016-0300.1

Jia, Y., Yu, S., and Ma, J. (2018). Intelligent interpolation by Monte Carlo machine learning. *Geophysics* 83 (2), 83–97. doi:10.1190/geo2017-0294.1

Jiang, J., Ren, H., and Zhang, M. (2021). A convolutional autoencoder method for simultaneous seismic data reconstruction and denoising. *IEEE Geosci. Remote Sens. Lett.* 19, 1–5. doi:10.1109/LGRS.2021.3073560 https://ieeexplore.ieee.org/abstract/document/9416991

Krizhevsky, A., Sutskever, I., and Hinton, G. (2012). Image Net classification with deep convolutional neural networks. *Adv. neural Inf. Process. Syst.* 25.

Li, W., and Wang, J. (2021). Residual learning of cycle-GAN for seismic data denoising. *IEEE Access* 9, 11585–11597. doi:10.1109/ACCESS.2021.3049479

Liu, G., Reda, F., Shih, K., Wang, T., Tao, A., and Catanzaro, B. (2018). "Image inpainting for irregular holes using partial convolutions," in Proceedings of the European Conference on Computer Vision (ECCV), 85–100.

Mandelli, S., Borra, F., Lipari, V., Bestagini, P., Sarti, A., and Tubaro, S. (2018). "Seismic data interpolation through convolutional auto encoder," in *SEG technical Program expanded abstracts 2018* (Anaheim, CA: Society of Exploration Geophysicists), 4101–4105. doi:10.1190/segm2018-2995428.1

Miller, D., Parker, T., Kashikar, S., Todorov, M., and Bostick, T. (2012). *Vertical seismic profiling using a fibre-optic cable as a distributed acoustic sensor*. Copenhagen, Denmark: EAGE publications. doi:10.3997/2214-4609.20148799

Oliveira, D., Ferreria, R., Silva, R., and Brazil, E. (2018). Interpolating seismic data with conditional generative adversarial networks. *IEEE Geosci. Remote Sens. Lett.* 15 (12), 1952–1956. doi:10.1109/LGRS.2018.2866199

Oropeza, V., and Sacchi, M. (2011). Simultaneous seismic data de-noising and reconstruction via multichannel singular spectrum analysis. *Geophysics* 76 (3), 25–32. doi:10.1190/1.3552706

Popa, J., Minkoff, S., and Lou, Y. (2021). An improved seismic data completion algorithm using low-rank tensor optimization: Cost reduction and optimal data orientation. *Geophysics* 86 (3), 219–232. doi:10.1190/geo2020-0539.1

Ronneberger, O., Fischer, P., and Brox, T. (2015). "U-Net: Convolutional network for biomedical image segmentation," in International Conference on Medical image computing and computer-assisted intervention (Cham: Springer), 234–241.

Sacchi, M. (2009). "FX singular spectrum analysis," in *Cspg cseg cwls convention*, 392–395.

Siahkoohi, A., Kumar, R., and Herrmann, F. (2019). "Deep-learning based ocean bottom seismic wavefield recovery," in *SEG technical Program expanded abstracts 2019* (San Antonio, Texas: Society of Exploration Geophysicists), 2232–2237. doi:10.1190/segm2019-3216632.1

Trickett, S. (2008). "F-xy Cadzow noise suppression," in *SEG technical Program expanded abstracts 2008* (Las Vegas, Nevada: Society of Exploration Geophysicists), 2586–2590. doi:10.1190/1.3063880

Wang, B., Zhang, N., Lu, W., and Wang, J. (2019). Deep-learning-based seismic data interpolation: A preliminary result. *Geophysics* 84 (1), 11–20. doi:10.1190/geo2017-0495.1

Wang, F. (2020). *Research on seismic data denosing and reconstruction using deep learning*. Hangzhou: Zhejiang University.

Wang, Y., Lu, W., Liu, J., Zhang, M., and Miao, Y. (2019). Random seismic noise attenuation based on data augmentation and CNN. *Chin. J. Geophys.* 62 (1), 421–433. doi:10.6038/cjg2019M0385

Zhong, T., Cheng, M., Lu, S., Dong, X., and Li, Y. (2021). Rcen: A deep-learning-based background noise suppression method for DAS-VSP records. *IEEE Geosci. Remote Sens. Lett.* 19, 1–5. doi:10.1109/LGRS.2021.3127637

frontiers | Frontiers in Earth Science

TYPE Original Research
PUBLISHED 10 January 2023
DOI 10.3389/feart.2022.992571

Traffic flow and vehicle speed monitoring with the object detection method from the roadside distributed acoustic sensing array

Zhipeng Ye[1], Weijun Wang[1]*, Xin Wang[2], Feng Yang[1], Fei Peng[1], Kun Yan[1], Huadong Kou[3] and Aijing Yuan[1]

[1]Institute of Earthquake Forecasting, China Earthquake Administration, Beijing, China, [2]Key Laboratory of Earth and Planetary Physics, Institute of Geology and Geophysics, Chinese Academy of Sciences, Beijing, China, [3]Institute of Geophysics, China Earthquake Administration, Beijing, China

OPEN ACCESS

EDITED BY
Yibo Wang,
Institute of Geology and Geophysics (CAS), China

REVIEWED BY
Siyuan Yuan,
Stanford University, United States
Hongrui Qiu,
Massachusetts Institute of Technology, United States

*CORRESPONDENCE
Weijun Wang,
wjwang@ief.ac.cn

SPECIALTY SECTION
This article was submitted to Solid Earth Geophysics,
a section of the journal
Frontiers in Earth Science

RECEIVED 12 July 2022
ACCEPTED 29 September 2022
PUBLISHED 10 January 2023

CITATION
Ye Z, Wang W, Wang X, Yang F, Peng F, Yan K, Kou H and Yuan A (2023), Traffic flow and vehicle speed monitoring with the object detection method from the roadside distributed acoustic sensing array.
Front. Earth Sci. 10:992571.
doi: 10.3389/feart.2022.992571

Distributed acoustic sensing (DAS) is an emerging technology that transforms a typical glass telecommunications cable into a network of seismic sensors. DAS may, therefore, concurrently record the vibrations of passing vehicles over tens of kilometers and shows potential to monitor traffic at a low cost with minimal maintenance. With big-data DAS recording, automatically recognizing and tracking vehicles on the road in real time still presents numerous obstacles. Therefore, we present a deep learning technique based on the unified real-time object detection algorithm to estimate traffic flow and vehicle speed in DAS data and evaluate them along a 500-m fiber length in Beijing's suburbs. We reconstructed the DAS recordings into 1-min temporal–spatial images over the fiber section and manually labeled about 10,000 images as vehicle passing or background noise. The precision to identify the passing cars can reach 95.9% after training. Based on the same DAS data, we compared the performance of our method to that of a beamforming technique, and the findings indicate that our method is significantly faster than the beamforming technique with equal performance. In addition, we examined the temporal traffic trend of the road segment and the classification of vehicles by weight.

KEYWORDS

distributed acoustic sensing, traffic monitoring, vehicle flow, vehicle speed, real-time object detection YOLO, slant stack, vehicle classification

Introduction

Traffic monitoring and management are essential links in the construction of smart cities. Comprehensively monitoring the densely distributed urban road network is still a challenging task. Surveillance cameras are the most intuitive monitoring method, but the construction and maintenance costs are high. At the same time, video processing is enormous, and monitoring coverage has dead spots and is also greatly affected by lighting and meteorological factors. Using the cell phone signals of people on the road network is an innovation to track road congestion in real time. However, both of the aforementioned methods have personal privacy concerns, so developing new monitoring methods complements the deficiencies of the existing observation systems.

The emergence of distributed acoustic sensing (DAS) applications in the city can revolutionize the smart city's sensing abilities as lots of dark fibers existing in the city can be transformed into vibration sensors. Because infrastructure optical cables for communication or traffic surveillance would cover almost every major road, building a DAS transport management system over the whole city will be possible with the benefits of fast construction and low maintenance cost. Hence, DAS could be another new way to continuously monitor the roads (Chambers, 2020).

Numerous examples have proved the effectiveness of the roadside DAS for traffic surveillance. Using a wavelet threshold method, Liu et al. (2019) identified the features of passing cars from DAS recordings and then estimated the number and speed ranges of the vehicles. In addition, automobiles were categorized using a support vector machine classifier. Lindsey et al. (2020) employed an automatic template-matching method to detect the changes in Palo Alto, California, automobile traffic patterns during the COVID-19 quarantine. They also effectively observed traffic over a 2-month period, including significant declines associated with the COVID-19 reaction. Chambers (2020) provided an automated approach for predicting vehicle counts and speeds at Brady Hot Springs, Nevada, United States, utilizing DAS array velocity stacking. Wang et al. (2021) monitored the number of cars and their average speed between December 2019 and August 2020 in Pasadena, California, using the slant stack method and analyzed the changes in traffic patterns caused by the COVID-19 lockdown. Wang et al. (2020) identified the "heaviest" float and the "loudest" band at the 2020 Rose Parade in Pasadena, California, based on the amplitudes recorded by the Pasadena DAS array. Weight estimation is a unique feature of DAS that differentiates it from video traffic surveillance. Clearly, dense DAS acquisition facilitates the processing of seismic arrays and improves the precision of vehicle identification and dynamic parameter estimations.

Although DAS has unparalleled advantages in continuous roadside traffic monitoring, the massive data produced by DAS are a barrier to mining. Traditional seismic array processing is used to analyze the traffic parameters, which frequently needs abundant computation and makes long-distance real-time monitoring inappropriate. Applying various machine learning algorithms on DAS waveforms or wavefield images is one of the popular approaches to reduce the processing time. Narisetty et al. (2021) introduced the SpeedNet model and used real-world and simulated data to determine the average vehicle speed each minute. In comparison to existing loop detector-based sensors, their model obtained an accuracy of over 90%. Wiesmeyr et al. (2021) utilized an image and signal processing technique to compute the vehicle speed and numbers for a highway DAS experiment and evaluate the findings in comparison to reference data from roadside sensors. Van den Ende et al. (2021) suggested a deconvolution auto-encoder (DAE) model for deconvolving the typical automobile impulse response from DAS data. The test on a 24-h traffic cycle using the DAE model demonstrates the viability of potentially processing massive DAS volumes in near real time.

YOLO (You only look once: Unified, real-time object detection, Redmon et al., 2016) is one of the fastest and most accurate object identification AI frameworks (https://pjreddie.com/yolo/). Stork et al. (2020) and Zhu and Shragge (2022) demonstrated that YOLO can detect weaker microseismic event signals with low signal-to-noise ratios and high average precision over DAS data in near real time. Numerous YOLO-based systems that rely on the road video network have been presented, and it has been proven that the algorithm is effective and viable for traffic monitoring in near real time (Cao et al., 2019; Ge et al., 2020; Mandal et al., 2020; Al-qaness et al., 2021; Amitha and Narayanan, 2021; Lin and Jhang, 2022; Zheng et al., 2022). To the best of our knowledge, however, YOLO has not been implemented for DAS traffic monitoring. Owing to the processing performance advantages of YOLO, it is possible to achieve a substantial advance in DAS traffic monitoring by employing this algorithm.

In this research, we will, therefore, offer another recognition model based on deep learning. This solution is mostly based on the YOLOv5 framework for real-time object detection. We will construct a collection of datasets, train them, then conduct a system evaluation, and compare the outcomes to the conventional method based on slant stacking (Wang et al., 2021). We will also measure vehicle weights and attempt to classify them in order to illustrate a second potential traffic monitoring capability of DAS.

Data and methods

We conducted a 15-day DAS experiment near the Wenyu River in the Changping area of Beijing in December 2021 (Figure 1). The fiber optical cable we utilized was 3.2 km in length and was primarily installed along the river. A Silixa iDAS interrogator was installed at the cable's eastern end and was let to continuously measure the strain rate changes along the cable with a 2000-Hz time sampling rate and 4-m spatial interval. Therefore, the experiment has about 800 channels in total.

On the riverbank is a road that serves as the primary transportation artery for the nearby residents. The passing vehicles on the road would cause vibrations and generate seismic waves that will propagate to nearby optical cables and generate cable strain deformations. These deformations will be densely recorded by the DAS array, and the movement of

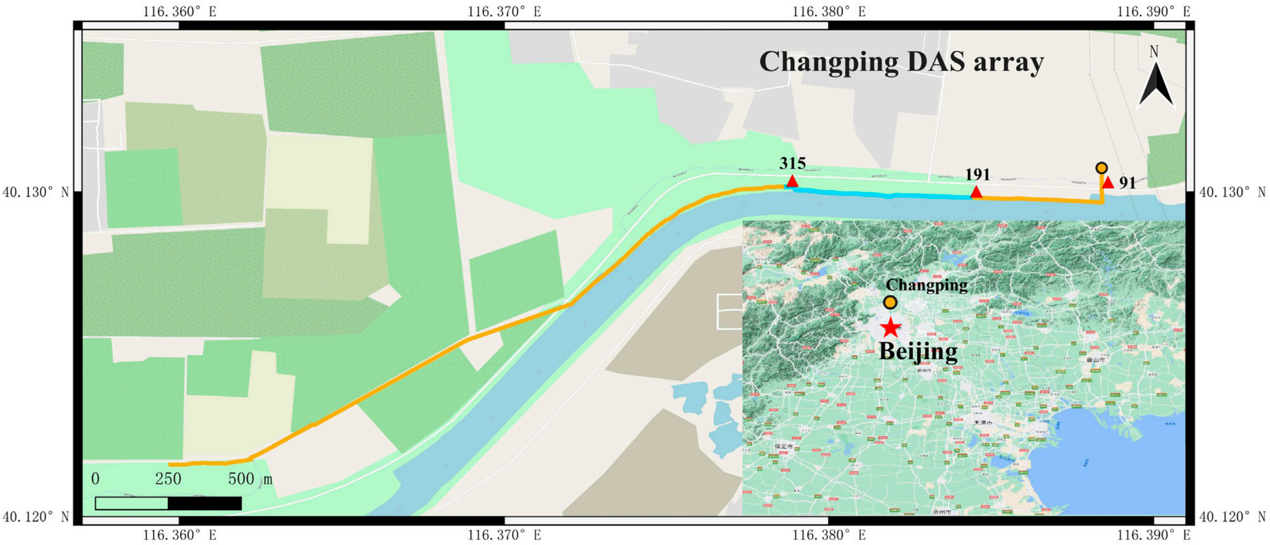

FIGURE 1
DAS array in Changping, Beijing. The yellow line is the optical cable, and the yellow circle indicates the location of the DAS interrogator. We used data from the sub-array (No. 191–315, blue line) and No. 91 (one of the cross-road channels) for traffic monitoring.

every vehicle appears as a trajectory in DAS temporal–spatial recordings. According to the existence of the trajectory and its pattern, we can judge the passing vehicle, its speed, and the direction through traditional seismic array processing, image recognition, or even direct visual inspection.

We utilized about 500 m of fiber in the east (channels from 191 to 315, Figure 1) to monitor the traffic flow. This section of the fiber is roughly parallel to the road but about 20 m apart (Figure 1). In addition, the eastern portion contains a piece of cable (channel 91) that spans the road and allows a direct measurement of the vehicle-caused road vibration. The flows at the east and west may be different since some vehicles may stop by a restaurant that is situated between channels 91 and 191. The overall processing flow is shown in Figure 2.

Distributed acoustic sensing data preprocessing

We first downsampled the continuous DAS data on channel 191–315 to 200 Hz and removed the linear trend, the mean value, and the common-mode noise. As the spectrum diagrams of two representative channels shown in Supplementary Figure S1, the background ambient noises are abundant at 1–20 Hz, while the vehicle signals above 20 Hz are easier to be separated from the background noises. On the other hand, vehicle signals below 1 Hz are only obvious for some heavy vehicles but not common for all; therefore, we apply a 20–50 Hz bandpass filter to the DAS data to improve the reliability of passing vehicle identification.

Passing vehicle detection and speed estimation with YOLOv5

YOLOv5 is the most recent version of the YOLO series (https://github.com/ultralytics/yolov5). One significant improvement is the detection speedup by PyTorch (Paszke et al., 2019), which can work with deeper networks for applications on more extensive datasets and real-time cases. The structure of YOLOv5 comprises four parts: the input, backbone network, neck network, and prediction network.

The principle of object detection is to use an anchor to select an image segment from the image and input it into the convolutional neural network model to identify the object category in the frame. By scanning the entire image with anchors of different sizes, we recognize and locate the object when the probability of the box-selected image segment predicted as ground truth is greater than the set threshold. The object detection algorithm is divided into two categories according to the processing steps. The two-stage method generates a series of region proposals through a particular module. It then uses a convolutional neural network for sample classification and regression positioning to detect objects represented by Faster R-CNN (Ren et al., 2015). The one-stage method directly extracts features from anchors to predict the object category and location, as described by SSD

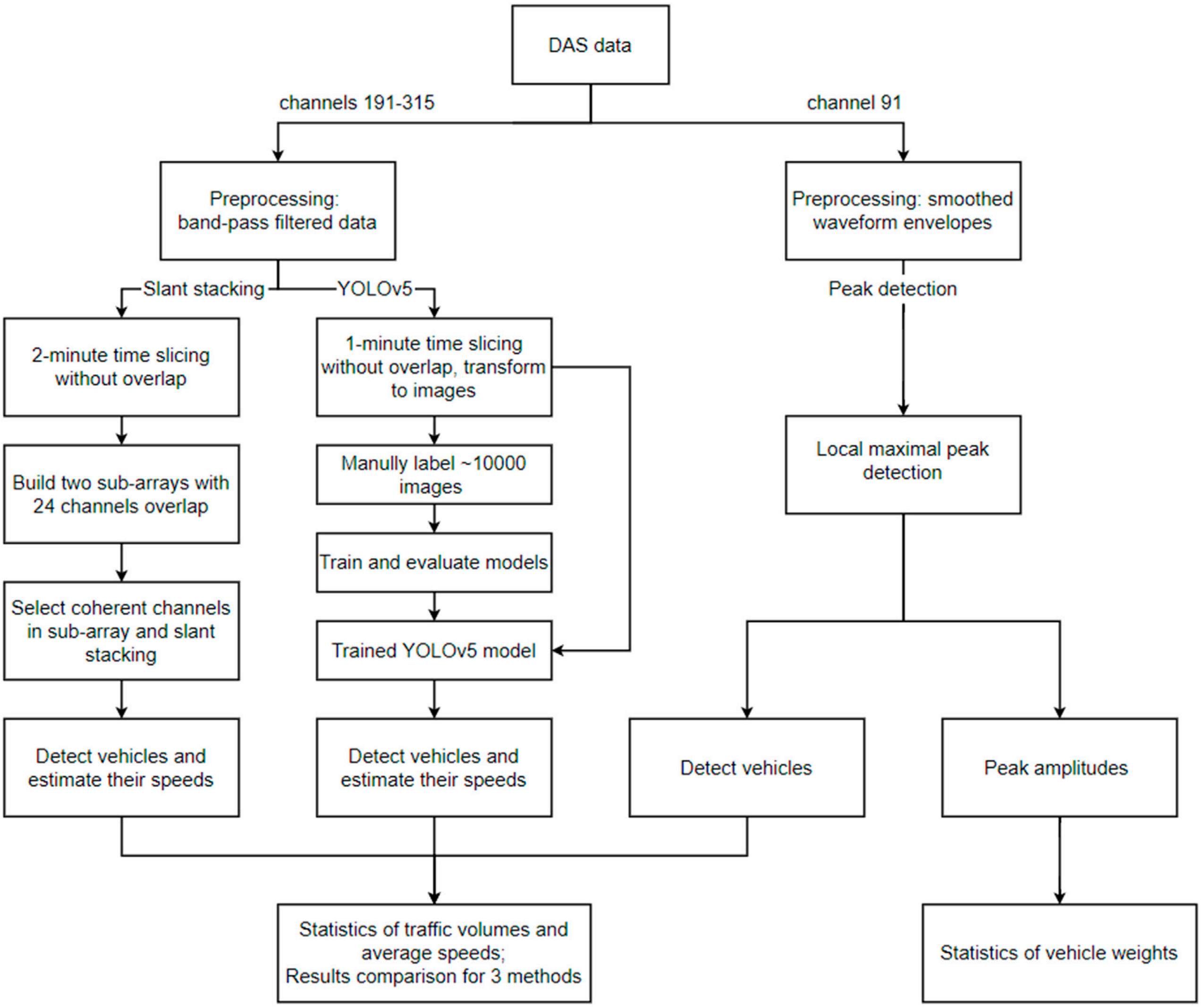

FIGURE 2
Overall data processing flow.

(Liu et al., 2016) and YOLO series (Redmon et al., 2016; Redmon and Farhadi, 2017; Redmon and Farhadi, 2018). Two-stage detection has high accuracy but slow detection speed. One-stage detection accuracy is low but much faster than the two-stage algorithm and is widely used in real-time object detection tasks.

We preprocessed DAS continuous waveforms for channels 191–315 into 1-min segments without overlap. The 1-min waveforms of 125 channels were converted to images in the size of 1167*875, resulting in around 21,000 photographs over the course of 15 days. To train a new YOLOv5 model for vehicle detection and speed estimation, we manually annotated a dataset of about 10,000 photographs.

For vehicle trace labeling in DAS images, LabelImg (2022) is employed. LabelImg is a graphical image annotation tool that labels object bounding boxes in images. These images are manually categorized as automobiles with varying speeds or noises without any car passing. First, we utilize bounding boxes for each image to entirely contain the vehicle traces with a predetermined size. One box represents an automobile that has been labeled, and the car number is the sum of the number of boxes. As the vehicle traces are contained within the boxes, the height and width of the boxes correspond to the driving distance and journey duration of the cars. Therefore, it is possible to determine the speed ranges of vehicles by calculating the aspect ratio of the bounding boxes. Once vehicle traces have been tagged, the width, height, and

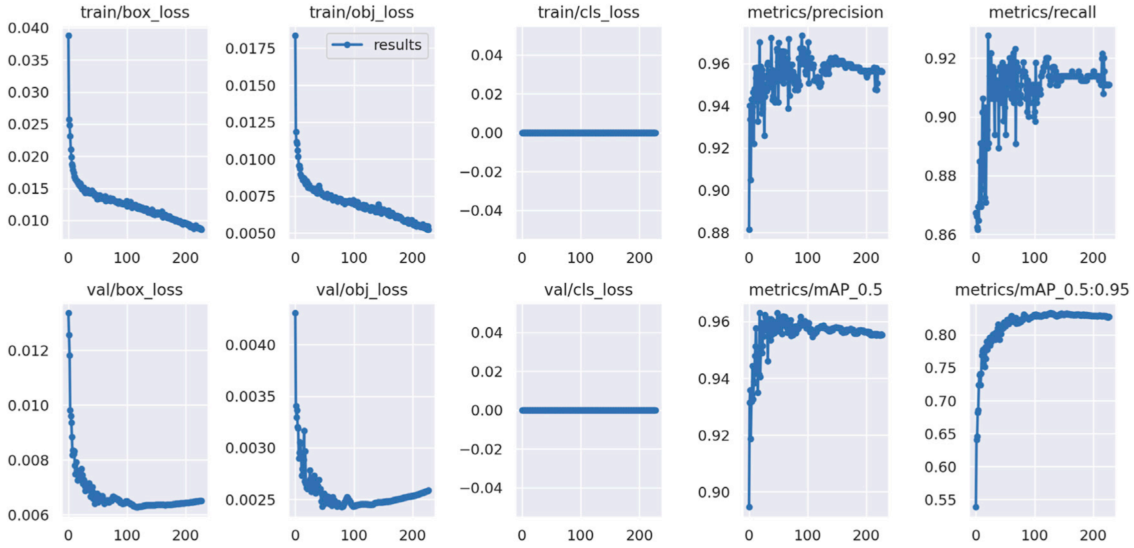

FIGURE 3
Vehicle detection YOLOv5 model training. Box regression loss (box loss), object loss (obj loss), class loss (cls loss), training accuracy, and recall are depicted in the top row, from the left to the right. Similar to the first row, the first three figures in the second row are loss functions for the validation set instead. The next two figures represent the mean average precision for IoU thresholds greater than 0.5 and for the range (0.5, 0.55, 0.60, ..., 0.95).

center coordinates of the boxes are automatically recorded as the ground-truth location for model training.

By counting the number of boxes and computing their box aspect ratio, we can determine the number of cars and their speed in each 1-min DAS image. In a ratio of 8:1:1, the dataset is randomly divided into training, validation, and testing sets. For training, we employ the SGD (Robbins and Monro, 1951) optimizer with momentum and weight decay coefficients of 0.937 and 0.0005, respectively. The learning rate is 0.01, and the initial training epoch has been set to 300. The deep learning processing flow of YOLOv5 is shown in Supplementary Figure S2. Due to the early stop mechanism, the training process on a server with two Nvidia GeForce RTX 3090 GPUs was terminated at epoch 228 after 10 h of training (Figure 3). Currently, the best model is the No. 128 epoch, with training precision as high as 95.9% (Figure 3).

Box loss, object loss, and class loss are the primary evaluative factors for object detection algorithms. Given that the length and width of the boxes are critical to the distance and travel time of vehicle traces in DAS photographs, the box's dimensions are crucial in this instance. The slight box loss provides a more precise bounding box position and enhances the speed estimation performance. YOLOv5's box loss is a CIoU (complete intersection over union) loss between the predicted and ground-truth box (Zheng et al., 2020). IoU (intersection over union) is computed in the following manner:

$$IoU = \frac{|B \cap B^{gt}|}{|B \cup B^{gt}|}, \tag{1}$$

where $B^{gt} = (x^{gt}, y^{gt}, w^{gt}, \text{and } h^{gt})$ is the ground-truth bounding box and B = (x, y, w, and h) is the predicted bounding box.

CIoU loss is defined as follows:

$$L_{CIoU} = 1 - IoU + \frac{\rho^2 (b, b^{gt})}{c^2} + \alpha v, \tag{2}$$

where b and b^{gt} denote the central points of B and B^{gt}, ρ^2 represents the square of the distance between the center points of the prediction box b and the gt (ground-truth) box b^{gt}, and c^2 represents the square of the diagonal length of the smallest box that can just contain the prediction box and the gt box.

α as a trade-off parameter is shown in Eq. 3:

$$\alpha = \frac{v}{(1 - IoU) + v}. \tag{3}$$

Here, ν is used to measure the consistency of the aspect ratio between the predicted box and the gt box, and its definition is shown in Eq. 4:

$$v = \frac{4}{\pi^2}\left(arctan\frac{w^{gt}}{h^{gt}} - arctan\frac{w}{h}\right)^2, \tag{4}$$

where w^{gt} and h^{gt}, respectively, represent the width and height of the gt box, and w and h, respectively, represent the width and height of the prediction box.

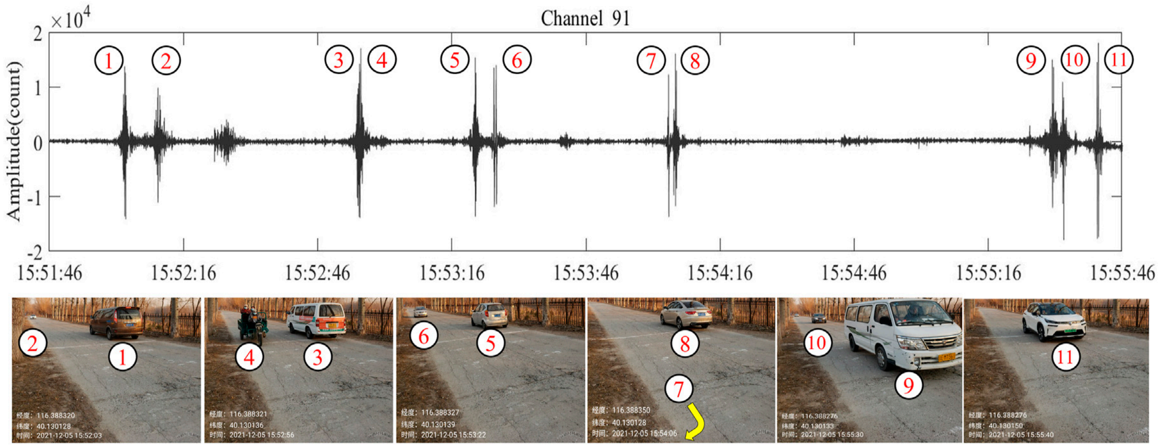

FIGURE 4
Cars across the cross-road fiber cable and their raw signals in the No. 91 DAS channel in the 4-min period. The cross-road fiber is beneath the white line in pictures. The events are labeled with numbers by time order. Cars No. 3 and No. 4 passed the channel almost the same time, and their waves are stacked together. Car No. 7 was not photographed since it turned to the restaurant as the yellow arrow indicates and did not have any signals captured on channels 191–315 during that time. Cars No. 2 and No. 4 also did not go through channels 191–315, according to our manual waveform inspection.

CIoU loss takes three geometric properties into account, i.e., the overlap area, central point distance, and aspect ratio, and leads to a faster convergence and better performance. It is apparent in the first column of Figure 4 that the box regression loss dropped rapidly within 10–20 epochs. Object loss is the confidence loss of ground-truth and predicted bounding boxes for determining the probability of whether there are objects in the predicted bounding box. Object loss uses BCE loss (binary cross-entropy loss) in YOLOv5. BCE loss is defined in Eq. 5:

$$L_{BCE} = \begin{cases} -log(p) & y = 1, \\ -log(1-p) & Otherwise, \end{cases} \tag{5}$$

where p is the probability of the predicted bounding box belonging to the gt box, y represents the value of the ground-truth bounding box, and the value range of y is {1, 0}.

Class loss used in YOLOv5 is focal loss. Focal loss is defined as follows:

$$L_{focal} = -(1-p_t)^{\gamma} log(p_t), \tag{6}$$

where p_t is the probability of the predicted class that belongs to the true class and γ is the focusing parameter ($\gamma \geq 0$).

We only identified one class of automobile trace in the DAS photographs; hence, the class loss values of training and validation are both zero. There are considerable fluctuations in the first 100 epochs of the training precision and recall curves, but after the first 100 epochs, the curves gradually converge, and the accuracy is over 94%, and the recall is over 91%. In addition, the mean average accuracy with an IoU threshold of more than 0.5 is greater than 95%, and the mean average precision with an IoU threshold between 0.5 and 0.95 is close to 83%.

After training the model, we applied it to all DAS data and systematically recognized passing vehicles and their speed in the 15-day period. In a laptop with an Nvidia GeForce RTX 3060 Laptop GPU, the detection procedure only takes a total of about 0.5 h.

Passing vehicle detection and speed estimation by slant stacking

We also applied the slant stacking approach developed by Wang et al. (2021) to detect the passing vehicle and its speed. Similar to previous YOLOv5 processing, we segmented the prepossessed continuous DAS time series from the same 125 channels (about 500 m, the blue line in Figure 1) at 2-min intervals. The longer interval instead of 1 min can provide a more stable estimation of vehicle speed but will be more time-consuming during the slant stacking procedure. We used 2-min intervals for accurate speed estimation and for speeding up the computation. The 125 channels were further divided into sub-arrays with 74 channels and overlapped by 24 channels (i.e., slide with 50 channels). In each sub-array, we first performed data quality control by deleting these channels with a cross-correlation coefficient with adjacent channels smaller than 0.5. We then stacked the waveforms in the sub-array with the fourth root method (Rost and Thomas, 2002) by scanning the different

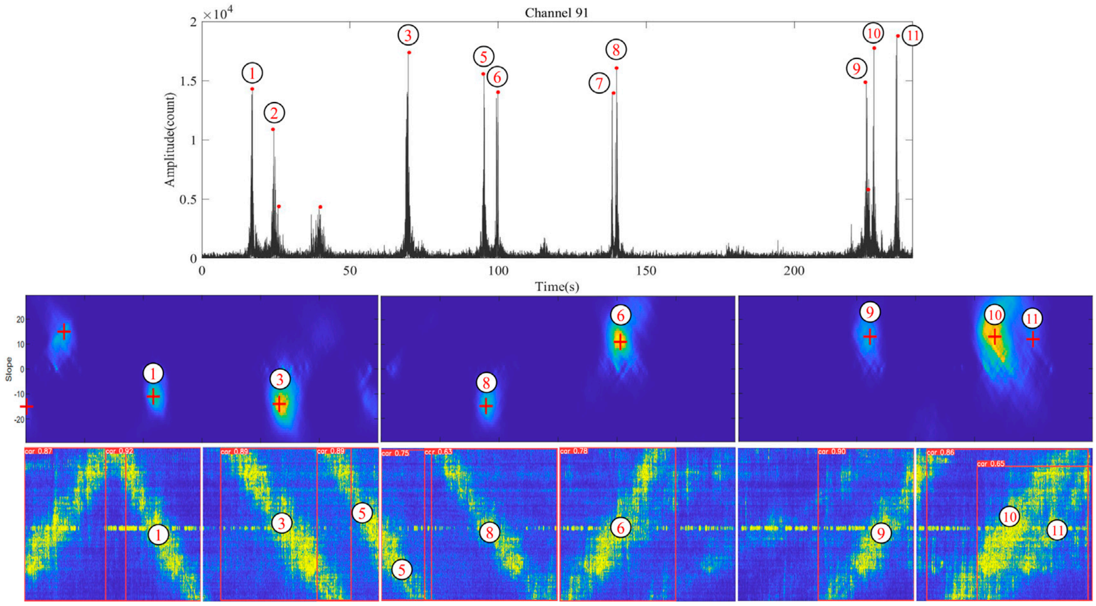

FIGURE 5
Vehicle detection comparisons. The three planes from up to down correspond to the findings of peak detection, slant stacking, and YOLOv5. Their respective detections are indicated by red dots, crosses, and boxes with correlation coefficients. The numbers in the circles are identical to those in Figure 4, but their order has altered due to their differing movement orientations. Cars 2, 4, and 7 do not pass through the DAS array on channels 191–315.

TABLE 1 Vehicle detection verification.

Method	Ground truth	Detection	Missed detection	False detection	Repeat detection
Peak detection (array at No.91)	11	13	1	3	0
Slant stacking (array at No. 191–315)	8	7	1	0	0
YOLOv5 (array at No. 191–315)	8	9	0	0	1

vehicle trace slopes (p). The vehicle's speed(c) can be determined as follows:

$$c = \frac{m*s}{p*dt}, \tag{7}$$

where m, s, and dt are the number of channels, the channel interval, and the time sampling rate, respectively. In this study, the values are 125, 4 m, and 0.05 s, respectively. We have established a speed estimation range of over 25 km/h to 100 km/h based on road conditions. This indicates that the slope p ranges from 28.8 to 115.2 in one direction and −115.2 to −28.8 in the opposite direction. The sign of p conveys information about the movement direction.

We shifted both sides of the middle channel of each subarray's $p*dt$ samples in the opposite direction and then stacked their energies. In addition, we utilized local maxima analysis to identify the peaks in order to estimate the number of vehicles and their speeds per 2 min. The results of the two sub-arrays are mutually verified for reducing vehicle detection and speed estimation errors by calculating the mean values of the vehicle numbers and speed ranges, respectively. All of the aforementioned DAS data slant stack processing procedures require roughly 85 h serially running on a Linux server with two AMD EPYC 7702 64-Core processors.

Due to the proximity of the fiber cable to the road in comparison to the measurement length, both the apparent speeds determined by YOLOv5 and slant stacking are considered to be the vehicle speed. Using the following formula, we estimated the hourly average speed (v_{avg}) as follows:

$$v_{avg} = \frac{\sum_{i=1}^{n} v_i}{n}, \tag{8}$$

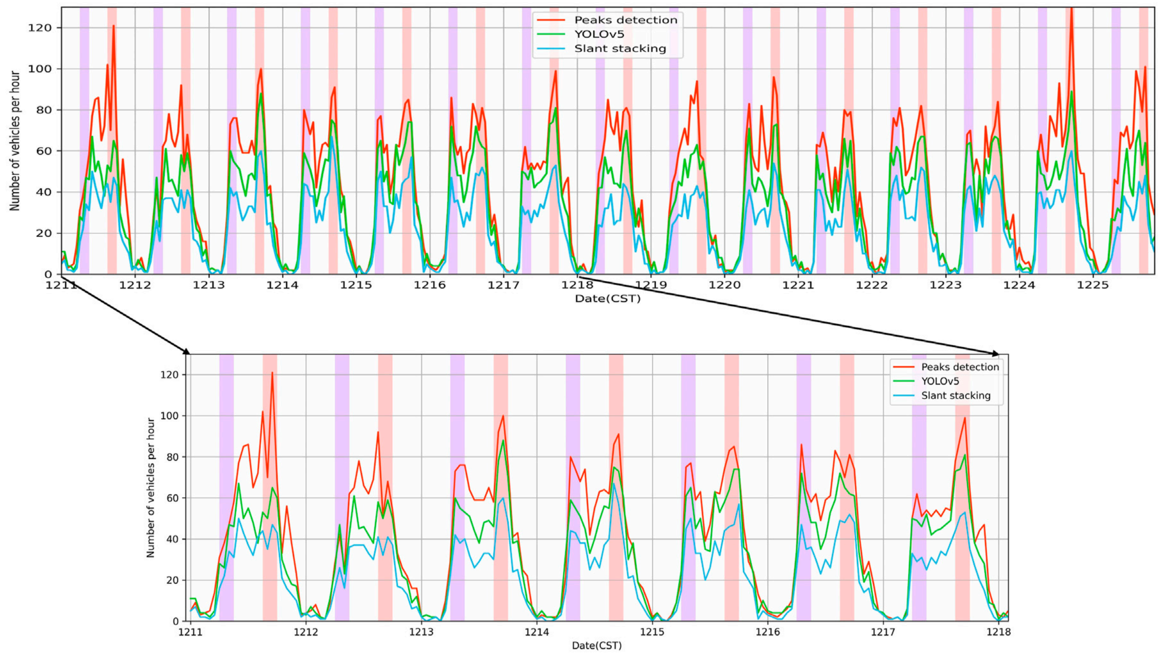

FIGURE 6
Daily variations in the traffic volume for event peak detection, YOLOv5, and slant stacking methods in 15 days. The zoom-in image in the lower panel highlights daily and weekly periodic patterns.

where v_i is the individual vehicle speed detected by YOLOv5 or the slant stacking method and n is the number of vehicles in 1 hour.

Detection of vehicles and analysis of their weights by waveform amplitudes

Using transient fluctuations in waveform energy (amplitude) is a conventional technique for detecting seismic events, and it can also be utilized to detect passing cars. This detection can be performed with a single sensor, which is simple and requires minimal computational resources. But the method is difficult to estimate the movement speed and is more likely to be falsely triggered by pedestrians or other non-vehicle vibrations in the vicinity.

The continuous waveforms in a piece of cross-road cable (channel 91 in Figure 1) were independently used to count the vehicle number. As shown in Figure 4, moving automobiles caused obvious waveform changes, and their amplitudes may be relative to the vehicle's weight. The original waveforms in this channel were downsampled, detrended and mean value removed, then transformed to waveform envelopes and smoothed with 2-s windows.

We used local maximal analysis to detect the events. Through several tests, the amplitude threshold and minimum event interval are set to 2000 count and 2 s, respectively.

Results

Vehicle detection comparison and verification

We begin by comparing the detections of the three techniques. On channel 91, we use a 4-min window for peak detection (Figure 4). During this time, we took photographs of vehicles crossing the channel. Photographs and waveforms on the channel confirm the passage of 11 vehicles within a 4-min period. For slant stacking and YOLOv5 methods, we extend the 4-min window on channels 191–315 by 1 minute at both ends. Due to the distance between the two observation sites (approximately 400 m) and the time shifts caused by passing vehicles, the 6-min window will ensure that the measurements for the three methods overlap.

We visually inspect the DAS array records for 11 vehicles that passed channel 91 and confirm that three of them (No.2, 4, and 7 in Figure 5) did not enter channels 191–315. Therefore, the ground-truth passed vehicle numbers for channel 91 are 11 and

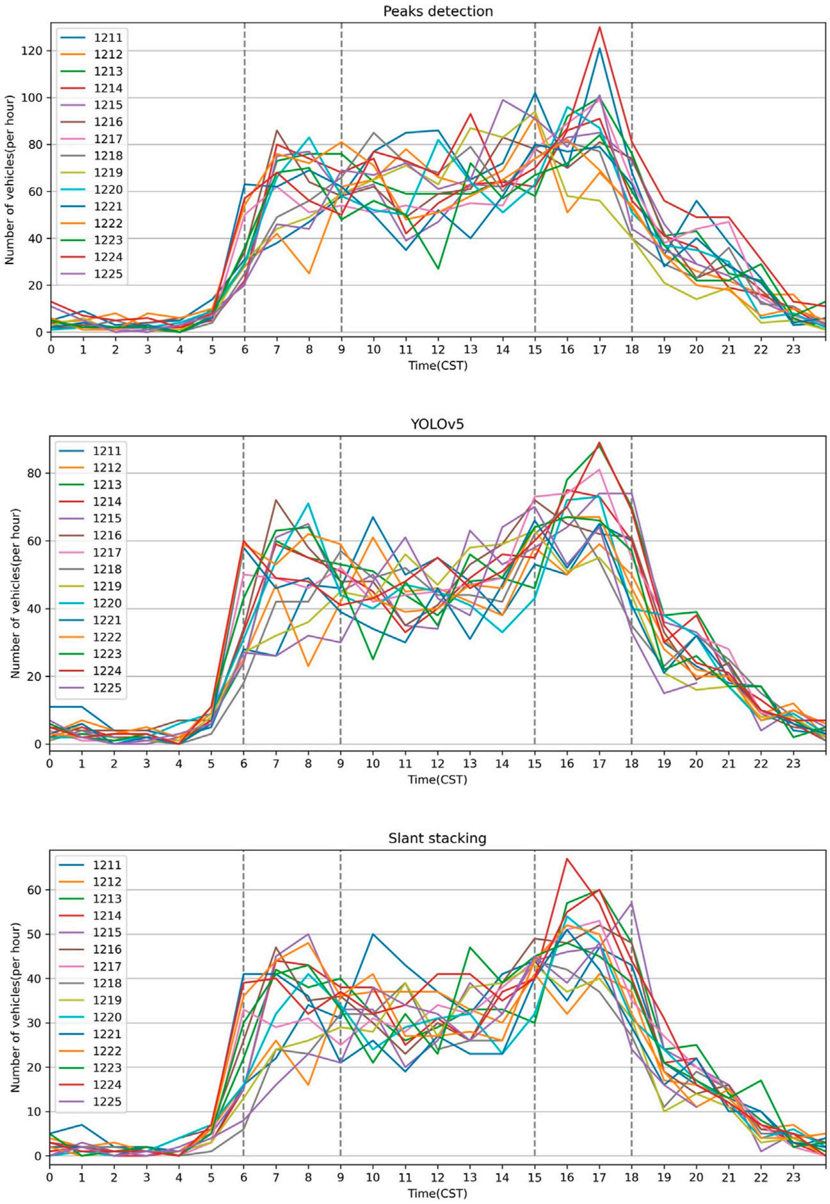

FIGURE 7
Hourly traffic volumes of 15 days derived from three detection methods. Different colored lines correspond to each day, and the gray vertical dot lines represent the rush hour.

those for the DAS array on channels 191–315 are 8. Table 1 shows the vehicle detection verification of peak detection, slant stacking, and YOLOv5 methods. The number detected by the peak method is 13, and the three incorrectly detected signals are likely the result of local vibrations, such as people walking or a stopped car with its engine running. Supplementary Figure S3 shows more similar wrong detection cases, implying that the single-channel detection approach is susceptible to both moving vehicles and local events. The slant stacking and YOLOv5 methods each identify seven and eight vehicles, respectively. The absence of a detected vehicle in slant stacking is primarily due to the fact that the event signals on the different channels are split by the time window, and the stacking energies in both windows are too weak to identify (Figure 5). Two cars (Nos. 10 and 11) that are following closely are correctly identified by either slant stacking or YOLOv5. Unlike the slant stacking, a trace across two windows may be detected twice by YOLOv5 (Figure 5), which needs to remove duplicates by comparing their speeds and corner coordinates at the adjacent boxes. Other strong vibrations on

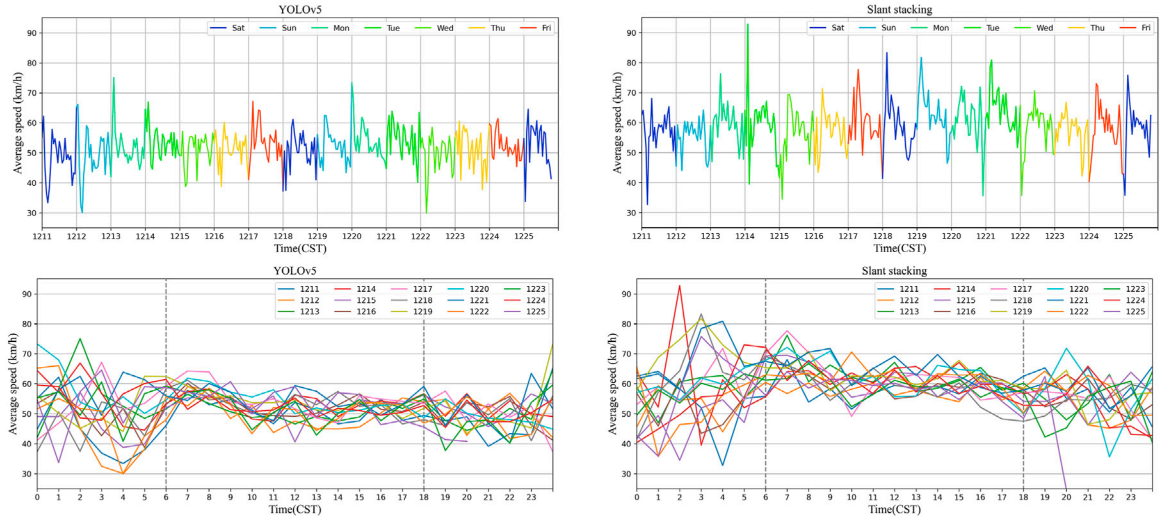

FIGURE 8

Figures in the top row represent the daily and weekly variations of the average speed, as estimated by YOLOv5 and the slant stacking technique. The figures in the second row represent hourly variations of the same methods. The gray dot line in the second row of figures divides each day into three distinct time intervals with varying average speed trends.

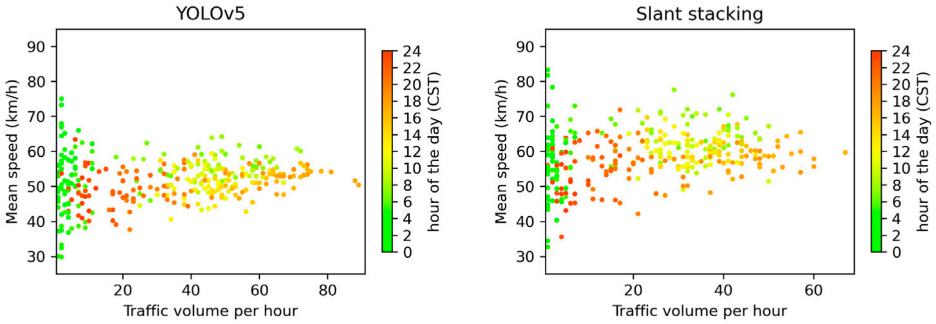

FIGURE 9

Relationship between the traffic volume and mean speed derived from the detection results of YOLOv5 (left) and slant stacking (right). The colors of the scatters represent the time of the day.

channels 191–315 that are unrelated to traffic can be efficiently suppressed using both array-based methods, as shown in Supplementary Figure S3.

Traffic flow estimation and analysis

We used YOLOv5, slant stacking, and event peak detection to identify passing vehicles in about 2 weeks' worth of DAS data between 11/12/2021 00:00 (Saturday) and 25/12/2021 20:00 (Monday) for the investigation of traffic patterns. We compared the variations in the number of automobiles per hour detected by the aforementioned three independent approaches. As seen in Figure 6, the three estimation methods for traffic volume yield comparable traffic patterns but differ in terms of the number of vehicles. The event peak detection method predicts the greatest number of vehicles, whilst the YOLOv5 method estimates a somewhat lower number, and the slant stacking method estimates the smallest number.

Traffic volume estimations are affected by a number of variables. One of the causes is the variance in the processing time window. With shorter time windows, more vehicles would be spotted, particularly during rush hour, but they would also be identified many times because the signals may span two units of

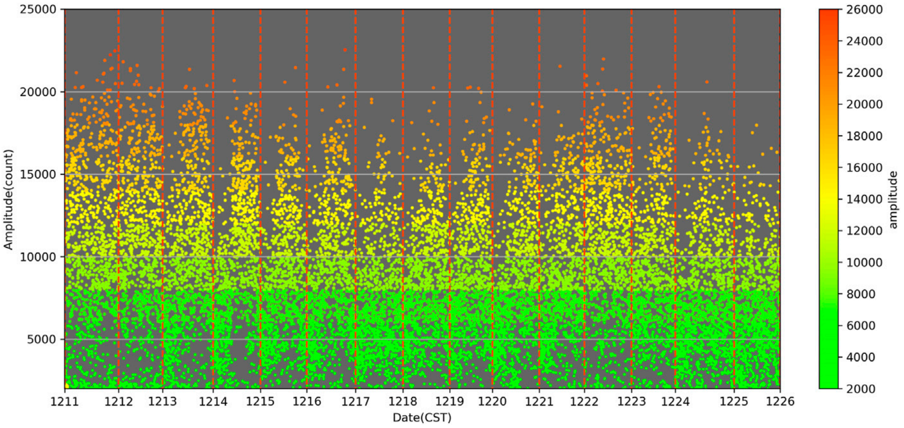

FIGURE 10
Passing vehicles' amplitudes over the time.

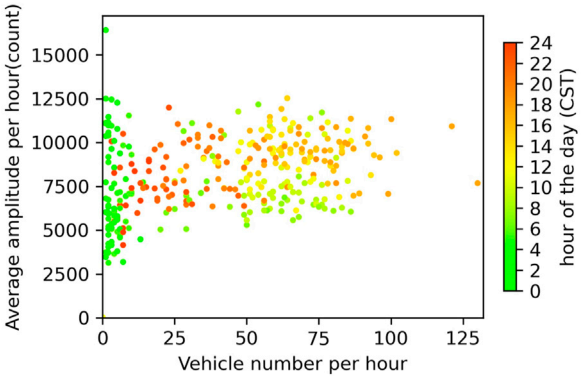

FIGURE 11
Hourly vehicle numbers and their mean amplitudes from peak detection. The colors of scatters represent the hour of the day.

data in continuous time series for array-based algorithms, such as YOLOv5 or slant stacking. False identifications can be avoided to a considerable extent with array-based approaches, which need coherent signals over many channels. In contrast, we discovered erroneous identifications in the peak detection method, where the erroneous peaks were likely generated by the neighboring tree swaying in windy conditions. In order to acquire more dependable traffic patterns, it is necessary to improve the detection algorithm, such as recognizing multiple objects simultaneously in an array-based approach.

Similar daily and weekly fluctuations exist for each of the three procedures. Each day's traffic volume peaks in the morning, lowers during the midday, reaches another peak in the afternoon, and finally declines in the evening. We emphasize the two traffic volume peaks that occur within a certain time period for each technique, illustrating the weekday peaks. On weekdays, the morning rush hour occurs between 6 and 9 h, and the afternoon rush hour occurs between 15 and 18 h. However, this tendency is not appropriate on weekends, as depicted in the graph. From the zoomed-in graph, we can note that the weekday traffic volume peaks are quite narrow. We also find it intriguing that all methodologies forecast Friday's morning rush hour to have significantly less traffic volume than other days. The weekly variations with a regular pattern may be related to the commute times of nearby neighbors.

We study the hourly traffic volume variations of event peak detection, YOLOv5, and the slant stacking method in greater detail (Figure 7). The majority of traffic volume accumulates between the morning and afternoon rush hours. During 6–18 h, the traffic volume of the event peak detection method ranges from 40 to 100 vehicles per hour, the YOLOv5 method ranges from 30 to 80 vehicles per hour, and the slant stacking method ranges from 20 to 60 vehicles per hour. The traffic volume estimation of the YOLOv5 approach is more accurate than that of the slant stacking method as the results of event peak detections represent the actual traffic volume. The hourly variance of each day is divided into five time-groups based on the morning and afternoon rush hours. From 0 to 6 h is the initial time where the majority of traffic volume is less than 10 vehicles per hour. The morning rush hour is the second interval between 6 and 9 a.m. Compared to 9–15 h, the third session has a relatively lower but stable volume of traffic. The afternoon rush hour is the fourth time between 15 and 18, characterized by the biggest volume of traffic. The final phase, between 18 and 0 h, is characterized by a sharp decline in the traffic volume.

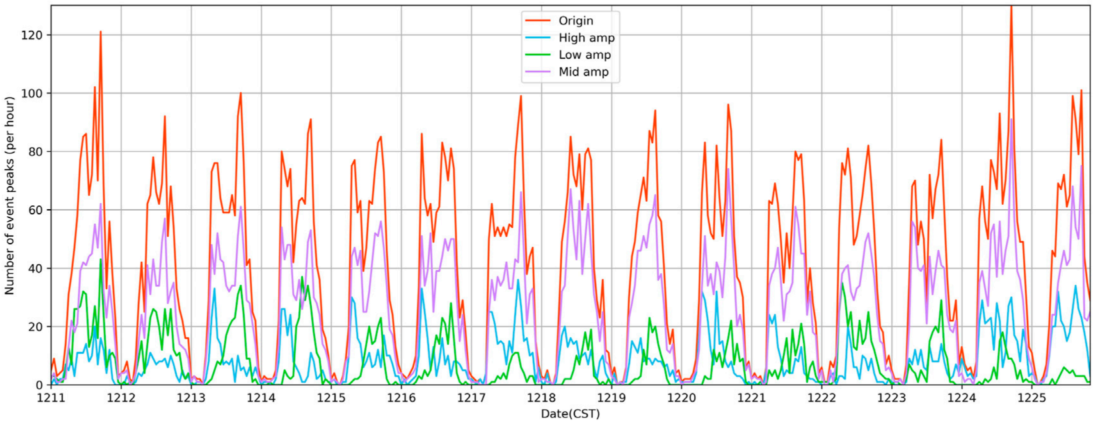

FIGURE 12
Distributions of vehicle numbers per hour for different vehicle weights. The vehicles are categorized into three classes: amplitude over 12,500 counts (High amp), lower than 5,000 counts (Low amp), and between 5,000 and 12,500 counts (Middle amp). The origin line is for total numbers.

Vehicle speed estimation

Figure 8 depicts the average speed variation of YOLOv5 and slant stacking. The YOLOv5 mean speed ranges between 30 km/h and 80 km/h, while the slant stacking method ranges between 30 km/h and 90 km/h. In general, the mean speed predicted by the slant stacking method is around 10 km per hour faster than YOLOv5. A vehicle trace in a DAS image is a width-measured line (the last panel in Figure 5). The slope of the middle section of the line is more representative of the actual vehicle speed. When the bounding box identified by YOLOv5 entirely encloses the entire vehicle trail, the speed calculated by the aspect ratio of the bounding box is always lower. The speed determined *via* slant stacking is more accurate than that of YOLOv5. The YOLOv5 technique speed range is upward and rises from 40 km/h to 60 km/h, whereas the slant stacking method speed range rises from 50 km/h to 70 km/h during the day. Figure 8's top row depicts the daily and weekly fluctuations of the average speed assessed using YOLOv5 and the slant stacking approach. The fluctuations in the average speed over time for YOLOv5 and slant stacking are comparable. During the interval between midnight and dawn, the average speed of both the techniques is very variable, and the period contains both the minimum and maximum average speeds. In the second row of Figure 8, both the methods exhibit a gradual decrease in the average speed from six to eighteen o'clock, which corresponds to the rush hour periods discussed in the previous section. The average speed decreases from 60 km/h to 50 km/h for the YOLOv5 method and from 70 km/h to 50 km/h for the slant stacking method.

On the graphs of the hourly traffic volume and mean speed, we compare the results of YOLOv5 and the slant stacking method (Figure 9). For YOLOv5, there are less vehicles between midnight and early morning with divergent average speeds between 30 km/h and 80 km/h, while the majority of the vehicles are concentrated during the day with convergent average speeds between 40 km/h and 60 km/h. Slant stacking demonstrates the same distribution as YOLOv5 but with greater mean speeds and smaller traffic volume; the midnight and early morning period mean speed range is over 30–90 km/h, and the daylight period mean speed range is over 50–70 km/h.

Vehicles classified by amplitude

The DAS-measured vehicle-passing amplitude is roughly proportional to the vehicle's mass and load. In general, the stronger the vibration, the greater the total mass is. Figure 10 depicts the distribution of amplitudes across time for all identified events, while Figure 11 compares the vehicle numbers and their average amplitudes during the daily hours. Similar distributions are seen to those depicted in Figure 9. On the basis of these distributions, we broadly split the amplitudes into three categories: amplitudes higher than 12,500 counts, amplitudes fewer than 5,000 counts, and amplitudes in between. Figure 12 shows the vehicle counts over time for the three groups and their respective totals, binned per hour. Similar time-distribution features exist across the medium-amplitude bins and the entire event volume. Generally, the high-amplitude and low-amplitude distributions exhibit contrasting characteristics. High-amplitude gears usually appear during the morning rush hour, whereas low-amplitude values typically appear during the evening rush hour. These periods include high and low vehicle speeds, respectively (Figure 8). Figure 8 depicts that the average hourly velocity variation during the morning rush is greater than that of the evening rush, which is consistent with the high and low amplitudes depicted in Figure 12. Consequently, we hypothesize that the vehicle speed can influence the amplitude. Also, there is a link between velocity and amplitude; the faster the velocity, the greater the amplitude is.

Conclusion

In this study, we present a deep learning strategy based on the YOLOv5 real-time object recognition framework for recognizing the passage and velocity of automobiles in DAS photographs. After training on a massive amount of labeled data, our model's precision is 95.9%. The new strategy for vehicle detection and speed estimation yields comparable results to the conventional slant stacking seismic array processing method. Unlike slant stacking, its processing speed for processing large DAS data is significantly faster, and it can be implemented in near-real-time data processing situations. With rapid data processing capacity, constructing a city-wide DAS network for traffic monitoring will be viable and operable using the city's existing densely packed communication optical fiber network. In addition to augmenting the existing traffic video surveillance network, the network will also help for the development of smart cities.

Traditional seismic array processing, such as slant stacking, can use wavefield attributes to reconstruct vehicle motion parameters, such as driving directions, and is immediately applicable in a number of contexts. Deep learning requires the training of pertinent models. Because we did not identify the driving direction to construct a comparable training set, the system cannot discern the driving direction of the car in this experiment. Currently, we lack more comprehensive training for difficult situations, such as multiple vehicles passing simultaneously. This area must be expanded in the near future. In addition, the model's ability to generalize across diverse circumstances has not been fully evaluated. In addition, integrating YOLOv5 with the slant stacking technique may help calibrate YOLOv5's speed estimation and improve the performance of the YOLOv5 algorithm.

Data availability statement

The original contributions presented in the study are included in the article/Supplementary Material; further inquiries can be directed to the corresponding author.

Author contributions

ZY and WW conceived the main ideas, led the project, and wrote the initial draft of the manuscript. XW provided the code of the slant stacking method. All authors reviewed the results and contributed to the writing of the final manuscript.

Funding

This work was supported by the Project of Basic Scientific Research Foundation of Institute of Earthquake Forecasting, China Earthquake Administration (Grant Nos. CEAIEF20220402 and 2020IEF0602) and the National Natural Science Foundation of China (Grant Nos. 41574050 and 41674058) and was also supported by the Young Elite Scientists Sponsorship Program by CAST (grant 2020QNRC001), and the Key Research Program of the Institute of Geology & Geophysics, CAS (grant IGGCAS-201904).

Acknowledgments

The authors thank the editor YW and two reviewers HQ and SY for their constructive comments.

Conflict of interest

The authors declare that the research was conducted in the absence of any commercial or financial relationships that could be construed as a potential conflict of interest.

Publisher's note

All claims expressed in this article are solely those of the authors and do not necessarily represent those of their affiliated organizations, or those of the publisher, the editors, and the reviewers. Any product that may be evaluated in this article, or claim that may be made by its manufacturer, is not guaranteed or endorsed by the publisher.

References

Al-qaness, M. A. A., Abbasi, A. A., Fan, H., Ibrahim, R. A., Alsamhi, S. H., and Hawbani, A. (2021). An improved YOLO-based road traffic monitoring system. *Computing* 103 (2), 211–230. doi:10.1007/s00607-020-00869-8

Amitha, I. C., and Narayanan, N. K. (2021). “Object detection using YOLO framework for intelligent traffic monitoring,” in *Machine vision and augmented intelligence—theory and applications*. Editors M. K. Bajpai, K. Kumar Singh, and G. Giakos (Singapore: Springer), 405–412. doi:10.1007/978-981-16-5078-9_34

Cao, C.-Y., Zheng, J.-C., Huang, Y.-Q., Liu, J., and Yang, C.-F. (2019). Investigation of a promoted you only look once algorithm and its application in traffic flow monitoring. *Appl. Sci.* 9 (17), 3619. doi:10.3390/app9173619

Chambers, K. (2020). Using DAS to investigate traffic patterns at Brady Hot Springs, Nevada, USA. *Lead. Edge* 39 (11), 819–827. doi:10.1190/tle39110819.1

Ge, L., Dan, D., and Li, H. (2020). An accurate and robust monitoring method of full-bridge traffic load distribution based on YOLO-v3 machine vision. *Struct. Control Health Monit.* 27 (12), e2636. doi:10.1002/stc.2636

LabelImg (2022). heartexlabs. Available at: https://github.com/heartexlabs/labelImg (Accessed August 10, 2022).

Lin, C.-J., and Jhang, J.-Y. (2022). Intelligent traffic-monitoring system based on YOLO and convolutional fuzzy neural networks. *IEEE Access* 10, 14120–14133. doi:10.1109/ACCESS.2022.3147866

Lindsey, N. J., Yuan, S., Lellouch, A., Gualtieri, L., Lecocq, T., and Biondi, B. (2020). City-scale dark fiber DAS measurements of infrastructure use during the COVID-19 pandemic. *Geophys. Res. Lett.* 47 (16), e2020GL089931. doi:10.1029/2020gl089931

Liu, H., Ma, J., Xu, T., Yan, W., Ma, L., and Zhang, X. (2019). Vehicle detection and classification using distributed fiber optic acoustic sensing. *IEEE Trans. Veh. Technol.* 69 (2), 1363–1374. doi:10.1109/tvt.2019.2962334

Liu, W., Anguelov, D., Erhan, D., Szegedy, C., Reed, S., Fu, C. Y., et al. (2016). “Ssd: Single shot multibox detector,” in *European conference on computer vision* (Cham: Springer), 21–37.

Mandal, V., Mussah, A. R., Jin, P., and Adu-Gyamfi, Y. (2020). Artificial intelligence-enabled traffic monitoring system. *Sustainability* 12 (21), 9177. doi:10.3390/su12219177

Narisetty, C., Hino, T., Huang, M. F., Ueda, R., Sakurai, H., Tanaka, A., et al. (2021). Overcoming challenges of distributed fiber-optic sensing for highway traffic monitoring. *Transp. Res. Rec.* 2675 (2), 233–242. doi:10.1177/0361198120960134

Paszke, A., Gross, S., Massa, F., Lerer, A., Bradbury, J., Chanan, G., et al. (2019). Pytorch: An imperative style, high-performance deep learning library. *Adv. neural Inf. Process. Syst.* 32.

Redmon, J., Divvala, S., Girshick, R., and Farhadi, A. (2016). “You only look once: Unified, real-time object detection,” in *Proceedings of the IEEE conference on computer vision and pattern recognition*, 779–788.

Redmon, J., and Farhadi, A. (2017). “YOLO9000: Better, faster, stronger,” in *Proceedings of the IEEE conference on computer vision and pattern recognition*, 7263–7271.

Redmon, J., and Farhadi, A. (2018). *Yolov3: An incremental improvement*. arXiv preprint arXiv:1804.02767.

Ren, S., He, K., Girshick, R., and Sun, J. (2015). Faster r-cnn: Towards real-time object detection with region proposal networks. *Adv. neural Inf. Process. Syst.* 28.

Robbins, H., and Monro, S. (1951). *A stochastic approximation method. The annals of mathematical statistics*, 400–407.

Rost, S., and Thomas, C. (2002). Array seismology: Methods and applications. *Rev. Geophys.* 40 (3), 2-1–2-27. doi:10.1029/2000rg000100

Stork, A. L., Baird, A. F., Horne, S. A., Naldrett, G., Lapins, S., Kendall, J.-M., et al. (2020). Application of machine learning to microseismic event detection in distributed acoustic sensing data. *GEOPHYSICS* 85 (5), KS149–KS160. doi:10.1190/geo2019-0774.1

van den Ende, M. P. A., Ferrari, A., Anthony, S., and Richard, C. (2021). *Deep deconvolution for traffic analysis with distributed acoustic sensing data*. hal-03352810.

Wang, X., Williams, E. F., Karrenbach, M., Herraez, M. G., Martins, H. F., and Zhan, Z. (2020). Rose parade seismology: Signatures of floats and bands on optical fiber. *Seismol. Res. Lett.* 91 (4), 2395–2398. doi:10.1785/0220200091

Wang, X., Zhan, Z., Williams, E. F., Herráez, M. G., Martins, H. F., and Karrenbach, M. (2021). Ground vibrations recorded by fiber-optic cables reveal traffic response to COVID-19 lockdown measures in Pasadena, California. *Commun. Earth Environ.* 2 (1), 160–169. doi:10.1038/s43247-021-00234-3

Wiesmeyr, C., Coronel, C., Litzenberger, M., Döller, H. J., Schweiger, H. B., and Calbris, G. (2021). “Distributed acoustic sensing for vehicle speed and traffic flow estimation,” in *2021 IEEE international intelligent transportation systems conference (ITSC)* (IEEE), 2596–2601.

YOLO (2022). Real-time object detection. Available at: https://pjreddie.com/darknet/yolo/ (Accessed July 10, 2022).

YOLOv5 framwork (2022). GitHub ultralytics. Available at: https://github.com/ultralytics/yolov5 (Accessed July 10, 2022).

Zheng, Y., Li, X., Xu, L., and Wen, N. (2022). A deep learning–based approach for moving vehicle counting and short-term traffic prediction from video images. *Front. Environ. Sci.* 10. doi:10.3389/fenvs.2022.905443

Zheng, Z., Wang, P., Liu, W., Li, J., Ye, R., and Ren, D. (2020). Distance-IoU loss: Faster and better learning for bounding box regression. *Proc. AAAI Conf. Artif. Intell.* 34 (07), 12993–13000. doi:10.1609/aaai.v34i07.6999

Zhu, X., and Shragge, J. (2022). *Toward real-time microseismic event detection using the YOLOv3 algorithm*. Retrieved from https://eartharxiv.org/repository/view/2926/.

Supplementary material

The Supplementary Material for this article can be found online at: https://www.frontiersin.org/articles/10.3389/feart.2022.992571/full#supplementary-material

Frontiers in Earth Science

TYPE Original Research
PUBLISHED 11 January 2023
DOI 10.3389/feart.2022.1018116

OPEN ACCESS

EDITED BY
Xiaowei Chen,
University of Oklahoma, United States

REVIEWED BY
Xiaoyun Wan,
China University of Geosciences, China
Ping Wang,
Lanzhou Earthquake Research Institute,
China Earthquake Administration, China

*CORRESPONDENCE
Heng Zhang,
zhangheng415@itpcas.ac.cn

SPECIALTY SECTION
This article was submitted to
Solid Earth Geophysics,
a section of the journal
Frontiers in Earth Science

RECEIVED 12 August 2022
ACCEPTED 17 October 2022
PUBLISHED 11 January 2023

CITATION
Yang J, Zhou J, Zhang H, Xu T, Deng D and Geng J (2023), Revealing the shallow soil structure of the Yigong Lake in the Tibetan Plateau using a portable distributed acoustic sensing interrogator.
Front. Earth Sci. 10:1018116.
doi: 10.3389/feart.2022.1018116

Revealing the shallow soil structure of the Yigong Lake in the Tibetan Plateau using a portable distributed acoustic sensing interrogator

Jizhong Yang[1,2], Jian Zhou[3], Heng Zhang[4]*, Tuanwei Xu[5,6], Dimin Deng[5] and Jianhua Geng[1]

[1]State Key Laboratory of Marine Geology, Tongji University, Shanghai, China, [2]Shanghai Sheshan National Geophysical Observatory, Shanghai, China, [3]School of Ocean and Earth Science, Tongji University, Shanghai, China, [4]State Key Laboratory of Tibetan Plateau Earth System, Environment and Resources (TPESER), Institute of Tibetan Plateau Research, Chinese Academy of Sciences, Beijing, China, [5]State Key Laboratory of Transducer Technology, Institute of Semiconductors, Chinese Academy of Sciences, Beijing, China, [6]College of Materials Science and Opto-Electronic Technology, University of Chinese Academy of Sciences, Beijing, China

The harsh and extreme environmental and near surface conditions of the Tibetan Plateau have limited the conventional electrical-based seismic instruments from obtaining high-quality seismic data through long-term and continuous observations, setting challenges for environmental seismology study and natural hazard monitoring in this area. Distributed acoustic sensing (DAS) is an emerging technique based on optical fiber communication and sensing. It provides a possible solution for subsurface imaging in extreme conditions at high spatiotemporal resolution by converting fiber-optic cables into dense seismic strainmeters. We deploy two survey lines with armored optical fiber cables in the Yigong Lake area, Southeastern Tibetan Plateau, to record ambient noise for a week. The DAS interrogator is specifically designed in a portable size with very low power consumption (25 W/h). Hence, we can use a 12V-DC battery for power supply to adjust the power limitation during the field recording. Ambient noise interferometry and multichannel analysis of surface waves are used to get 2D shear wave velocity profiles along the fiber paths. The results highlight the great potential of DAS for dynamic monitoring of the geological evolution of lakes and rivers in areas of extreme environments as in the Tibetan Plateau.

KEYWORDS

distributed acoustic sensing, sedimentary thickness, Tibetan Plateau, ambient noise tomography, seismic interferometry

Introduction

Seismic data acquisition is the foundation of data processing and interpretation in seismological research. High-quality seismic data may significantly improve the accuracy of geological understanding. Recently, seismologists have tried to use denser and denser observational networks to obtain high-spatiotemporal-resolution seismic data for a better knowledge of the Earth's dynamic processes and monitoring of natural hazards (Karplus and Schmandt, 2018; Nishikawa et al., 2019; Kohler et al., 2020). Although conventional electrical seismic instruments can be deployed in most areas for seismological research, it is very challenging to meet the aims of long-term monitoring in harsh environments, such as the volcano, glaciers, and plateaus due to the high cost of deployment and maintaining.

Distributed acoustic sensing (DAS) is an emerging seismic measurement technique that benefits from the development of optical fiber communication and sensing. Typically, a DAS system is composed of a standard optical fiber cable and an interrogation unit (IU). The IU lights the fiber using short laser pulses and measures Rayleigh back-scattering (RBS) along the fiber through a form of coherent optical time domain interferometry. A phase shift in the RBS is caused by the compression or elongation along the fiber, which is proportional to axial strain along the cable. Thus, DAS is working as a dense network for dynamic strain measurements (Parker et al., 2014; Hartog, 2017). DAS has initially been used for downhole applications in oil and gas exploration (Mateeva et al., 2014; Daley et al., 2016; Lellouch and Biondi, 2021). Currently, it has been widely adapted to seismological investigations, such as earthquake detection (Lindsey et al., 2017; Jousset et al., 2018; Wang et al., 2018; Yu et al., 2019), near-surface characterization (Dou et al., 2017; Fang et al., 2020; Spica et al., 2020; Shao et al., 2022), observing oceanic and atmospheric phenomena (Lindsey et al., 2019; Sladen et al., 2019; Williams et al., 2019; Zhu and Stensrud, 2019; Shinohara et al., 2022), monitoring volcano and glacier (Booth et al., 2020; Walter et al., 2020; Klaasen et al., 2021; Nishimura et al., 2021), and so forth. For the most up-to-date review of DAS application in seismology, we refer the readers to Lindsey and Martin (2021).

In this study, we use DAS to record continuous ambient noise in the Yigong Lake area in Tibetan Plateau. Yigong Lake is a barrier lake in the Yigong village, Bome County, Nyingchi, Tibet, characterized by a high altitude, a weak geological foundation, and an active modern crustal movement. It is located in the southeast of the Tibetan Plateau, about 2,600 m above sea level and spanned about 20 square kilometers (Figure 1). The strong uplift of the Earth's crust makes it the heaviest and wettest region on the Tibetan Plateau and prone to natural disasters such as landslides, avalanches, and debris flows. Historic records show that two giant landslides occurred in 1,900–2,000 resulting a deposit of total volume about 5 × 10^8 m^3 and 3 × 10^8 m^3,

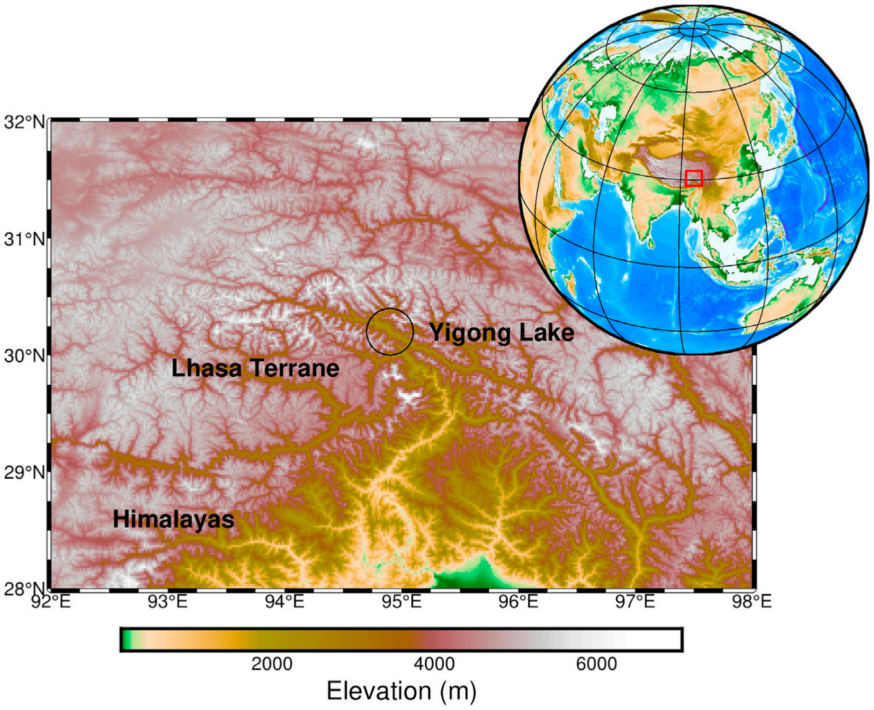

FIGURE 1
Geographic location and map overview.

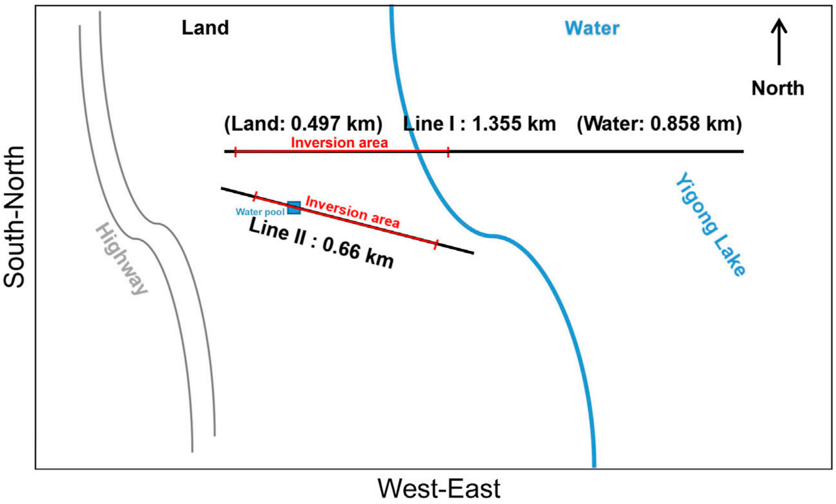

FIGURE 2
Schematic layout of the trenched optical fiber cables.

respectively (Shang et al., 2003; Zhou et al., 2016). A recent study utilizing radiocarbon dating of detrital materials provides pieces of evidence that there were at least eight large landslide events in this area over the past 5,500 years (Guo et al., 2020). As a result, these repeated landslides can change the sedimentary structure and further influence the development of river profiles. Revealing the sedimentary thickness could help us to better understand the geological evolution of the Yigong Lake. However, we should note that most of the previous studies in this area were focused on using satellite remote sensing technologies to study landslides, and these methods were hard to detect the underground structures. Due to the high content of water in the soil, it is infeasible to use the traditional electronic seismic instruments for data acquisition (Zhang et al., 2021). In addition, acquiring drilling data is very expensive. As a result, there is no previous study in this area for shallow structure characterization using seismic data. The emergence of DAS enables us to obtain field seismic data for the first time.

In the following parts, we first introduce the field deployment of seismic data acquisition using DAS. Thereafter, seismic interferometry is applied to the pre-processed data to obtain the noise correlation functions (NCFs) following the workflow of Bensen et al. (2007). After extracting surface waves from NCFs, multichannel analysis of surface waves (MASW) (Park et al., 1999) is utilized to retrieve dispersion curves and invert the shear wave velocity. According to the variations of the shear wave velocity, the sedimentary thickness in the study area can be inferred. These results confirm the reliability of DAS in capturing data and performing near-surface characterization in extreme environments.

DAS data acquisition and pre-processing

The ambient noise data acquisition is located between a highway and the Yigong Lake, as shown in Figure 2. In this area, it is not readily available to get access to the industrial power supply, and there is no facility room for equipment installation. To perform seismic data acquisition under such an extreme condition, the DAS IU is specially manufactured to have a portable size of 150 mm × 300 mm × 110 mm (Figure 3A), much smaller than the already commercialized IUs, such as from Silixa (444 mm × 518 mm × 178 mm) or Schlumberger (559 mm × 955 mm × 244 mm). The full-load power consumption is 25 W, lower than an ordinary laptop. Because of these adjustments, we are able to use a 12V-DC battery for the power supply, as shown in Figure 3B. More details about the IU are referred to Xu T et al. (2021) and Zhang et al. (2021).

DAS data were acquired during the local daytime from 10 a.m. to 7 p.m. on 28 October 2021 to 3 November 2021. The maximum continuous recording length is 8 h because of running out of battery power. We installed two trenched DAS arrays. The surface trenches, which are 10cm–20 cm deep, are dug with hand tools. The optical fiber cables were backfilled with excavated soil to ensure coupling between DAS and the ground, as shown in Figure 4A. Line I is 1.355 km long with 755 channels. A 0.497 km-long session of the line was settled on the ground while the rest of the line was deployed underwater across the Yigong Lake. This line was originally installed in April 2021, when the Yigong Lake is in the dry season so that we could easily get access to the lake bottom to deploy optical fiber cables. During the data acquisition time, the Yigong Lake is in the wet season and optical fiber cables are

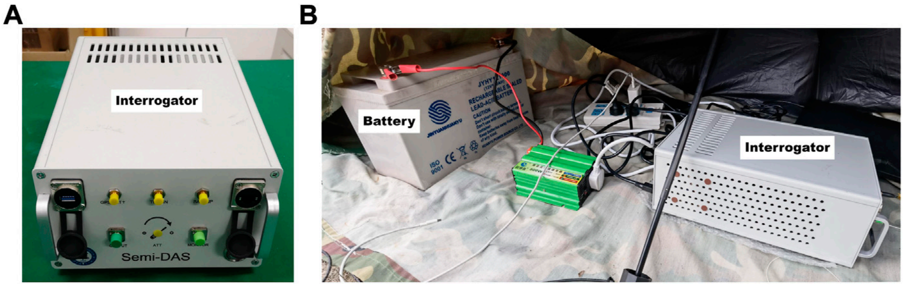

FIGURE 3
Photos for the interrogator in a front view **(A)** and the battery connection during field data acquisition **(B)**.

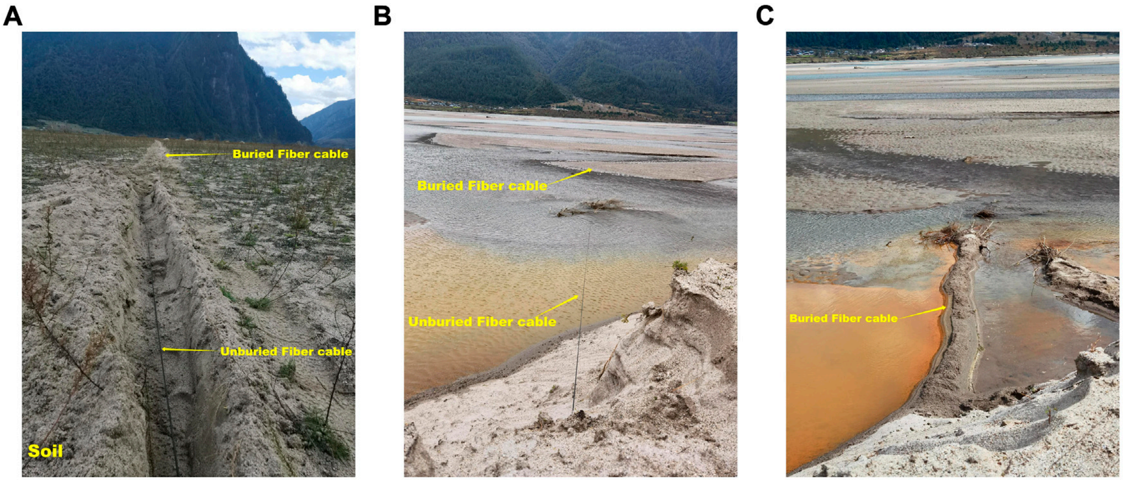

FIGURE 4
Field deployment of the optical fiber cables on land **(A)** and underwater across the Yigong Lake **(B,C)**.

buried underwater. At the transition zone from the land to the water, parts of optical fiber cables are suspended in the air, as shown in Figure 4B. Consequently, the DAS data are discontinuously recorded during the test stage. After realizing this, we buried the suspended parts using the sand nearby, as shown in Figure 4C. Line II is 0.66 km long with 410 channels. Most parts are located on land, and only a small portion was across a water pool.

We select a 5-h DAS dataset in Line I and an 8-h DAS dataset in Line II for analysis, respectively. The sampling rate is 1000 Hz, and the gauge length is 10 m. The channel spacing is 1.6 m. We drop the data in the first 10 channels of Line I and the first 50 channels of Line II because of the contamination by the wandering man-walks.

Following Bensen et al. (2007), we process the DAS data with the workflow as summarized in Figure 5. The long-time raw data are split into short-time windows of 30-min long. The two ends of the segmented time series became discontinuous. We performed 10% tapering to reduce the numerical oscillation known as the Gibbs effect when filtering and performing Fourier transforms and to minimize the impact of discontinuities at both ends of the signal (Figure 6) (Xu Y et al., 2021). The influence of the DC component and linear trend is removed by de-meaning and de-trending. According to the spectrum of the original data in Figure 6, the energy is mainly concentrated below 25 Hz. We down-sample the data to 50 Hz to reduce the computational time and the memory requirements. The corresponding resampled waveform and its spectrum are shown in Figure 7. When seismic data are collected in the field, it is inevitable to be affected by environmental and human factors, resulting in a high amplitude in the time-domain signal, as shown in the red box in Figure 7.

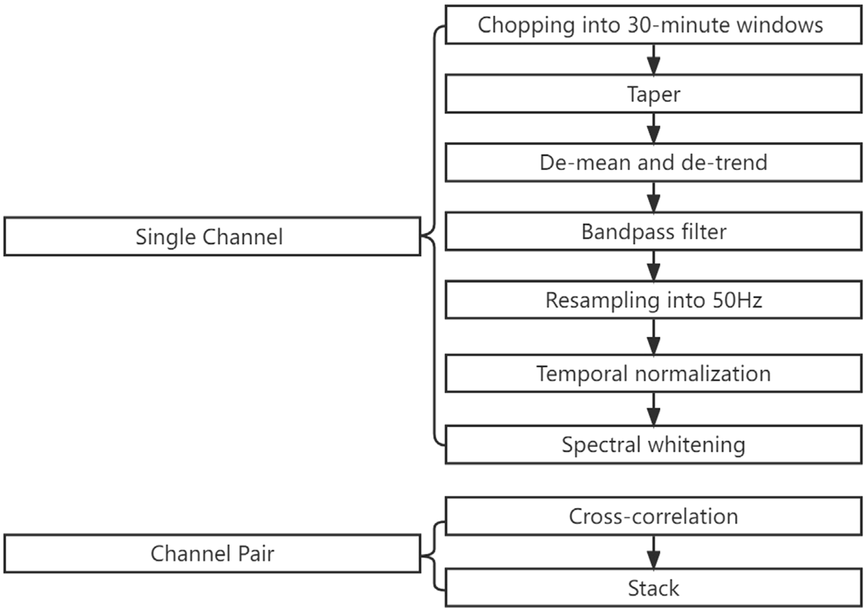

FIGURE 5
Data processing procedure to compute NCFs in this study.

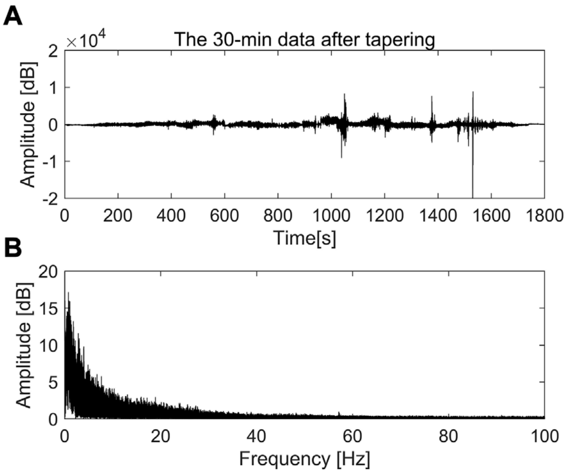

FIGURE 6
(A) Waveform, and **(B)** corresponding spectrum of the 30-min record of Channel 200 in Line II after tapering.

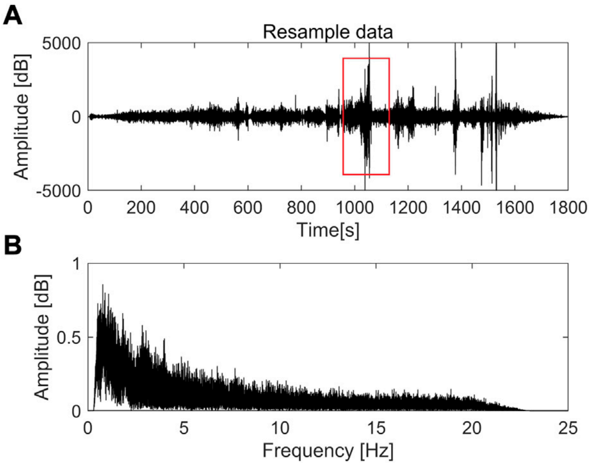

FIGURE 7
(A) Waveform, and **(B)** corresponding spectrum of the resampled 30-min record of Channel 200 in Line II. The red box denotes the high amplitude signal caused by environmental and human factors.

The introduction of temporal normalization can eliminate the effect of strong signals and improve the quality of the correlation results (Bensen et al., 2007). By selecting a time window of a certain length, the average of the absolute amplitude value is obtained in the time window, which is used as the weight of the center of the time window. The weight of all data is calculated by sliding the window, and then the original data is divided by the corresponding weight. Finally, the normalized sequence in the time domain is obtained. This procedure can be formulated as follows:

$$w(i) = \frac{1}{2N+1}\sum_{j=i-N}^{j=i+N} d(i), \tag{1}$$

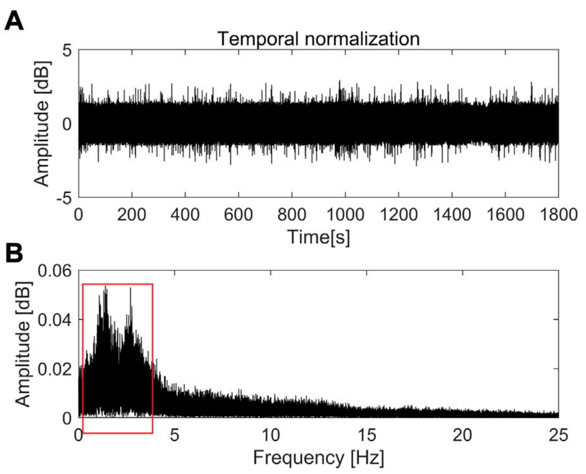

FIGURE 8
(A) Waveform, and **(B)** corresponding spectrum of the 30-min record of Channel 200 in Line II after temporal normalization. The red box denotes that the signal still has unbalanced high and low-frequency energy after the temporal normalization.

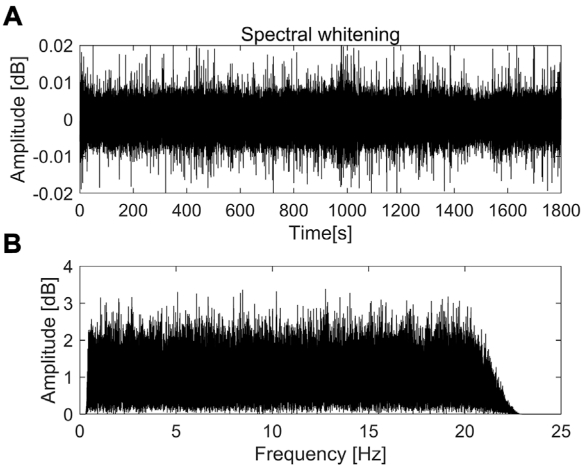

FIGURE 9
(A) Waveform, and **(B)** corresponding spectrum of the 30-min record of Channel 200 in Line II after spectral whitening.

$$\bar{d}(i) = \frac{d(i)}{w(i)}, \tag{2}$$

in which $d(i)$ is the seismograph that has been band-pass filtered between 0.3 and 23Hz, $\bar{d}(i)$ is the temporal normalized seismograph, and $2N+1$ is the number of points in the normalization window. Figure 8A shows that the strong energy effect has been effectively reduced after the running-absolute-mean normalization.

After the temporal normalization, the signal still has unbalanced high and low-frequency energy, and the signal spectrum is not flat, as shown in the red box in Figure 8B. Therefore, it needs to be "flattened", also called spectrum whitening. The Hanning window $W(f)$ with a 0.3–23 Hz pass-band is applied to the smoothed complex spectrum $D(f)$ of the signal time series $d(t)$:

$$Y(f) = W(f) \times D(f)/|\bar{D}(f)|, \tag{3}$$

in which $|\bar{D}(f)|$ is the smoothed amplitude spectrum. The Fourier transform $Y(f)$ is inversely transformed to the time domain for subsequent data processing. Figure 9 shows the final processed waveform and its spectrum. The resulting signal is more like white noise with a "flat" spectrum in the frequency domain.

Methods

Ambient noise interferometry for surface wave reconstruction

Surface waves are reconstructed by using ambient noise interferometry, which has been of great interests in variant research areas (Claerbout, 1968; Weaver and Lobkis, 2001; Shapiro et al., 2005). By cross-correlating the continuous recorded ambient noise at two receiver locations, empirical Green's functions between these two receivers can be obtained. After temporal stacking of the correlations in a long range, coherent waveforms will emerge (Campillo and Paul, 2003; Shapiro and Campillo, 2004). In the frequency domain, the cross-correlation can be formulated as:

$$C_{AB}(\omega) = \langle u_A^*(\omega) u_B(\omega) \rangle, \tag{4}$$

where $u_A(\omega)$ and $u_B(\omega)$ denote the pre-processed wavefields in the frequency domain recorded at receiver A and receiver B, respectively, following the workflow in Figure 5. The symbol ω is the angular frequency, $*$ denotes complex conjugate, and $\langle \cdot \rangle$ denotes temporal average.

Multichannel analysis of surface waves for shear wave velocity inversion

After the surface wave reconstruction using ambient noise interferometry, we apply MASW (Park et al., 1999) to extract dispersion curves. First, the data in the time-offset domain are slant-stack-transformed into the frequency-velocity domain as follows:

$$\mathrm{E}(\omega, c) = \int e^{-i\frac{\omega}{c}x} \frac{U(x,\omega)}{|U(x,\omega)|} dx, \tag{5}$$

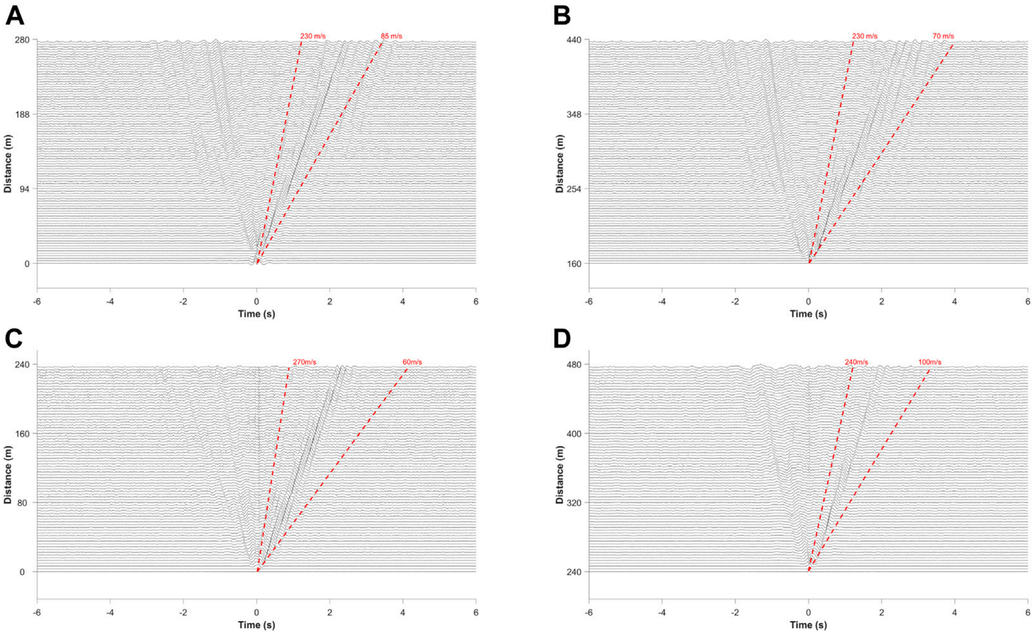

FIGURE 10
NCFs of the virtual source at Channel 11 **(A)**, and Channel 175 **(B)** in Line I, and at Channel 51 **(C)**, and Channel 200 **(D)** in Line II, respectively. The red dashed lines show the apparent velocity.

in which $E(\omega, c)$ is the dispersion image, c is the phase velocity at the angular frequency $\omega, U(x, \omega)$ is the amplitude spectrum of the time-domain data $u(x, t)$ through Fourier transform. Next, the dispersion curves are identified by picking the maximum value in the dispersion image $E(\omega, c)$ at each frequency-velocity pair.

The extracted dispersion curves are further used to invert the shear wave velocity. The misfit function is defined as minimizing the difference between the picked dispersion curves and the theoretical dispersion curves calculated using the fast delta-matrix algorithm (Buchen and Ben-Hador, 1996). Considering the non-linearity and non-convexity of the inverse problem, a Mente Carlo-based global search method is used to potentially escape from being stuck at the local minimum. Detailed description of the software used in this study can be found in Olafsdottir et al. (2018) and Olafsdottir et al. (2020).

Results

In Line I, data from Channel 11 to Channel 360 are used for calculating NCFs. From Channel 11 to Channel 185, we select every channel as a virtual source, and the other 175 channels on the right of the virtual source are cross-correlated with the virtual source. From Channel 186 to Channel 360, we select every channel as a virtual source, and the other 175 channels on the left of the virtual source are cross-correlated with the virtual source. In Line II, data from Channel 51 to Channel 350 are used for calculating NCFs. From Channel 51 to Channel 200, we select every channel as a virtual source, and the other 150 channels on the right of the virtual source are cross-correlated with the virtual source. From Channel 201 to Channel 350, we select every channel as a virtual source, and the other 150 channels on the left of the virtual source are cross-correlated with the virtual source. Next, we perform linear stacking of all the time segments for each cross-correlation pair to average the effect of temporal noise and spatial irregularity. Finally, we get 350 virtual gathers for Line I and 300 virtual gathers for Line II.

Figure 10 shows the NCFs in Line I at Channel 11 (Figure 10A) and Channel 175 (Figure 10B), and in Line II at Channel 51 (Figure 10C) and Channel 200 (Figure 10D) as virtual sources, respectively. From the reconstructed virtual gathers, it can be seen that NCFs are bilateral time functions divided into positive and negative half lags, representing positive and negative wave propagation directions, respectively. There is an obvious asymmetry that the dispersive Rayleigh-wave on the positive lag is much stronger than that on the negative lag, suggesting that the azimuth of the ambient noise is not uniformly distributed. According to the schematic layout in Figure 2, we can infer that the higher energy results from the traffic noise on the highway. Similar asymmetry is also observed by Zeng et al. (2017) from field DAS data.

Before the dispersion curve extraction, the positive and negative half branches of NCFs are stacked in reverse order, and the positive half lags are reserved for subsequent processing to improve the signal-to-noise ratio (Huang et al., 2021). Such a procedure can help to

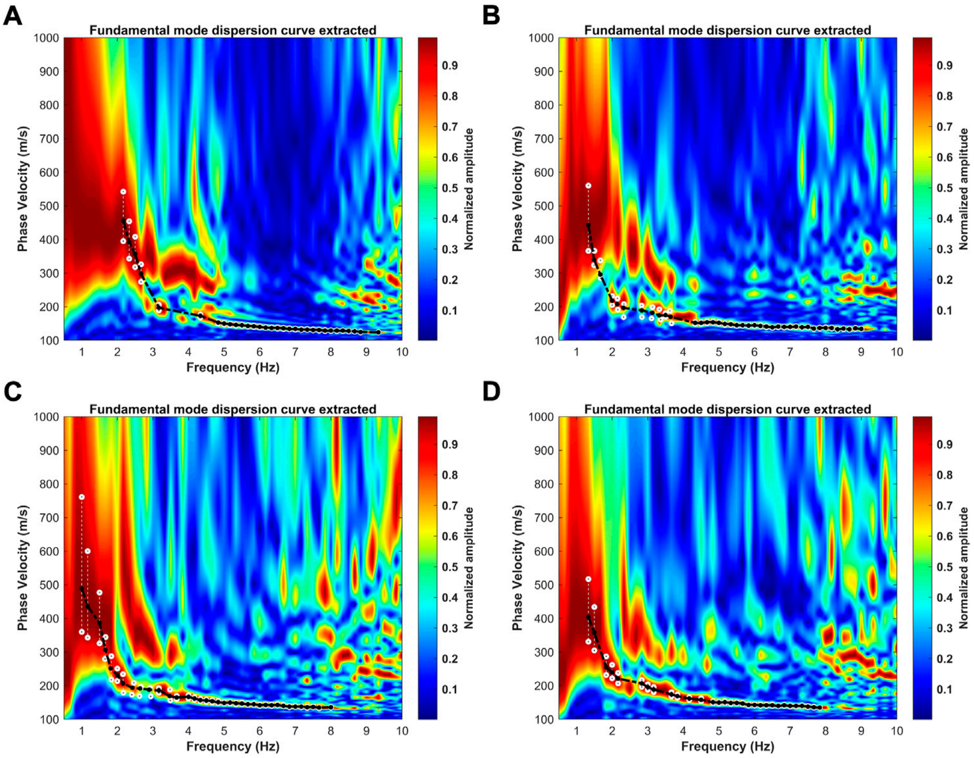

FIGURE 11
Dispersion images from the virtual gathers at Channel 11 **(A)** and Channel 175 **(B)** in Line I, and at Channel 51 **(C)** and Channel 200 **(D)** in Line II, respectively. The black curves with solid circles are the extracted fundamental model dispersion curves for inversion. The while open circles denote the upper and lower boundaries by setting as 95% of the peak value.

mitigate the influence of uneven energy distribution of noise sources on surface wave velocity measurements.

The initial phase velocity picks are automatically chosen as the maximum value of the dispersion image in each frequency bin. Then, they are manually assigned with mode numbers and spurious picks are removed.

For the inversion of each 1D dispersion curve, we set the depth of the bottom of the interface to 90 m, and the whole model is divided into six layers. The thickness of the first layer is 8 m, the thickness of the second layer is 10 m, and the thickness of all other layers is 18 m. Since both P-wave velocity and density can affect the dispersion curve, the empirical formula of Brocher (2005) is used to convert the shear wave velocity into P-wave velocity and density. Finally, we obtain the 2D shear wave velocity profiles using cubic spline interpolation.

Figure 11 shows the dispersion images of NCFs at Channel 11 (Figure 11A) and Channel 175 (Figure 11B) in Line I, and at Channel 51 (Figure 11C) and Channel 200 (Figure 11D) in Line II, respectively. Although fundamental- and higher-mode surface waves are visible, only the fundamental mode dispersion curves, the black lines in Figure 11, are used for inversion.

Figure 12 shows the 1D dispersion curve inversion results of the fundamental mode in Figure 11. The red lines denote the best inverted velocities which have the lowest misfit values. The other lines denote the top 2% best fitting models. To evaluate the accuracy of the inverted velocity models, we calculate the theoretical dispersion curves using the best inverted velocities in Figure 12. The corresponding results are shown in Figure 13 as the red lines, and they match well with the picked dispersion curves marked by the blue circles in Figure 13. Such a comparison suggests that the inverted velocity models could interpret the observed data in a good performance.

The final 2D shear wave velocity profiles are shown in Figure 14. The shear wave velocity variation above 40 m depth along the two survey lines is small. There is no obvious velocity discontinuity interface, and the shear wave velocity is between 100 and 320 m/s. When the depth exceeds 40 m, the shear wave velocity gradually decreases from west to east. The lateral velocity change in Line II is greater than that in Line I. In Line I, the stratification is obvious, and the shear wave gradually decreases in the horizontal direction at the depth range of 50–70 m. In Line

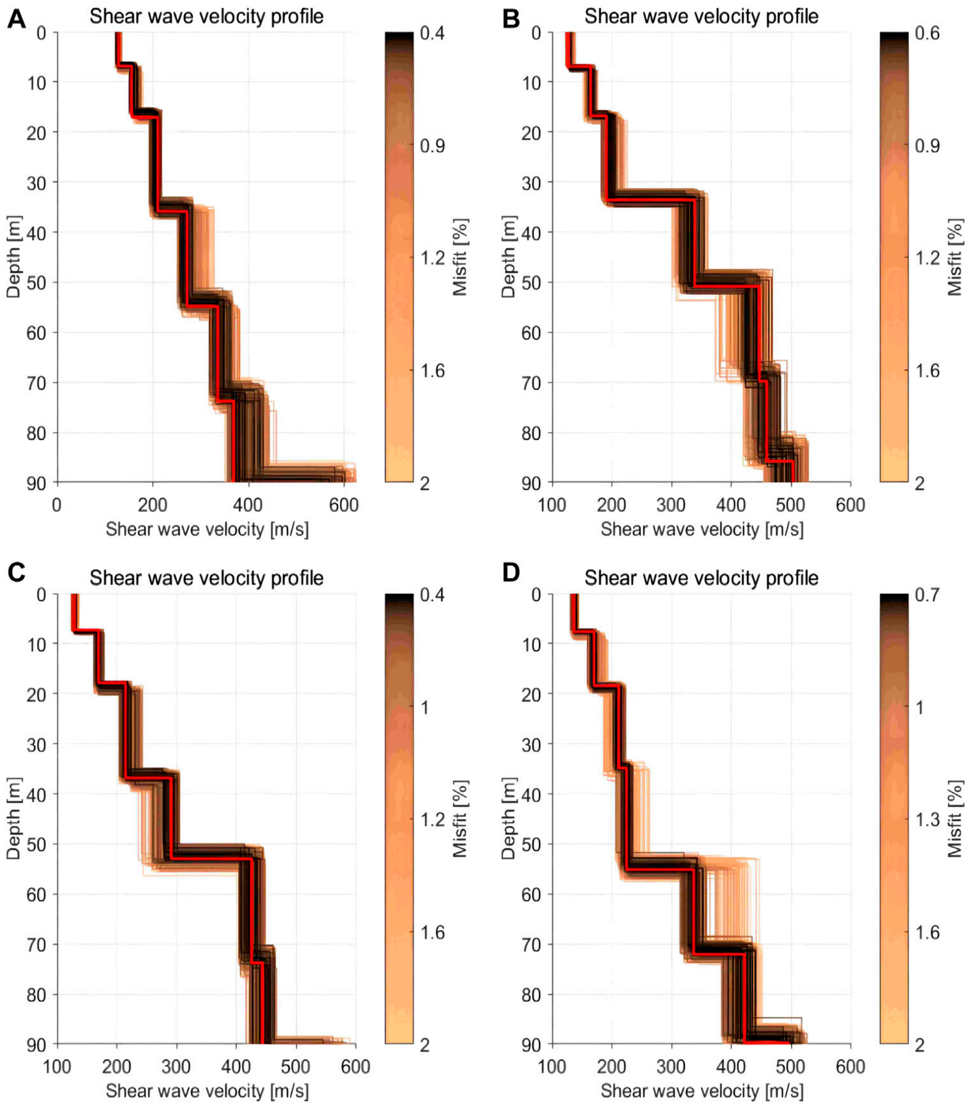

FIGURE 12
The inverted 1D shear wave velocities using the fundamental-mode dispersion curves in Figures 11A–D at Channel 11 **(A)** and Channel 175 **(B)** in Line I, and at Channel 51 **(C)** and Channel 200 **(D)** in Line II, respectively. The red lines denote the best fitted models that have the lowest misfit, and the other lines denote the top 2% best fitting models.

II, starting from the depth of 40 m, shear wave velocity presents lateral variation, and the velocity is between 250 and 350 m/s. The lateral variation of shear wave velocity increases with the gradual increase of depth, and the shear wave velocity decreases in the horizontal direction at a depth of 58–60 m.

The maximum velocity of the two profiles above the depth of 80 m is only 700 m/s, which is smaller than the velocity of the shear wave in the bedrock, so it can be inferred that the thickness of the sedimentary layer in this area should be greater than 80 m. In addition, the different features between these two profiles suggest a strong lateral variation of the sedimentary layer along the Yigong Lake. Considering the location of the lake water (blue line in Figure 2), the different shallow structures and increased thickness of the sediments in the Yigong Lake can be attributed to the accumulation of debris flow alluvium from the surrounding mountains (Zhang et al., 2021).

Discussion

We have demonstrated the feasibility of using DAS to record ambient noise data in the Tibetan Plateau. By applying the well-established seismic interferometry to the DAS data,

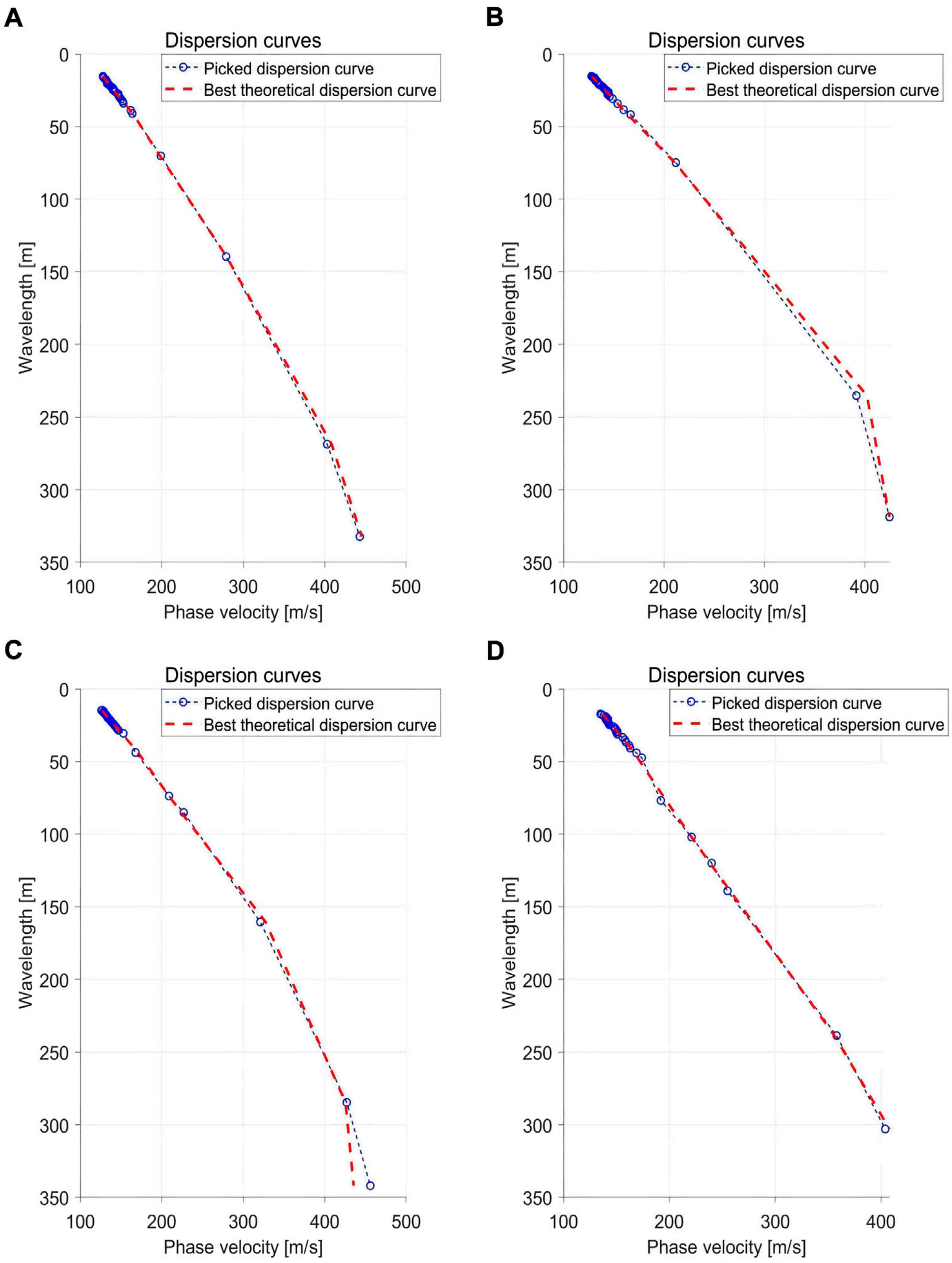

FIGURE 13
The fitting of the theoretical fundamental-mode dispersion curve using the inverted velocity in Figures 12A–D to the picked ones in Figures 11A–D at Channel 11 **(A)** and Channel 175 **(B)** in Line I, and at Channel 51 **(C)** and Channel 200 **(D)** in Line II, respectively.

we can reveal the shallow sedimentary structure of the Yigong Lake, which is very helpful to understand the dynamic evolution of this area. Considering the extreme conditions of the Tibetan Plateau, it is difficult, if not possible, to deploy traditional geophones or portable nodes for environmental seismology study, our method can be a promising alternative for the interested readers.

We should note that since the surface wave inversion is highly non-unique, further studies are needed to verify the reliability of the inversion results by incorporating other geological information, such as the drilling data. Due to the limited recording time, we could not get enough low frequency information below 1 Hz. Only when these low frequency data are available, we can get access to the

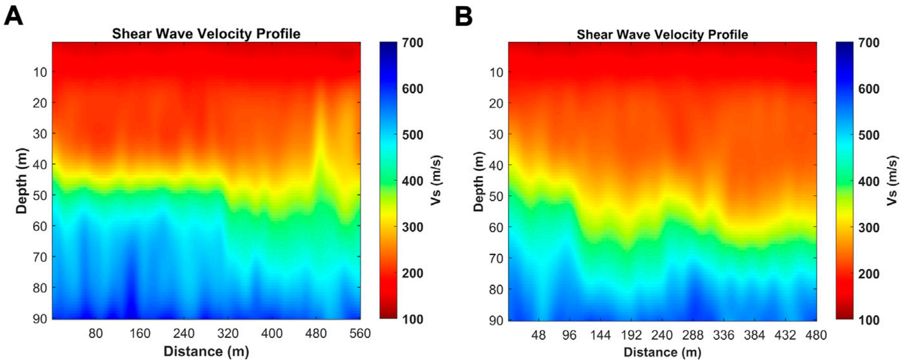

FIGURE 14
The 2D shear wave velocity profiles along the DAS Line I **(A)** and Line II **(B)**.

deeper parts to reveal the actual depth of the bedrock. In addition, we only use the land data and a small portion of the underwater data of Line I in this study. The noise characteristics in the rest parts are more complex than those used in this study, which need further processing and evaluation. Future work with integration of the complete DAS dataset might give chances for a better interpretation of the geologic evolution history of the Yigong Lake.

Conclusion

This study introduces a shallow sedimentary structure imaging method in extreme conditions of the Yigong Lake in the Tibetan Plateau using ambient noise data recorded by DAS. By applying proper data pre-processing and seismic interferometry to the ambient noise data, clear NCFs are obtained and surface waves can be easily identified. Dispersion curves are then extracted using MASW and are inverted to get the shear wave velocity model of the study area. The results show that the lateral variation is not evident in the shallow subsurface layer, and the lateral inhomogeneity of shear wave velocity increases with depth. Since the shear wave velocity is smaller than conventional bedrock at depths greater than 80 m, it can be assumed that the sedimentary thickness is greater than 80 m in the Yigong Lake area. The increased thickness is likely due to debris-flow deposits in the surrounding mountains. The low-cost, high-density acquisition and processing of DAS data demonstrate the effectiveness and practicality of DAS in detecting shallow sedimentary structures in extreme environments in the Tibetan Plateau. We are expecting that DAS will be a powerful tool for studies of remote and harsh environments in the future.

Data availability statement

The datasets presented in this article are not readily available because it is still being used for scientific research. Requests to access the datasets should be directed to the corresponding author.

Author contributions

JY, JZ, and JG studied the method, processed the data and wrote the draft of the manuscript. JY, HZ, and DD acquired the DAS data in the field. HZ planned the project, and TX designed the DAS system. All the authors contributed to the final manuscript.

Funding

This research was financially supported by the Second Tibetan Plateau Scientific Expedition and Research Program (Grant No. 2019QZKK0708), the National Natural Science Foundation of China (Grant Nos. 42004096, 41974109, and 61875184), Shanghai Sheshan National Geophysical Observatory (No. SSOP202205), the Fundamental Research Funds for the Central Universities of China, the Scientific Instrument Developing Project of the Chinese Academy of Sciences (Grant No. YJKYYQ20190075), the Strategic Priority Research Program of the Chinese Academy of Sciences (Grant Nos. XDA20070301 and XDA22040105), the Grants of the Wong K.C. Education Foundation (No. GJTD-201904), and the Research Program of Sanya Yazhou Bay Science and Technology City (Grant No. SKJC-2020-01-009).

Conflict of interest

The authors declare that the research was conducted in the absence of any commercial or financial relationships that could be construed as a potential conflict of interest.

Publisher's note

References

Bensen, G. D., Ritzwoller, M. H., Barmin, M. P., Levshin, A. L., Lin, F. F., Moschetti, M. P., et al. (2007). Processing seismic ambient noise data to obtain reliable broad-band surface wave dispersion measurements. *Geophys. J. Int.* 169, 1239–1260. doi:10.1111/j.1365-246X.2007.03374.x

Booth, A. D., Christoffersen, P., Schoonman, C., Clarke, A., Hubbard, B., Law, R., et al. (2020). Distributed acoustic sensing of seismic properties in a borehole drilled on a fast-flowing Greenlandic outlet glacier. *Geophys. Res. Lett.* 47, e2020GL088148. doi:10.1029/2020GL088148

Brocher, T. M. (2005). Empirical relations between elastic wavespeeds and density in the Earth's crust. *Bull. Seismol. Soc. Am.* 95 (6), 2081–2092. doi:10.1785/0120050077

Campillo, M., and Paul, A. (2003). Long-range correlations in the diffuse seismic coda. *Science* 299, 547–549. doi:10.1126/science.1078551

Claerbout, J. F. (1968). Synthesis of a layered medium from its acoustic transmission response. *Geophysics* 33, 264–269. doi:10.1190/1.1439927

Daley, T. M., Miller, D. E., Dodds, K., Cook, P., and Freifeld, B. M. (2016). Field testing of modular borehole monitoring with simultaneous distributed acoustic sensing and geophone vertical seismic profiles at Citronelle, Alabama. *Geophys. Prospect.* 64 (5), 1318–1334. doi:10.1111/1365-2478.12324

Dou, S., Lindsey, N., Wagner, A. M., Daley, T. M., Freifeld, B., Robertson, M., et al. (2017). Distributed acoustic sensing for seismic monitoring of the near surface: A traffic-noise interferometry case study. *Sci. Rep.* 7, 11620. doi:10.1038/s41598-017-11986-4

Fang, G., Li, Y. E., Zhao, Y., and Martin, E. R. (2020). Urban near-surface seismic monitoring using distributed acoustic sensing. *Geophys. Res. Lett.* 47 (6), e2019GL086115. doi:10.1029/2019GL086115

Guo, C., Montgomery, D. R., Zhang, Y., Zhong, N., Fan, C., Wu, R., et al. (2020). Evidence for repeated failure of the giant Yigong landslide on the edge of the Tibetan Plateau. *Sci. Rep.* 10, 14371. doi:10.1038/s41598-020-71335-w

Hartog, A. H. (2017). *An introduction to distributed optical fibre sensors*. Florida, United States: CRC Press.

Huang, X., Ding, Z. F., Ning, J. Y., and Chang, L. J. (2021). Rayleigh wave phase velocity and azimuthal anisotropy of central North China Craton derived from ambient noise tomography. *Chin. J. Geophys.* 64, 2701–2715. doi:10.6038/cjg2021O0442

Jousset, P., Reinsch, T., Ryberg, T., Blanck, H., Clarke, A., Aghayev, R., et al. (2018). Dynamic strain determination using fibre-optic cables allows imaging of seismological and structural features. *Nat. Commun.* 9, 2509. doi:10.1038/s41467-018-04860-y

Karplus, M., and Schmandt, B. (2018). Preface to the focus section on geophone array seismology. *Seismol. Res. Lett.* 89 (5), 1597–1600. doi:10.1785/0220180212

Klaasen, S., Paitz, P., Lindner, N., Dettmer, J., and Fichtner, A. (2021). Distributed acoustic sensing in volcano-glacial environments-Mount Meager, British Columbia. *JGR. Solid Earth* 126, e2021JB022358. doi:10.1029/2021JB022358

Kohler, M. D., Hafner, K., Park, J., Irving, J. C., Caplan-Auerbach, J., Collins, J., et al. (2020). A plan for a long-term, automated, broadband seismic monitoring network on the global seafloor. *Seismol. Res. Lett.* 91, 1343–1355. doi:10.1785/0220190123

Lellouch, A., and Biondi, B. L. (2021). Seismic applications of downhole DAS. *Sensors* 21 (9), 2897. doi:10.3390/s21092897

Lindsey, N. J., Dawe, T. C., and Ajo-Franklin, J. B. (2019). Illuminating seafloor faults and ocean dynamics with dark fiber distributed acoustic sensing. *Science* 366, 1103–1107. doi:10.1126/science.aay5881

Lindsey, N. J., Martin, E. R., Dreger, D. S., Freifeld, B., Cole, S., James, S. R., et al. (2017). Fiber-optic network observations of earthquake wavefields. *Geophys. Res. Lett.* 44 (23), 11–792. doi:10.1002/2017GL075722

Lindsey, N. J., and Martin, E. R. (2021). Fiber-optic seismology. *Annu. Rev. Earth Planet. Sci.* 49, 309–336. doi:10.1146/annurev-earth-072420-065213

Mateeva, A., Lopez, J., Potters, H., Mestayer, J., Cox, B., Kiyashchenko, D., et al. (2014). Distributed acoustic sensing for reservoir monitoring with vertical seismic profiling. *Geophys. Prospect.* 62, 679–692. doi:10.1111/1365-2478.12116

Nishikawa, T., Matsuzawa, T., Ohta, K., Uchida, N., Nishimura, T., and Ide, S. (2019). The slow earthquake spectrum in the Japan Trench illuminated by the S-net seafloor observatories. *Science* 365, 808–813. doi:10.1126/science.aax5618

Nishimura, T., Emoto, K., Nakahara, H., Miura, S., Yamamoto, M., Sugimura, S., et al. (2021). Source location of volcanic earthquakes and subsurface characterization using fiber-optic cable and distributed acoustic sensing system. *Sci. Rep.* 11, 6319. doi:10.1038/s41598-021-85621-8

Olafsdottir, E. A., Erlingsson, S., and Bessason, B. (2020). Open-source MASW inversion tool aimed at shear wave velocity profiling for soil site explorations. *Geosciences* 10 (8), 322. doi:10.3390/geosciences10080322

Olafsdottir, E. A., Erlingsson, S., and Bessason, B. (2018). Tool for analysis of multichannel analysis of surface waves (MASW) field data and evaluation of shear wave velocity profiles of soils. *Can. Geotech. J.* 55, 217–233. doi:10.1139/cgj-2016-0302

Park, C. B., Miller, R. D., and Xia, J. H. (1999). Multichannel analysis of surface waves. *Geophysics* 64, 800–808. doi:10.1190/1.1444590

Parker, T., Shatalin, S., and Farhadiroushan, M. (2014). Distributed Acoustic Sensing–a new tool for seismic applications. *First Break* 32 (2), 61–69. doi:10.3997/1365-2397.2013034

Shang, Y., Yang, Z., Li, L., Liao, Q., and Wang, Y. (2003). A super-large landslide in Tibet in 2000: Background, occurrence, disaster, and origin. *Geomorphology* 54, 225–243. doi:10.1016/S0169-555X(02)00358-6

Shao, J., Wang, Y., Zheng, Y., Yao, Y., Wu, S., Yang, Z., et al. (2022). Near-surface characterization using urban traffic noise recorded by fiber-optic distributed acoustic sensing. *Front. Earth Sci. (Lausanne).* 10, 943424. doi:10.3389/feart.2022.943424

Shapiro, N. M., and Campillo, M. (2004). Emergence of broadband Rayleigh waves from correlations of the ambient seismic noise. *Geophys. Res. Lett.* 31, L07614. doi:10.1029/2004GL019491

Shapiro, N. M., Campillo, M., Stehly, L., and Ritzwoller, M. H. (2005). High-resolution surface-wave tomography from ambient seismic noise. *Science* 307, 1615–1618. doi:10.1126/science.1108339

Shinohara, M., Yamada, T., Akuhara, T., Mochizuki, K., and Sakai, S. I. (2022). Performance of seismic observation by distributed acoustic sensing technology using a seafloor cable off Sanriku, Japan. *Front. Mar. Sci.* 9, 844506. doi:10.3389/fmars.2022.844506

Sladen, A., Rivet, D., Ampuero, J. P., De Barros, L., Hello, Y., Calbris, G., et al. (2019). Distributed sensing of earthquakes and ocean-solid Earth interactions on seafloor telecom cables. *Nat. Commun.* 10, 5777. doi:10.1038/s41467-019-13793-z

Spica, Z. J., Perton, M., Martin, E. R., Beroza, G. C., and Biondi, B. (2020). Urban seismic site characterization by fiber-optic seismology. *J. Geophys. Res. Solid Earth* 125 (3), e2019JB018656. doi:10.1029/2019JB018656

Walter, F., Gräff, D., Lindner, F., Paitz, P., Köpfli, M., Chmiel, M., et al. (2020). Distributed acoustic sensing of microseismic sources and wave propagation in glaciated terrain. *Nat. Commun.* 11, 2436. doi:10.1038/s41467-020-15824-6

Wang, H. F., Zeng, X., Miller, D. E., Fratta, D., Feigl, K. L., Thurber, C. H., et al. (2018). Ground motion response to an ML 4.3 earthquake using co-located distributed acoustic sensing and seismometer arrays. *Geophys. J. Int.* 213 (3), 2020–2036. doi:10.1093/gji/ggy102

Weaver, R. L., and Lobkis, O. I. (2001). Ultrasonics without a source: Thermal fluctuation correlations at MHz frequencies. *Phys. Rev. Lett.* 87 (13), 134301. doi:10.1103/PhysRevLett.87.134301

Williams, E. F., Fernández-Ruiz, M. R., Magalhaes, R., Vanthillo, R., Zhan, Z., González-Herráez, M., et al. (2019). Distributed sensing of microseisms and teleseisms with submarine dark fibers. *Nat. Commun.* 10, 5778. doi:10.1038/s41467-019-13262-7

Xu, T., Feng, S., Li, F., Ma, L., and Yang, K. (2021). "Distributed acoustic sensing system based on phase-generated carrier demodulation algorithm," in *Distributed Acoustic Sensing in Geophysics*, Editor Y. Li, M. Karrenbach, and J. B. Ajo-Franklin. doi:10.1002/9781119521808.ch4

Xu, Y., Lebedev, S., Meier, T., Bonadio, R., and Bean, C. J. (2021). Optimized workflows for high-frequency seismic interferometry using dense arrays. *Geophys. J. Int.* 227, 875–897. doi:10.1093/gji/ggab260

Yu, C., Zhan, Z., Lindsey, N. J., Ajo-Franklin, J. B., and Robertson, M. (2019). The potential of DAS in teleseismic studies: Insights from the Goldstone experiment. *Geophys. Res. Lett.* 46 (3), 1320–1328. doi:10.1029/2018GL081195

Zeng, X., Lancelle, C., Thurber, C., Fratta, D., Wang, H., Lord, N., et al. (2017). Properties of noise cross-correlation functions obtained from a distributed acoustic sensing array at Garner Valley, California. *Bull. Seismol. Soc. Am.* 107 (2), 603–610. doi:10.1785/0120160168

Zhang, H., Xu, T. W., Pei, S. P., and Zhao, J. M. (2021). Application of distributed acoustic sensing in structural investigation of Lake Yigong in Tibet. *Earth Sci. Front.* 28, 227–234. doi:10.13745/j.esf.sf.2021.11.10

Zhou, J. W., Cui, P., and Hao, M. H. (2016). Comprehensive analyses of the initiation and entrainment processes of the 2000 Yigong catastrophic landslide in Tibet, China. *Landslides* 13, 39–54. doi:10.1007/s10346-014-0553-2

Zhu, T., and Stensrud, D. J. (2019). Characterizing thunder-induced ground motions using fiber-optic distributed acoustic sensing array. *JGR. Atmos.* 124 (12), 12810823–12812823. doi:10.1029/2019JD031453

frontiers | Frontiers in Earth Science

TYPE Original Research
PUBLISHED 12 January 2023
DOI 10.3389/feart.2022.991893

OPEN ACCESS

EDITED BY
Yang Zhao,
China University of Petroleum, Beijing, China

REVIEWED BY
Subhayan Mukherjee,
John Deere, United States
Qiangqiang Yuan,
Wuhan University, China

*CORRESPONDENCE
Jun Lin,
lin_jun@jlu.edu.cn
Shaoping Lu,
lushaoping@mail.sysu.edu.cn
Tie Zhong,
zht@neepu.edu.cn

SPECIALTY SECTION
This article was submitted to Solid Earth Geophysics,
a section of the journal
Frontiers in Earth Science

RECEIVED 12 July 2022
ACCEPTED 31 October 2022
PUBLISHED 12 January 2023

CITATION
Dong X, Lin J, Lu S, Zhong T and Li Y (2023), A multi-scale dense-connection denoising network for DAS-VSP records.
Front. Earth Sci. 10:991893.
doi: 10.3389/feart.2022.991893

A multi-scale dense-connection denoising network for DAS-VSP records

Xintong Dong[1,2], Jun Lin[1,2]*, Shaoping Lu[3,4]*, Tie Zhong[5]* and Yue Li[6]

[1]Southern Marine Science and Engineering Guangdong Laboratory (Zhanjiang), Zhanjiang, China, [2]College of Instrumentation and Electrical Engineering, Jilin University, Changchun, China, [3]School of Earth Sciences and Engineering, Guangdong Provincial Key Lab of Geodynamics and Geohazards, Sun Yat-sen University, Guangzhou, China, [4]Southern Marine Science and Engineering Guangdong Laboratory (Zhuhai), Zhuhai, China, [5]Key Laboratory of Modern Power System Simulation and Control and Renewable Energy Technology of the Ministry of Education, China and College of Electric Engineering, Northeast Electric Power University, Jilin, China, [6]College of Communication Engineering, Jilin University, Changchun, China

Due to high spatial resolution, low cost, and wide bandwidth, distributed optical fiber acoustic sensing (DAS) is regarded as a potential tool for data acquisition in vertical seismic profile (VSP) surveys. However, in real DAS-VSP records, desired signals are often seriously plagued by various noise, which does not appear in the conventional seismic data received by electronic geophones. Exploring a high-performing attenuation method for the background noise can significantly improve the quality of DAS-VSP records and has essential impacts on the following imaging and interpretation. Deep-learning-based methods, especially convolutional neural network (CNN), have shown remarkable performance in seismic data denoising. However, the conventional CNN-based methods may degrade when dealing with DAS-VSP records in low signal-to-noise ratio. In this study, we propose a novel multi-scale dense-connection denoising network (MDD-Net) to achieve high-accuracy processing of the complex DAS background noise. Unlike conventional multi-scale networks, MDD-Net utilizes widen convolution block to capture the multi-scale features of the analyzed data. On this basis, dense connection operations are employed to fuse the features and improve the network efficiency. Meanwhile, an enhanced spatial attention (ESA) block is designed to reinforce the features, which are helpful for noise suppression and weak signal recovery. Both synthetic and field DAS-VSP records are processed to verify the effectiveness of MDD-Net. Meanwhile, we also compare the denoising results with other competing methods. The experimental results demonstrate that MDD-Net can significantly attenuate the complex DAS background noise and restore the desired signals, even for the weak upgoing signals.

KEYWORDS

distributed optical fiber acoustic sensing, seismic exploration, deep learning, noise suppression, vertical seismic profile, weak reflection

1 Introduction

Distributed optical fiber acoustic sensing (DAS) is a novel acquisition method that uses the phase information of the scattered signals to receive the deformation induced by the seismic wave field (Spikes et al., 2019; Dong and Li, 2020). Compared with traditional geophones, DAS is superior in terms of recording resolution and acquisition cost, such as easy arrangement and high-observation density (Bellefleur et al., 2020; Feng and Li, 2022). Due to its advantages, DAS has begun to apply in seismic surveillance and seismic exploration. Moreover, some successful applications are reported in vertical seismic profile (VSP) data acquisition (Yu et al., 2016). Nonetheless, the weak scatter optical signals tend to be contaminated by the DAS background noise, resulting in a low signal-to-noise ratio (SNR) for field DAS data (Binder et al., 2020). In addition, rare studies focus on analyzing the properties of DAS noise, which has become one of the obstacles to designing effective attenuation methods. To our knowledge, DAS noise is mainly composed of instrument noise and coupled interferences, representing differently from the noise in the geophones-acquired seismic records (Dong et al., 2020; Tian et al., 2022). Notably, some types of background noise, such as time-frequency variant noise and horizontal noise, uniquely exist in DAS records (Zhong et al., 2022a). Thus, we can deduce that it is challenging for the available denoising methods to deal with the DAS background noise. Attenuating the seismic background noise is significant for the following process, such as seismic inversion and interpretation. Therefore, research on effective approaches to suppress the DAS background noise has attracted increasing attention in the seismic data processing.

To suppress the DAS background noise, some attempts are put into practice to improve the data quality. However, due to the short development time of DAS technology, only some simple denoising methods, such as weighted-mean stack (Kobayashi et al., 2020) and linear filtering techniques (Soto et al., 2016), are applied to the issue of background noise suppression. In addition, the denoising performance for these methods may degenerate when confronted with complex DAS data. Although the denoising issues for DAS data have not been extensively studied, we still can get references from similar research in conventional seismic data processing. The conventional denoising methods can be roughly divided into five categories according to the denoising principles, including classical methods, time-frequency-based methods, decomposition methods, sparse transform methods, and diffusion filtering. Here, the classical methods refer to the methods derived from Applied Mathematics and Physics, such as Wiener filtering (Mendel, 1977), median filtering (Huang et al., 2017), band-pass filtering (Stein and Bartley, 1983), and f-x deconvolution (Canales, 1984). All these methods attempt to utilize the differences between the signals and interferences in physical properties, such as propagation velocity and frequency components. To simplify the problem, these methods also make some prior assumptions, such as the noise should be stationary (Zhong et al., 2015). It means that these methods will suffer from degraded performance if the assumptions are not tally with the actual noise properties. Thus, the classical methods fall short of expectations when dealing with complex seismic data, although they are still widely used in the exploration industry due to their stableness and efficiency. Inspired by the classical methods, the denoising methods, which utilized the features of time-frequency plate, have been employed to cope with the seismic noise. The time-frequency-based attenuation methods, such as S-transform (Stockwell et al., 1996), short-time-Fourier-transform and time-frequency peak filtering (TFPF) (Xiong et al., 2014; Zhuang et al., 2015), outperform the classical methods in denoising capability. The good performances of these methods are built on good separation ability and appropriate threshold setting. However, the reflection signals always overlap with the background noise in the frequency domain, and these methods have very limited effects on the spectral aliasing noise (Wu et al., 2014). Similar to time-frequency-based methods, the noisy seismic data can also be sparse decomposed, thereby reconstructing the desired signals by leveraging the decomposition results. Typical decomposition methods, such as wavelet transform (WT) (Chakraborty and Okaya, 1995), empirical mode decomposition (EMD) (Bekara and van der Baan, 2009), and ensemble empirical mode decomposition (EEMD) (Gaci, 2016), can separate the effective signals and unwanted noise into different intrinsic modes or decomposition coefficients, then the noise-dominated components are discarded to recover the desired signals. Nonetheless, it is challenging to determine the optimal reconstruction strategy for the seismic records in low-SNR conditions, resulting in severe residual noise and signal amplitude loss (Dong et al., 2020). Besides, sparse transform methods, including but not limited to curvelet transform (Herrmann et al., 2008), shearlet (Liu et al., 2019), seislet (Liu et al., 2015), and dictionary learning method (Chen et al., 2016), are proposed to suppress the complex seismic noise. The basic principle for these methods is to take advantage of the differences within the sparse properties to recover reflection signals from the field noisy records. However, the huge computational cost becomes an obstacle to the widespread use of the corresponding methods, especially for the massive exploration data processing. Moreover, due to the parameter selection dilemma, some untrue information, such as false events, may be restored and mistaken for effective signals, bringing negative impacts on the subsequent processing of the seismic records (Zhong et al., 2020). To further improve the denoising capability, the diffusion filtering methods, such as fractal conservation law (Meng et al., 2015), fractional anisotropic diffusion (Zhou et al., 2016), and deep complex reaction-diffusion model (Zhang et al., 2022), are gradually applied in the complex seismic data processing. As we know, the denoising process has similarities

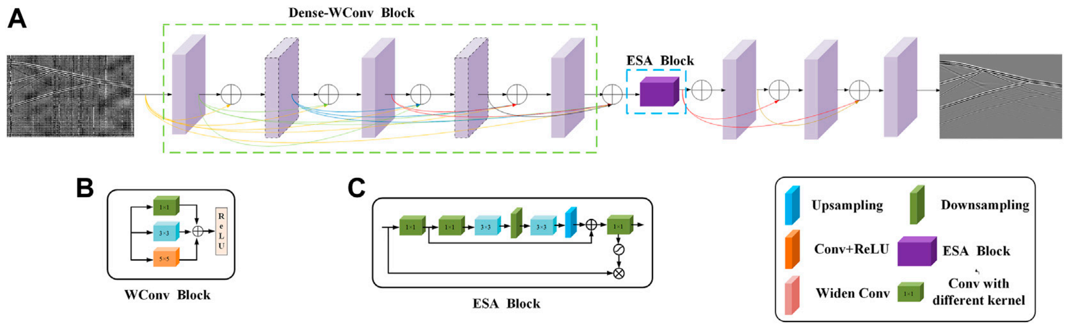

FIGURE 1
The Architecture for MDD-Net: **(A)** the architecture, **(B)** widen convolution block, and **(C)** ESA block.

TABLE 1 Physical parameters for the forward models.

Parameters	Specifications
Seismic wavelet	Ricker, single, double, symmetrical wavelets
Central frequency of seismic wavelets	10–80 Hz
Well depth	500–5,000 m
Trace interval	1 m
Sampling frequency	2,000 Hz
Wave velocity	1,000–4,500 m/s
Density	1,272–2,500 kg/m^3

to the thermal diffusion phenomenon, and the diffusion process can be modified by a given partial differential equation (PDE). Notably, we can control the noise attenuation and signal preservation ability by amending the diffusion term and anti-diffusion term of the PDE. Like time-frequency-based methods, diffusion filtering always shows its downside when attenuating spectral aliasing noise (Zhong et al., 2022b). Other denoising methods, including singular value decomposition (Oropeza and Sacchi, 2011), robust principal component analysis (RPCA) (Cheng et al., 2015), and local-feature-based methods (Bonar and Sacchi, 2012), are also introduced to suppress the complex seismic noise, however, their applications in DAS data processing are rarely reported. Overall, although the conventional denoising methods can improve seismic data quality to a certain extent, it still has an urgency to design powerful denoising methods to meet the requirements of DAS data processing.

In recent years, convolutional neural networks (CNN) have achieved significant breakthroughs with the development of hardware and optimal algorithms (Sun et al., 2018). In addition, some CNN-based denoising methods, such as generative adversarial network (GAN) (Wang et al., 2020) and feedforward denoising CNNs (DnCNNs) (Zhao et al., 2019), are also introduced to cope with the complex seismic noise. Inspired by these researches, deep learning networks are also utilized to achieve the DAS noise attenuation (van den Ende et al., 2021). On this basis, a series of important findings are obtained (Zhu et al., 2019). These denoising networks aim to establish a non-linear high-dimensional mapping relationship between desired signals and noisy records. Meanwhile, we can use training data to strengthen the learned mapping, and the final denoising models are obtained after the training process. Notably, unlike conventional methods, the denoising network can be considered a “data-driven” approach to adaptively accomplish complex seismic noise suppression without parameter fine-tuning (Dong et al., 2022). It is always true that CNN-based networks have advantages over conventional methods if appropriate training data can feed into the networks. Although CNN-based methods can provide excellent results, the denoising performance can be further improved since most networks only utilize single-scale information. Taking DnCNN as an instance, it only uses a simple architecture with unitary convolutional layers to extract the potential features of the analyzed data, leading to the degeneration of trained models for the seismic data with a low SNR (Ma et al., 2020). Another important factor that hinders the improvement in denoising capability is the generalization and authenticity of the training dataset (Zhong et al., 2022c). It is known that we cannot separate the clean signals from the real seismic records. Thus, finding an

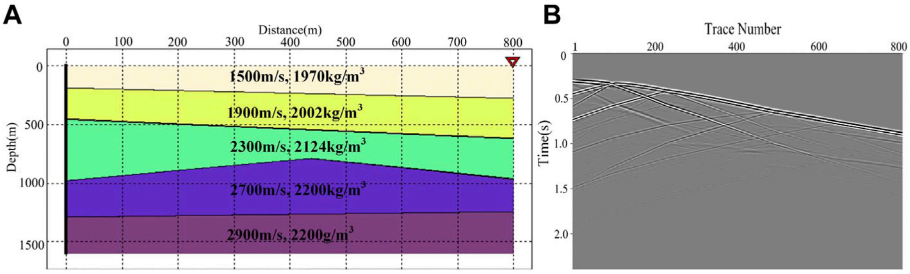

FIGURE 2
The forward model and corresponding synthetic DAS record: **(A)** the forward model, and **(B)** the synthetic DAS data.

appropriate way to construct the training dataset is challenging, having critical effects on the attenuation results.

To break through the predicament in DAS data processing, we propose a multi-scale dense-connection denoising network (MDD-Net) in this paper. Here, the multi-scale strategy for MDD-Net is accomplished by applying the widen convolution block. Compared with conventional convolution, widen convolution block utilizes the convolution layers with different kernel sizes to capture the multi-scale features of the analyzed seismic data. It means that the features neglected by the conventional networks, such as DnCNN, could be extracted and used by MDD-Net, thereby improving the representability of the effective features. On this basis, we employ dense connections to guide feature extraction and promote feature fusion. Meanwhile, we design an enhanced spatial attention (ESA) block to improve denoising performance by reinforcing discriminatory features. Furthermore, we combine the synthetic data and field DAS noise records to construct a high-quality training dataset to meet the network training requirements. For investigating the denoising capability, a detailed comparison with other popular methods is made, both for synthetic and field data processing. The experimental results indicate that MDD-Net can tell the desired signals from the complex DAS noise, even for the weak upgoing signals.

2 Network architecture and training process

2.1 Architecture for MDD-Net

Recently, multi-scale networks have achieved attention in signal processing due to their excellent performance. However, the feature interactions between different scales are time-consuming, resulting in the low efficiency of the corresponding networks. Here, a novel multi-scale strategy, combing widen convolution block with dense connection operations, is utilized in MDD-Net to ensure processing accuracy and improve network efficiency. Figure 1A shows the network architecture. Specifically, the widen convolution block can significantly reinforce the feature extraction ability and effectively reduce the elapsed time in the interaction process. On this basis, the dense connection operations are established to fuse the potential features. The feature extraction capability for MDD-Net can be strengthened by changing the connection fashion rather than stacking convolutional layers. We can use fewer convolutional layers to obtain excellent performance by applying dense connections, further reducing the network size. Besides, the ESA block is also applied to refine and enhance the effective features, minimizing the impact of negative samples and secondary features. The descriptions for the network components are shown below:

TABLE 2 Network parameters of MDD-Net.

Hyper-parameter	Specification
Optimizer	ADAM
Patch size	64×64
Batch size	64
Epoch number	50
Learning rate range	$[10^{-3},10^{-5}]$
Input channels	1
Total Layers	24
Convolution kernel size	3×3×64、1×1×64 or 5×5×64

2.1.1 Widen convolution block

As shown in Figure 1B, the widen convolution block is composed of three convolutional layers with kernel sizes of 1×1, 3×3, and 5×5. Therefore, widen convolution block can use different receptive fields to extract the multi-scale features. Unlike conventional multi-scale networks, we use novel convolutional layers to exact multi-scale features, not through multi-scale network architectures. Here, the output of the widen convolution block o_i can be expressed as:

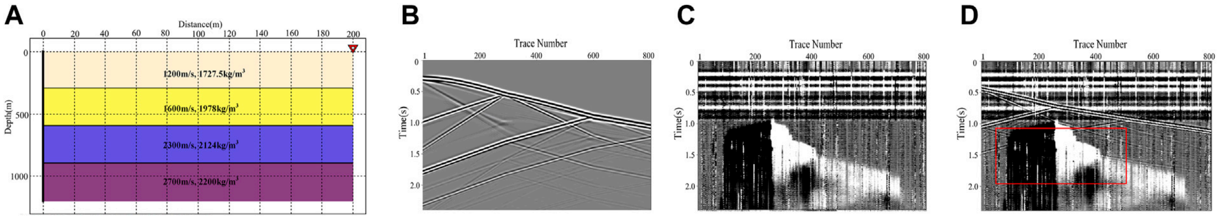

FIGURE 3
The generation of the noisy DAS data: **(A)** the forward model, **(B)** the clean synthetic record, **(C)** the added field DAS background noise, and **(D)** the noisy synthetic record.

TABLE 3 Network parameters of DnCNN, U-Net and RED-Net.

Hyper-parameter	DnCNN	U-Net	RED-Net
Optimizer	ADAM	ADAM	ADAM
Patch size	64×64	64×64	64×64
Batch size	64	64	64
Epoch number	50	50	50
Learning rate range	$[10^{-3},10^{-5}]$	$[10^{-3},10^{-5}]$	$[10^{-3},10^{-5}]$
Input channels	1	1	1
Total Layers	20	28	35
Convolution kernel size	3×3×64	3×3×64	3×3×64

$$o_i = \sum_{k=1,3,5} \omega_k x_i + \sum_{k=1,3,5} b_k \tag{1}$$

where x_i is the input data, while ω_k and b_k are the weight and bias parameters.

2.1.2 Dense connection block

The shallow features will have limited contribution on the deep features with the increase of the network depth, resulting in the loss of the features. To make full use of the features, the dense connection operations have been applied in MDD-Net. Specifically, the input of each module is also connected to the subsequent modules, serving as the guide information, achieving great feature fusion results and enhancing the accuracy of the captured features. In addition, a 1×1 convolutional layer, right after the widen convolution block, is applied to maintain the channel number to a proper size, thus further reducing the model complexity.

2.1.3.Enhanced spatial attention block

In this study, an ESA block is designed to refine the extracted features and improve the denoising performance, while the detailed architecture is depicted in Figure 1C. To minimize the computational cost, a 1×1 convolutional layer is utilized to reduce the channel number. On this basis, we use down-sampling and up-sampling blocks to modify the feature map size, and then the detailed features are captured by two 3×3 convolutional layers. Here, we use a sigmoid function to obtain the probability distributions for different features. Therefore, the attention mechanism is accomplished by multiplying the input features with the probability distributions, thereby enhancing the effective features. On the whole, the effects of the ESA block can be denoted as follows:

$$\begin{aligned} A_E\left(F^I\right) &= \sigma\left(W_1\left(F^I_{avg}\left(W_3\left(F^I_{up}\left(W_3\left(W_1\right)\right)\right)\right)\right)+1\right) \\ F^o &= A_E\left(F^I\right) \otimes F^I \end{aligned} \tag{2}$$

where F^I and F^O are the input and output of the ESA block. In addition, W_1 and W_3 denote the 1×1 and 3×3 convolutional layers, while σ represents the sigmoid function.

2.1.4 Denoising principle

In seismic data processing, we also assume that the noisy data y can be regarded as the combination of effective signals x and unwanted noise n, denoted as $y=x+n$ (Zhong et al., 2022a). After the training process, a non-linear mapping R is established between the noisy record and desired signals, and the estimated signals x_{est} are represented as:

$$x_{est} = R(y,\theta) \tag{3}$$

where network parameter $\theta=\{\omega, b\}$is composed of weight ω and bias b, respectively. For optimizing the learning process, a loss function based on l_2 norm is utilized, as shown below:

$$l(\theta) = \frac{1}{2M}\sum_{i=1}^{M}\left\|R(y_i,\theta) - x_i\right\| \tag{4}$$

where $\|\cdot\|$ is the Frobenius norm, while x_i and y_i represent the signal and noisy data patches in the training dataset. The optimal parameters θ_{opt} can be obtained by minimizing the loss function. On this basis, we can reconstruct the desired signal x_{opt}.

$$x_{opt} = R\left(y,\theta_{opt}\right) \tag{5}$$

2.2 Training process

2.2.1 Construction of the training dataset

As we know, the supervised network can derive the potential features from the training dataset. Thus, the

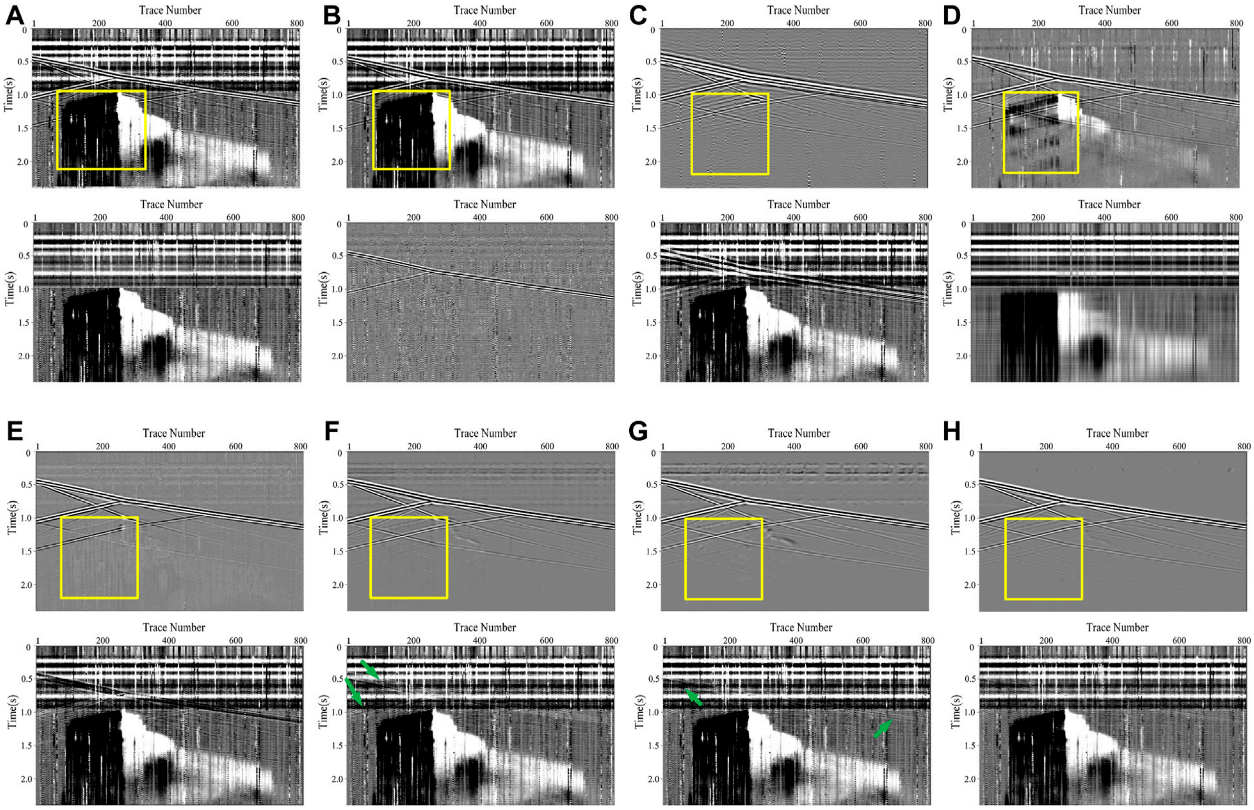

FIGURE 4
The processing results for different methods: **(A)** the clean data and the added DAS noise, and **(B–H)** represent the processing results of TFPF, BPF, RPCA, DnCNN, U-Net, RED-Net and MDD-Net, respectively.

quality of training data has a significant impact on the denoising performance of the trained models (Dong et al., 2022). In MDD-Net, we need to construct two training datasets, a signal set and a noise set, to support the network training process. Meanwhile, it is unable to separate pure signals from the field DAS records. To solve the problem of clean signal scarcity, the synthetic data, generated by forward modeling methods, is utilized to constitute the signal set. Specifically, we generate 60 geological models, considering the pre-acquired profile records. It can ensure that the geological models conform to the actual characteristics and guarantee the rationality of the generated synthetic data. By utilizing the elastic wave equation, the corresponding forward models are excited by the seismic wavelets with different dominant frequencies. On this basis, a series of synthetic records are obtained. Table 1 lists the detailed parameters for the forward models. Figure 2 gives a typical forward model and the generated clean signal records. We can observe that the synthetic record has similar properties to the field DAS data. Finally, the clean signal records are intercepted, and 17004 64×64 signal patches are randomly selected to compose the signal set. Similarly, we extract 19003 64×64 noise patches from the field DAS background noise records to compose the noise set. Then, both signal patches and noise patches are fed into the network, and the signal patches are taken as the label data.

2.2.2 Training process and experimental environment

The excellent performance of CNN-based methods mainly relies on the hardware condition and computational efficiency. In this study, the configuration of the experimental environment can be concluded as follows: a CPU (Intel i9-9990K, 3.6 Hz), an NVidia GeForce GTX 1080Ti, and a RAM (16 GB). All the experiments are conducted in Matlab 2016b, and the CNN-based methods use the same training dataset. In general, the batch size and the initial learning rate of the network are set to 32 and $[10^{-3}, 10^{-5}]$, respectively. Here, we use ADAM algorithm to optimize the training process, and the training process is composed of 50 epochs. Table 2 lists the network parameters for MDD-Net.

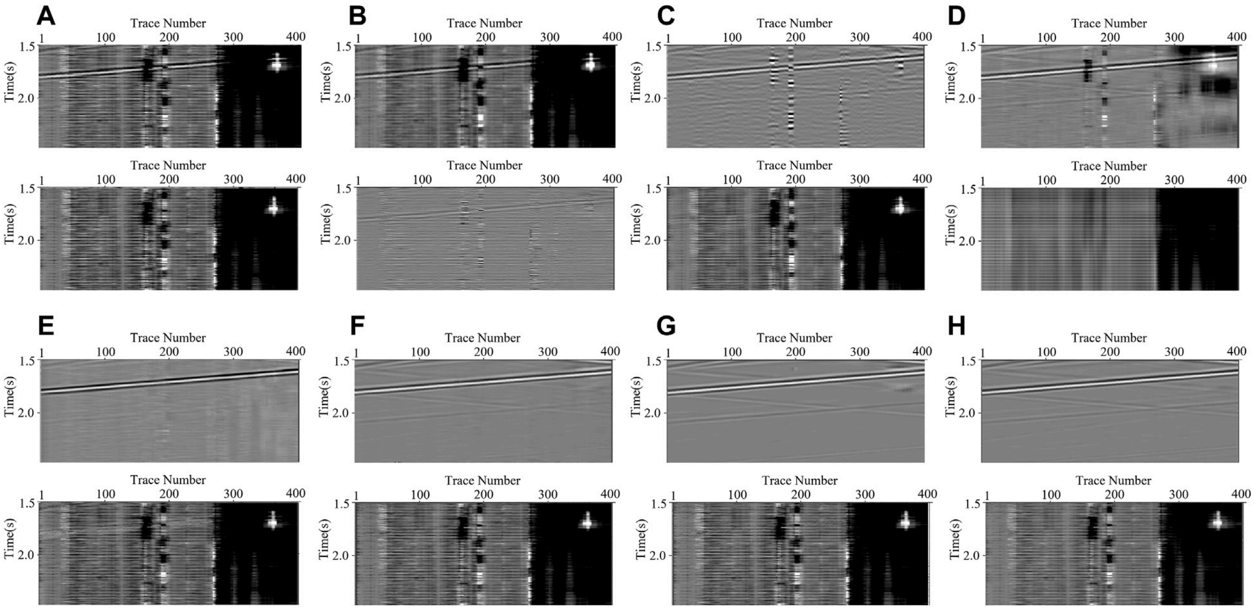

FIGURE 5
The enlargements for the results shown in the yellow blocks in Figure 4: **(A)** the enlargements for the clean data and the added DAS noise, and **(B–H)** represent the enlarged processing results of TFPF, BPF, RPCA, DnCNN, U-Net, RED-Net, and MDD-Net, respectively.

TABLE 4 The comparisons of SNR and RMSE for different attenuation methods.

Original record/ dB	TFPF		BPF		RPCA		DnCNN		U-Net		RED-Net		MDD-Net	
	SNR/ dB	RMSE	SNR/ dB	RMSE	SNR/ dB	RMSE	SNR/ dB	RMSE	SNR/ dB	RMSE	SNR/ dB	RMSE	SNR/ dB	RMSE
0	3.78	0.605	9.42	0.916	5.87	0.475	15.18	0.163	17.91	0.119	20.63	0.087	22.56	0.070
−2	2.06	0.737	7.31	0.403	4.19	0.577	12.02	0.234	14.37	0.178	17.66	0.122	19.98	0.094
−5	0.07	0.927	5.79	0.480	2.01	0.741	9.89	0.299	12.29	0.227	14.26	0.181	17.07	0.131
−7	−3.18	1.347	3.65	0.614	−1.56	1.182	7.76	0.382	11.01	0.263	11.99	0.235	14.37	0.179
−10	−7.88	2.315	1.07	0.826	−3.23	1.355	5.73	0.483	8.24	0.362	9.53	0.312	12.79	0.214

TABLE 5 The computational cost for different attenuation methods.

Specification	TFPF	BPF	RPCA	DnCNN	U-Net	RED-Net	MDD-Net
Training time (hour)	0	0	0	6.10	12.21	9.87	6.56
Processing time (s)	3.71	0.101	1.378	0.165	0.314	0.267	0.171

3 Processing results for synthetic data and field DAS-VSP records

3.1 Synthetic data analysis

For investigating the denoising performance, a synthetic record, shown in Figure 3B, is generated based on the forward model in Figure 3A. The forward model contains four formations with different geometric features. Notably, for a fair comparison, the forward model and the synthetic record are not included in the training dataset. On this basis, we add the field DAS noise data (Figure 3C) to the clean synthetic record, then the noisy record with an SNR of -5 dB (Figure 3D) is obtained. By observing the figures, the effective signals are seriously

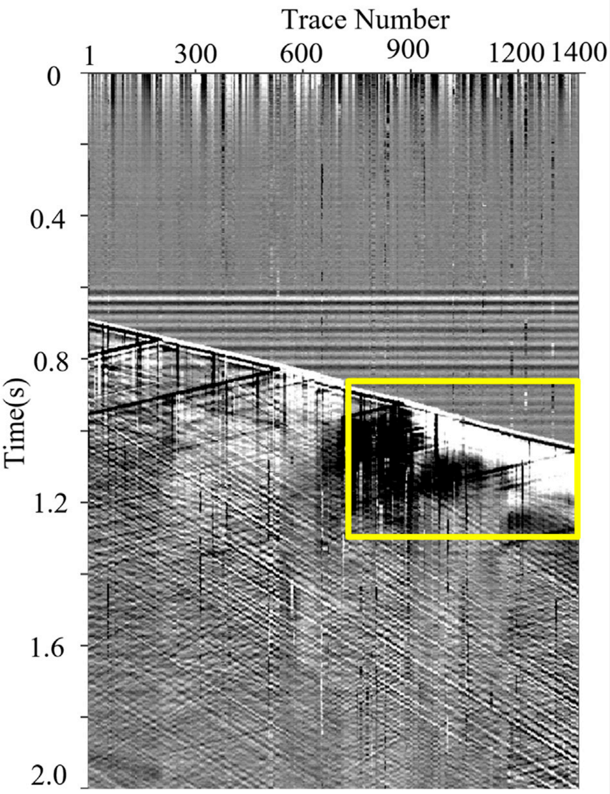

FIGURE 6
The field DAS-VSP record.

contaminated by the complex DAS noise. Thus, it is challenging to recover effective signals, especially for the weak events buried in the intense interferences.

3.1.1 Comparisons of denoising results

For getting compelling results, we choose some conventional methods and classical denoising networks as the competing methods to verify the effectiveness of MDD-Net. Here, the conventional methods mainly include BPF, TFPF, and RPCA. By analyzing the energy distribution of DAS data, the pass-band for BPF is set to [30–70 Hz], and the window length for TFPF is selected to 11. In addition, for RPCA, we set the weight on sparse error term in loss function to 0.025. Besides, the classical denoising network, including DnCNN, Residual Encoder-Decoder Networks (RED-Net), and U-Net, are also taken as the competing methods. Table 3 lists the corresponding network parameters. To facilitate comparison, we train the competing denoising networks with the same dataset, as MDD-Net used.

We use the aforementioned methods to process the noisy record shown in Figure 3D, and the denoising results are displayed in Figure 4. As shown in Figure 4B, TFPF fails to attenuate the DAS noise and only suppress some high-frequency components. Although BPF and RPCA, depicted in Figures 4C,D, can achieve better results, the recovered signals of BPF are disordered, and plenty of residual interferences still severely influence the recognition of the effective signals for RPCA results. On the contrary, the CNN-based methods outperform the conventional methods both in noise attenuation and signal preservation, such as the recovery of the weak upgoing signals. Overall, MDD-Net (Figure 4H) has the best performance in complex DAS noise suppression, compared with the results of competing CNN-based networks represented in Figures 4E–G. On this basis, we also enlarge the area marked by the yellow block for detailed comparisons. Notably, the effective signals are seriously contaminated by the time-variant noise, and no reflection events can be clearly observed in the area of interest. By observing the results shown in Figure 5, MDD-Net can recover the signals with great continuity and smoothness.

3.1.2 Quantitative comparison and computational cost analysis

In this study, we use SNR and root-mean-square error (RMSE) to quantitatively evaluate the denoising results for different methods (Zhao et al., 2019). In general, SNR is the energy ratio of clean signals and residual noise, and RMSE is the estimated errors between the clean signals and recovered results. Thus, SNR can reflect the noise attenuation capability, while small RMSE demonstrates that the corresponding method performs well in signal amplitude preservation. The definition equations for SNR and RMSE are shown below:

$$SNR(dB) = 10\log_{10}\left(\frac{\sum_{i=1}^{N}\sum_{j=1}^{M}u(i,j)^2}{\sum_{i=1}^{N}\sum_{j=1}^{M}\left[u(i,j)-v(i,j)\right]^2}\right) \quad (6)$$

$$RMSE = \sqrt{\frac{1}{MN}\sum_{i=1}^{N}\sum_{j=1}^{M}\left[u(i,j)-v(i,j)\right]^2} \quad (7)$$

where the $v(i,j)$ and $u(i,j)$ are the clean record and recovered signals. Meanwhile, M and N represent the time samples and the trace index, respectively. Here, we use the aforementioned methods to process the noisy synthetic records with different SNR. Table 4 shows the improved SNR and RMSE. By observing the results, we can obtain that the CNN-based networks precede the conventional methods in denoising capability since the improved SNR for the denoising networks surpass the conventional methods. Among these denoising methods, MDD-Net can obtain the most significant improvement in SNR, such as over 22 dB increment for the noisy DAS data. Thus, we can conclude that MDD-Net is effective in DAS noise attenuation and desired signal recovery. In addition, the computational cost for different methods is also analyzed, as listed in Table 5. Compared with conventional methods, the training process for CNN-based methods is time-consuming, such as that for U-Net is over 12 h. Among these denoising

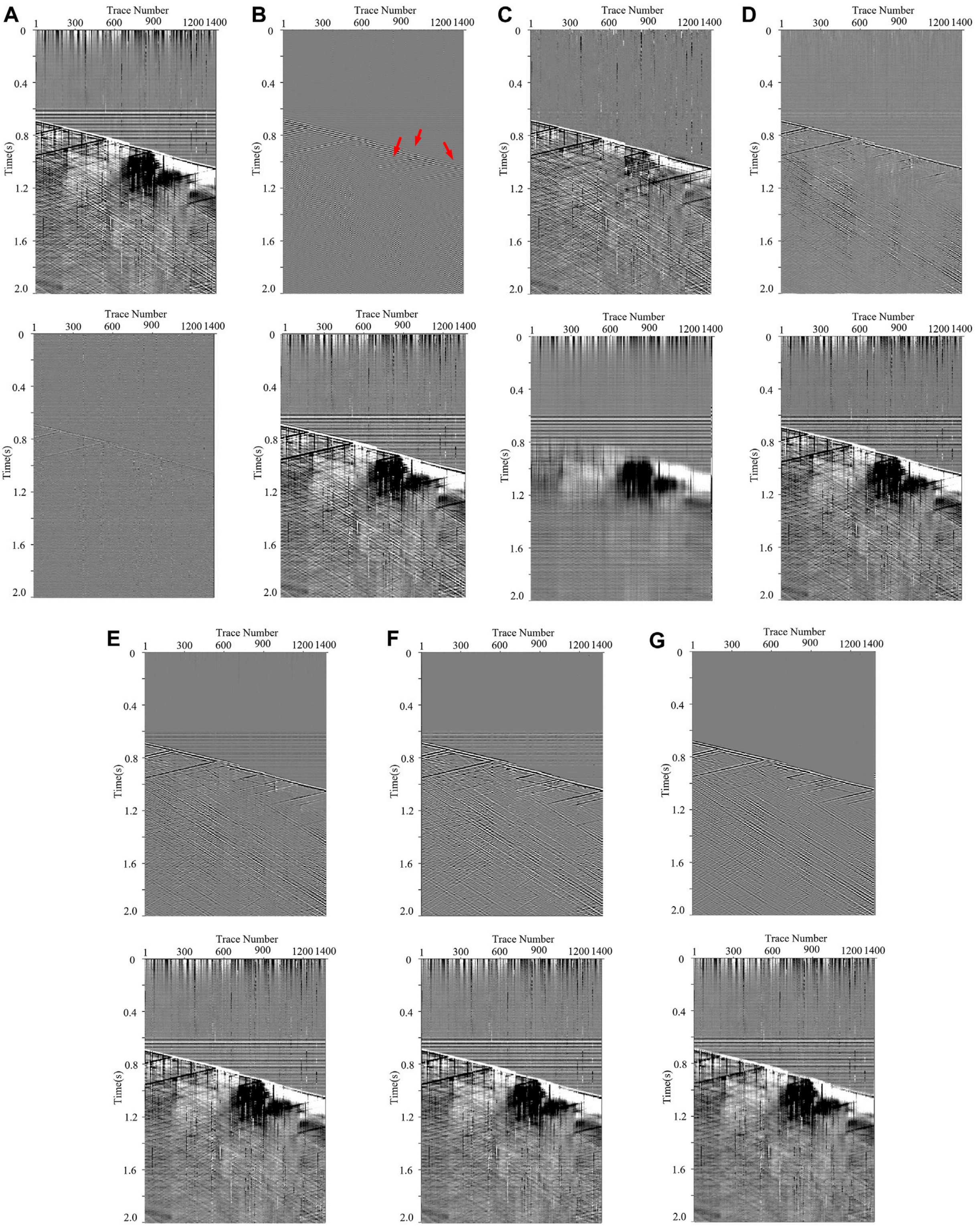

FIGURE 7
The processing results for the field DAS data in Figure 6: **(A–G)** are the denoising results (top subfigures) and filtered noise (bottom subfigures) obtained by TFPF, BPF, RPCA, DnCNN, U-Net, RED-Net and MDD-Net.

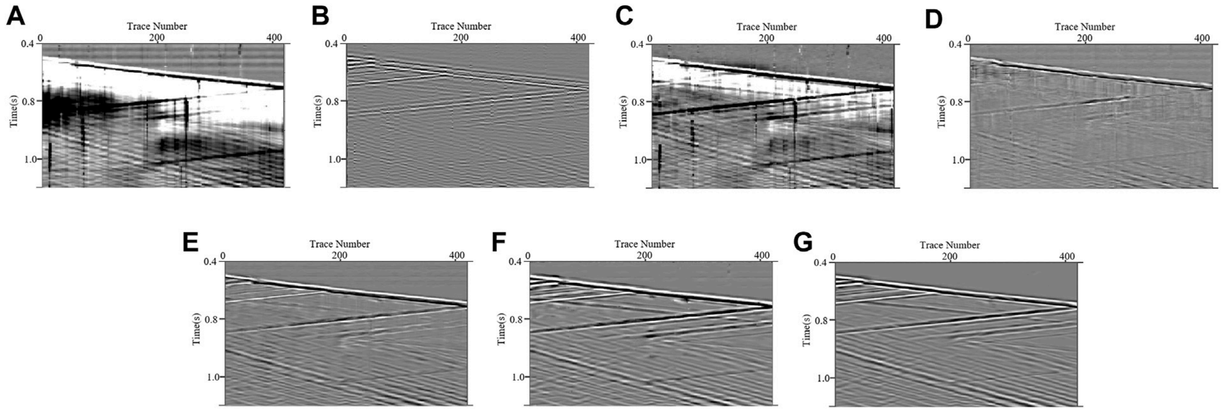

FIGURE 8
The enlargements for the results shown in Figure 7: **(A–G)** represent the enlarged denoising results obtained by TFPF, BPF, RPCA, DnCNN, U-Net, RED-Net and MDD-Net.

networks, MDD-Net has a similar backbone and number of convolutional layers with DnCNN. Avoiding the sampling operating in U-Net, their training costs are relatively small, such as those for DnCNN and MDD-Net are 6.10 and 6.56 h. Although the training time cannot be neglected, the processing time for these networks is competitive by comparing with conventional methods. Taking MDD-Net as an example, the average processing time is only 0.171 s, only inferior to BPF. Notably, CNN-based networks always have generalization ability. The trained models can be applied to plenty of DAS records with similar properties to the training datasets. From this view, the high computational cost is acceptable, and the situation will be relieved with the development of hardware and optimization algorithms.

3.2 Field data processing results

In this subsection, we process some field DAS-VSP records to verify the effectiveness of our proposed method. Figure 6 represents a field DAS-VSP record that contained 1400 trace records with a sampling frequency of 2500 Hz. It is shown that the field DAS data are affected by various types of interferences, resulting the challenges in detecting the weak upgoing signals. We apply the aforementioned methods to process the DAS record, and the corresponding results are shown in Figure 7. Here, for the CNN-based methods, we utilize the denoised models, having the best performance in synthetic data processing, to tell the desired signals from the unwanted noise. As shown in Figures 7A,B, TFPF and BPF cannot offer satisfactory denoising results. TFPF can only eliminate a small quantity of noise, and the obvious horizontal noise leakage (marked by the red arrows) remains in the denoising results of BPF. Meanwhile, although RPCA (Figure 7C) can attenuate the complex noise to some extent, the residual noise still influences signal recognition and negatively impacts the DAS data processing. Consistent with the synthetic data results, CNN-based networks, shown in Figures 7D–G, can separate the weak events from the intense interferences, representing better performance by comparing them with conventional methods. Notably, only MDD-Net can effectively suppress the horizontal noise owing to its efficient multi-scale strategy. On this basis, a comparison for the area of interest (the yellow block in Figure 6) is also conducted, and the corresponding results are plotted in Figure 8. It is shown that the conventional methods all have limitations in DAS background noise attenuation, while the denoising results, as shown in Figures 8A–C, suffer from the apparent residual noise. In contrast, CNN-based methods, plotted in Figures 8D–G, can almost eliminate the noise impacts and recover the signals. Compared with other CNN-based methods, MDD-Net has the best performance with the smooth recovered signals and a clean background.

Meanwhile, another field DAS-VSP record (Figure 9A) is processed to further investigate the generalization and denoising capability of MDD-Net. Notably, the effective signals in the DAS data are different from those in Figure 7. On this basis, the DAS data is processed by MDD-Net and other competing methods. Figures 9B–H give the denoising results. It is demonstrated that TFPF and BPF fail to provide acceptable attenuation results, similar to the finding reflected in Figure 7. Moreover, RPCA still cannot eliminate time-variant noise, and the noise leakage impedes the detection of weak events. Furthermore, although the CNN-based methods can effectively suppress the DAS background noise, the performances of the competing networks also need further improvement in attenuating the horizontal noise. By observing the results, MDD-Net (Figure 9H) outperforms the other denoising networks, while no conspicuous residual noise or signal leakage can be observed.

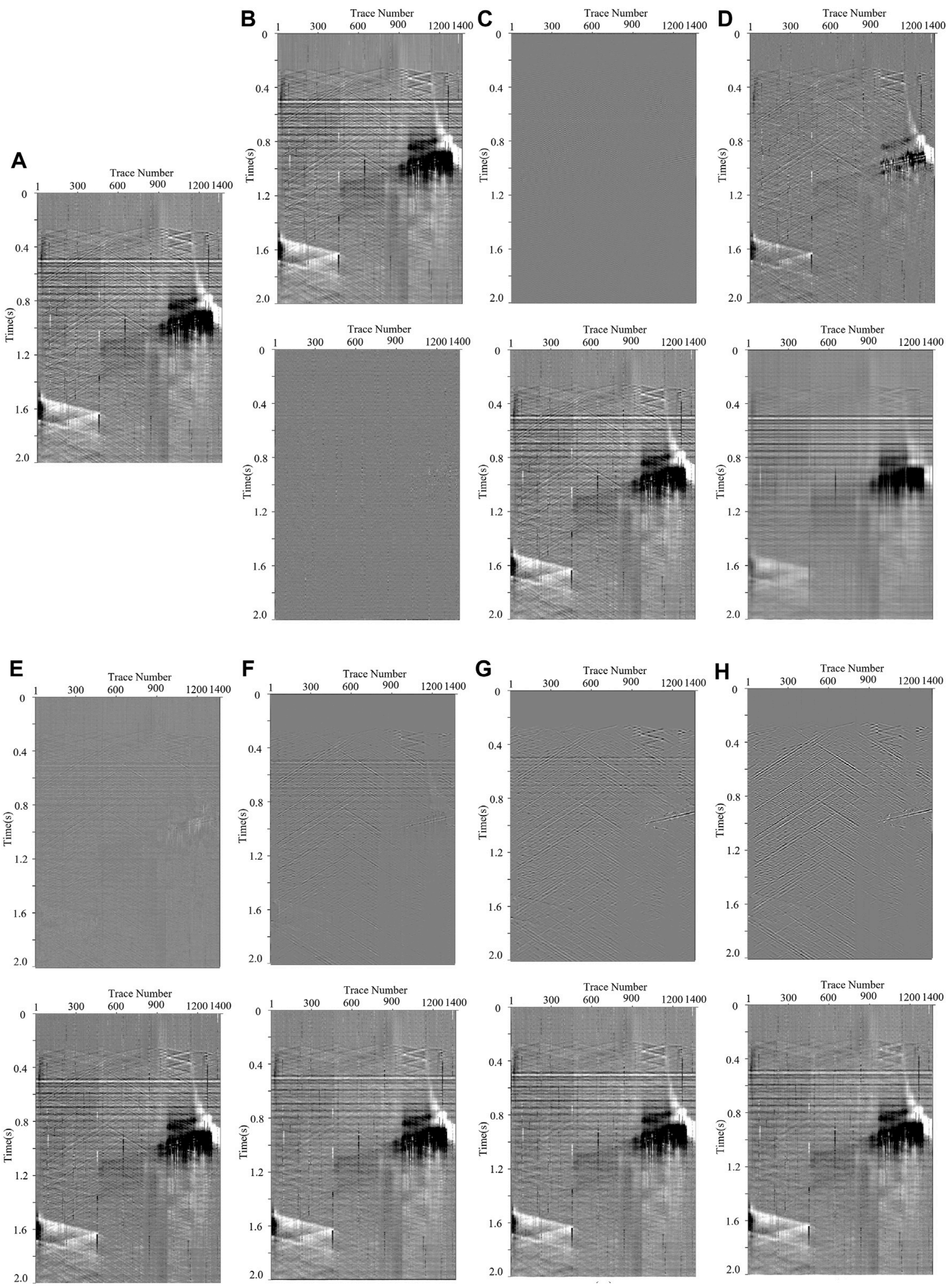

FIGURE 9
The denoising results for another field DAS-VSP record: **(A)** is the field DAS data, and **(B–H)** are the attenuation results after TFPF, BPF, RPCA, DnCNN, U-Net, RED-Net and MDD-Net, respectively.

In summary, all the corresponding results demonstrate that MDD-Net is a competent method to cope with complex DAS background noise.

4 Conclusion

In this study, a novel denoising network, called MDD-Net, is proposed for DAS-VSP data processing. In general, MDD-Net use the multi-scale strategy, combined widen convolution with dense connections, to accurately extract the potential features in seismic data. At the same time, an ESA block is also applied to fuse the features and enhance those beneficial to the denoising task. To guarantee the denoising performance, we generate high-quality training data according to DAS data properties. On this basis, synthetic and field DAS-VSP records are processed. We compare the denoising results with other popular denoising methods. It is shown that MDD-Net can achieve the best denoising performance with an SNR increment over 22dB, reflecting the superiority over the competing methods in complex DAS noise attenuation. Overall, the experimental results prove the effectiveness of the proposed methods, especially for the recovery of the desired signals seriously contaminated by the intense interferences. It means that the MDD-Net can significantly improve the quality of seismic data, bringing convenience for the following procedure of seismic data processing, such as imaging and inversion. However, the denoising ability of MDD-Net is related to the quality of the training data. The performance may degenerate if the seismic data has different properties from the training dataset.

Data availability statement

The original contributions presented in the study are included in the article/Supplementary Material, further inquiries can be directed to the corresponding authors.

Author contributions

XD was responsible for data curation, methodology and writing original draft preparation. JL contributed to the conceptualization and supervision. SL carried out the software, visualization, and validation. TZ carried out the methodology and reviewing and editing of the manuscript. YL helped with the visualization and supervision.

Funding

This work was financially supported by Key Project of Guangdong Province for Promoting High-quality Economic Development (Marine Economic Development) in 2022: Research and development of key technology and equipment for Marine vibroseis system Grants GDNRC[2022]29, National Natural Science Foundation of China under Grants 42204114 and 42074123, China Postdoctoral Science Foundation Grants 2021M701378, Natural Science Foundation of Jilin Province Grants 20220101190JC, and Research Project of Jilin Province Education Department under Grants JJKH20210094KJ.

Conflict of interest

The authors declare that the research was conducted in the absence of any commercial or financial relationships that could be construed as a potential conflict of interest.

Publisher's note

References

Bekara, M., and van der Baan, M. (2009). Random and coherent noise attenuation by empirical mode decomposition. *Geophysics* 74 (5), V89–V98. doi:10.1190/1.3157244

Bellefleur, G., Schetselaar, E., Wade, D., White, D., Enkin, R., and Schmitt, D. R. (2020). Vertical seismic profiling using distributed acoustic sensing with scatter-enhanced fibre-optic cable at the Cu-Au new afton porphyry deposit, British columbia, Canada. *Geophys. Prospect.* 68 (1), 313–333. doi:10.1111/1365-2478.12828

Binder, G., Titov, A., Liu, Y., Simmons, J., Monk, D., Byerley, G., et al. (2020). Modeling the seismic response of individual hydraulic fracturing stages observed in a time-lapse distributed acoustic sensing vertical seismic profiling survey. *Geophysics* 85 (4), T225–T235. doi:10.1190/GEO2019-0819.1

Bonar, D., and Sacchi, M. D. (2012). Denoising seismic data using the nonlocal means algorithm. *Geophysics* 77 (1), A5–A8. doi:10.1190/GEO2011-0235.1

Canales, L. L. (1984). "Random noise reduction," in *54th annual international meeting, SEG.*, 525–527. doi:10.1190/1.1894168

Chakraborty, A., and Okaya, D. (1995). Frequency-time decomposition of seismic data using wavelet-based methods. *Geophisics* 60 (6), 1906–1916. doi:10.1190/1.1443922

Chen, Y. K., Ma, J. W., and Fomel, S. (2016). Double-sparsity dictionary for seismic noise attenuation. *Geophysics* 81 (2), V103–V116. doi:10.1190/GEO2014-0525.1

Cheng, J., Chen, K., and Sacchi, M. D. (2015). Application of robust principal component analysis (RPCA) to suppress erratic noise in seismic records. *Seg. Tech. Program Expand. Abstr.* 34, 4646–4651. doi:10.1190/segam2015-5869427.1

Dong, X., and Li, Y. (2020). Denoising the optical fiber seismic data by using convolutional adversarial network based on loss balance. *IEEE Trans. Geosci. Remote Sens.* 59 (12), 10544–10554. doi:10.1109/TGRS.2020.3036065

Dong, X., Lin, J., Lu, S. P., Huang, X. G., Wang, H. Z., and Li, Y. (2022). Seismic shot gather denoising by using a supervised-deep-learning method with weak dependence on real noise data: A solution to the lack of real noise data. *Surv. Geophys.* 43, 1363–1394. doi:10.1007/s10712-022-09702-7

Dong, X., Zhong, T., and Li, Y. (2020). New suppression technology for low-frequency noise in desert region: The improved robust principal component analysis based on prediction of neural network. *IEEE Trans. Geosci. Remote Sens.* 58 (7), 4680–4690. doi:10.1109/TGRS.2020.2966054

Feng, Q., and Li, Y. (2022). Denoising deep learning network based on singular spectrum analysis—DAS seismic data denoising with multichannel SVDDCNN. *IEEE Trans. Geosci. Remote Sens.* 60, 1–11. doi:10.1109/TGRS.2021.3071189

Gaci, S. (2016). A new ensemble empirical mode decomposition (EEMD) denoising method for seismic signals. *Energy Procedia* 97, 84–91. doi:10.1016/j.egypro.2016.10.026

Herrmann, F. J., Wang, D., Hennenfent, G., and Moghaddam, P. (2008). Curvelet-based seismic data processing: A multiscale and nonlinear approach. *Geophysics* 73 (1), A1–A5. doi:10.1190/1.2799517

Huang, W., Wang, R., Gong, X., and Chen, Y. K. (2017). Iterative deblending of simultaneous-source seismic data with structuring median constraint. *IEEE Geosci. Remote Sens. Lett.* 15 (1), 58–62. doi:10.1109/LGRS.2017.2772857

Kobayashi, Y., Uematsu, Y., Mochiji, S., and Xue, Z. (2020). A field experiment of walkaway distributed acoustic sensing vertical seismic profile in A deep and deviated onshore well in Japan using A fibre optic cable deployed inside coiled tubing. *Geophys. Prospect.* 68 (2), 501–520. doi:10.1111/1365-2478.12863

Liu, J., Gu, Y., Chou, Y., and Gu, J. F. (2019). Seismic random noise reduction using adaptive threshold combined scale and directional characteristics of shearlet transform. *IEEE Geosci. Remote Sens. Lett.* 17 (9), 1637–1641. doi:10.1109/LGRS.2019.2949806

Liu, Y., Fomel, S., and Liu, C. (2015). Signal and noise separation in prestack seismic data using velocity-dependent seislet transform. *Geophysics* 80 (6), WD117–WD128. doi:10.1190/GEO2014-0234.1

Ma, H., Yao, H., Li, Y., and Wang, H. (2020). Deep residual encoder-decoder networks for desert seismic noise suppression. *IEEE Geosci. Remote Sens. Lett.* 17 (3), 529–533. doi:10.1109/LGRS.2019.2925062

Mendel, J. (1977). White-noise estimators for seismic data processing in oil exploration. *IEEE Trans. Autom. Contr.* 22 (5), 694–706. doi:10.1109/TAC.1977.1101597

Meng, F., Li, Y., Wu, N., Tian, Y., and Lin, H. (2015). A fractal conservation law for simultaneous denoising and enhancement of seismic data. *IEEE Geosci. Remote Sens. Lett.* 12 (2), 374–378. doi:10.1109/LGRS.2014.2342731

Oropeza, V., and Sacchi, M. D. (2011). Simultaneous seismic data denoising and reconstruction via multichannel singular spectrum analysis. *Geophysics* 76 (3), V25–V32. doi:10.1190/1.3552706

Soto, M. A., Ramírez, J., and Thévenaz, A. L. (2016). Intensifying the response of distributed optical fibre sensors using 2D and 3D image restoration. *Nat. Commun.* 7, 10870. doi:10.1038/ncomms10870

Spikes, K. T., Tisato, N., Hess, T. E., and Holt, J. W. (2019). Comparison of geophone and surface-deployed distributed acoustic sensing seismic data. *Geophysics* 84 (2), A25–A29. doi:10.1190/geo2018-0528.1

Stein, R. A., and Bartley, N. R. (1983). Continuously time-variable recursive digital band-pass filters for seismic signal processing. *Geophysics* 48 (6), 702–712. doi:10.1190/1.1441500

Stockwell, R. G., Mansinha, L., and Lowe, R. P. (1996). Localization of the complex spectrum: The S transform. *IEEE Trans. Signal Process.* 44 (4), 998–1001. doi:10.1109/78.492555

Sun, X., Kottayil, N. K., Mukherjee, S., and Cheng, I. (2018). "Adversarial training for dual-stage image denoising enhanced with feature matching," in *International conference on smart multimedia*. Springer, 357–366. doi:10.1007/978-3-030-04375-9_30

Tian, Y., Sui, J., Li, Y., Wu, N., and Shao, D. (2022). A novel iterative PA-MRNET: Multiple noise suppression and weak signals recovery for downhole DAS data. *IEEE Trans. Geosci. Remote Sens.* 60, 1–14. doi:10.1109/TGRS.2022.3170635

van den Ende, M., Lior, I., Ampuero, J. P., Sladen, A., Ferrari, A., and Richard, C. (2021). A self-supervised deep learning approach for blind denoising and waveform coherence enhancement in distributed acoustic sensing data. *IEEE Trans. Neural Netw. Learn. Syst.*, 1–14. doi:10.1109/TNNLS.2021.3132832

Wang, H., Li, Y., and Dong, X. (2020). Generative adversarial network for desert seismic data denoising. *IEEE Trans. Geosci. Remote Sens.* 59 (8), 7062–7075. doi:10.1109/TGRS.2020.3030692

Wu, N., Li, Y., Ma, H. T., and Xu, X. C. (2014). Intermediate-frequency seismic record discrimination by radial trace time–frequency filtering. *IEEE Geosci. Remote Sens. Lett.* 11 (7), 1280–1284. doi:10.1109/LGRS.2013.2292114

Xiong, M., Li, Y., and Ni, W. (2014). Random-noise attenuation for seismic data by local parallel radial-trace TFPF. *IEEE Trans. Geosci. Remote Sens.* 52 (7), 4025–4031. doi:10.1109/TGRS.2013.2278981

Yu, G., Cai, Z. D., Chen, Y. Z., Wang, X. M., Zhang, Q. H., Li, Y. P., et al. (2016). Borehole seismic survey using multimode optical fibers in A hybrid wireline. *Measurement* 125, 694–703. doi:10.1016/j.measurement.2018.04.058

Zhang, Y., Lin, H., Li, Y., Ma, H., and Yao, G. (2022). Low-frequency seismic noise reduction based on deep complex reaction–diffusion model. *IEEE Trans. Geosci. Remote Sens.* 60, 1–14. doi:10.1109/TGRS.2021.3086317

Zhao, Y., Li, Y., Dong, X., and Yang, B. (2019). Low-frequency noise suppression method based on improved DNCNN in desert seismic data. *IEEE Geosci. Remote Sens. Lett.* 16 (5), 811–815. doi:10.1109/LGRS.2018.2882058

Zhong, T., Cheng, M., Dong, X., and Li, Y. (2020). Seismic random noise suppression by using adaptive fractal conservation law method based on stationarity testing. *IEEE Trans. Geosci. Remote Sens.* 59 (4), 3588–3600. doi:10.1109/TGRS.2020.3016922

Zhong, T., Cheng, M., Dong, X., Li, Y., and Wu, N. (2022a). Seismic random noise suppression by using deep residual U-net. *J. Petroleum Sci. Eng.* 209, 109901. doi:10.1016/j.petrol.2021.109901

Zhong, T., Cheng, M., Dong, X. T., and Wu, N. (2022b). Seismic random noise attenuation by applying multiscale denoising convolutional neural network. *IEEE Trans. Geosci. Remote Sens.* 60, 1–13. doi:10.1109/TGRS.2021.3095922

Zhong, T., Cheng, M., Lu, S., Dong, X., and Li, Y. (2022c). Rcen: A deep-learning-based background noise suppression method for DAS-VSP records. *IEEE Geosci. Remote Sens. Lett.* 19, 1–5. doi:10.1109/LGRS.2021.3127637

Zhong, T., Li, Y., Wu, N., Nie, P., and Yang, B. (2015). A study on the stationarity and gaussianity of the background noise in land seismic prospecting. *Geophysics* 80 (4), V67–V82. doi:10.1190/GEO2014-0153.1

Zhou, Q., Gao, J., Wang, Z., and Li, K. (2016). Adaptive variable time fractional anisotropic diffusion filtering for seismic data noise attenuation. *IEEE Trans. Geosci. Remote Sens.* 54 (4), 1905–1917. doi:10.1109/TGRS.2015.2490158

Zhu, W., Mousavi, S. M., and Beroza, G. C. (2019). Seismic signal denoising and decomposition using deep neural networks. *IEEE Trans. Geosci. Remote Sens.* 57 (11), 9476–9488. doi:10.1109/TGRS.2019.2926772

Zhuang, G., Li, Y., Wu, N., and Tian, Y. (2015). Curvature-varying hyperbolic trace TFPF for seismic random noise attenuation. *IEEE Geosci. Remote Sens. Lett.* 12 (11), 2252–2256. doi:10.1109/LGRS.2015.2464233